7th Numerical Towing Tank Symposium

3.-5. October 2004

Hamburg/Germany

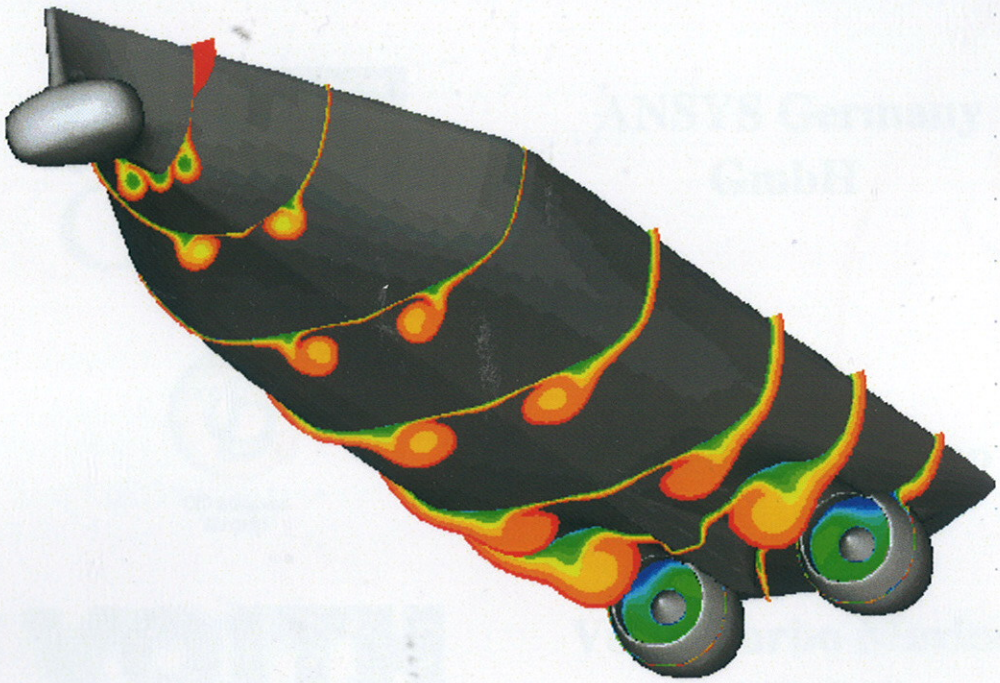

Volker Bertram, Heinrich Söding (Ed)

We thank our sponsors

Office of Naval Research (Dr. Pat Purtell)

Germanischer Lloyd

ANSYS Germany GmbH

CD adapco Group

Voith Turbo Marine GmbH & Co

Blohm & Voss

Fr. Lürssen Werft

INDEX OF PAPERS

(in alphabetical order of first author)

Tommi MIKKOLA
Time Accurate Simulation of Free Surface Flows in 2D Using Unstructured Grids

Christian.NIENHÜSER, Marco SCHNEIDER
Grid generation for ships and propellers

Jil-Pyo OK
Numerical Investigation of Scale Effects of the Wake Equalizing Duct

Tobias PERSSON, R.E. BENSOW, C. FUREBY, U. SVENNBERG
Flow around a Circular Cylinder at Re=3900 and 140000

S.H. SADATHOSSEINI, S.M. MOUSAVIRAAD, Mohammed S. SEIF
Numerical Simulation of Free Surface Flow around a Surface Piercing NACA0024 Hydrofoil

Bram STARKE
The Prediction of Scale Effects on the Ship Wave Systems using a Steady Iterative RANS Method

Arthur STÜCK, Gerhard JENSEN, Daniel SCHMODE
Yet Another Coupled Navier-Stokes Solver

Serge TOXOPEUS
Simulation and Validation of the Viscous Flow around the Series 60 HullForm at 10 Drift Angle

Sofia WERNER, Lars LARSSON, Björn REGNSTRÖM
Towards a CFD Validation Test Case - Wind Tunnel Test of a Winglet Keel

Yan XING-KAEDING, Gerhard JENSEN
RANSE Simulation of Flow and Ship Motion in Manoeuvring

Chi YANG, Francis NOBLESSE, Rainald LÖHNER
Comparison of Alternative Boundary-Integral Representations

Application of a RANSE Method to Predict Temperature Distribution and Gas Concentration in Air Ventilated Cargo Holds

Andreas Brehm, Ould El Moctar, Germanischer Lloyd, Hamburg/Germany, moct@GL-group.com

The transport of perishable goods in integral refrigerated containers has rapidly increased over the past 15 years. The advantage of the refrigerated container lies in the uninterrupted refrigerated chain of transport from the producer to the consumer. Normed container sizes allow in addition fast cargo handling. Ripening fruits produce thermal energy which needs to be extracted by the cooling aggregates to slow down the ripening process. The trend towards stowing refrigerated containers under deck poses additional challenges as there is no cooling by wind as for on-deck containers. Instead, the cargo holds need ventilation. The ripening process produces CO_2 which passes into the cargo hold. The cargo holds can be equipped with gas systems, which are able to reduce the oxygen content by blowing N_2 into the containers. Reducing the oxygen, it is possible to control the ripening process. This is denoted by *controlled atmosphere* (CA) or *modified atmosphere* (MA). Unavoidable leakages let escape a part of the CO_2 and N_2 mixture into the Cargo hold. To maintain safe work conditions for crews, the cargo holds are constantly ventilated with fresh air. Design of these ventilation systems is so far based on simple, analytical methods and sometimes model tests, Hanel (1996). More recently, CFD has been employed as modern design support tool.

We used the commercial RANSE solver CFX with the SST (shear stress transport) turbulence model, Vieser et al. (2002). The near-wall region was modeled with an automatic switch from wall functions to a Low-Re model. See Ferziger and Peric (1996) for a general discussion of near-wall treatment. CFX employs a multi-grid method to solve the system of equations. All computations shown here used unsteady simulations with time steps between 0.1 and 1s. A radiation model was not employed.

The box shape of containers leads also to geometrically simple cargo holds. Smaller details such as ladders, railings, brackets, thin pipes etc are neglected in the CFD model. The remaining cargo holds can be easily meshed using orthogonal block grids. The applications shown here used 2.2 million hexahedral cells, Figs. 1 and 2.

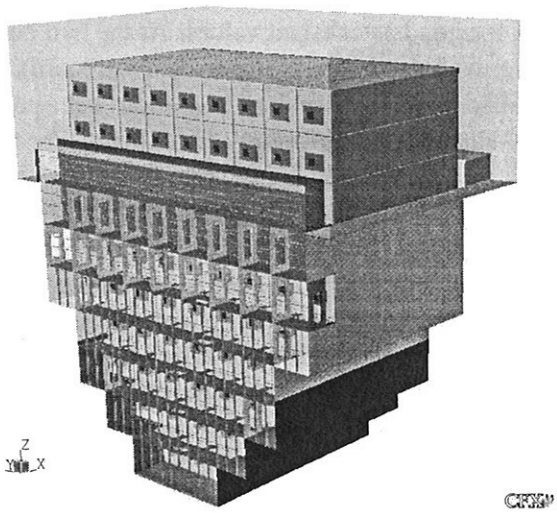

Fig.1: Example for geometric cargo hold model: Open Top cargo hold

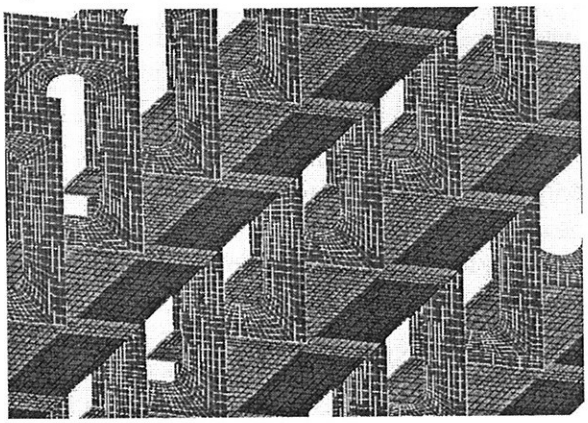

Fig.2: Detail of geometric grid: Transverse girders, gratings and manholes

As first example, we show a closed cargo hold ventilated by a pressure ventilation system (15000 m^3/h) each at port and starboard. Air is taken in above deck and pressed through a pipe system into the cargo hold. The port pipe system has three inlets, the starboard system four. At the simulation start, six refrigerated containers are air-cooled and the remaining 52 refrigerated con-

tainers are water-cooled. After a simulation time of 15 minutes, eight refrigerated containers in the sixth layer are switched from water to air cooling. The switch increases the heat transfer into the cargo hold considerably from 52.5 kW to 71.2 kW. Subsequently, temperatures in the hold rise.

Inlet boundary conditions were specified following anemometer measurements for all seven inlets. At all inlets, temperatures and inlet fluxes were specified as constant values. At the two outlets in the hatch coamings (port and starboard), a so-called opening boundary condition was specified, allowing either inflow or outflow. For an influx, temperature and pressure at the opening are specified. At the face surfaces of each container, a 1.5m^2 area was defined as heat transfer area, with heat transfer 3 kW for air-cooled and 0.66 kW for water-cooled containers. All other walls in the cargo hold were taken as adiabatic. Gratings in the transverse corridors in front of the container slots were modeled as porous materials. The resistance coefficient c_w=0.49 was estimated following Idelchik (1994). In addition, the momentum added by the ventilators of the air-cooled aggregates was simulated by defining additional source terms in the local momentum conservation equations. The additional momentum creates velocities up to 5 m/s in the fluid in front of the ventilators.

The first computation showed a quasi-steady condition after approximately 250 s. After switching the eight refrigerated containers to air-cooling, the heat transfer into the cargo hold is considerably increased, Figs.3 and 4.

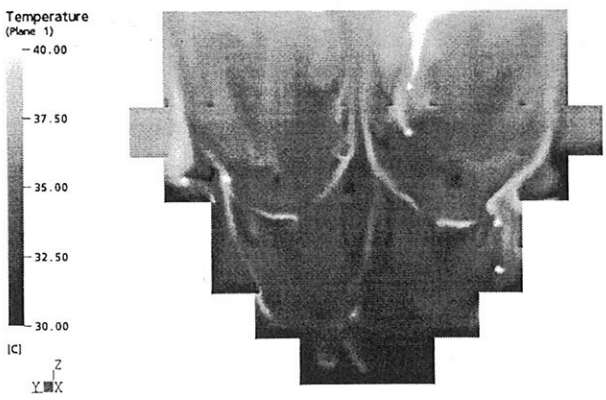

Fig.3: Temperature distribution: Six air-cooled container

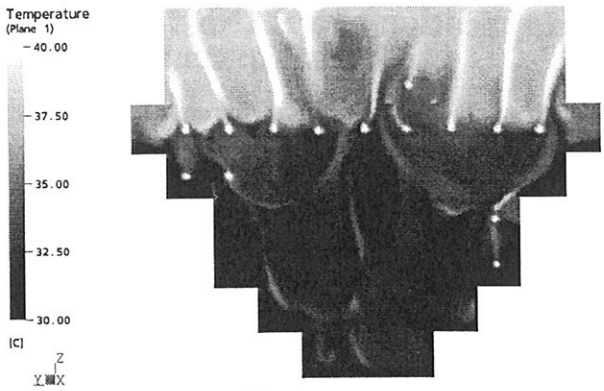

Fig.4: Temperature distribution: 14 air-cooled container

The second application concerns the cargo hold of an open-top container vessel. Open-top container vessels have often only a weak mechanical ventilation system relying predominantly on natural ventilation due to the apparent wind. The cargo hold was taken as completely filled with container stacks exceeding the main deck by two layers. A first simulation considered a stop of the vessel assuming all containers to operate on air-cooling transferring 12.5 kW heat each to the cargo hold. We further assumed that there is no mechanical ventilation. A second simulation considered 10 kn apparent wind speed downstream along the ship's longitudinal axis. A third simulation increased the apparent wind speed to 20 kn.

There is no clearly defined inlet and outlet as in the first case. At the sides and above the two top container layers, an air layer of approximately 2 m thickness is modeled.

At the outer boundaries of this computational domain an 'opening' boundary condition is imposed. For the second and third simulation, an inlet condition with corresponding influx is specified at the upstream domain boundary. We assumed a 'worst case' scenario where all refrigerated containers had to cool the transported cargo from ambient temperature down to transport temperature. This leads for each container to a heat flow of 8333 W/m^2 [= 12.5 kW], at the front faces of the containers. All other walls were assumed as adiabatic.

During the computations, temperatures were recorded at different grid points in the transverse corridor region, Fig.5. Temperatures decrease

with increased apparent wind speed. Fig.6 shows the temperature distribution at a cross section 0.2 m in front of the container front faces for apparent wind speed v = 0 kn. A chimney effect lets warm air rise in the center while cold air falls at the sides into the cargo hold. With increasing apparent wind speed, cooler air flows downstream through the gaps in the container stack convecting the heat downstream. Fig.7 shows the cooling effect in the cross section in front of the container stacks.

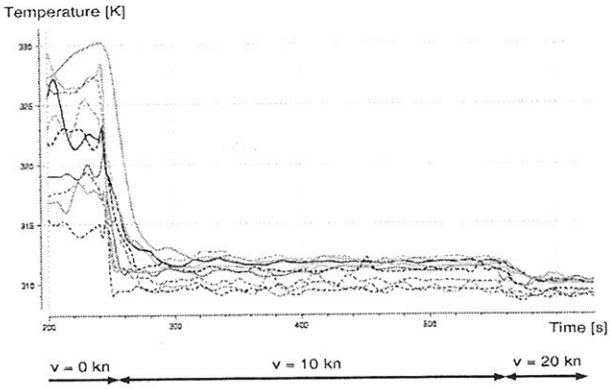

Fig.5: Temperature distribution at various grid points in the transverse corridor

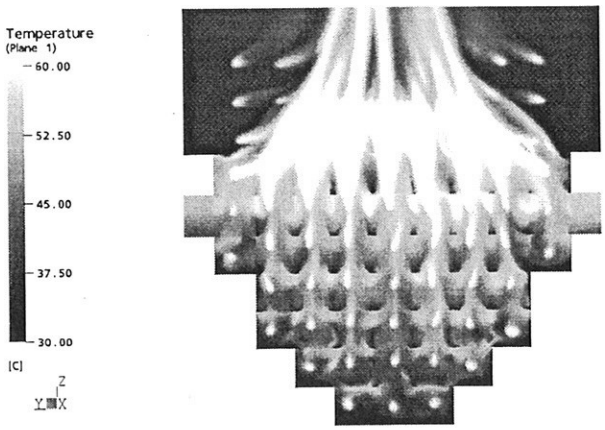

Fig.6: Temperature distribution in open top cargo hold, v_s=0kn

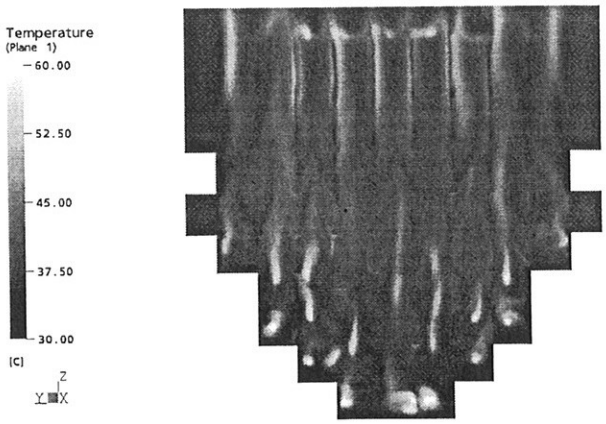

Fig.7: Temperature distribution in open top cargo hold, v_s = 10 kn

The final application concerns a cargo hold with a pure CO_2 volume of 160 m^3 at t=0 s at the bottom of the cargo hold. Two computations compare pressure respectively suction ventilation for the cargo hold with otherwise unchanged parameters.

For pressure ventilation, constant inlet velocities are specified at the ventilation openings, for suction ventilation correspondingly constant exit velocities. At the openings at the hatch coamings, we specify opening boundary conditions. At the warm front faces of the cooled containers, a constant heat flux was specified with 12.5 kW per container. All other walls are taken as adiabatic. The CFD simulation shows that the CO_2 (at 1.799 kg/m^3 at 25°C, 1bar much heavier than air with 1.184 kg/m^3 at 25°C, 1bar) is removed much faster from the cargo hold by the suction ventilation as expected. Figs.9 and 10 show the volume with a CO_2 concentration $\geq$ 4 volume percent at different simulation times. This concentration would induce nausea, headache, fuzzy vision and breathing problems in men. Concentrations of 12 volume percent CO_2 induce unconsciousness in short time and concentrations above 15% can be lethal. The suction ventilation, Fig.9, has removed the CO_2 after 180 s almost completely from the cargo hold. The pressure ventilation, Fig.10, has after 1000 s simulation time still a residual volume of 76m^3 with a CO_2 volume concentration of $\geq$4%.

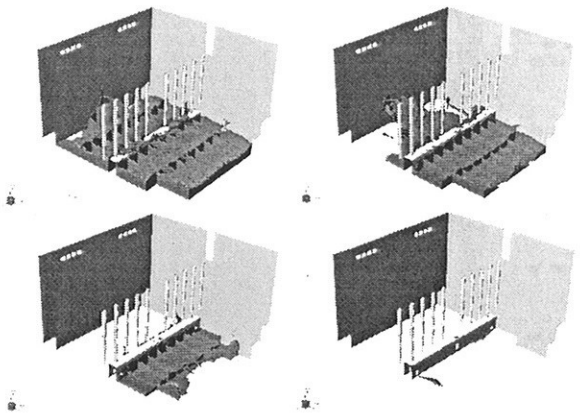

Fig.9: Gas volume with $\geq$4% CO_2 concentration for suction ventilation at times t=20, 50, 100, 180s

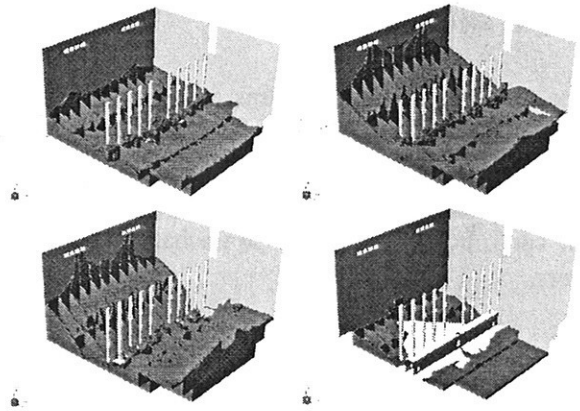

Fig.10: Gas volume with $\geq$4% CO_2 concentration for pressure ventilation at times t=20, 50, 180, 1000s

In conclusion, RANSE methods can be employed to improve the design of cargo holds in ships. Local effects of heat transport cannot be resolved with the coarse grids employed here. But global effects as the difference between pressure and suction ventilation and the influence of natural thermal buoyancy flow can be reproduced. Further validation of the method is desirable. Continued research is recommended to investigate e.g. the influence of cooling walls (below the waterline) and heating walls (above the water line due to sunshine).

References

HANEL, B.M. (1996), *Raumluftströmung*, 2^{nd} Ed., C.F.Müller Verlag, Heidelberg

VIESER, W.; ESCH, T.; MENTER, F. (2002), *Heat transfer prediction using advanced two-equation turbulence models*, CFX Technical Memorandum, CFX-VAL 10/0602, Otterfing

FERZIGER, J.H.; PERIC, M. (1996), *Computational Methods for Fluid Dynamics*, Springer-Verlag, Berlin

IDELCHIK, I.E. (1994), *Handbook of hydraulic resistance*, 3^{rd} Ed., CRC Press, Boca Raton

7^{th} Numerical Towing Tank Symposium
Hamburg, Oct. 2004

Prediction of Ship Motions in Waves Using RANSE

Jörg Brunswig (Technical University Hamburg-Harburg)
jbrw@gl-group.com
Ould el Moctar (Germanischer Lloyd)
moct@gl-group.com

Nomenclature

$\vec{F}$	=	forces acting on floating body
$\vec{M}$	=	moments acting on floating body
$\vec{x}_G$	=	origin of local reference frame
	=	centre of gravity of floating body
$\vec{\omega}$	=	vector of angular velocity
ψ	=	yaw angle
θ	=	pitch angle
ϕ	=	roll angle
$\vec{\alpha} = (\psi, \theta, \phi)^T$	=	rotations in general coordinates
$\mathbf{S}$	=	rotary matrix
$\mathbf{J_R}$	=	jacobian of rotation
$\vec{x}$	=	location vector with respect to global reference frame
$\vec{\xi}$	=	location vector with respect to local reference frame
$\mathbf{I_L}$	=	tensor of inertia
m	=	mass of floating body
Δt	=	time step
σ_j	=	time integration coefficients
γ	=	underrelaxation factor
μ	=	wave direction
$Z(x, y)$	=	wave elevation
$\hat{Z}$	=	wave amplitude
ω	=	wave frequency
k	=	wave number

1 Numerical Method

RANSE Solver

The main assumptions and the more significant features of the RANSE solver Comet are discussed here. For details, see e.g. [3]. The conservation equations for mass and momentum in their integral form serve as the starting point. The solution domain is subdivided into a finite number of control volumes that may be of arbitrary shape. The integrals are numerically approximated using the midpoint rule. The mass flux through the cell face is taken from the previous iteration, following a simple Picard iteration approach. The remaining unknown variables at the centre of the cell face are determined by combining a central difference scheme (CDS) with an upwind differencing scheme (UDS). The CDS employs a correction to ensure second-order accuracy for an arbitrary cell. Second-order central difference schemes can lead to unrealistic oscillations if the Peclet number exceeds two and if large gradients are involved. On the other hand, upstream difference schemes are stable, but lead to higher numerical diffusion. To obtain a good compromise between accuracy and stability, the schemes are blended. The three-time-level implicit method is used to integrate in time. Pressure and velocity are coupled by a variant of the SIMPLE algorithm. The system of equations is under-relaxed to dampen changes between iterations. All equations except the pressure correction equations are under-relaxed, using a relaxation factor of 0.8. The under-relaxation factor for the pressure correction was chosen between 0.2 and 0.4. The interface between water and air is determined using the two-phase volume of fluid method (VOF).

Equations of Motion

The equations of motion are solved in a Newtonian frame of reference which is either fixed or moved with constant speed. To simplify the formulation of angular momentum the origin of (O, ξ, η, ζ) lies at the centre of gravity of the floating body. The coordinate transformation between the Newtonian and the local frame of reference is defined as

$$\vec{x} = \vec{x}_G + \mathbf{S}\vec{\xi} \tag{1}$$

where the matrix $\mathbf{S} = \mathbf{S}_\psi \cdot \mathbf{S}_\theta \cdot \mathbf{S}_\phi$ is the result of three consecutive rotations.

The rotations used in this work are
1. Rotation around global z axis: yaw angle ψ
2. Rotation around new local η^* axis: pitch angle θ
3. Rotation around new local ξ axis: roll angle ϕ

The equations of motion can be then written as follows:

$$\vec{F} = \ddot{\vec{x}}_G \cdot m \tag{2}$$

$$\vec{M} = \mathbf{SI_L S^T}\dot{\vec{\omega}} + \vec{\omega} \times \mathbf{SI_L S^T}\vec{\omega} \tag{3}$$

The tensor of inertia given within the ship's local coordinate system is:

$$\mathbf{I_L} = \int_V \rho(\vec{\xi}) \begin{bmatrix} \eta^2+\zeta^2 & -\xi\eta & -\xi\zeta \\ -\xi\eta & \xi^2+\zeta^2 & -\eta\zeta \\ -\xi\zeta & -\eta\zeta & \xi^2+\eta^2 \end{bmatrix} dV \tag{4}$$

For the angular velocities and accelerations the transformations between global and general coordinates are:

$$\vec{\omega} = \mathbf{J_R}\dot{\vec{\alpha}} \tag{5}$$

$$\dot{\vec{\omega}} = \mathbf{J_R}\ddot{\vec{\alpha}} + \mathbf{K_R}\dot{\vec{\alpha}} \tag{6}$$

with

$$\mathbf{J_R} = \begin{pmatrix} 0 \\ 0 \\ \psi \end{pmatrix} + \mathbf{S}_\psi \begin{pmatrix} 0 \\ \theta \\ 0 \end{pmatrix} + \mathbf{S}_\psi \cdot \mathbf{S}_\theta \begin{pmatrix} \phi \\ 0 \\ 0 \end{pmatrix} \tag{7}$$

and

$$\mathbf{K_R} = \frac{\partial(\mathbf{J_R}\dot{\vec{\alpha}})}{\partial\vec{\alpha}} \tag{8}$$

Time Integration

The accelerations are obtained by solving equations (2) and (3) for $\ddot{\vec{x}}_G$ and $\dot{\vec{\omega}}$:

$$\ddot{\vec{x}}_G = \frac{1}{m}\vec{F} \tag{9}$$

$$\dot{\vec{\omega}} = \mathbf{SI_L^{-1} S^T}(\vec{M} - \vec{\omega} \times \mathbf{SI_L S^T}\vec{\omega}) \tag{10}$$

The values of the next time step are calculated by the following method:

$$\dot{\vec{x}}_G^{(i+1)} = \dot{\vec{x}}_G^{(i)} + \Delta t \sum_{j=i-1}^{i+1} \sigma_j \cdot \ddot{\vec{x}}_G^{(j)} \tag{11}$$

$$\vec{x}_G^{(i+1)} = \vec{x}_G^{(i)} + \Delta t \sum_{j=i-1}^{i+1} \sigma_j \cdot \dot{\vec{x}}_G^{(j)} \tag{12}$$

The superscript index indicates the time level, e.g. $\vec{x}_G^{(i)}$ denotes the position of the body at the previous time step. If $\sigma_{i+1} = 0$ the method is explicit and the above formulae can be directly used to integrate the motions. Otherwise the method is of implicit nature and equations (11) and (12) have to be modified to allow for the iteration process within a time step:

$$\begin{aligned} \dot{\vec{x}}_G^{(i+1,k+1)} = {} & \gamma[\dot{\vec{x}}_G^{(i)} + \Delta t(\sigma_{i+1} \cdot \ddot{\vec{x}}_G^{(i+1,k+1)} \\ & + \sum_{j=i-1}^{i} \sigma_j \cdot \ddot{\vec{x}}_G^{(j)})] \\ & + (1-\gamma)\dot{\vec{x}}_G^{(i+1,k)} \end{aligned} \tag{13}$$

$$\begin{aligned} \vec{x}_G^{(i+1,k+1)} = {} & \gamma[\vec{x}_G^{(i)} + \Delta t(\sigma_{i+1} \cdot \dot{\vec{x}}_G^{(i+1,k+1)} \\ & + \sum_{j=i-1}^{i} \sigma_j \cdot \dot{\vec{x}}_G^{(j)})] \\ & + (1-\gamma)\vec{x}_G^{(i+1,k)} \end{aligned} \tag{14}$$

As in the original equations the first superscript index denotes the time level. The second index indicates the outer iteration step. Omitting the second index indicates the value of the last outer iteration at the timestep denoted by the first index. If the underrelaxation factor is $\gamma < 1$ the solution of the new outer iteration is mixed with the value from the previous one. This will slow down the iteration process but can also stabilize it in case of highly accelerated motions, see [2]. The choice of the initial value at a new time step can also have an influence on the speed of the iteration process. The easiest choice is

$$\dot{\vec{x}}_G^{(i+1,1)} = \dot{\vec{x}}_G^{(i,n)} \tag{15}$$

where n is the number of outer iterations.
Using more than only the previous time step to obtain a starting value can improve the convergence rate, for example:

$$\dot{\vec{x}}_G^{(i+1,1)} = 2\dot{\vec{x}}_G^{(i,n)} - \dot{\vec{x}}_G^{(i-1,n)} \tag{16}$$

An integration algorithm using the latter as a starting value would be called a predictor-corrector method.

The method is applied to a simple differential equation, [1] to show the accuracy of different coefficients σ_j:

$$\begin{aligned} (m+a)\ddot{x} &= \sin(\omega t) - \kappa x \\ m = 1; a = 10; \omega = 6; \kappa &= 10 \end{aligned} \tag{17}$$

The analytical solution of (17) is:

$$\begin{aligned} x(t) &= \frac{\lambda\sin(\omega t) - \omega\sin(\lambda t)}{\lambda[\kappa - (m+a)\omega^2]} \\ \lambda &= \sqrt{\frac{\kappa}{m+a}} \end{aligned} \tag{18}$$

See Figure 1 for graphical representation.

The following sets of coefficients were tested without a predictor:

Method	σ_{i-1}	σ_i	σ_{i+1}
Euler-Forward	0	1	0
Euler-Backward	0	0	1
Expl. Trapezoid	0.5	0.5	0
Impl. Trapezoid	0	0.5	0.5

The results show the first order characteristics of all methods except the implicit trapezoid scheme. Increasing the time step by factor two results for all above listed time integration methods except the implicit trapezoid scheme in a two times higher error, see Figures 2,3,4. Dividing the time step by factor two decreases the error of the implicit trapezoid scheme by a factor of four indicating a second order scheme behaviour, See Fig. 5. It can also be seen that the errors of the second order implicit method are about one order of magnitude smaller than those of the other methods, using the same time step.

Boundary Conditions

At the inlet boundaries the velocities and the elevation of the free surface is given according to the linear wave theory:

$$Z = \hat{Z}\cos(\omega t - k\tilde{x}) \tag{19}$$

$$u = \omega\hat{Z}e^{kz}\cos(\omega t - k\tilde{x})\cos\mu \tag{20}$$

$$v = \omega\hat{Z}e^{kz}\cos(\omega t - k\tilde{x})\sin\mu \tag{21}$$

$$w = -\omega\hat{Z}e^{kz}\sin(\omega t - k\tilde{x}) \tag{22}$$

with $\tilde{x} = x\cos\mu + y\sin\mu$. The horizontal velocities u and v are of opposite sign in the air.

A hydrostatic pressure distribution is given at the outlet boundaries. To avoid wave reflection at these boundaries the mesh is coarsened towards the outlet resulting in a strong damping of the waves.

Special care is taken at the wall boundaries. Due to the fact that the boundary elements are moving, the wall velocity has to be set to the total velocity of the boundary element:

$$\dot{\vec{x}}_B = \dot{\vec{x}}_G + \vec{\omega} \times (\vec{x}_B - \vec{x}_G) \tag{23}$$

2 Numerical Results

Since parts of the method are still under development only a few simulations have been performed so far, all using the explicit time integration scheme. The first test case was taken from [2]. The 2d case had a geometry similar to the main section of a ship. The mesh was divided in two parts: a cylinder around the body that performs translations and rotations, and an outer part that does only the translations. The parts were connected by a sliding interface. The number of cells was a about 18000. No measurements exist for this case so the results could only be compared to those in [2]. The simulation showed similar results to [2] regarding the roll angle (a maximum roll angle of 25 to 30 degrees), see Fig. 8 and translation in z direction, Fig. 7, but they differed with respect to translations in x direction. This might be due to differences in numerical grid. Figure 6 shows the computational mesh. An example for the free surface and the body attitude can be seen in Fig. 9.

The second testcase (vessel 1) was a 70m vessel in headwaves of length $\lambda = 113m$ and wave amplitude $\hat{Z} = 3.5m$. The computational mesh had approximately 220000 cells. The RANSE results were compared to results obtained by the linear panel method GLPANEL, see Figures 10,11 and 12. The forces show some significant disturbances related to the numerical solution. A smoothing algorithm was used to dampen these superimposed high-frequency oscillations. The heave motion calculated with the presented method was smaller than the heave motion by GLPANEL. The reason might be the relatively coarse computational grid which leads to smaller wave amplitudes at the ship than those defined at the inlet boundary. Due to natural damping, one would expect a slightly smaller heave amplitude compared to the nonlinear inviscid GLPANEL results.

The last testcase (vessel 2) was a 120m vessel in waves of 1.5m height coming from 60°. The wavelength was $\lambda = 113m$. The results (Figures 13,14,15) were compared to towing tank results. The model tests were performed in irregular waves with a significant amplitude of 1.5m and a period of 8.5 seconds. The maximum significant pitch measured was about 1°, the significant roll amplitude was 9°. The maximum values were 1.4° and 14.5°, respectively. The heave motion was not measured.

The software of the presented method is in a very early development stage, so more work has to be done in the future to validate the results.

References

[1] R. Azcueta: Computation of Turbulent Flows Around Ships and Floating Bodies, Hamburg 2001

[2] I. Hadžić, Y. Xing, M. Perić: Simulation turbulenter Strömung und stömungsbedingter Bewegung schwimmender Körper, Hamburg 2002

[3] ICCM, User Manuel COMET Version 2.0, Institute of Computational Continuum Mechanics GmbH, Hamburg, 2000.

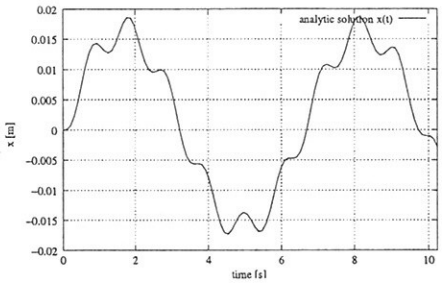

Figure 1: Analytical soultion of (17)

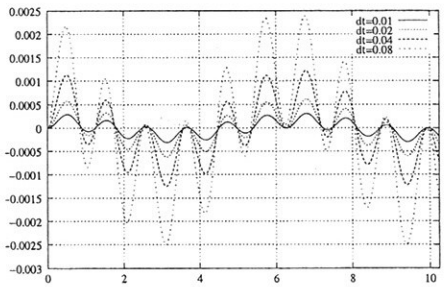

Figure 2: Solution of (17) using expl. Euler

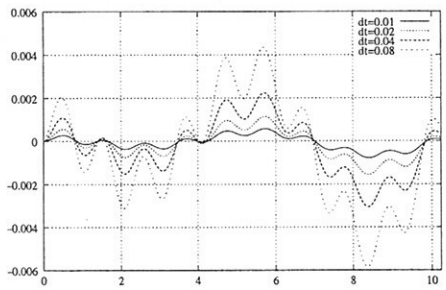

Figure 3: Solution of (17) using impl. Euler

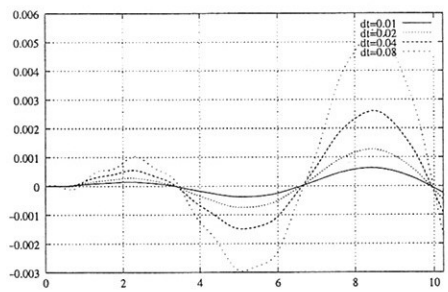

Figure 4: Solution of (17) using expl. trapezoid

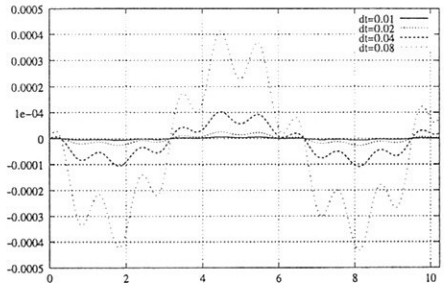

Figure 5: Solution of (17) using impl. trapezoid

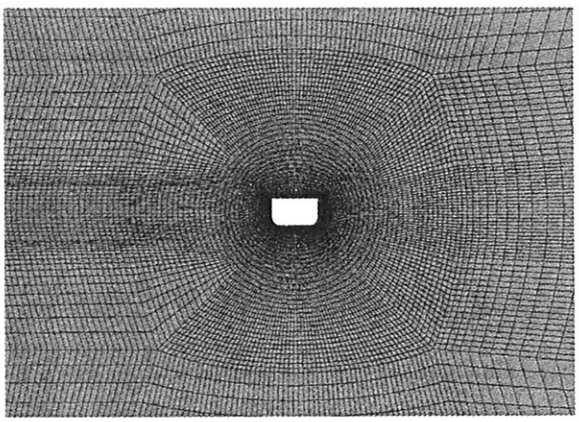

Figure 6: Numerical grid, 2d testcase

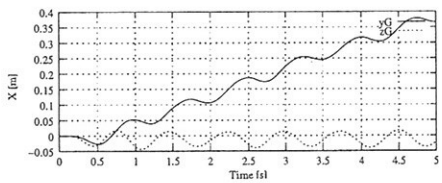

Figure 7: Translations, 2d testcase

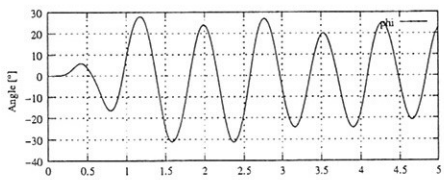

Figure 8: Roll Angle, 2d testcase

Figure 9: Free surface shape at t=3.0s, 2d test case

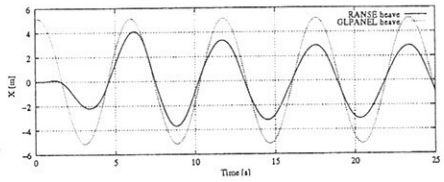

Figure 10: Heave motion, vessel 1

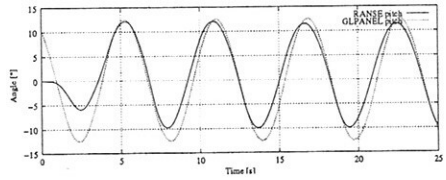

Figure 11: Pitch motion, vessel 1

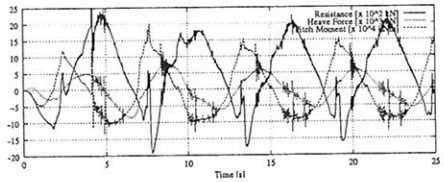

Figure 12: Forces and pitch moment, vessel 1

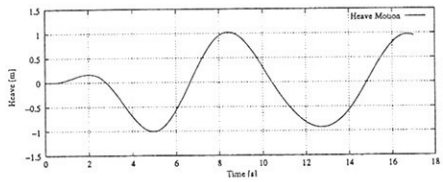

Figure 13: Heave motion, vessel 2

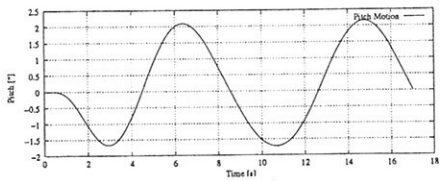

Figure 14: Pitch motion, vessel 2

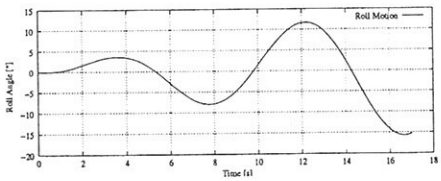

Figure 15: Roll motion, vessel 2

Numerical investigation of viscid flow around ship propeller with particular consideration of leading edge area and tip vortex modelling.

Tomasz Bugalski
tomasz.bugalski@cto.gda.pl
Paweł Dymarski
padym@cto.gda.pl
Marek Kraskowski
marek.kraskowski@cto.gda.pl
Ship Design and Research Centre, Gdansk, POLAND.

The topic of the presentation is RANS computation of the flow around the ship propeller, performed by Ship Design and Research Centre, Gdansk, Poland (CTO) within the framework of the LEADING EDGE project. The objectives of the computation are:

- to work out a quite simple meshing method for conventional propellers;
- to predict the K_T and K_Q;
- to investigate the grid requirements for detecting the leading edge vortex.

The RANS solver COMET was used for the computations. After few initial trials of the propeller computations performed by CTO, the following troubles were observed:

- it is very hard to apply the cyclic boundary conditions in COMET, either in case of non-matching grid or matching one; the solution diverges very fast;
- while using the grid without cyclic boundary conditions, but with non-matching connections of the blocks, the solution also diverges.

Taking these observations into account, there was generated a grid of relative low cells quality, but with perfectly continuous structure. The computations performed with this grid will allow to assess whether such grid is sufficient to predict the propeller hydrodynamic characteristics and the vortices around the leading edge and the tip.

Basic features of the grid:

- the commercial grid generator ICEM CFD-Hexa was used;
- the grid is generated around whole propeller;
- the grid has high density around only one of the blades, and it is coarse in the rest of the domain;
- the domain shape is cylindrical;
- number of cells: about 700 000;

The geometry of the propeller, received in the IGES format, was imported to GiD commercial code, where the outer boundaries of the domain were generated. The domain dimensions are:

- 1.5 D upstream,
- 2.5 D downstream,
- radius: 2.5 D,

where D is the propeller diameter.

Figure 1 shows the general idea of the meshing: in the inner region of the domain the cells are skewed according to the propeller's pitch.

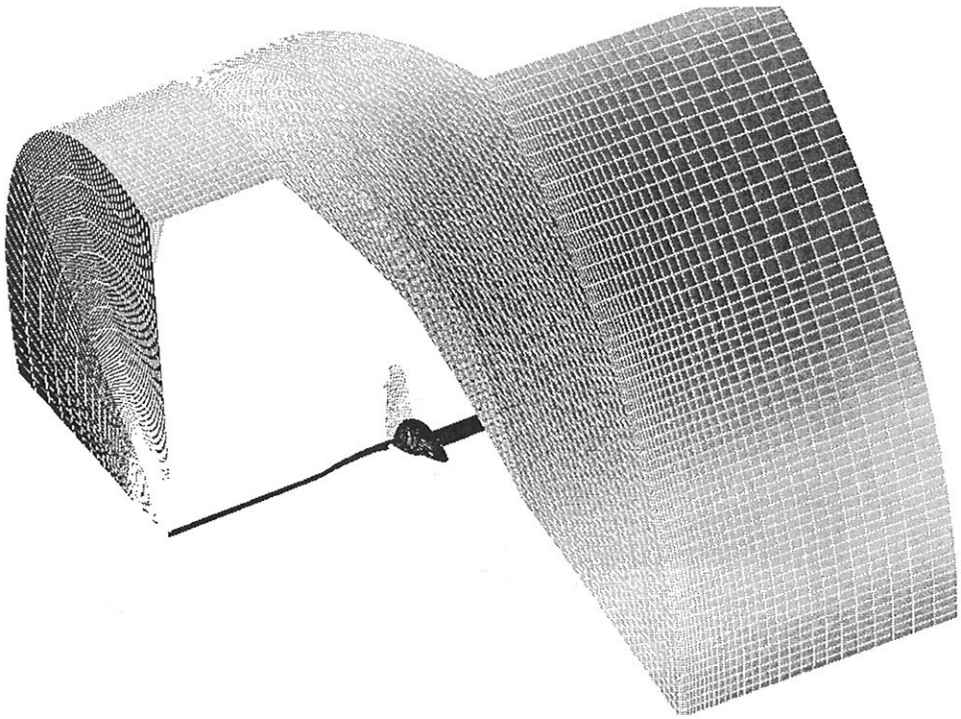

Fig.1. Circular sector of the domain.

In figure 2 one can see the structure of fine and coarse grid around the blades. Because of using the h-type grid around three blades, their geometry was slightly modified to improve the cells quality.

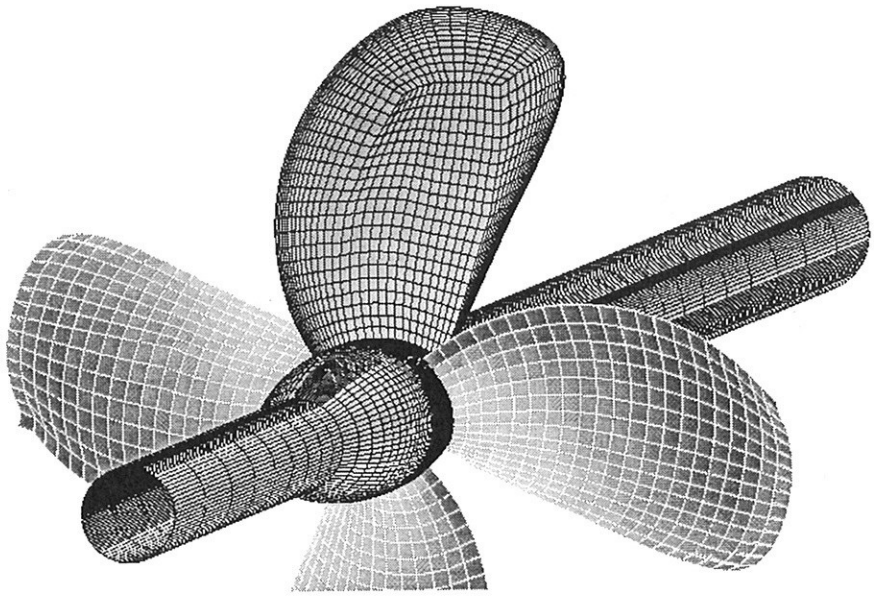

Fig.2. Surface grid details.

The hub shape was simplified in order to ease the grid generation.

Figure 3 shows the blocking structure, allowing to refine the grid around one of the blades, with keeping the grid structure continuous.

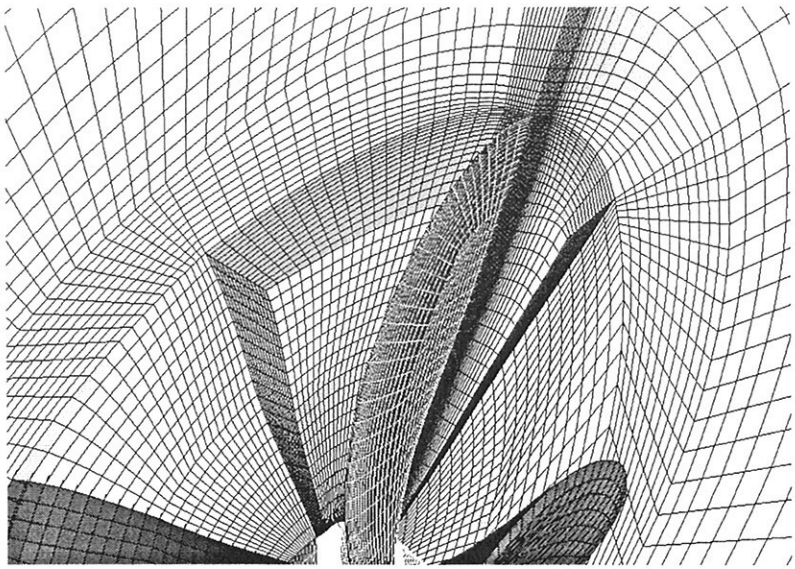

Fig.3. Transverse section of the grid.

The following settings of the solver was applied:

- rotating grid approach used;
- the boundary conditions are: velocity inlet, pressure outlet, slip wall on the outer boundary of the domain and on the shaft, no-slip wall on the blades;
- problem treated as a time–transient one;
- turbulence model: $k-\omega$.

A few sketches given below show, that the presented grid is able to produce the reasonable results. The work is still in progress, especially the influence of the grid cells distribution on the results should be checked.

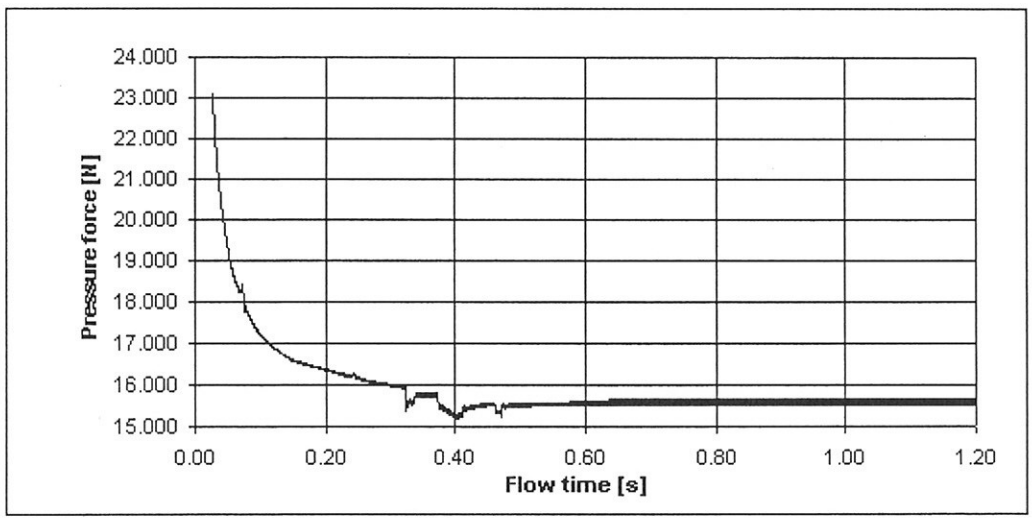

Fig.4. Convergence history of the pressure force.

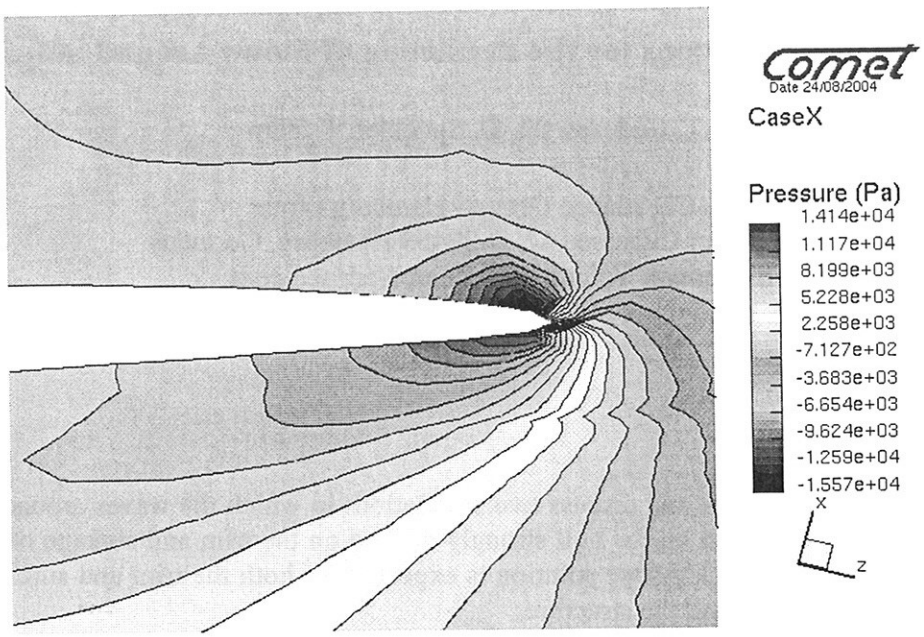

Fig.5. Pressure distribution in the leading edge region – radial section of the domain.

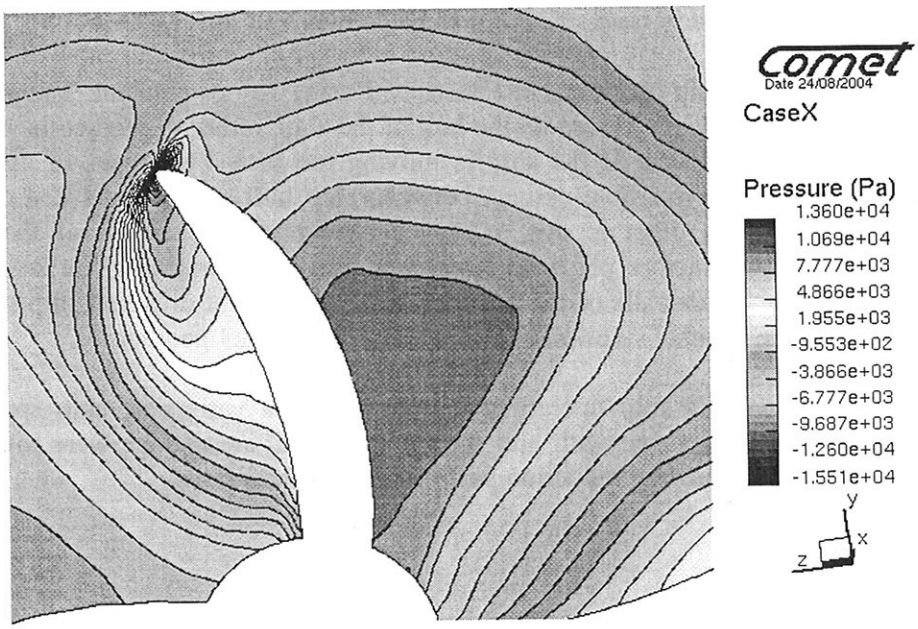

Fig.6. Pressure distribution around the blade – transverse section of the domain.

The Ship Design and Research Centre also works on the own–developed RANS solver SOLAGA, which will be tested by computing the foil flow firstly, than for the propeller. First results are expected to appear soon.

Comet Applications for the Prediction of Flows Around Ships

T. Chyczewski, D. Spuckler, T. Zorn

CD adapco Group - Hamburg office
Borsteler Chaussee 47, D-22453 Hamburg, Germany
email: Tobias.Zorn@de.cd-adapco.com

1. Introduction

In this paper we will present and discuss two simulations in which the waves around the ship and the pressure distribution on the hull strongly depend on the trim and sinkage of the ship. For these applications a steady-state solution is expected for both the trim and sinkage of the ship and for the waves around the structure.

A fast and efficient way of predicting the position of the ship is required in such applications to minimise simulation time. For the two applications presented in this paper, different methods to calculate the steady state solution will be shown.

The first application is a ship operating in a restricted waterway or channel. The goal of the simulation is not to calculate the forces on the hull of the ship, rather to predict the damage to the waterway, which may occur if the ship is moving too fast. Two types of damage can occur: one is related to the possible contact between ship hull and channel bed due to the squat of the ship and the other is due to waves hitting the side walls of the channel. Understanding these two factors plays an important role in determining the best material structure for the bed and sidewalls of the channel. Here we present different ship speeds and positions relative to the channel sidewall and also different channel geometries.

The second application is a ship operating in open sea at a variety of ship speeds. Two different designs of the ship, one with and the other without stern flaps were investigated. Here we are interested in the drag reduction performance of stern flaps.

2. Numerical Method

The RANS solver COMET from the CD adapco Group was used to calculate the free surface flow around the structures. The equations for mass, momentum and scalars are solved in their integral form using a finite-volume method and grids made of arbitrary control volumes. The integrals are numerically approximated using the midpoint rule. For the moving grid applications, the space conservation law is also taken into account. The free surface calculation is modelled by a VOF-like method, implemented with the High Resolution Interface Capturing scheme [1]. Because a steady state solution is expected, the so-called time marching approach was used to calculate the flow around the ship, free surface deformation, and ship position. In this approach convergence is accelerated by integrating in time without converging at each time step.

3. Setup for the ship in waterways

In reality, ships operate with different loads, but for this study, the fully loaded ship was expected to cause the highest damage to the waterway.

In the simulation the reference point was fixed to the ship. That means the ship hull is kept stationary while the fluid and channel walls are moving with the ship speed. Due to the restricted area of the channel and the limited space between the ship and the bottom of the channel, an iterative methodology was developed to find out the steady-state position of the ship.

After positioning the ship in the channel, the initial squat was calculated by balancing the force due to displacement with the force on wetted hull surface for the undisturbed water level. Then the free surface calculation was started with the full ship speed velocity. At each time step the force on wetted hull surface was compared with the force due to displacement. A differential volume was calculated to compensate the mismatch of the forces. This volume was then divided by the projection the wetted hull surface onto a horizontal plane and multiplied by a block coefficient to get an approximate sinkage.

After a significant reduction of oscillations of the forces acting on the hull at the beginning of the calculation and the formation of nearly steady wave patterns around the hull, the simulation was automatically stopped and the position of the ship was adapted to the new predicted position. For this adaptation a structured grid block was used at the channel bottom, which could be scaled in vertical direction, or if necessary layers of cells could be removed. The first two layers of cells at the bottom were here kept fixed to maintain acceptable y^+-values. The rest of the grid around the ship was of the structured C grid type with local refinements in areas of high gradients.

After moving the ship relative to the channel, the old solution was mapped onto the new grid. Then the simulation was continued. This explicit iterative process of recalculating the position of the ship and updating the grid to the new position relative to the channel was normally performed three to five times until the force on the wetted hull surface balanced the force due to displacement.

4. Results and discussions for a ship in waterways

The wave elevation around the ship is shown for the trapezoid channel *(Fig. 1)*. The influence of the two different positions, the centre and the off-centre position of the ship, can be seen in *Fig. 2a* and *Fig. 2b*. For the off-centre position, wave reflections and diffraction can be observed. The channel sidewalls are more often loaded but the magnitude of the loads are smaller than for the centre position. The sinkage for the position of the ship driving in the middle of the channel is also higher than for the off-centre position.

It can be seen that in these simulations the water level upstream in far distance of the ship is higher than downstream. It was found out during the simulations, that the energy loss of the water flow when passing the ship and forming the squat was too high to be neglected. Therefore, in a second step a propulsion system was added to the ship, modelled by body forces, to get closer to the real conditions of the operating ship *(Fig. 3)*. The magnitude of

body forces in the propeller plane was obtained by integrating the forces acting on the hull. Every 500 time steps the body forces in the propeller plane were updated. These body forces were than scaled along the radius of the propeller with the forces of a propeller for which measurements exist.

Fig. 4 shows the ship in a channel with propulsion system. By comparison with *Fig. 2*, one can see that the water level in front of and behind the hull is equal when ship propulsion is included in the model.

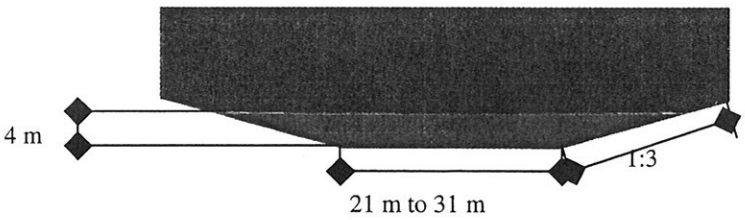

Fig. 1: Geometry of the trapezoid channel

Fig. 2a: Free surface elevation for ship in off-centre position

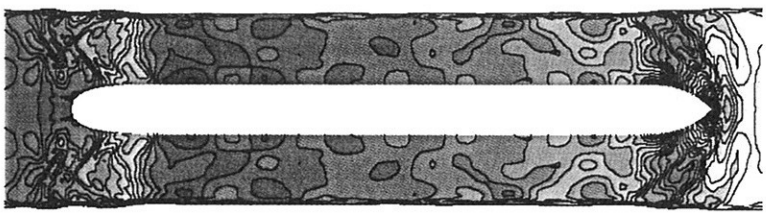

Fig. 2b: Free surface elevation for ship in centre position

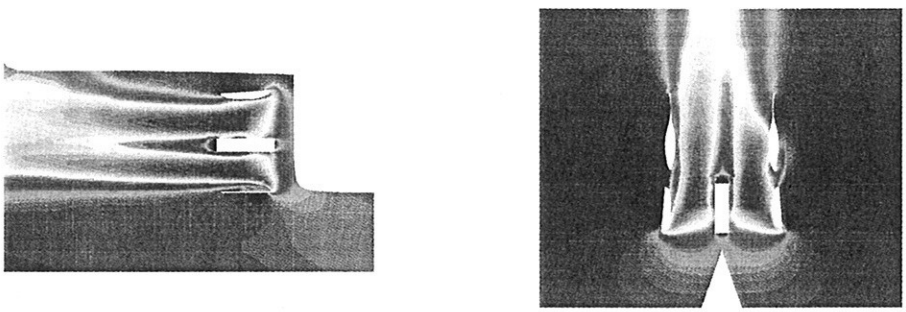

Fig. 3: Velocity magnitude in the area of the propulsion

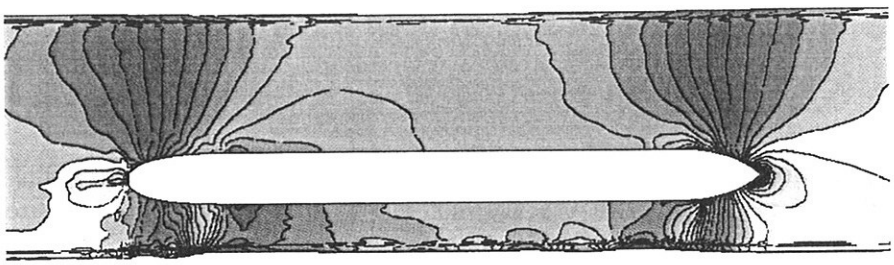

Fig 4: Free surface elevation with propulsion in the 31 m channel

5. Setup for a ship in deep water with and without stern flaps

Again the reference point is fixed to the ship. A six degrees of freedom (6-DOF) model was used [2] to calculate the trim and sinkage of the two different design studies. Four of the six degrees of freedom were held fixed and the other two were under-relaxed in motion in order to find the steady state position of the ship using the time marching approach. Each run consisted of three stages. First the sinkage and trim were kept fixed to get the initial free surface deformation around the hull. Then the heaving motion of the 6-DOF model was activated. After the oscillations for the heave motion were significantly reduced, the next degree of freedom was switched on. The ship was then also allowed to trim.

For the motion of the ship, a moving mesh approach was used. Here the single grid approach was taken, which means that the whole grid was moved. The boundary conditions, for example setting the water level at inlet, were then adapted to the new grid position after each time step. In order to do this, special boundary conditions were used to set the species concentration at the inlet to the solution domain. For each boundary element where all the vertices are below the undisturbed reference water level, the concentration of the scalar species representing water was set to 1 while for the ones completely above the reference water level, the concentration were set to 0. In the intermediate region the concentration was determined geometrically from the ratio of the submerged to total boundary element area. This method was implemented and works also for arbitrary polyhedral faces.

Slip wall boundary conditions were used as the sidewalls of the solution domain. The bottom of the solution domain was modelled using an inlet condition with the ship speed velocity; thus, inflow and outflow due to mesh motion during trim and heave motion is enabled. Downstream in far distance of the ship, the hydrostatic pressure corresponding to the undisturbed water level was set. For the ship hull itself the no-slip condition was used, with wall velocity components – which depend on the heave and trim motion – being updated at each time step. At the top surface, the atmospheric pressure in air was prescribed.

The grid was generated in proSTAR using the trimmed-cell approach with extrusion layers along walls [3]. In this process, a background grid is created and then arbitrarily refined in the areas of interest such as the high gradient regions near the ship hull or in ship wake. This grid is then cut by a blown-up hull surface and in this process polyhedral cells are locally generated. The final step is to create the extrusion layer of prisms between the ship hull and the trimmed surrounding mesh to resolve the boundary layer.

6. Results and discussions for a ship in deep water with and without stern flaps

The results for this ship will be presented and discussed. Due to the confidentiality of the data, the results could not be included in the abstract but will be shown and discussed in the presentation.

7. References

[1] "COMET - User Manual", CD adapco Group

[2] Hadzic I., Muzaferija S., Peric M. and Xing Y. Numerical Simulation of Interaction of a Floating Body and a Free-Surface Flow with Waves, Fifth World Congress on Computational Mechanics, Vienna/Austria 2002

[3] "Advanced Meshing" STAR-CD Version 3.20, CD adapco Group

Validated numerical results for 2D roll forced motion

Giuseppina Colicchio, Luigi Fabbri, Lanfranco Benedetti, Claudio Lugni

INSEAN, *The Italian Ship Model Basin*, Roma - Italy, g.colicchio@insean.it

1 Introduction

The prediction of roll motion is one of the most difficult task in the analysis of the general motion of ships. From a theoretical point of view, this is due to the fact that the roll motion is lightly damped and restored and to the fact that the roll natural period of conventional ship is very close to the rich regions in the wave energy spectrum. The coupling of this two factors can cause large amplitudes of roll oscillations even in moderate sea states. From a computational point of view, the difficulties are due to the role played by the vorticity and its damping, so that only full Navier-Stokes equations are able to model the roll behaviour properly. Moreover the damping of roll motion is highly influenced by the presence of bilge keels, this means that the proper modelling of these appendices is important.

Empirical method have been developed for the modelling of the appendices [6]. In particular in [4], the effects of several contributes to the roll damping terms have been examined. From a numerical point of view numerical predictions have been obtained in [1].

To properly capture the features of the flow around rotating patches of ships however dedicated 2D numerical and experimental investigations have been carried out in [10], [8] and [9]

Here we analyze 2D ship sections in order to understand the physical features developing in 3D. This work is a part of the cooperative project 6DOF-RANS with the US navy aiming to study the roll damping of ships and to develop unsteady RANSE codes. The choice of the radiation test allows a straightforward comparison with the numerical data.

In particular the results has been used to validate the modelling of the body. Usually a boundary fitted mesh is used to model the presence of bodies inside the fluid domain (see [7]). Such a mesh presents two fundamental drawbacks: a re-mesh is necessary every time the body moves, or the calculations have to be performed in the frame of reference of the body. Both these approaches can present some problems; more precisely, in the first case, the computation becomes inefficient if the body moves continuously and the second option becomes inapplicable if two bodies moving differently are present in the fluid domain. Here we adopt a fixed mesh and a special treatment of the position of the body.

2 Description of the problem and experimental set-up

In the following we study the velocity field around a 2D section of a ship corresponding to the station 17 of the Frigate DDG51 (INSEAN model C2340 $\lambda = 24.824$) as indicated in figure 1. The section is forced to oscillate in calm water around the point C, coincident with the center of gravity of the 3D model, with an angle

$$\alpha = \alpha_{max} \cos(\Omega t) \qquad \dot{\alpha} = -\alpha_{max}\Omega \sin(\Omega t) = -\Omega_{max} \sin(\Omega t) \tag{1}$$

where Ω_{max} is the maximum angular velocity. The immersion of the lower tip of the section is indicated with D and its distance from the centre of rotation C is the radius R.

Two pictures of the experimental set-up are also shown in figure 1. A $1m$ long cylindric fiberglass section (label 4 in picture) has been built using a CNC milling technique. To permit the

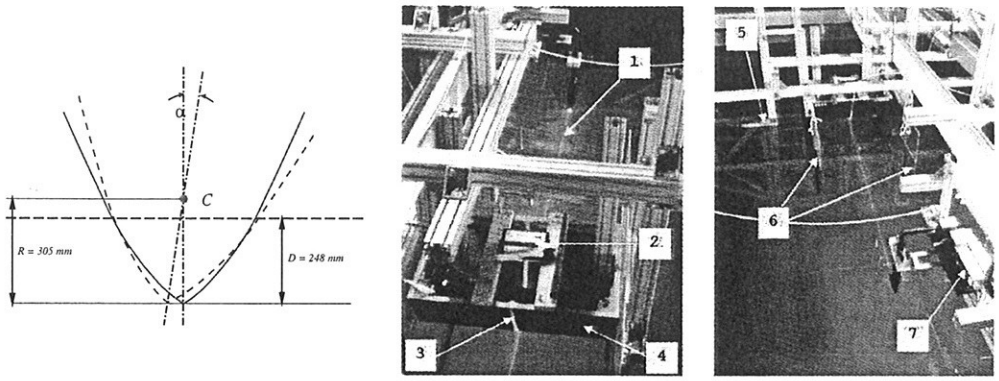

Figure 1: Left: Sketch of the problem and definition of the variables. Center and right: pictures of the experimental set-up, with 1. Laser beam, 2. Inclinometer, 3. Plexiglas sheet, 4. Model, 5. CCD Camera, 6. Plexiglas walls and 7. Laser Heads.

measurements of the velocity field with the PIV technique, a $2cm$ wide window of Perspex (label 3) has been inserted in correspondence with the medium transverse section of the ashlar.

The 2D-model was placed between two Plexiglas walls (label 6) with a narrow gap between the section and them. This feature reduces the boundary effect caused by the finite length of the ashlar in the transverse direction. In this way a 2-D flow inside the wall is almost assured. The ashlar is forced to roll by a step-by-step motor driving the rotation axis of the model. The initial roll angle is also monitored with an inclinometer (label 2) placed inside the model. A trigger signal is emitted when the model reaches a stated position during its motion. This trigger activates the heads of a double laser (label 7) and then a laser beam (label 1) is emitted and catches the Perspex slice of the ashlar. The light emitted during the laser pulses is reflected by tracer particles seeded in the water, whose position is thus recorded by a CCD camera (label 5). For each trigger, two successive images are recorded, and their post-processing allows the calculation of the velocity flow field. A preliminary analysis of convergence of the velocity vector in several points of the measurement field has permitted to determine the number of images needed to obtain an accurate average velocity field. For each run, 129 double images were recorded during 129 successive periods of the phenomenon. This procedure is reiterated for each position of the model, and for each combination of frequency and amplitude. Once an acquisition has passed a quality control (check of the inclinometer, coherences of the images sequence, etc ...) the 129 images are analyzed.

To improve the resolution of the velocity field, we have adopted a multi-zonal approach: In 2 we show the dimensions of the main measurement area (zone 'a') and the spatial resolution of the images. Very close to the keel the main window has been carefully analyzed using other two sub-windows (zone 'b' and 'c', respectively). These latter have the same spatial resolution which corresponds to a double spatial resolution with respect to the main window. A suitable technique of analysis has been developed to reconstruct the whole hydrodynamic field.

3 Numerical modelling

A Navier-Stokes solver has been used to simulate the flow field around a moving body partially immersed in water. The solver is able to handle very different flow conditions including wave braking and air entrainment and arbitrary body motions. For these purposes the Navier-Stokes

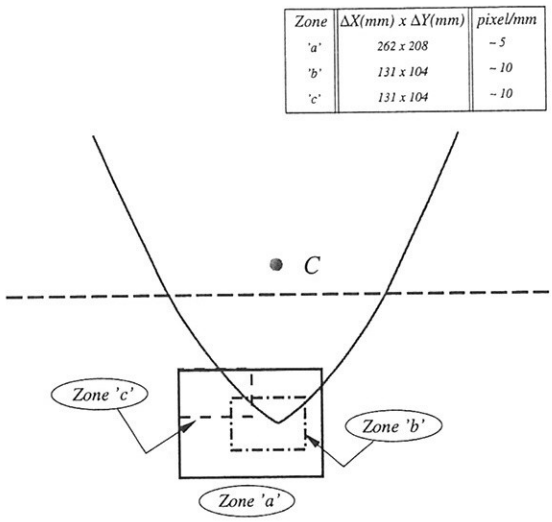

Figure 2: Example of multi-zonal approach for evaluation of the velocity field. Zone a: main measurement area, zone b and c: sub-windows with double resolution.

equations

$$\begin{cases} \nabla \cdot \boldsymbol{u} = 0 \\ \\ \rho \dfrac{D\boldsymbol{u}}{Dt} = -\nabla p + 2\nabla \cdot \mu \boldsymbol{D} + 2\sigma\kappa\delta_S \boldsymbol{n} + \rho \boldsymbol{g} \ , \qquad (\boldsymbol{D})_{ij} = D_{ij} = \dfrac{1}{2}\left(\dfrac{\partial u_j}{\partial x_i} + \dfrac{\partial u_i}{\partial x_j}\right) \end{cases} \tag{2}$$

where μ is the viscosity, σ the surface tension, κ the curvature of the free surface S, and δ_S a Dirac function with values different from zero only on S. Eq. 2 have been written for a two phase flow composed of air and water, so that ρ and μ vary from one fluid to the other. An approximate projection method has been used to solve pressure and, consequently, velocity in the equations 2. The application of this method requires a smooth transition of the density and viscosity from air to water.

The tracking of the interface is obtained using a level set function $\phi(x, y)$. It is defined as the signed distance between the point (x, y) and the interface curve. More in particular it is positive when the point is in air, negative when it is in the water and null on the interface. This function is also used to model the transition between ρ_{water} and ρ_{air}. A more detailed description of the numerical model can be found in [3] and [2].

3.1 A generic body on a Cartesian grid

The problem analyzed here does not involve fragmentation of the free surface, but a large motion of the body. Generally two boundary conditions can be applied on the body: 1) no slip condition, 2) free slip condition. In both cases special care has to be taken writing the equations around the solid boundary and in discretizing the mesh.

Here a no slip condition is implemented and the position of the body is followed through a second level set function ψ defined on the Cartesian grid. ψ is positive in the points outside the body and negative otherwise. A function $s(\psi)$ is introduced with

$$s(\psi) = \begin{cases} 1 & \text{if } \psi > 0 \\ 0 & \text{if } \psi \leq 0 \end{cases} \tag{3}$$

And the Navier-Stokes equations are written as [1]:

$$\boldsymbol{u}^{n+1} = s(\psi)[\boldsymbol{u}^n - \Delta t[(\boldsymbol{u}\cdot\nabla)\boldsymbol{u}]^{n+1/2} - \Delta t\frac{\nabla p}{\rho} + g\Delta t] + (1 - s(\psi))\boldsymbol{U}^{n+1} \tag{4}$$

where $\boldsymbol{U}^{n+1}$ is the velocity of the body. Applying the divergence operator:

$$\begin{aligned}\nabla\cdot\boldsymbol{u}^{n+1} &= s(\psi)\nabla\cdot[\boldsymbol{u}^n - \Delta t[(\boldsymbol{u}\cdot\nabla)\boldsymbol{u}]^{n+1/2} - \Delta t\tfrac{\nabla p}{\rho} + g\Delta t] - s(\psi)\nabla\cdot\boldsymbol{U}^{n+1} \\ &+ \tfrac{\partial s(\psi)}{\partial\psi}\boldsymbol{n}\cdot[\boldsymbol{u}^n - \Delta t[(\boldsymbol{u}\cdot\nabla)\boldsymbol{u}]^{n+1/2} - \Delta t\tfrac{\nabla p}{\rho} + g\Delta t] - \tfrac{\partial s(\psi)}{\partial\psi}\boldsymbol{n}\cdot\boldsymbol{U}^{n+1}\end{aligned} \tag{5}$$

The left hand side is zero by definition and the equation can be written as:

$$\begin{aligned}0 &= s(\psi)\nabla\cdot[\boldsymbol{u}^n - \Delta t[(\boldsymbol{u}\cdot\nabla)\boldsymbol{u}]^{n+1/2} - \Delta t\tfrac{\nabla p}{\rho} + g\Delta t - \boldsymbol{U}^{n+1}] \\ &+ \tfrac{\partial s(\psi)}{\partial\psi}\boldsymbol{n}\cdot[\boldsymbol{u}^n - \Delta t[(\boldsymbol{u}\cdot\nabla)\boldsymbol{u}]^{n+1/2} - \Delta t\tfrac{\nabla p}{\rho} + g\Delta t - \boldsymbol{U}^{n+1}]\end{aligned} \tag{6}$$

As $\partial s(\psi)/\partial\psi$ is a Dirac delta function, different from zero if $\psi = 0$, then the pressure gradient on the body is such that the normal velocity of the fluid becomes equal to the velocity of the wall. In the numerical simulations the function $s(\psi)$ is smoothed on a finite number of cells across the body boundary.

This method has been preliminarily applied to study the classical problem of the wake length downstream of a circular cylinder moving in a single fluid for a low Reynolds number (so that the flow is laminar). Figure 3 presents the numerical results (solid line) compared to the experimental data by [5] (symbol). The regime of laminar flow is well captured by this method.

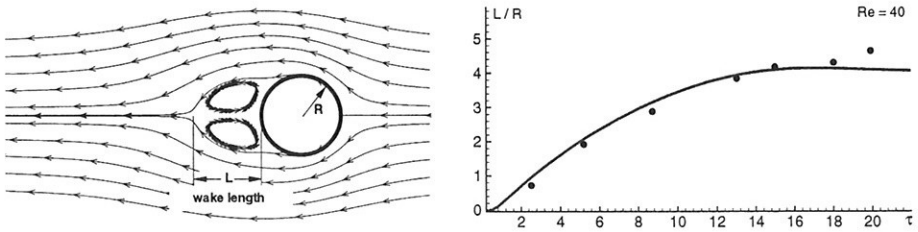

Figure 3: Length of the wake downstream a circular cylinder in the horizontal plane. The numerical results (solid line) are compared with the experiments by Honji & Taneda, (1972) (dots).

4 Comparison between numerical and experimental data

Here we report the comparisons between numerical and experimental data for the case characterized by a maximum angle of rotation $\alpha_{max} = 7.5^o$ and by a frequency $\nu = \Omega/(2\pi) = 0.4$Hz. Figure 4 shows the general behaviour of the vorticity $\omega = (\nabla\times\boldsymbol{u})$ in a semi-period in *steady regime.* In fact, after a large number of cycles, the transient phase can be neglected and the flow evolves periodically in time. Moreover in two successive semi-periods, we assume that the features of the flow field are symmetric with respect to the y axes, that is $u(x,y,t) = -u(-x,y,t+T/2)$ and $v(x,y,t) = v(-x,y,t+T/2)$.

[1]The discrete equations are written here in the non viscous case for simplicity but their extension to the viscous case is straightforward.

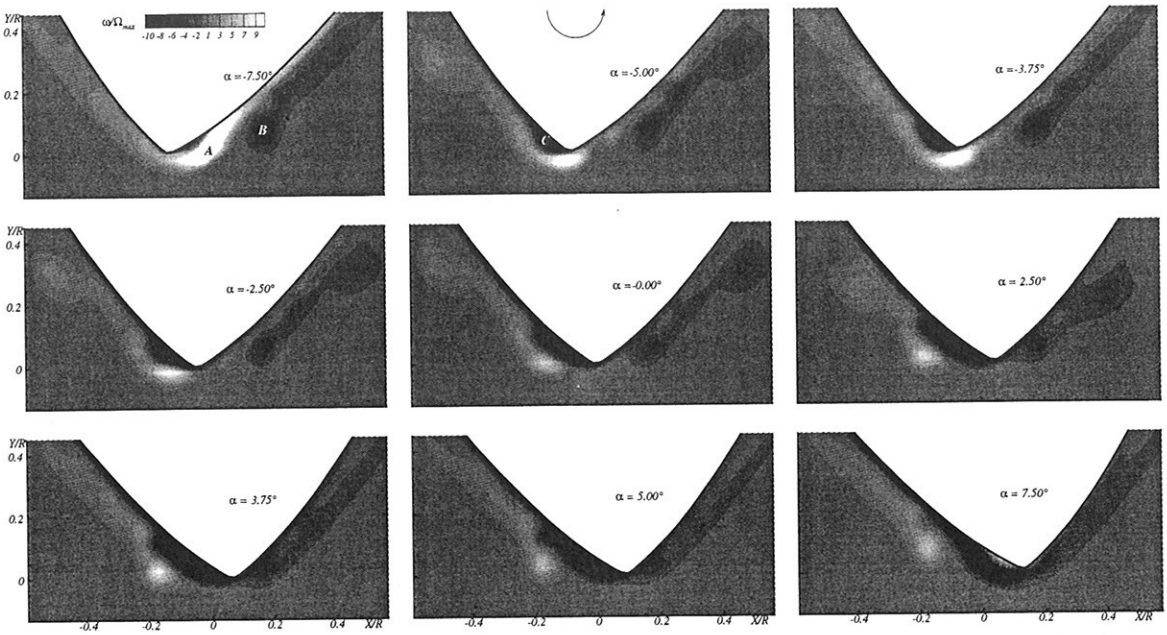

Figure 4: Evolution of the flow field for a semi-period of oscillation of the ashlar. The time increases left to right and from top to bottom.

At the extreme angle $\alpha = -7.5^o$ (top left plot of figure 4), a positive vorticity A is present close to the right side of the tip of the ashlar and a negative one B further away from it. When the section starts its motion rightwards, a new negative vorticity is formed at the lower tip and we shall name it C. This one enlarges and is shed as the time goes on. At the same time, the counter-rotating vorticity A rounds it and diffuses to the left where it joins a region characterized by counter-clockwise vorticity is always present. At the end of this semi-cycle B and C merge and form the symmetric of the initial vorticity A.

To validate this behaviour the numerical data have been compared with the experimental ones in figure 5 for the velocity and in table 1 for the maximum intensity and position of the vortices. The overall agreement is good, the velocity field, the intensity and the position of the vorticity

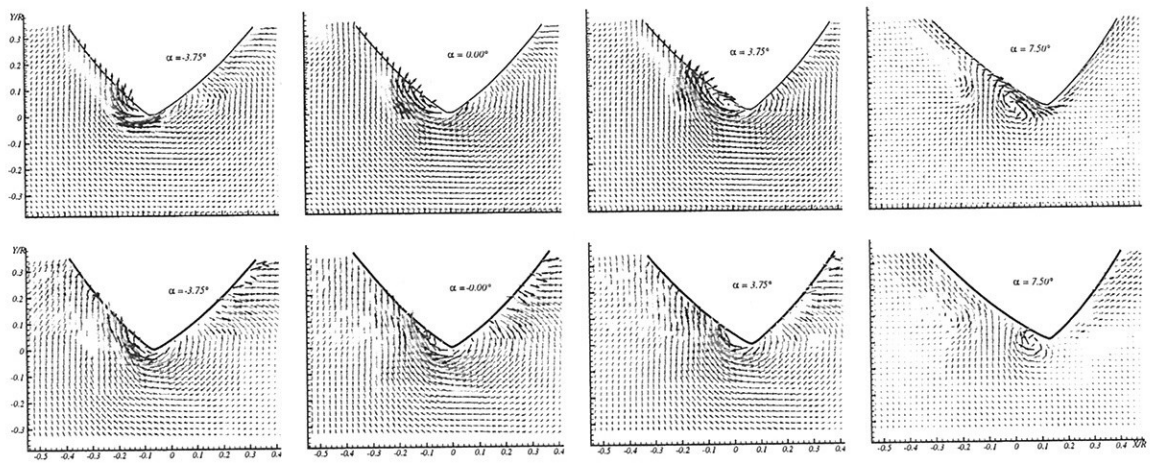

Figure 5: Numerical (top) and experimental (bottom) velocity field.

are similar. The most important differences appear at the lower tip for positive larger angle of rotation. This is due to the coarse mesh adopted in the numerical simulation, $\Delta x/R = 0.02$.

Such a coarse mesh implies a poor description of the boundary layer, with a displacement of the vorticity; moreover it causes the vortex to be more largely diffused. This explanation is supported by the fact that the maximum of the vorticity is almost always lower in the numerical simulations because of the diffusion.

	$(X/R)_{num}$	$(Y/R)_{num}$	$I_{max,num}$	$(X/R)_{exp}$	$(Y/R)_{exp}$	$I_{max,exp}/\Omega_{max}$
A	-0.07	-0.03	13.1	-0.17	-0.0	12.0
B	0.17	0.07	-6.3	0.21	0.08	-9.2
C	-0.11	0.03	-38.3	-0.07	-0.01	-40.0
A	-0.17	0.06	7.9	-0.18	0.05	14.3
B	0.17	0.05	-4.5	0.19	0.05	-8.3
C	-.05	0.03	-33.5	-0.05	-0.0	-34.5
A	-0.17	0.03	9.1	-0.20	0.08	9.9
B	0.17	0.03	-4.8	0.23	0.04	-7.2
C	-0.01	0.03	-35.1	-0.04	0.02	-13.5
A	-0.17	0.09	7.0	-0.21	0.07	9.0
B	N/A	N/A	N/A	0.25	0.04	-5.5
C	-0.01	0.03	-28.2	0.06	-0.01	-36.4

Table 1: Charachteristics of the vorticity in the numerical and experimental data (position $(X/R, Y/R)$ and intensity I). From top to bottom the tables refer to $\alpha = -3.75, 0.00, 3.75, 7, 50^o$.

Acknowlegments

A special thanks to 'il Maresciallo' (alias Massimo Palini) for his fundamental contribution in the successful performance of the experiments.

Present research activity was by the Italian Navy within the framework of the *Programma di Ricerca sulla Sicurezza* funded by *Ministero Infrastrutture e Trasporti.*

References

[1] R Broglia and A Di Mascio. Unsteady ranse calculations of the fow around a moving ship hull. *8th NSH Busan, Korea.*

[2] G Colicchio. Violent disturbance and fragmentation of free surfaces. *PhD thesis*, 2004.

[3] G Colicchio, M Landrini, and J Chaplin. Level-set modelling of the two-pahse flow generated by a surface piericing body. *Proc. 18th IWWWFB03, Le Croisic, France*, 2003.

[4] Y Himeno. Prediction of ship roll damping-state of art. *Dept.of Naval Arch. And Marine Eng, Univ. of Michigan, Rep. No. 239*, 1981.

[5] Honji and Taneda. *Rep. Res. Inst. Appl. Mech. Kyushu University*, 19:265, 1972.

[6] Y Ikeda, Y Himeno, and N Tanaka. A prediction method for ship roll damping. *Rep. No. 00405 of Dep. of Naval Arch., Univ. of Osaka*, 1978.

[7] B Perot and R Nallapati. A moving unstructured staggered mesh method for the simulation of incompressible free-surface flows. *J. Comp. Phys.*, 184:192–214, 2003.

[8] D Roddier, S Liao, and R Yeung. On freely-floating cylinders fitted with bilge keels. *Proc. Int. Off. and Polar Eng. Conf., Seattle*, 2000.

[9] R Yeung, C Cermelli, and S Liao. Vorticity fields due to rolling bodies in a free surface-experiment and theory. *21st ONR Symposium*, 1996.

[10] R Yeung, S Liao, and D Roddier. On roll hydrodynamics of rectangular cylinders. *Proc. Int. Off. and Polar Eng. Conf., Montreal*, 1998.

A Multi-Stage Approach to Ship Slamming Load Prediction

Ould El Moctar, Andreas Brehm, Thomas E. Schellin, Germanischer Lloyd,
moct@GL-group.com
Volker Bertram, ENSIETA

We present here a numerical procedure to predict slamming loads by using a chain of seakeeping codes. The procedure was applied to predict slamming loads for three ships, *El Moctar et al. (2004)*. Here, results for the so-called Hull 2 and the RoRo Ferry are shown. The computational procedure consisted of the following steps:

1. The linear, frequency-domain Green-function panel code GLPANEL, Papanikolaou and Schellin (1991), uses zero-speed Green functions and a forward-speed correction based on the encounter frequency approach. GLPANEL computed ship responses in unit amplitude regular waves. Wave frequency and wave heading were systematically varied to cover all possible combinations that are likely to cause slamming. Results were then linearly extrapolated to obtain responses in wave heights that represent severe conditions, here characterized by steep waves close to breaking. Under such conditions, a conservative one-third (voluntary or unvoluntary) speed reduction was assumed be realistic for Hull 2. For the RoRo Ferry, the ship speed used in the computations was governed by the model test runs.

2. Regular design waves were selected on the basis of maximum magnitudes of relative normal velocity between ship critical areas and wave, averaged over the critical areas.

3. The nonlinear strip method SIMBEL, Pereira (1988), determined motions of the ship under design wave conditions, thereby accounting for the ship's forward speed, the swell-up of water in finite amplitude waves, as well as the ship's wake that influences the wave elevation around the ship, particularly at moderate to high forward speeds. SIMBEL simulates large-amplitude rigid-body motions of a ship in six degrees of freedom by time-domain integration of the motion equations. Considered are forces and moments caused by gravity, Froude-Krylov pressure, radiation and diffraction pressure, speed effects, rudder and propeller actions, and wind. The stationary seaway is approximated by superposition of a large number of regular waves of different frequencies and directions. Forces and moments caused by radiation and diffraction are deduced from the two-dimensional potential flow at each of the transverse ship sections (strips). For large-amplitude motions, radiation and diffraction forces and moments are obtained by integrating the pressure over the instantaneously wetted surface. Pressure distributions depend not only on the instantaneous position, velocity and acceleration of the ship, but also on the motion's history (memory effect). Terms account for effects of viscous hull damping in roll using Froude number dependent coefficients. The influence of bilge keels is approximated semi-empirically. Propeller thrust is considered, whereby a motion equation for the propulsion system determines the propeller rate of rotation. Rudder forces and moments are determined by considering the orbital motion of water particles and the immersion of the rudder in the seaway.

4. These nonlinearly computed ship motions constituted part of the input for the RANSE code. The RANSE solver COMET employs interface-capturing techniques of the volume-of-fluid (VOF) type, proved to be suitable for handling strong nonlinearities. Today, this kind of code is the obvious choice for computing complex free-surface shapes with breaking waves, sprays and air trapping, hydrodynamic phenomena that should be considered to predict slamming pressures. The conservation equations for mass and momentum in their

integral form (finite-volume method) serve as the starting point. The integrals are numerically approximated using the midpoint rule. The mass flux through the cell face is taken from the previous iteration, following a simple Picard iteration approach. The remaining unknown variables at the center of the cell face are determined by combining a central difference scheme (CDS) with an upwind differencing scheme (UDS). The CDS employs a correction to ensure second-order accuracy for an arbitrary cell. A second-order central difference scheme (CDS) can lead to unrealistic oscillations if the Peclet number exceeds two and large gradients are involved. On the other hand, an upstream difference scheme (UDS) is unconditionally stable, but leads to higher numerical diffusion. To obtain a good compromise between accuracy and stability, the schemes are blended. Near the ship hull, the blending factor is chosen between 0.8 and 0.9. The Euler implicit and the three time level methods are used to integrate in time. Pressure and velocity are coupled by a variant of the SIMPLE algorithm. All equations except the pressure correction equations are under-relaxed using a relaxation factor 0.8. The pressure correction equations are under-relaxed using a relaxation factor between 0.2 and 0.4 for unsteady simulations, finding in each case a suitable compromise between stability and convergence speed. The two-fluid system is modelled by a two-phase formulation of the governing equations. No explicit free surface is defined during the computations, and overturning (breaking) waves as well as buoyancy effects of trapped air are accounted for. The special distribution of each of the two fluids is obtained by solving an additional transport equation for the volume fraction of one of the fluids. To accurately simulate the convective transport of the two immiscible fluids, the discretization must be nearly free of numerical diffusion and must not violate the boundedness criteria. For this purpose, the high resolution interface capturing (HRIC) scheme is used. This scheme is a nonlinear blend of upwind and downwind discretization, and the blending is a function of the distribution of the volume fraction and the local Courant number. The free surface is smeared over two to three control volumes. Fluid structure interaction effects are presently not accounted for, i.e., the body is assumed to be rigid, and the fluid is assumed to be viscous and incompressible.

The numerical volume grids surrounding the ships comprised one million hexahedral control volumes. Because only head wave conditions were examined, one half of the ships were modeled by setting a symmetry plane at the centerline. To avoid flow disturbances at outer grid boundaries, these boundaries were located at a distance of one ship length L ahead of the bow, $2L$ aft of the stern, and $1L$ beneath the keel. The top grid boundary was located above the deck at a distance equal to the length of the ship. The large domain of the mesh, especially above the deck, was chosen to allow for large pitch motions in head waves. Near the ship hull and ahead of the ship grid density was high to resolve the wave, whereas aft of the ship the grid became course to dampen the waves. The innermost cell thickness was chosen such that $y^+ = 100$ on average.

Front, side, bottom and top flow boundaries were specified as inlets of known velocities and known void fraction distributions defining water and air regions, Azcueta (2001). On the hull surface a no-slip condition was enforced on fluid velocities and on the turbulent kinetic energy. At the outlet boundary a zero gradient pressure boundary condition had to be satisfied. The wake flow boundary was specified as a zero-gradient pressure boundary (hydrostatic pressure). All computations were performed using the RNG-k-ε turbulence model with wall functions. The time step size was chosen such that the Courant number was unity on average. The impulse equations were discretized using 85% central differences and 15% upwind differences. Ship motions were realized by moving the entire grid at each time step. Thus, all boundary conditions were newly computed at each time step.

Volume fractions and velocities that initialized the flow field arose from superposition of ship

speed and orbital particle velocities of the linear Airy wave. Because of natural dissipation originating from the wave as well as numerical dissipation associated with the applied VOF method, the profile of the generated wave took on a more natural shape than the sinusoidal shape of an Airy wave. The influence of numerical damping on the wave height was taken into account. Numerical diffusion caused by the course grid aft of the ships dampened the incident wave to such an extent that no significant wave reflection occurred at the outlet boundary. Simulation of the flow field continued until a periodic solution was reached. After a simulation time of two to five encounter periods, depending on ship motions, ship speed, wave height and position of the investigated plate fields, periodically converging solutions were obtained. For each time step up to ten outer iterations were needed.

Design wave conditions and ship speeds are for Hull 2 wave height $\zeta_w = 7$ m, $\lambda/L_{pp} = 1.2$, $V = 10.7$ kn; for the RoRo ferry $\zeta_w = 7.3$ m, $\lambda/L_{pp} = 1.0$, $V = 26.0$ kn. Extreme loads caused by slamming were predicted at two selected plate fields located on the separated bow section of Hull 2. Global data of seakeeping model tests of HSVA, including ship motions and accelerations, generally compared favorably with nonlinear computations from SIMBEL. Under the HSVA test conditions ($H_w = 3.5$m, $\lambda/L = 1.2$, $V = 14$ kn), the RANSE solver performed computations of wave-induced impact-related slamming loads and local pressures acting on the separated bow segment of the ship, using the computed motions as part of the input. Simulations of the flow field were performed for two consecutive encounter periods, while the measurements lasted over several periods. Computed forces and pressures hardly changed after the first period; however, the corresponding measurements varied. Over the first two periods, the computed vertical force on the separated bow section compared favorably with the experimental data, Fig.1. For the corresponding slamming pressures, Fig.2, the functional relationship of computed values correlated well with measurements, but peak values differed. This deviation was largely attributed to the relatively strong variation of the measured peaks, most likely caused by the inability of the model to attain steady state conditions during tests in regular waves.

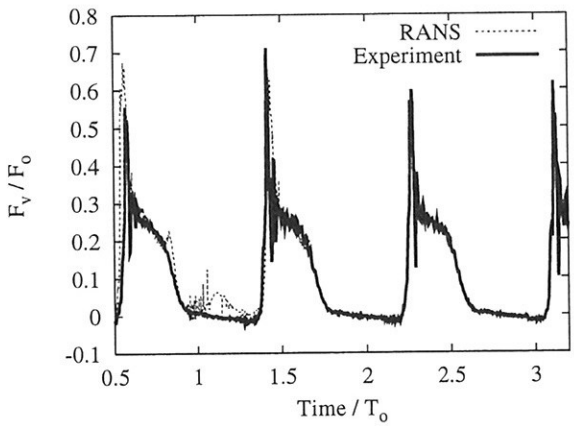

Fig.1: Time history of vertical force on bow section of Hull 2

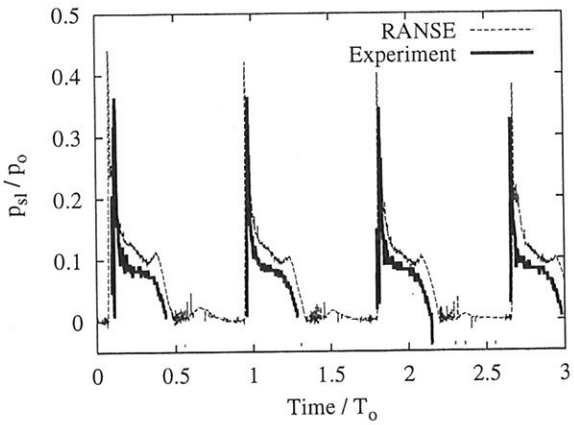

Fig.2: Time history of pressure on plate field 1 of Hull 2

To validate the employed methods, comparative computations were performed for the RoRo Ferry under conditions corresponding to MARIN model test no.112006, representing a run in regular head waves of 7.30 m height and 10.5 s period with the ship advancing at a constant forward speed of 26 kn. For this ship, GLPANEL was used to obtain ship motions, albeit with additional terms introduced in the damping matrix to account for nonlinear damping in heave and pitch. The subsequent COMET computations, using these motions as input, yielded wave elevations, relative motions along the hull, and local pressures acting at the hull surface. For the forth period of simulations, Fig.3 presents sample plots of comparable pressure traces at selected sensor locations in the bow region. To obtain forces on bow doors, local pressures

were integrated over the area of the bow doors, Fig.4. Close agreement with measurements was achieved only for the horizontal force component; vertical force predictions were significantly higher than measurements. Although the vertical force predictions were obtained by integrating pressures over actual (reduced) bow area, this apparent disagreement was mainly caused by the flawed idealization of the ship's forebody in that the height to main deck of the idealized hull exceeded the corresponding height of the model by 1.80 m, a significant amount of more than 11%. As this test was run in relatively high waves (7.30 m), an additional simulation was carried out in waves of lower height (4.46 m), where water did not flow over the deck. The resulting bow door forces, Fig.5, now agreed favorably with model test measurements.

Computed results of wave-induced slamming loads demonstrated that the procedure presented here was capable of predicting slamming suitable for design of a ship's structure. The generally favorable comparison of computations with model test measurements validated the methods used. The presented procedure relied on the combined use of potential flow codes and a RANSE solver. It was first necessary to obtain reliable predictions of ship motions. As slamming typically occurs in high waves, motions could not be obtained directly from the linear seakeeping code GLPANEL. However, the efficient application of GLPANEL served to identify the design wave conditions. Subsequently, the nonlinear code SIMBEL yielded sufficiently accurate motion predictions that were used as input for the RANSE code COMET. This code is currently being modified to also solve the ship motion equations, so that in future ship motions will no longer have to be supplied as part of the input.

The investigation so far (numerical and experimental) concerns rigid bodies. Full-scale ship structures are relatively thin, stiffened shells in the bow region. The effect of hydro-elasticity on slamming loads remains as a topic for further detailed research and development activities.

Acknowledgement

Thanks are due to A. Köhlmoos and R. Pereira for their assistance with the numerical computations. The opinions expressed herein are those of the authors.

References

AZCUETA, R. (2001), *Computation of turbulent free-surface flows around ships and floating bodies*, Ph.D. thesis, TU Hamburg-Harburg (in German)

EL MOCTAR, O.; BREHM, A.; SCHELLIN, T.E. (2004), *Prediction of slamming loads for ship structural design using potential flow and RANSE codes*, 25^{th} Symp. Naval Hydrodyn., St. John's

PAPANIKOLAOU, A.D.; SCHELLIN, T.E. (1991), *A three-dimensional panel method for motions and loads of ships with forward speed*, Ship Technology Research 39, pp.147-156

PEREIRA, R. (1988), *Simulation of nonlinear sea loads*, Ship Technology Research 35, pp.173-193

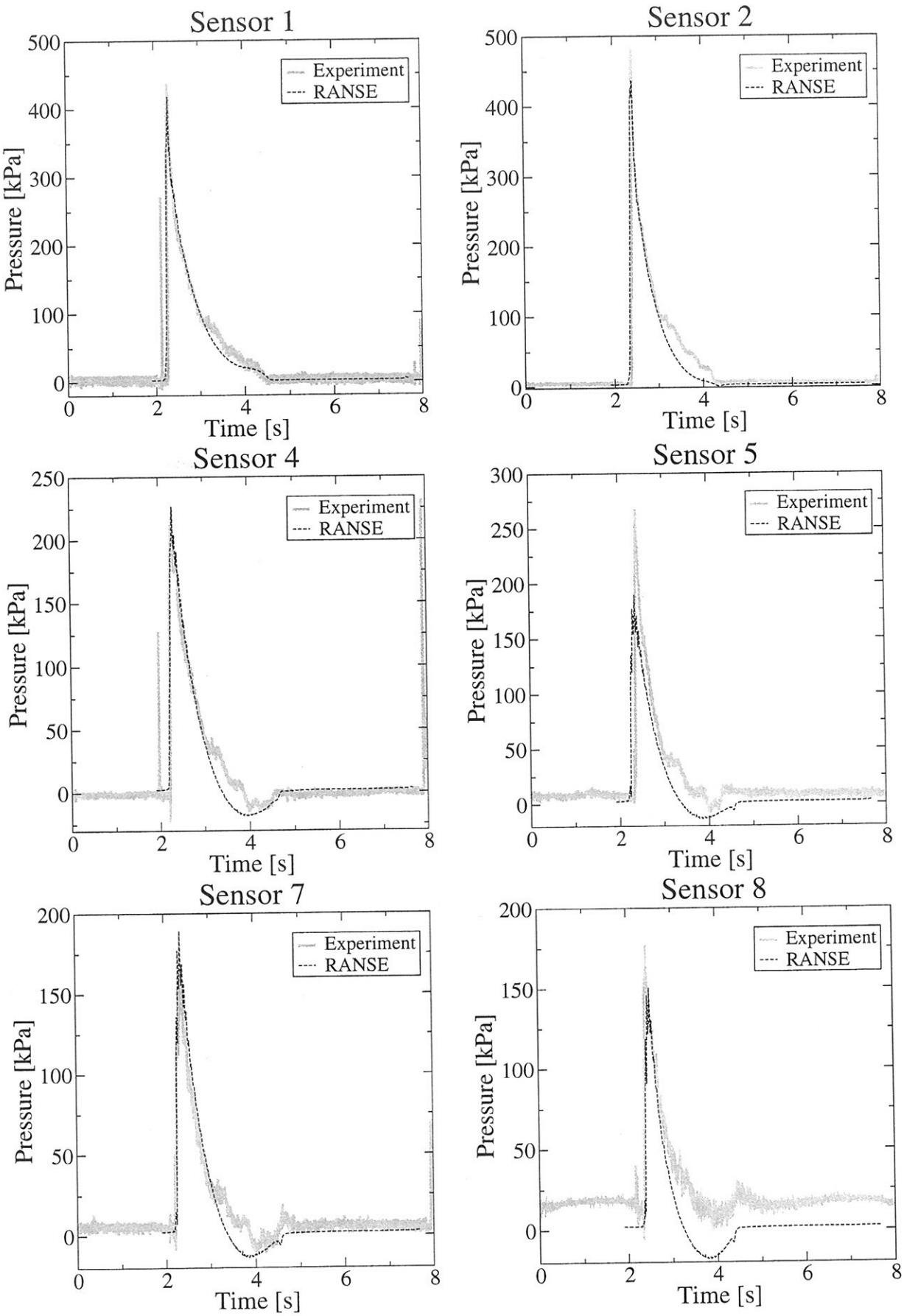

Fig.3: Time histories of bow door pressures at selected pressure sensors for RoRo Ferry

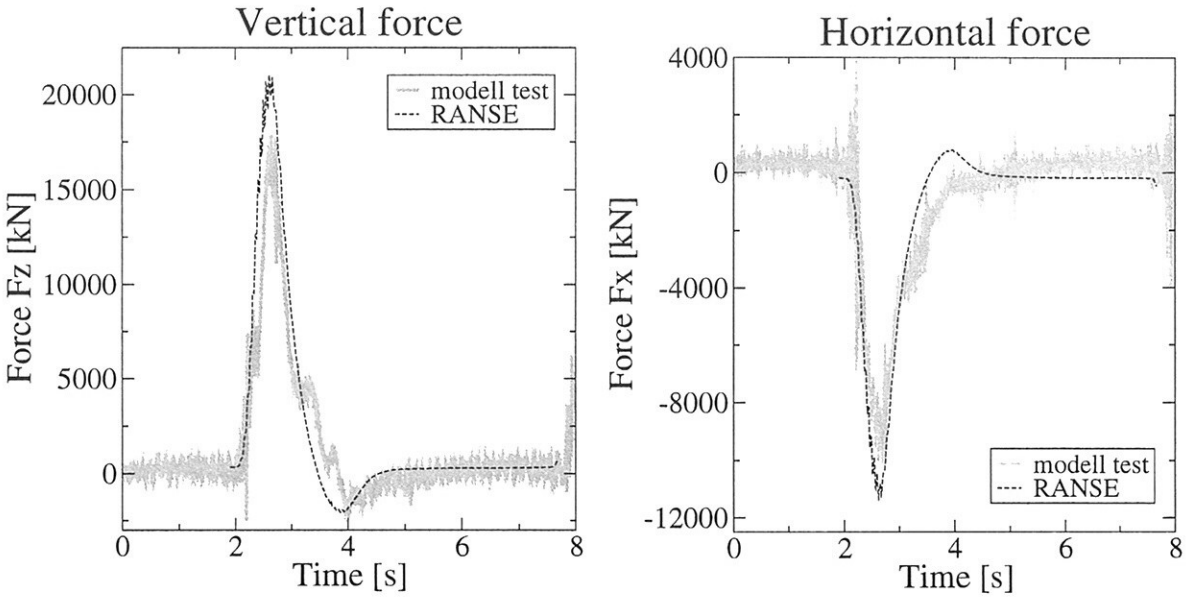

Fig.4: Vertical (left) and horizontal (right) force history on bow door of RoRo Ferry in 7.30 m high waves

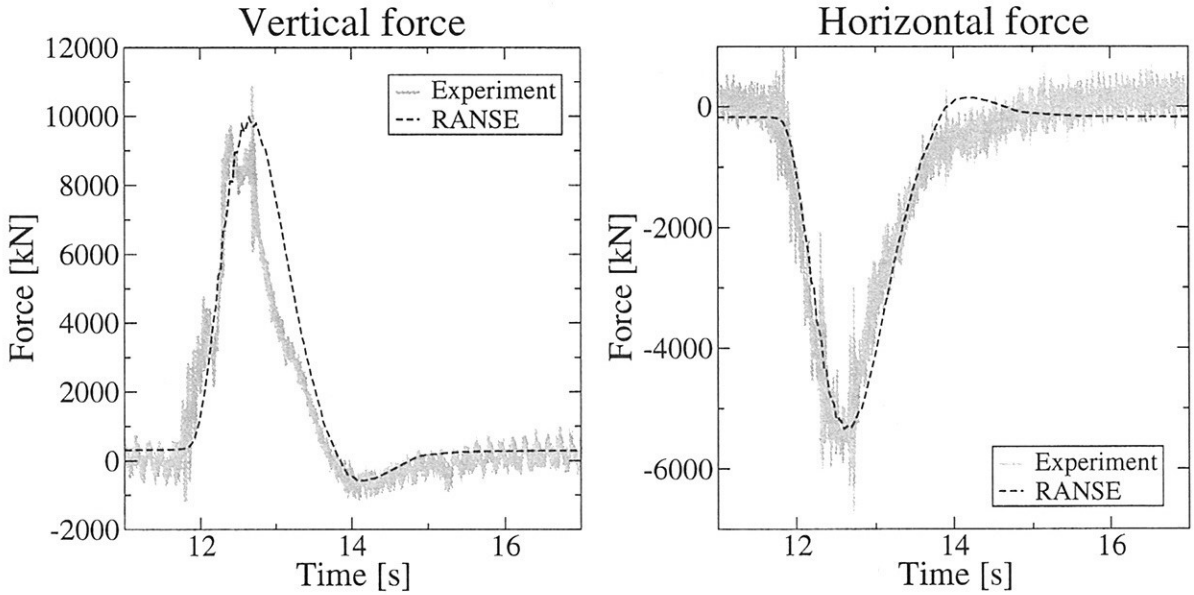

Fig.5: Vertical (left) and horizontal (right) force history on bow door of RoRo Ferry in 4.46 m high waves

Calculation of unsteady cavitation behaviour on a plan-convex foil

Katerina Franzen, Moustafa Abdel-Maksoud
Institute for Ship Technology and Transport Systems, Duisburg-Essen University
maksoud@nav.uni-duisburg.de

The development of cavitation models for CFD remains important. The unsteady cavitating flow is a two-phase flow with a strong interaction between the two phases. Another important factor which affects the behaviour of unsteady cavitation is the nuclei distribution in the flow, Hsiao and Chahine (2004). An experimental determination of this distribution requires very expensive equipment and is very time consuming. The consideration of this nuclei spectrum in the simulation is still limited to a very small number of nuclei, Choi et al. (2004). Another important aspect is that the re-entrant jet has a strong influence on the behaviour of the flow. The numerical determination of the sharp surface between the vapour region and the surrounding water is very important in order to simulate the kinematics of the re-entrant jet. This condition is difficult to achieve numerically due to the high gradients in this region.

Le at el. (1993) studied the unsteady behaviour of the cavitating flow of a foil. The measuring section of the cavitation tunnel has a free surface. The water depth in the tunnel was 40 cm, its breadth 12 cm. The foil was placed at 20 cm water depth. The upper side of the foil is plane, its lower side circular (radius 26 cm) with maximum thickness of 2 cm. The leading edge is rounded with radius of 1 mm and the chord length is 196. mm. The velocity in the measuring section was varied between 5 to 10 m/s, which corresponds to Reynolds number of $R_n 1x10^6$ to $2x10^6$ respectively. The range of the cavitation number investigated σ is between 0.05 - 1.3. The angle of incidence was varied between -6° and 8°. The results of the experimental study include the cavitation pattern for various cavitation numbers and angle of incidence. The cavity length and information on periodic shedding are also available.

The computations used the commercial CFD software package CFX-5.7. CFX-5.7 models the equations for the conservation of mass, momentum and energy in terms of the dependent variables velocity and pressure in their Reynolds averaged form. The Finite Volume method has been applied. The variables are discretised on a co-located unstructured grid with a second order fully conservative vertex based scheme. In the computations the hybrid "high resolution scheme" was applied. In this scheme the blending factor between central and upwind difference schemes is varied locally. The high resolution scheme computes a blending factor as close to 1 as possible, which means pure central difference, without violating the boundedness principle. The scheme is reduced to first order near discontinuities and in the free stream, where the solution has a little variation. Rhie and Chow's method has been applied to achieve a strong coupling between the pressure and the velocity fields - in which the continuity equation is modified by a fourth derivative in pressure which acts to redistribute the influence of the pressure. The computations were started with the standard k-εturbulence model. After about 250 iterations the SST turbulence model was switched on. A short description of the applied cavitation model is given below.

For the purpose of cavitation modelling, it is desirable to re-cast the mass fraction conservation equation in terms of a volume-fraction equation. The volume fraction field may vary continuously from 0 to 1 in the cavitation zone. The added complexity in comparison with the traditional VOF approach is that a source term is now added to the volume fraction equation to model the creation and destruction of vapour. This source term introduces a very strong coupling between the volume-fraction equation and the mass-momentum equation set, since the source term depends on the local pressure difference. The resulting volume-fraction field strongly influences the mixture density used in the mass/momentum

equations. It is this strong coupling that makes even the VOF cavitation model difficult to solve, most notably when the liquid/vapour density ratio becomes large (i.e. 1,000 or larger). The calculated average values of the properties of the mixture in each control volume in the flow domain will depend both on component property values and on the proportion of each component present in the control volume

The governing equations describe the cavitation process involving a two-phase three-component system, where it is assumed that no-slip between the phases takes place and thermal equilibrium between all phases exists. The three components are:

1. Non-condensable gas in the form of micro-bubbles
2. Vapour (primary phase)
3. Liquid (primary phase)

The mass fraction of the non-condensable gas and the radius of the micro-bubbles have to be defined at the start of the computation. The mass exchange between the vapour and liquid in the primary phases during cavitation is taken into account by the source terms. The rate of vapour production of the source term $\dot{S}_v$ has been derived by considering the Rayleigh-Plesset equation (RPE) for bubble dynamics.

For a vapour bubble nucleated in a surrounding liquid the dynamic growth of the bubble radius RB can be described by the RPE as follows:

$$R_B \ddot{R}_B + \frac{3}{2}\dot{R}_B^{\,2} + \frac{2\sigma}{R_B} = \frac{p_v - p}{\rho_l} \tag{1}$$

where p_v is the vapour pressure in the bubble, p represents the pressure in the surrounding liquid, σ is the surface tension coefficient between the liquid and vapour and ρ_l is the liquid density. In the applied cavitation model a first order approximation for RPE is used:

$$\dot{R}_B = \sqrt{\frac{2}{3}\frac{p_v - p}{\rho_l}} \tag{2}$$

It is also assumed that there are no thermal barriers to droplet growth. The growth of the bubbles takes place from an initial average radius of R_B and return (when condensing) to bubbles of the same size. The mass rate for vaporization and condensation of liquid can be calculated as follows:

$$S_l = -S_v = 4\pi R_B^2 N_B \rho_v R_B \tag{3}$$

where NB is the number of bubbles per unit volume of the mixture which are available as nucleation sites.

$$\dot{S}_l = -F_c\, 4\pi R_B^2 N_B \rho_v \dot{R}_B \sqrt{\frac{2}{3}\frac{p_v - p}{\rho_l}}\, sign(p_v - p) \tag{4}$$

In practice, the vaporization and condensation processes have different time scales, the condensation process typically being the slower. An empirical constant, F_c is introduced in equation (4) to allow for these constraints: with a typical value of $F_c = 50$ when vaporization occurs ($p_v - p > 0$) and $F_c = 0.01$

with condensation ($p_v - p < 0$). The factor F_c is a dimensionless value.

A block structured grid is applied. The number of nodes in the numerical grid is about 3.5 million, Figs.1 to 3. The simple foil geometry allowed a high-quality numerical grid. The inflow velocity and the cavitation number in the numerical study are 10.0 m/s and 0.5 respectively. Five angles of incidence were investigated: -4°, -2°, 2°, 4° and 6°. The turbulence degree was considered to be 3%. The mass fraction of the non-condensable component was assumed to be $5x10^{-4}$ and the typical radius for the nucleation sites was $1x10^{-6}$ m. For the investigation of the influence of the nucleation radius sites on the calculated cavitation behaviour, the computation for 2° angle of incidence were repeated with a nucleation radius of $16 x10^{-6}$ m.

The cavitation behaviour on the foil as a function of angle of incidence and cavitation number was measured by Le et al. (1993). The experimental results show that different regimes of cavitation can take places on the foil from non-cavitation to supercavitation. The cavitation patterns calculated are shown in Fig.4 for angles of incidence -4° and -2°, in Fig.5 for 2°, 4° and 6°. The calculated cavitation pattern for -4° agrees well with that observed . At this angle of incidence, cavitation takes place the whole lower side of the foil. The observed cavitation pattern at -2° angle of incidence shows that the volume of the cavitation region on the lower side of the foil is reduced and no cavitation takes place on the upper side. The calculated cavitation pattern in Fig.4 follows this tendency. The numerical and measured results at positive angles of incidence show that cavitation takes place only on the upper side of the foil, but the calculated volume of the cavitation regions are much smaller than those observed. This is true for all the three angles investigated. The experimental results show that the cavitation region at 6° angle of incidence covers the whole upper side of the profile. The area of calculated cavitation patterns is only about 20 % of the chord length of the foil.

Fig.6 shows the calculated pressure distribution on the foil at different angles of incidence. Two figures are included for 2° angle of incidence because the computations were carried out at two radius of nucleation site $1x10^{-6}$ and $16x10^{-6}$ m. The pressure distribution at -4° shows two regions of low pressure on the lower side of the foil. The first is small and located very close to the leading edge. The second region is large and begins behind the leading edge and continues until the trailing edge. At this edge there is a strong reduction in the pressure. The calculated pressure distribution gives an explanation for the numerically estimated cavitation pattern. At -2° angle of incidence the low pressure area on the lower size of the foil is reduced in comparison with results of -4°. The low pressure region near the leading edge no longer exists. However in this case two small low pressure regions can be seen directly behind the trailing edge. These regions are the centre of vortex shedding from the trailing edge of the foil. There are two low pressure regions on the foil at the investigated positive angles of incidence. The first is located near the leading edge on the upper side of the foil and the second can be seen near the maximum thickness of the foil on the lower side. When increasing the angle of incidence, the volume of the low pressure region on the upper side of the foil grows and the volume of the region on lower side shrinks.

The simulations for every angle of incidence were carried out for about 2 seconds real time. The variations of calculated drag and lift coefficients during the last half-second of simulation are given in Figs7 and 8. Fig.9 includes the ratio of the drag to the lift. The calculated drag and lift coefficients for -4° angle of incidence show a high frequent character compared with the other investigated angles of incidence. The difference between the maximum and the minimum is limited compared with the results of -2° angle of incidence. Although the strong unsteady behaviour of drag and lift coefficients for -4°, the ratio between the drag and the lift coefficient is nearly constant, Fig.9. The fluctuation of the drag coefficient at -2° angle of incidence is much stronger than that of the lift. The reason is the strong vortex

shedding from the trailing edge of the foil. The ratio of drag coefficient to lift coefficient at this angle of attack has a periodical character. The drag and the lift coefficients of the 2° and 4° angles of incidence are nearly constant during the simulation time. The angle of incidence equals 6°, a periodical character can been seen for the drag and the lift coefficients. The mean value of the lift coefficient was nearly zero. Therefore, it was not possible to include the drag lift ratio in Fig.9.

The influence of the radius of nucleation site on calculated drag and lift coefficients was investigated for 2° angle of incidence, Figs.10 and 11. Fig.12 shows the variation of the ratio of the drag to the lift for the two investigated radius of nucleation site: $1x10^{-6}$ and $16x10^{-6}$. Fig.10 shows that with increasing the radius of nucleation site the drag coefficient is reduced. On the other hand, the lift coefficient does not show any noticeable influences, Fig.12. The unsteady behaviour of the drag and lift coefficients are also unaffected by changing the radius of nucleation site. Due to the reduced drag coefficient at large radius of nucleation site, the drag lift ratio of coefficient is reduced, Fig.12.

For the calculation of the cavitation pattern it is important to be able to resolve high local velocity and pressure gradients. In the case investigated, the cavitation model applied is able to calculate realistic cavitation patterns for many conditions, especially when the cavitation covers 5% or 95% of the chord length. For partially cavitating flow in region between 40 or 60% of the chord length, it was difficult to obtain the observed cavitation pattern in the experiments. It should be mentioned that it is now possible to include the influence of the water quality in the numerical computation, but in the most cases this information is not available from the experimental study.

Hsiao, C.-T., Chahine, G.L. (2004), *Numerical Study of Cavitation Inception due to Vortex/Vortex Interaction*, 25th Symp. Naval Hydrodyn., St. John's, 2004.

Choi, J.-K., Hsiao, C.-T., Chahine, G.L. (2004), *Tip Vortex Cavitation Inception Study Using The Surface Averaged Pressure (SAP) Model Combined with a Bubble Splitting Model*, 25th Symp. Naval Hydrodyn., St. John's, 2004

Le, Q., Franc, J.P., Michel, J. M. (1993), *Partial Cavities, Global Behaviour and Mean Pressure Distribution,* J. Fluids Engineering, Vol. 115/2, pp. 243-248

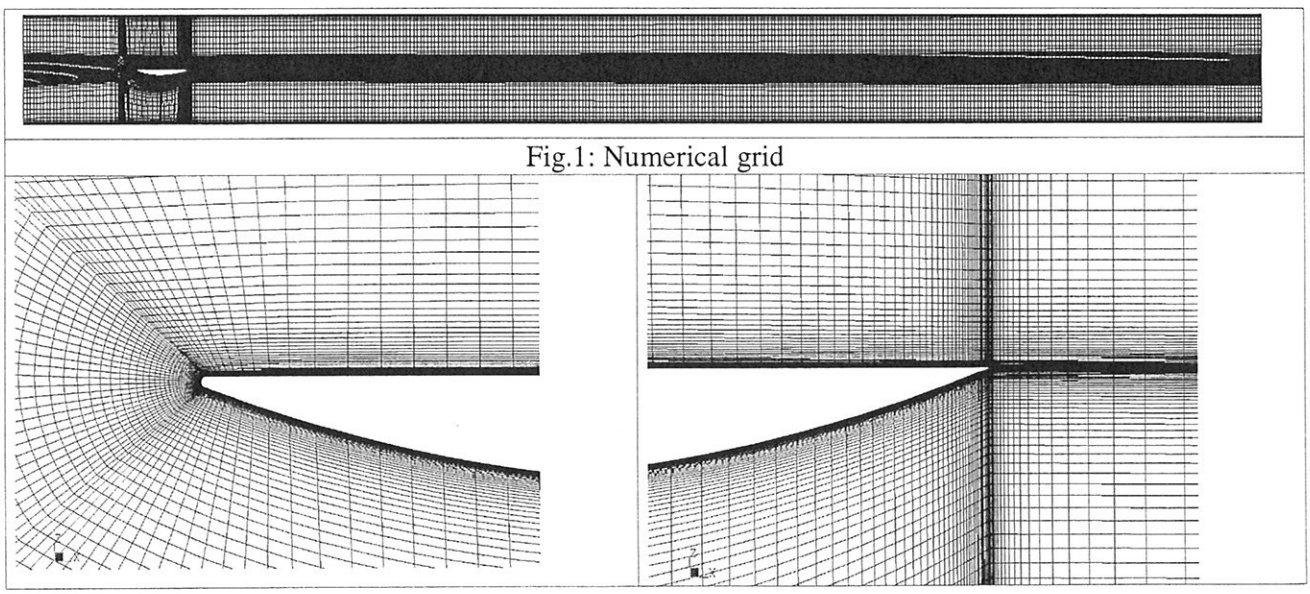

Fig.1: Numerical grid

Fig.2: Numerical grid on the leading edge

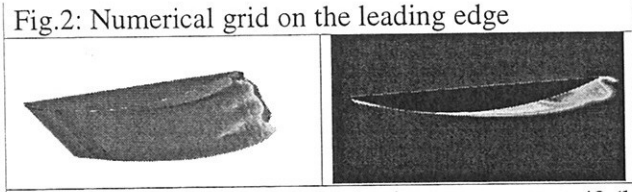

Fig.3: Numerical grid on the trailing edge

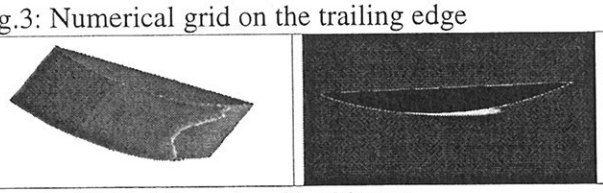

Fig.4: Cavitation patterns at -4° (left) and –2° (right) angle of incidence

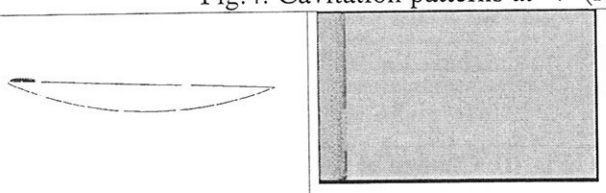

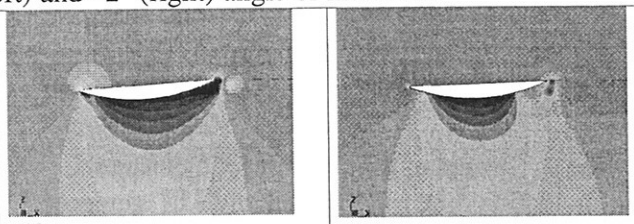

-4° -2°

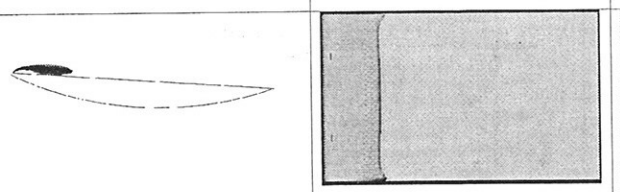

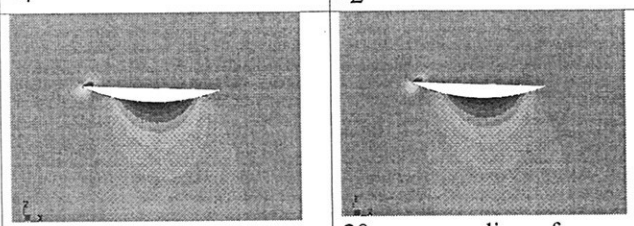

2°, mean radius of nucleation site 1e-6

2°, mean radius of nucleation site 16e-6

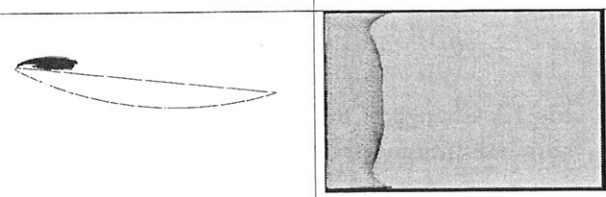

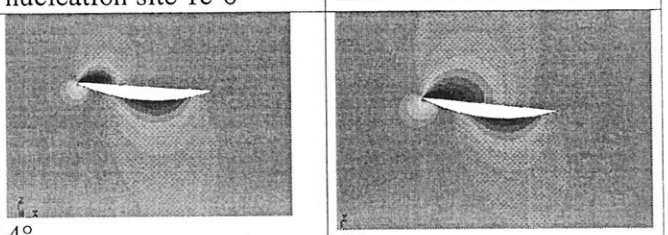

4° 6°

Fig.5: Cavitation patterns for 2° (top), 4° (centre) and 6° (bottom) angle of incidence

Fig.6: Pressure distribution on foil

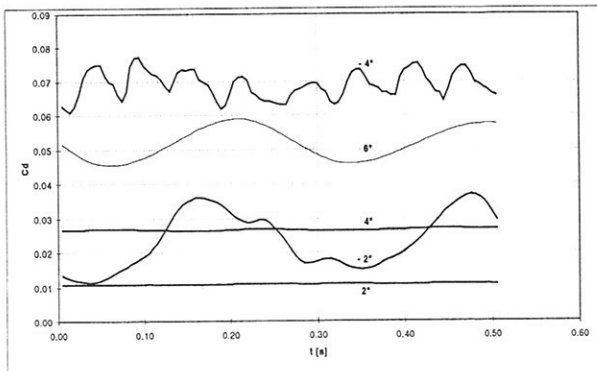

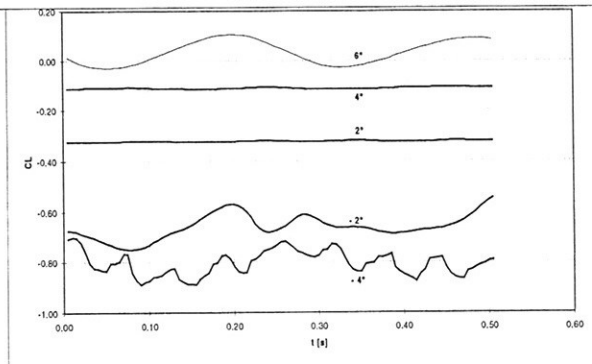

Fig.7: Change of the drag coefficient during the simulation time for different angle of incidence

Fig.8: Change of the lift coefficient during the simulation time for different angle of incidence

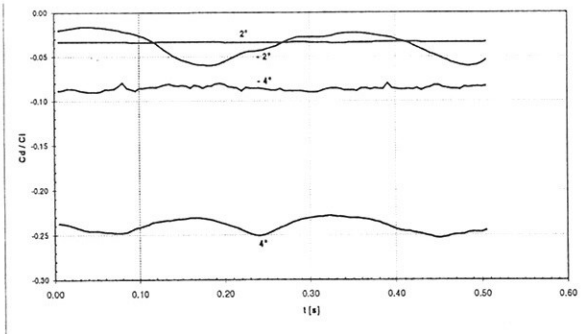

Fig.9: Change of the drag lift ratio during the simulation time for different angle of incidence

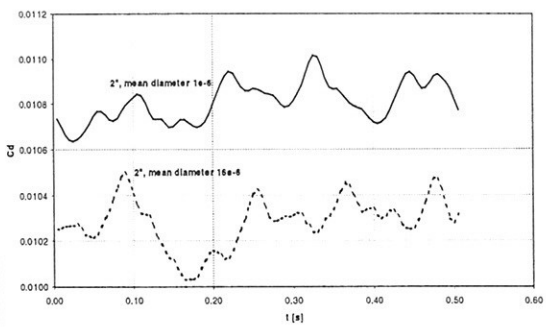

Fig.10: Change of the drag coefficient during the simulation time for 2° angle of incidence

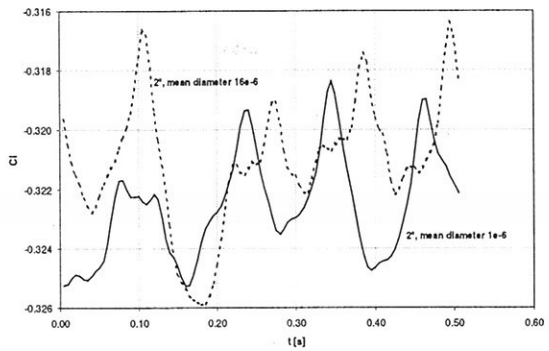

Fig.11: Change of the lift coefficient during the simulation time for 2° angle of incidence

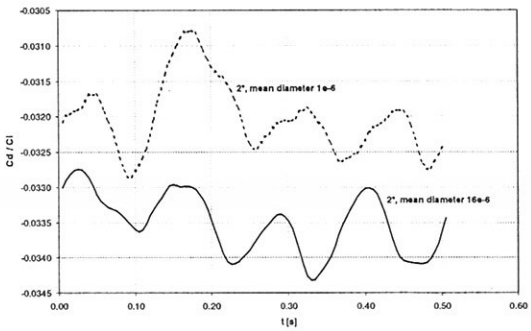

Fig.12: Change of the drag lift t ratio during the simulation time for different angle of incidence

Numerical Simulation of Damage Ship Flooding

Q. Gao, F. Kara, V. Shigunov, D. Vassalos
University of Strathclyde, UK

Abstract

Damage ship flooding was simulated numerically by coupling RANS and potential solvers. The approach was validated on forced heave motion of Burgundy section model. Computational results show that water flooding through damaged opening can be evaluated numerically and computed hydrodynamic forces agree well with experiment measurement.

Introduction

When a ship is damaged, seawater floods from outside into a damaged compartment. During initial several minutes, flooding appears to be very violent. Because of high hydrostatic pressure across the opening, water gain large momentum flooding into the empty compartment. After this initial stage, flooding becomes more or less quasistationary and water flows both in and out of the compartment depending on ship motion and seaway outside of the opening. Obviously, flooding has significant effect on ship safety and stability. Some ships may capsize due to damaged flooding. Therefore, the study of damage ship flooding is gaining wide attention.

The experimental and numerical study on damage ship flooding is scarce.

Jasionowski etc (2001) measured hydrodynamic force of damaged Burgundy section model under sinusoidal heave and roll motions in NEREUS project []. However, it is very difficult to measure velocity field and water pattern around opening to obtain detailed information around opening.

Damage ship flooding is an interactive dynamic process. Ship motion affects water flooding and water sloshing in the tank. In turn, liquid loads due to sloshing of water in tank influence the ship motion.

For the numerical work of coupling problem of water sloshing in tank and ship motion, most numerical studies are on intact ship.

Kim (2002) presents a computational study on the antirolling tank problem. The three-dimensional sloshing flow is simulated using a finite-difference method, and the ship motions are obtained by using LAMP [].

Rognebakke etc (2003) studied interaction between ship motions and sloshing for a two-dimensional model in one degree of freedom sway motion [].

For damaged case, Woodburn (2000) studied damaged ship motion problem by a simplified water column model for external water. The ship dynamics program NEREID and CFD solver CFX were coupled as external and internal flow solver [].

In this research, damaged ship hydrodynamics was studied by coupling commercial solver FLUENT and in-house time domain motion program. The coupling method was validated on Burgundy section model test data, available at the Ship Stability Research Centre (SSRC) of the Strathclyde University in Glasgow.

Mathematical Modelling

Three-dimensional unsteady flow of incompressible fluid in the tank and an external domain surrounding opening was calculated using RANS equations. VOF and geometric reconstruction approach were applied to locate the free surface.
For the flow outside the opening, potential approach was used and coupled with RANS solver to reduce the computational time.

The mathematical modeling for RANS solver are given below

Volume fraction constraint

$$r_w + r_a = 1. \tag{1}$$

Continuity equation

$$\frac{\partial}{\partial t}(r_w \rho_w) + \nabla \bullet (r_w \rho_w \vec{V}) = 0. \tag{2}$$

Momentum equation

$$\frac{\partial}{\partial t}(\rho \vec{V}) + \nabla \bullet (\rho \vec{V}\vec{V}) = \rho \vec{g} - \nabla p + \nabla \bullet (\mu(\nabla \vec{V} + (\nabla \vec{V})^T)) + S \tag{3}$$

Where r_w and r_a are water and air volume fraction, ρ_w and ρ_a are water and air density, μ_w and μ_a are water and air dynamic viscosity, $\vec{V}$ is velocity vector, $\rho = r_w \rho_w + r_a \rho_a$ is composite density, $\mu = r_w \mu_w + r_a \mu_a$ is composite viscosity.

Numerical scheme

The differential equations are discretized by finite volume method. Physical variables are stored in the cell center. Second order upwinding difference scheme was used for convective fluxes. Rhie and Chow interpolation was used to avoid checker-boarding problem. The geometric reconstruction scheme was applied to solve volume fraction equation. SIMPLEC algorithm is used to couple velocity and pressure.

An in-house time domain hydrodynamic program [] was used to solve external potential flow. The method is based on transient free surface Green function.

Coupling interface

The difference between intact and damaged vessel for coupling problem lies on the complexity of flow at damaged opening. For damaged case, no physical boundary at the opening exists for water sloshing in the tank. A virtue numerical boundary should be set and an appropriate boundary condition should be imposed. The boundary is located at about two-model-breadth away from the model. The velocity boundary condition from potential solver was imposed. For the time domain hydrodynamic program, flooding velocity at opening calculated by RANSE solver was used as part of boundary condition. On other part of ship boundary, non-penetrating boundary condition was applied.

In order to couple RANSE solver and potential hydrodynamic solver, communication interface between two codes was created which allows interactive data exchange between two codes to update boundary condition. The time steps for two solvers are different and controlled by coupling interface. Normally, RANS solver uses a time step 0.003 and potential solver for a 0.05.

Test case

Burgundy section model of scale 1:40 is 1.5m long and has a tank with a length of 0.48m. The damage scenario chosen was based on the worst case (D901) from the SOLAS stability criteria point of view. The side and deck opening are shown in figure 1-2. The draft is 0.15m and the opening was open from beginning of the model test. In the damage tank, internal water was leveled at external water.

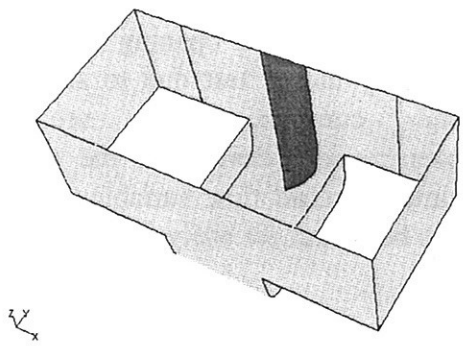

Figure 1 side opening of the model

The model test was performed in Denny tank. Heave force for forced heave motion was measured by 6 DOF load cell. Experimental data were used to validate the numerical results [].

The forced heave motion is sinusoidal and has an amplitude 0.075 m for both hull and deck damage case. The frequency ranges from 0.2 to 1 Hz.

The frequencies 0.2, 0.5 and 1 Hz were selected as validation case.

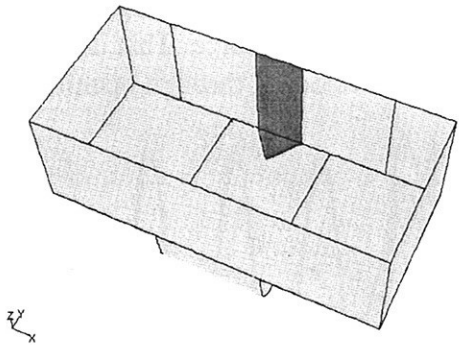

Figure 2 deck opening of the model

The computational domain of RANS calculation covers space inside the ship and some area outside opening as shown in figure 3. The structured grids for RANS simulation and quadrilateral panels on hull surface for potential program comprise overall 180000 finite volumes and 225 surface panels respectively.

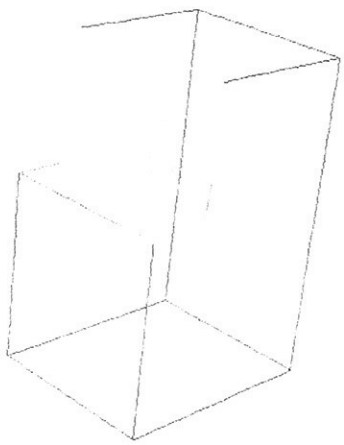

Figure 3 Domain of RANS calculation

Results and discussion

The vertical hydrodynamic force results for frequency 0.5 are given in Figure 4.

The potential external force is about 5/6 and the sloshing force from CFD simulation (remove initial hydrostatic force) is about 1/6 of the total force. The phase of the force history is different. The CFD force shows a larger phase lag than the potential force. This is related to the water flooding through opening.

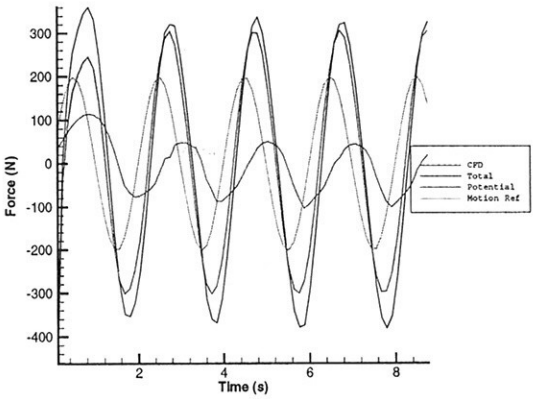

Figure 4 Vertical hydrodynamic forces

The mass of the water in tank is shown in figure 5. The time history of mass shows that the amount of water in the tank changes harmonically in time with the phase different from that of the heave motion (the lag is about 180 degrees). Amplitude of the mass curve is proportional to heave amplitude and opening size, but inversely proportional to the frequency.

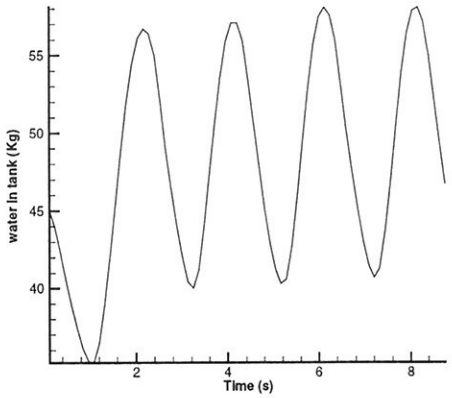

Figure 5 Mass of the water in the tank

The mean velocity through the opening is shown in figure 6. The amplitude of mean velocity is about 20% of square root of 2×gravity-acceleration×heave-amplitude. The flooding velocity at opening is mainly determined by the motion amplitude, not by frequency. It is not completely symmetric. There is a difference between peak and trough parts.

It is very difficult to measure velocity field at damaged opening and water in tank by model test due to small space and complexity to setup the measurement device. In the numerical simulation, all flow variables of interest can be output for analysis.

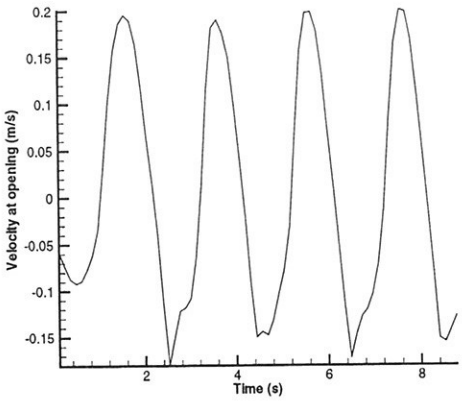

Figure 6 Mean velocity through opening

The wave pattern is displayed in figure 7. It gives a general view of effect of ship heave motion on water in and outside the tank. The heave motion of the model results in the motion of water surrounding the opening. However, due to the size of the opening, the water in the tank cannot reach the same level as water outside. Figure 7 shows a difference of water level between the water in the tank and water in sea.

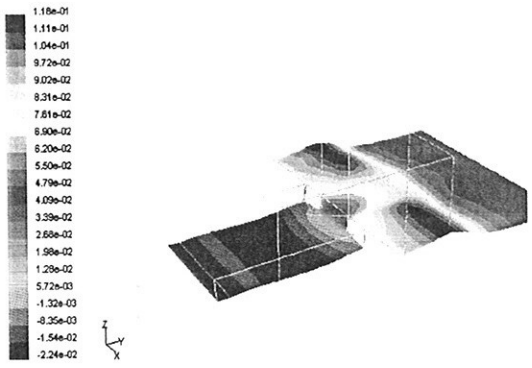

Figure 7 Free surface around damage opening

Because the amplitudes of heave motion and deck height above the static waterline is both 0.075 m, there is little water flooding onto the deck as shown in both experiment and numerical simulation. A typical picture of water on deck from numerical simulation is shown in Figure 8. It can be seen that around the damage opening, there is some water on the deck. Most of the remaining other area is dry except some area at corners.

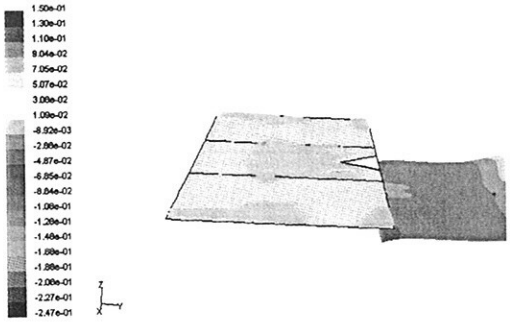

Figure 8 Water on deck

Model tests were carried out at low frequency (0.05Hz) to measure the restoring force for the test conditions. Based on this, an equivalent linear restoring term was calculated for each test case. A restoring force signal was synthesized for each test run and subtracted from the measured force signal time history.

The experimental estimation of virtual inertial force and damping force derived from the measured restoring force is related to as method 1.

The numerical results of virtual inertial force and damping force derived by this method are called as method 2.

Besides, two other methods were used to estimate virtual inertial force and damping force. One, called method 3, is based on the extraction of the fixed mean hydrostatic force due to the water in the tank in still state. The other called method 4 is to extract actual hydrostatic force from water in tank.

The virtual inertial force at frequency 0.5 Hz is given in Figure 9.

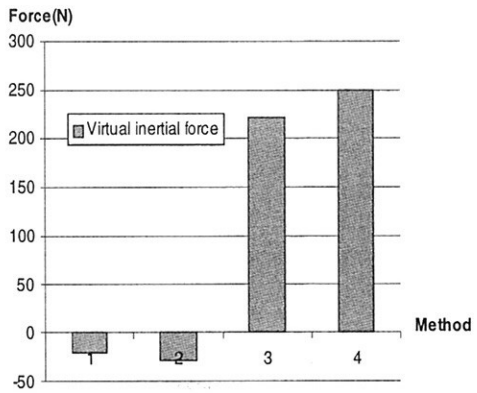

Figure 9 Virtual inertial force

As can be seen, the results depend strongly on the methods used to process data. Experimental and computational virtual inertial forces (method 1 and 2) compare well. However, they were negative. The virtual inertial force by method 3 is positive and much larger than that by methods 1 and 2. The difference of virtual inertial force between method 2 and 3 (the same computational dataset) shows that the method how to extract hydrostatic force is very sensitive to virtual inertial force. Therefore, only virtual inertial force obtained with method 4 is correct.

The damping forces from four different methods are given in figure 10. The results show that the damping forces from methods 1-3 are very close but larger than with method 4. The experimental and computational damping forces from methods 1 and 2 agree well. However, only damping force from method 4 is correct.

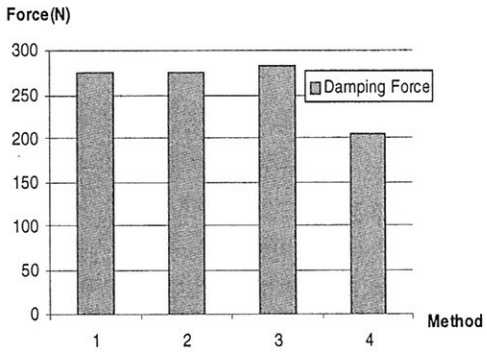

Figure 10 Damping force

Conclusion

The coupling method between CFD simulation and a potential code for damage ship flooding was created. The method was applied to forced heave motion problem as a validation test case. Based on the results, the following conclusions could be drawn

The flooding mean velocity amplitude at the opening is determined mainly by heave amplitude.

The mass of water in tank is affected by frequency largely

The predicted virtual inertial force and damping force agreed well with measured data.

Virtual inertial force and damping force should be obtained by accurate restoring

force. Error on estimation of restoring force results in unphysical hydrodynamic force.

Reference

1. Jasionowski, A., Vassalos, D.,*"First Principles for Damage resistance against Capsize"*, Progress Report for Jan-Nov 2001, 6 Dec 2001, NEREUS

2. Kim. Y, 2002, A numerical study on sloshing flows coupled with ship motion, Journal of Ship Research 46, 1,52-62

3. Olav F. Rognebakke and Odd M. Faltinsen, 2003 Coupling of Sloshing and Ship Motions, Journal of Ship Research, Volume 47 Number 3 Page 208 – 221

4. Peter Woodburn, 2000, Fundamentals of damaged ship survivability, WSAtkins Consultants Ltd report

5. Fuat Kara, 2000, Time domain hydrodynamic and hydroelastic analysis of floating bodies with forward speed, PHD thesis

6. Michaal mirfield, 2001 Burgundy 2-D forced motion experiment, SSRC internal report.

FlowGrid: Flow Simulations On-Demand using Grid Computing

Scott Gatchell, Heinrich Streckwall

Simulations involving free surface computations, fully modeled rotating propellers, cavitation, and more complex geometry require extensive computing resources. Until recently, these simulations were the subjects of long-term, well-funded research projects. Today, customers ask for these kinds of analyses as standard services during consultation projects, thus requiring short response time and competitive costs. In addition, the results from these simulations must meet the quality standards customers have come to expect from HSVA. Decreasing time and costs, while increasing complexity and quality are conflicting issues.

Until now, many applications (Computational Fluid Dynamics, Structural Mechanics, etc.) required large and expensive computers to run realistic simulations. Although these applications are universally accepted as core technology in many large organizations, there are significant barriers to their acceptance in smaller organizations. One of the primary reasons why industries are failing to use 'computationally intensive applications' (i.e. CFD) is the lack of computing resources and accessibility. These resources, until now, had to be located in a single site, and be accessed and maintained from that site.

HSVA is working together with Symban Power Systems Ltd (UK), the Computer Science Research department at the Zuse Institute (Germany), Skoda VYZKUM (Czech Republic), CERTH/CPERI (Greece), and the Fluid Mechanics Group at the University of Zaragoza (Spain) to provide a platform for on-demand computing resources for CFD applications without the enormous costs of building and maintaining a computing cluster. FlowGrid is a European R+D project funded in the context of the IST program. The objective of the FlowGrid project is to establish a virtual organization for the computation of CFD simulations. FlowGrid is an example of a Grid computing environment, with a new method for running CFD simulations.

In this EU project, a distributed computing environment is assembled for preparing, executing and monitoring CFD computations on geographically and organizationally dispersed computing resources. The CFD Client provides access to Grid-enabled computing resources via middleware developed by ZIB. The CFD solver in this environment has been developed by the London based Symban Power Systems Ltd.

The components of the FlowGrid architecture are organized into four layers: actor, front-end, middleware and backend. Figure 1 depicts these layers and the distribution of the components. The dependencies and interactions between the components are also shown. The actor layer consists of actual persons taking different roles in the interaction with FlowGrid:

- resource providers
- administrators
- subscribers

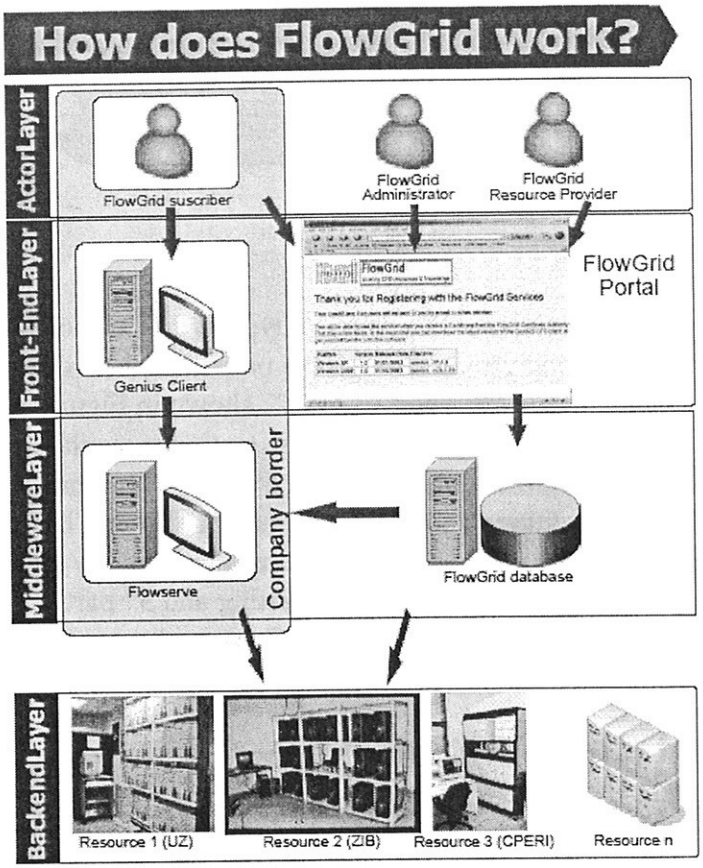

Figure 1 FlowGrid Architecture

The front-end layer consists of two graphical user interfaces- the client interface and a web portal. In the middleware layer, the FlowServe system manages the jobs on behalf of the user.

The middleware is the key to the FlowGrid system. This software provides the infrastructure for communication between the client and the distributed computing resources, maintains the user access database, and- once the commercial model is implemented- the billing database. For the interfaces with the other FlowGrid components, the middleware (FlowServe) uses the protocols HTTPS and SOAP, the markup language XML as well as the Globus 2.x protocols and languages. The middleware has been developed in such a way that it can be universally used by other (CFD-)applications as well. For this purpose FlowServe has been specified as a web service which provides an open and extensible interface to the CFD front-end. Based on this interface the FlowServe protocol has been developed which builds on generally available and commonly used protocols.

At the bottom, the backend layer contains the resource managers for the different clusters as well as the actual CFD solver software. This architecture allows for a user-friendly problem set-up and definition as well as a most transparent submission of actual computing jobs on remote machines, the "Grid".

The official project for development and testing of the FlowGrid system continues until November 2004. During the testing phase, each of the partners executes example CFD cases. Over the course of the FlowGrid project, these test cases are expanded beyond the limits of the industrial partner's own computational resources. This demonstrates the advantages of the FlowGrid system.

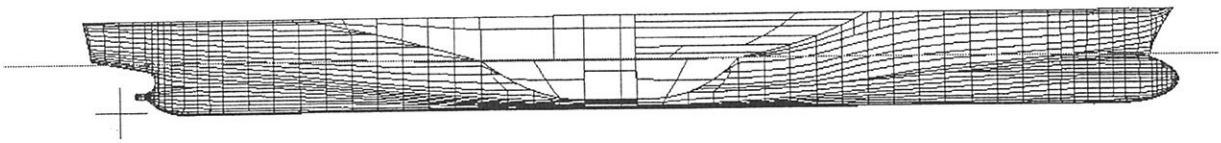

Figure 2 "Sydney Express" profile

HSVA is computing various shipbuilding-related test cases. The first is a typical double-body computation, emphasizing the wake field and flow conditions through the propeller plane of a single-screw containership. The geometry from the ship "Sydney Express", shown in Figure 2, was chosen for this test case. Extensive experimental data from in-house testing is available for validation of the results. Concurrent to the FlowGrid computations, a 3rd party commercial RANS solver computes the same grid and flow conditions on HSVA's Linux PC cluster. The FlowGrid results are benchmarked against the 3rd party software for speed-ups and quality of the results. Figure 3 shows the axial component of velocity from model testing and 3rd party commercial computation. The presentation will compare these with FlowGrid results.

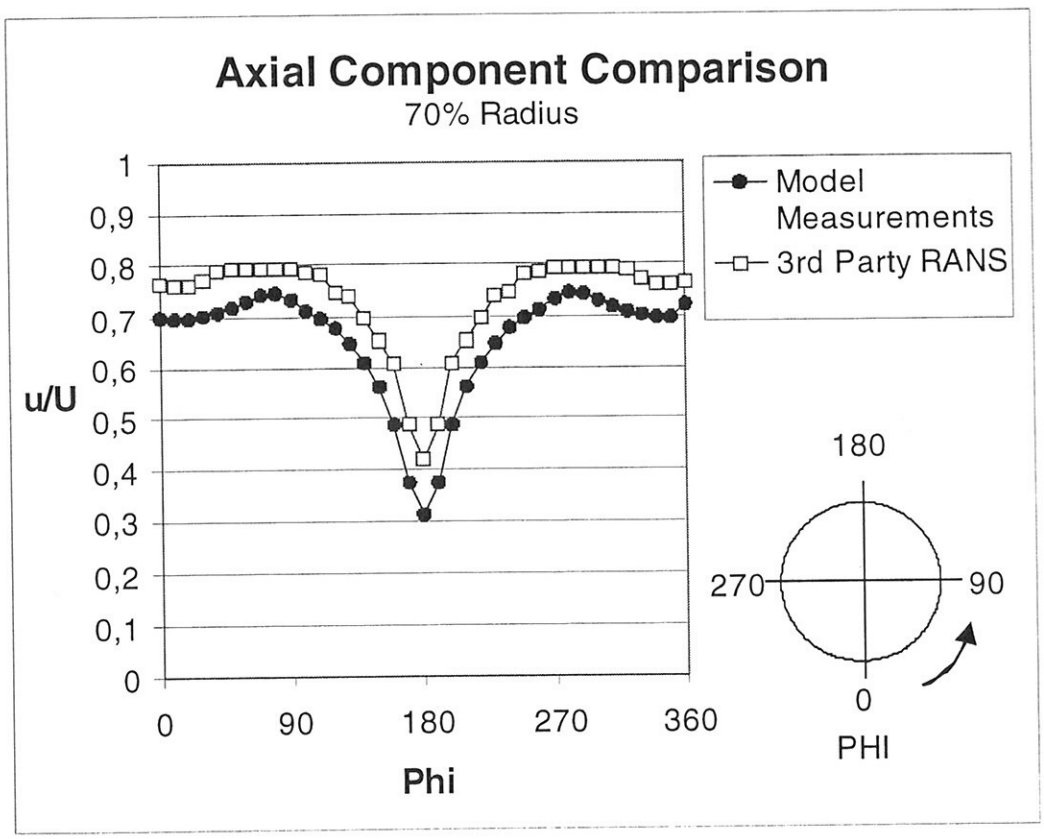

Figure 3 Model testing, 3rd party software results

The official project for development and testing of the FlowGrid system continues until November 2004. Present evaluations of the system show promising results. Significant speed-ups have been obtained when dealing with very large-scale problems, typically involving grid sizes of several million cells already. Future problems and applications are expected to exceed these model sizes even further, thus making it almost impossible to address them by typical in-house hardware available.

The "Grid Computing" approach for the first time ever allows addressing today's large-scale problems in an efficient – with respect to time and cost – way. Based on the promising results obtained with test cases so far, HSVA expects to fully utilize the "Grid" for CFD analysis for their customers in the near future, after the FlowGrid project has been completed.

A Brief Overview of Recent RANS Progress for U. S. Navy Surface Ships

Joseph Gorski, Naval Surface Warfare Center, Carderock Division,
West Bethesda, Maryland (gorskijj@nswccd.navy.mil)

Introduction

Marine vehicles require streamlined hull forms that offer a minimum of resistance to move efficiently through water so that the vehicles can be economically powered. Because of this, the boundary layer around the ship and the wake region are very important since the viscous resistance is often the dominant resistance component. Surface ships must also operate in calm and rough seas for long periods of time and tradeoffs must be made between designs that offer a minimum of resistance and those that behave well in various sea states and meet other requirem ents. Various features of surface ships, such as the bow, bow dome, bilges, and stern will interact with the boundary layer and can generate significant vortical flows [1]. Besides impacting resistance these viscous related phenomena are important since marine propulsors act in the wake of the ship and the velocity distribution entering the propulsor is critical to the performance and cavitation characteristics of it. Consequently, viscous based calculation techniques, primarily Reynolds Averaged Navier-Stokes (RANS) methods, have received considerable attention for U. S. Navy applications as they can provide the entire flow field, including the free surface, in the immediate vicinity of the ship.

Although there have been various levels of development of RANS techniques within the U. S. Navy over the years arguably the focus has been on the application to real problems of naval interest, particularly of late. To this end submarine oriented applications were where the first truly realistic applications were performed, with the computation of the fully appended SUBOFF configuration by Gorski et al.,[2] being one of the first ever. RANS has further progressed with submarine applications and provided significant guidance for the Advance Sail design effort [3], which has been built and tested at ¼ scale. Lately, efforts related to submarines have moved from steady drag and propulsor inflow evaluations to maneuvering simulations for turns (e.g. Sung et al., [4]) and even full six-degree-of-freedom simulations of fully appended hulls (e.g. Purtell [5]).

Surface ship efforts with RANS have not lagged far behind. Early calculations with the Wigley hull and Series 60 progressed much as in the general RANS surface ship community. However, configurations such as Model 5415, with its bow wave and transom, highlighted the difficulties for naval combatant applications. As pointed out by Haussling et al., [6] accurate predictions of wave height could be made, but because of the challenges of dealing with recirculation behind a wet transom and wave breaking it would be quite some time before highly-accurate RANS analysis of transom stern flows would be routine. They relied on a surface tracking method for the free surface prediction where the free surface is tracked as part of the calculations. Dealing with the free surface is largely what distinguishes submarine from surface ship RANS calculations, numerically. Significant progress has been made since then with increased computer power and parallel processing being a significant catalyst for progress with RANS codes for surface ship calculations [7], but the free surface remains an issue. For U. S. Navy applications much of the success with RANS codes for surface ship simulations have been in the area of predicting propeller inflow. The catalyst for this was the effort described by Rood [8] for revolutionary naval combatants. Here teams used RANS codes for predicting surface ship turbulent flow with high performance computing assets to develop a capability to compute the flow about hulls that were sufficiently revolutionary that existing databases did not provide necessary design information. The successes set the stage for an accurate propulsor inflow computational capability not only for the revolutionary hulls of interest [9], but also conventional hulls [10], and waterjets [11].

Similar to progress with submarines, the surface ship community is also moving towards demonstrating capability for maneuvering and seakeeping. RANS has a niche to provide force coefficients for seakeeping codes as discussed by Gorski [12]. Roll motions is an area where viscous effects are important and RANS computations can provide meaningful results [13]. Maneuvering coefficients is another likely area where RANS can contribute. In addition, providing fully dynamic simulations is possible for surface ships with RANS, and efforts are proceeding in this direction as discussed by Kim et al., [14].

Propulsor Inflow

As stated, much of the success with RANS for U. S. Navy surface ships has been in the area of predicting propulsor inflow. Perhaps the catalyst for much of this was the ONR initiated Surface Combatant Accelerated Hydrodynamics S&T Initiative. The objective of this effort was to apply

verified, validated, and benchmarked computational ship hydrodynamics to the exploration of innovative propulsor/hull concepts and to develop tools and concepts for technology options for DD(X) and beyond. To adequately test the computational tools a complex surface ship geometry with strong propulsor/hull interaction was desired. To this end a hull form was designed and built at model scale, and a variety of computations and experiments performed on it as described by Gorski et al., [9]. The hull form is a tumblehome design with a wave piercing bow and ducted propulsors, which are embedded in the hull, and there is also a hub inside the duct. The computed axial velocity contours at several longitudinal positions along the body are shown in Figure 1. It is clearly evident that the vortical structures from the bow dome flow along the hull and enter directly into the propulsors.

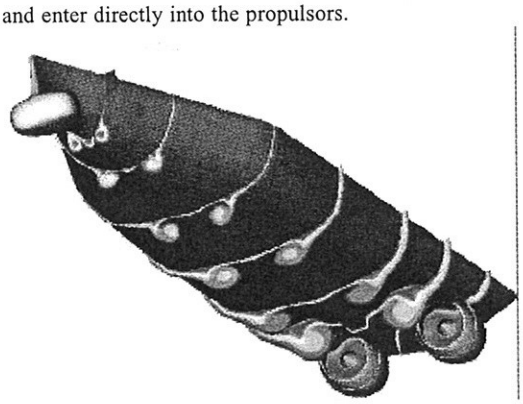

Figure 1: Computed axial velocity contours for the advanced hull form.

Comparisons with free surface heights measured immediately downstream of the hull are shown in Figure 2 with the computed wave height on top and the measured wave height on the bottom. The data shows a rooster tail forming immediately aft of the hull with a trough downstream of that. The computed solution captures the flow extremely well.

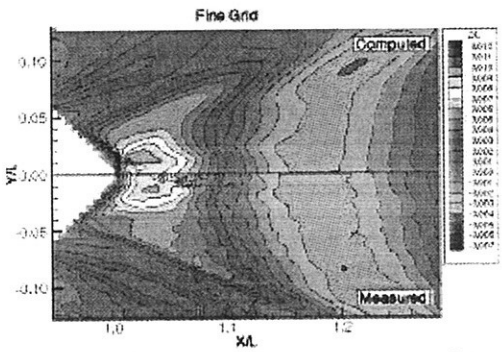

Figure 2: Computed and measured free surface height in the stern region.

The measured and computed axial and secondary flow velocity at X/L = 0.77 is shown in Figure 3, which is in the scooped out area just upstream of the propulsor. This data was taken with a LDV system and axial velocity contours are shown with secondary flow vectors. The dominant feature is the vortex, which is generated at the bow dome. The most apparent difference between the computed and measured data is a slight shift of the vortex location. This shift is probably due to the computed vortex not being as strong as the actual vortex, which can be inferred from the secondary flow vectors. However, the agreement is very good and the predictions are accurate enough to provide cavitation estimates for the propulsor.

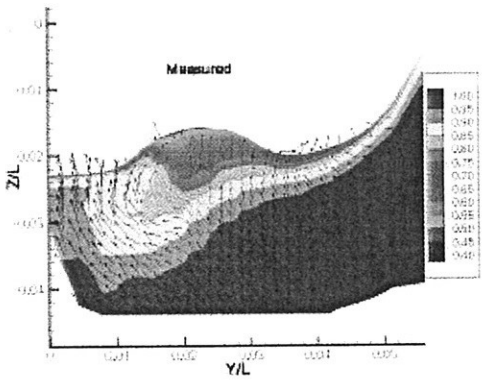

a) Measured

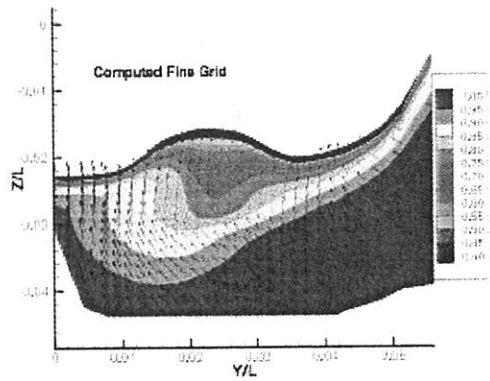

b) Computed

Figure 3: Axial velocities at X/L = 0.77: a) Measured, b) Computed.

Of a more conventional nature is the DDG-51 hull form and its model counterpart, DTMB Model 5415, whose bare hull variant and geosyms is perhaps the most extensively measured naval combatant. A fully appended model was also tested at DTMB including shafts, struts, and rudders. The model was run straight ahead at a speed of 4.0 knots

for a corresponding model scale Reynolds number of 12 million, based on length, and Froude number of 0.277. Detailed computations are performed by Gorski et al.,[10], which also includes results for an aircraft carrier, with highlights of the Model 5415 computation shown here. When shafts and struts are included, the upward and inward flow at the stern due to the decrease in draft and width of the hull, results in a shaft wake above the shaft and beneath the hull. A bow dome vortex still persists at the propeller plane. However, the shaft and strut wakes combine with the bow dome vortex and the hull boundary layer to complicate the flow into the propeller plane, Figure 4.

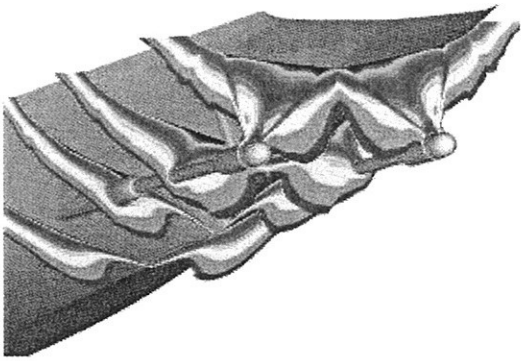

Figure 4: Computed shaft and strut wakes for Model 5415.

A comparison of the calculated axial velocity at the propeller plane with the measured data is shown in Figure 5. The calculation captures the angled v-shaped wake formed from the combination of the bow dome vortex, hull boundary layer and the shaft wake. The calculation also shows the presence of strut wakes in the flow field. This feature is missing in the experimental data, probably due to the coarseness of the measurement data locations.

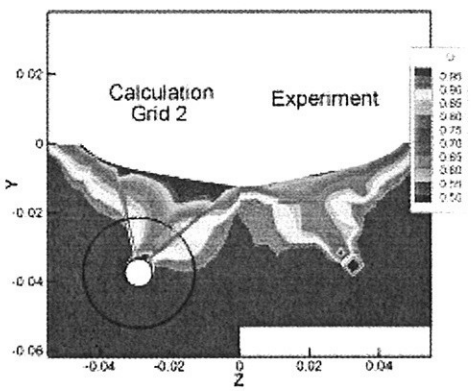

Figure 5: Computed and measured axial velocity at the propeller plane.

A comparison of the averaged axial velocity through the propeller disk area is shown in Figure 6. The results for the calculated shafts-and-struts case is Uave = 0.939. Because of the added disturbance from both the shafts and struts the average velocity is smaller than the measured value. However, it could conceivably be more accurate than the measured value due to the better resolution of the strut wakes. A full-scale result for the shafts-and-struts configuration, where the wakes provide less velocity deficit than the model scale case, raises the average velocity to Uave = 0.972.

a) Experiment; Uave = 0.945

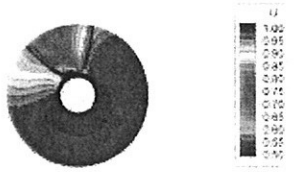

b) Shaft and strut calculation; Uave = 0.939

c) Full scale calculation; Uave = 0.972.

Figure 6: Comparison of flow at the propeller disk and average axial velocity.

With an increased interest in shallow-water missions the U. S. Navy has been exploring concepts for small, fast ships, particularly in regards to the Littoral Combat Ship (LCS). One propulsion system under consideration for such ships is the waterjet and efforts have been underway to apply RANS codes to the study of waterjet propulsion in regards to the propulsor inflow. One effort is described by Ebert et al.,[11], where computations are performed for a conventional hull that corresponds to the research vessel Athena, a former U.S. Navy PG 84 class ship. Dual flush, elliptical inlets were developed as part of a research program (Allison et al.,[15]) where computations were undertaken to help evaluate and

support the design of the waterjet propulsion system. Shown in Figure 7 is the axial velocity through the inlet at various locations with the shaft present. As can be seen in Figure 8, which is the axial velocity at the pump inlet, the shaft creates a wake due to the upward component of velocity coming through the inlet. In practice, the shaft rotates and can have a significant effect on the pump inflow as shown in Figure 9. Here it is shown that the rotating shaft tends to drag its wake around behind it creating a different propeller inflow than when the shaft is not rotating. Also shown in Ebert et al.,[11] are computations for a notional future naval destroyer fitted with twin waterjet propulsion units which are fully submerged with below water discharge.

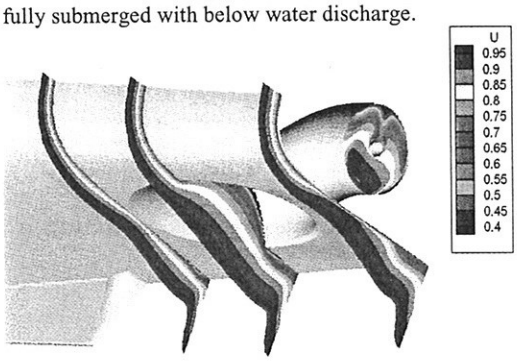

Figure 7: Axial velocity contours through the inlet of the Athena with shaft included.

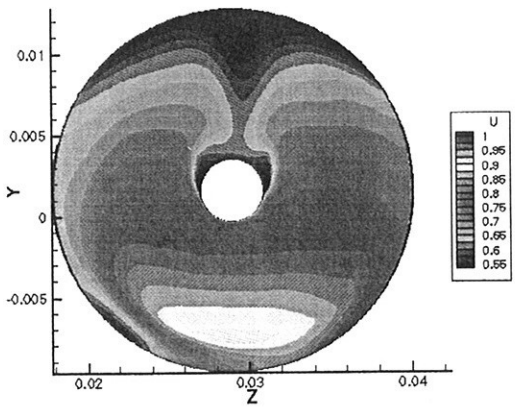

Figure 8: Predicted axial velocity contours at the pump inlet with a non-rotating shaft.

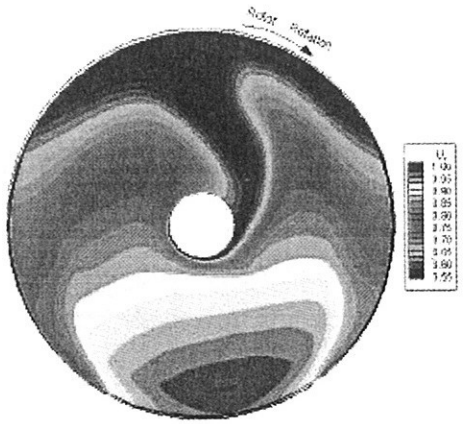

Figure 9: Predicted axial velocity contours with a rotating shaft.

Motions Predictions

Ship roll motion is an area where it is expected RANS codes can contribute. The roll motion of a ship is significantly influenced by viscous effects. The frictional roll damping on a hull form may not be significant, particularly at forward speeds. However, viscous related phenomena such as flow separation from the bilge and keels, with the subsequent vortex formation, account for a large amount of the roll damping. An effort by Miller et al.,[13] demonstrates RANS simulations of roll motion for a 3-D cylinder, including bilge keels, with and without forward speeds. The calculations correspond to a 35.3 -inch (0.897m) diameter cylinder with 2-inch (0.051m) wide bilge keels as tested in the Circulating Water Channel at the Naval Surface Warfare Center, Carderock Division. Measurements were made with the model fully and partially submerged. Forces were obtained over a 2-foot (0.61m) section of the keels as roll motions were imposed at different frequencies and amplitudes. The vortices shedding from the bilge keels were measured using a Particle Image Velocimetry (PIV) system attached to the rolling cylinder. Time dependent RANS calculations were performed and representative comparisons of the calculated and measured force on the bilge keel for one period of roll motion are shown in Figure 10. This is for a 15 degree amplitude roll with and without forward speed. The angular roll velocity at which the model is forced to roll is also shown in the figure. The figure shows that the RANS calculations accurately predict both the magnitude and phase of the measured data as well as the highly oscillating variations in the force data.

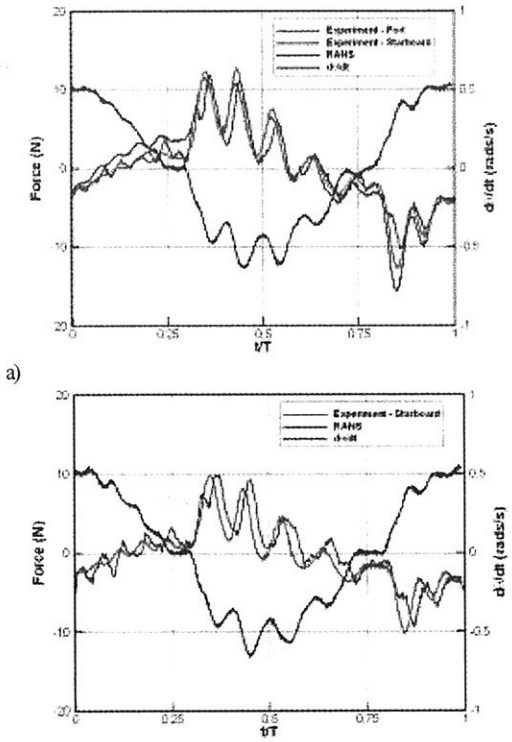

a)

b)

Figure 10: Forces for cylinder roll; a) zero forward speed, b) forward speed = 1.0 m/s (2kts)

Another area where RANS capability can contribute is in the prediction of maneuvering forces. At any yaw angle vortices are shed from the underside of a ship much like tip vortices from a wing. Surface ship hulls in particular can produce very complicated vortical flow fields depending on the hull shape. RANS calculations should be able to predict this flow field. In addition, one of the great potentials for RANS is to evaluate scale effects. At full scale the boundary layers are relatively thinner, compared to ship length, and the resulting vortical flow structure will also be affected. Thus, the larger Reynolds numbers at full scale require finer grids, but large computers can handle this and full scale calculations are becoming more routine. A comparison of the computed axial velocity at X/L = 0.895 for a destroyer hull form at both model and full scale Reynolds numbers, of 12 and 900 million based on body length, is shown in Figure 11 for a 20 degree yaw angle. Although the flow is similar, the different hull wakes and vortex strengths lead to differing flow fields on the hull. This can be seen in Figure 12, which has surface streamlines and pressures for these two calculations. The limiting streamlines created by the hull generated vortex as well as the surface pressure has changed near the stern. These changes provide force differences between model and full scale.

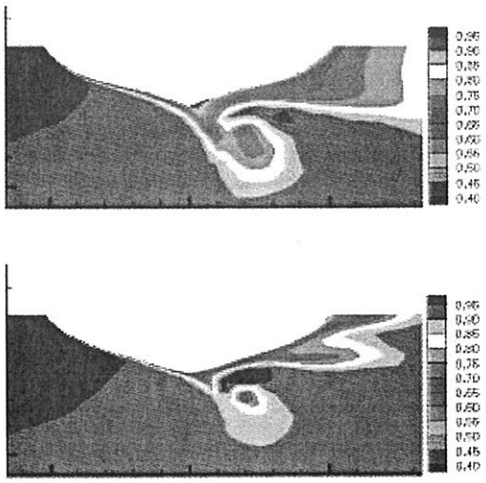

a)

b)

Figure 11: Computed axial velocity contours at X/L = 0.895: a) model scale, b) full scale.

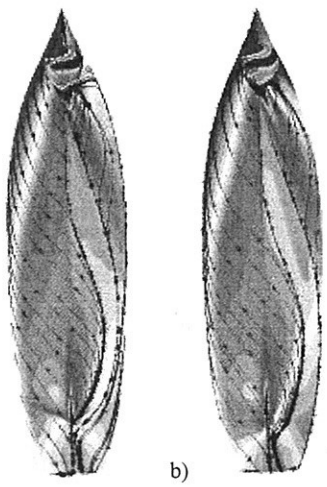

a) b)

Figure 12: Surface pressure and streamlines for 20 degree yaw case; a) model scale, b) full scale.

All of the surface ship calculations in this paper use structured grids. As shown by Ebert et al., [11] unstructured grids can handle complicated geometry more easily than structured grids and provide accurate answers. Consequently, there is a definite move to doing more calculations with unstructured grids in the future. Additionally, for the calculations done here, a double body assumption, linearized free surface boundary conditions, or a surface tracking method has been used where the computational domain and grid are dynamically conformed to the evolving free surface at each time step. This technique has worked very well for a variety of hull

forms, but can be very problematic. Considering how difficult it can be to generate a good grid with predefined surfaces one can easily see that it will be difficult to automatically adjust a grid to any new water surface, particularly for steep or breaking waves. The lack of a robust free surface capability has hampered RANS computations of surface ships. Capturing methods are receiving increased attention in ship hydrodynamics in general and efforts are underway to use these methods more routinely for U. S. Navy applications as discussed by Kim et al., [14].

Conclusions

RANS codes are starting to play a larger role in the study of viscous flow fields generated by marine vehicles of naval interest. With increased accuracy and robustness, due in part to the advent of parallel computer capabilities and increased experience, it has been possible to move such computations to the point where they can impact design studies. Although this has largely been done for steady studies of resistance and propulsor inflow it is also progressing to dynamic areas for maneuvering and seakeeping. It seems inevitable that RANS will have an even larger role in the future as computer power increases and the application of such codes matures even further. RANS predictions can be a time and cost effective way to improve prediction capability for new designs where experimental data bases do not exist. However, it will still take considerable effort to have the confidence in the RANS codes that currently exists with the model tests. To expect to be able to simply replace such techniques with RANS simulations is unrealistic. It has taken considerable time, effort, and resources for model tests to evolve to their current state of usefulness. To reach this level has not only involved improvements to the basic methods, but determination to use these techniques despite their limitations. RANS is already capable of impacting some of these areas as demonstrated here. The level to which RANS is ultimately used will depend on the level of effort put forth to use it.

Acknowledgement

Many of the calculations performed here were supported by ONR under the direction of Dr. L. Patrick Purtell. The computations were performed using facilities of the DOD High Performance Computing Modernization Office (HPCMO).

References

[1] Gorski, J. J., "Marine Vortices and Their Computation," *Proc. NATO RTO App. Vehicle Tech. Panel Symp.*, Loen, Norway, May 2001.

[2] Gorski, J. J., Coleman, R. M., and Haussling, H. J., "Computation of Incompressible Flow Around the DARPA SUBOFF Bodies," David Taylor Research Center Report, DTRC-90/016, 1990.

[3] Gorski, J. J. and Coleman, R. M., "Use of RANS Calculations in the Design of a Submarine Sail," *Proc. NATO RTO App. Vehicle Tech. Panel Symp.*, Paris, France, April, 2002.

[4] Sung, C.-H., et al., "Validation of the Flow Around a Turning Submarine," *Proc. 24th Symposium on Naval Hydrodynamics*, Fukuoka, Japan, July, 2002.

[5] Purtell, L. P., "Submerged Wakes in Littoral Regions," *Proc. DOD HPCMP 2002 User's Group Conf.*, Austin, TX, June, 2002.

[6] Haussling, H. J., Miller, R. W., and Coleman, R. M., "Computation of High-Speed Turbulent Flow About a Ship Model with a Transom Stern," ASME Paper FEDSM97-3398, 1997.

[7] Gorski, J. J., "Present State of Numerical Ship Hydrodynamics and Validation Experiments," *Journal of Offshore Mechanics and Arctic Engineering*, Vol. 124, pp. 74 - 80, May 2002.

[8] Rood, E. P., "Computational Ship Hydrodynamics for Revolutionary Naval Combatants," *Proc. DoD HPC User's Group Conf.*, Albuquerque, 2000.

[9] Gorski, J. J., Haussling, H. J., Percival, A. S., Shaughnessy, J. J., and Buley, G. M., "The Use of a RANS Code in the Design and Analysis of a Naval Combatant," *Proc. 24th Symposium on Naval Hydrodynamics*, Fukuoka, Japan, July, 2002.

[10] Gorski, J. J., Miller, R. W., and Coleman, R. M., "An Investigation of Propeller Inflow for Naval Surface Combatants," *Proc. 25th Symposium on Naval Hydrodynamics*, St. John's, Newfoundland, August, 2004.

[11] Ebert, M. P., Gorski, J. J., and Coleman, R. M., "Viscous Flow Calculations of Waterjet Propelled Ships," *Proc. 8th Int. Conf. Numerical Ship Hydrodynamics*, Busan, Korea, Sept. 2003.

[12] Gorski, J. J., "A Perspective on the Role of RANS Codes for Predicting Large Amplitude Ship Motions," *Proc., 6th Int. Ship Stability Workshop,* Glen Cove, New York, Oct., 2002.

[13] Miller, R. W., Gorski, J. J., and Fry, D., "Viscous Roll Predictions of a Circular Cylinder with Bilge Keels," *Proc. 24th Symposium on Naval Hydrodynamics*, Fukuoka, Japan, July, 2002.

[14] Kim, K-H., Gorski, J. J., Wilson, R. W., and Hyman, M., "Simulation of Surface Ship Dynamics," *Proc. DOD HPCMO User's Group Conf.*, Bellevue, WA, June, 2003.

[15] Allison, J. L., et al., "Research in Waterjet Inlet, Hull,and Jet Interactions," *Proc. Int. Conf. Waterjet Propulsion III*, Gothenburg, Sweden, Feb., 2001.

The Use of Locally Refined Unstructured Grids for Free-Surface Flows Computations

A. Hay, P. Queutey, M. Visonneau
Laboratoire de Mécanique des Fluides, CNRS UMR 6598
Ecole Centrale de Nantes, B.P. 92101
44321 Nantes Cedex 3, France

1 INTRODUCTION

It has been observed during the last Gothenburg 2000 workshop (1) that the free-surface capturing methodology was more and more popular among the CFD developers dealing with viscous naval hydrodynamics. This increasing interest is due to the fact that this approach is more robust than those based on a free-surface fitting methodology since no regridding is necessary and the numerical wave-breaking which may occur during the initialization period, is perfectly tolerated. When specific compressive discretisation schemes are used to discretize the concentration transport equation, one can ensure that the density discontinuity between air and water is captured on three to five control volumes. However, if the discontinuity occurs in a region where there are not enough grid points, the free-surface elevation is dramatically smeared, making the free-surface capturing strategy far less accurate (and far more expensive) than the classical algorithms based on free-surface fitting. Therefore, the almost perfect numerical strategy should integrate a coupling between a free-surface capturing approach and an automatic adaptive mesh refinement and coarsening methodology in order to maintain dynamically a prescribed density of grid points around the steady or unsteady interface between air and water. During the last two years, such a capability was first implemented in our CFD code for error-estimation purposes during the PhD thesis of A. Hay (2). For instance, the study described in (3) presented a new a-posteriori error estimate for a finite volume method based on a transport equation for the error. Recently, our group has also extended this method to the computation of three-dimensional free-surface flows by using an explicit error indicator. Firstly, this paper is devoted to a brief presentation of the specific discretisation schemes which are required to get an accurate description of a density discontinuity. Moreover, the influence of discretisation schemes is analysed by comparing the respective numerical solutions to an extensive experimental database (4) related to the Series 60. In a second part, an automatic grid refinement and coarsening strategy is proposed and applied to the simulation of the free-surface flow around a Wigley hull. The advantages of this approach are demonstrated in terms of accuracy, optimal use of discretisation points and user-friendliness.

2 COMPUTATIONAL APPROACH

2.1 Flow solver

The ISIS flow solver, developed by DMN (Division Modélisation Numérique i.e. CFD Department of the Fluid Mechanics Laboratory), uses the incompressible unsteady Reynolds-averaged Navier Stokes equations (RANSE). The solver is based on the finite volume method to build the spatial discretisation of the transport equations. The face-based method is generalized to two-dimensional, rotationally-symmetric, or three-dimensional unstructured meshes for which non-overlapping control volumes are bounded by an arbitrary number of constitutive faces. The velocity field is obtained from the momentum conservation equations and the pressure field is extracted from the mass conservation constraint, or continuity equation, transformed into a pressure-equation. In the case of turbulent flows, additional transport equations for modeled variables are solved in a form similar to the momentum equations and they can be discretized and solved using the same principles. Incompressible and non-miscible flow phases are modelized through the use of conservation equations for each volume fraction of phase.

2.2 Discretisation schemes for the transport equation of concentration

To check the influence of ddiscretisation schemes, two different methods have been evaluated. The first one, called GDS, was first introduced by (5). However, the GDS scheme is based on upwind or centered differencing

and could not be appropriate for maintaining the sharpness of an interface since numerical diffusion is introduced. On the other hand, this scheme does not suffer from any Courant number limitation. An alternate treatment of numerical diffusion problem for interface capturing method is to use the donor-acceptor cell concept. This can be realized with the GDS scheme if one introduces downwind differencing (DDS) to build the Inter-Gamma scheme (5) since compressive characteristics are required for an accurate interface capturing. The main disadvantage of the IGDS scheme is a Courant number limitation : $Co < 0.3$ in multidimensional cases. To overcome that difficulty, the following correction (1) is used which proved satisfactory in most applications. Then, the second adopted scheme for interface capturing MGDS, results from the Courant number limited scheme IGDS with corrections from (1).

$$\tilde{q}_f = \tilde{q}_C + (\tilde{q}_f - \tilde{q}_C)\frac{0.7 - Co}{0.7 - 0.3} \quad \text{if} \quad 0.3 \leqslant Co \leqslant 0.7$$
$$\tilde{q}_f = \tilde{q}_C \quad \text{if} \quad Co \geqslant 0.7 \tag{1}$$

3 SERIES 60 HULL IN DRIFT

3.1 Description of the test case

In order to assess the reliability of this free-surface capturing strategy, the Series 60 database (4) with a drift angle of 10 degrees has been chosen. The computations are performed on a parallel computer using MPI and the $k - \omega$ SST model is selected to model the turbulent correlations. An original and robust wall-function (6) boundary condition is employed on the wall instead of a near-wall low Reynolds number formulation in order to avoid, until now, any difficulty related with the behavior of the interface in the vicinity of the wall when very fine grids suited to a low Reynolds number formulation are employed.

3.2 Influence of the discretisation scheme

From the previous section, it appears that the compressivity is theoretically crucial to keep the interface between air and water as sharp as possible, even if this property is satisfied through a severe Courant number limitation. It is therefore interesting to evaluate on fine grids and real-life problems, the influence of the discretisation error to check if it is realistic to use the faster non-compressive discretisation schemes. If one considers Figs.1 which compare the free-surface elevation field all around the ship hull, it is clear that the discretisation schemes still play a central role even if these results are obtained on a very fine grid. Not only the amplitudes of the main divergent waves are modified but one can observe that the free-surface field computed with MGDS contain many secondary waves inside the Kelvin angle in good agreement with the experiments, a behavior which is not simulated by the cheaper GDS scheme. The wave contours are significantly influenced by the drift angle since the wave amplitudes are drastically increased/decreased on the port/starboard sides. It appears that the influence of the compressive MGDS scheme is far more important on the port side because the water is pushed away from the hull resulting in a downwind dependency, only accounted for by the compressive scheme. Particularly, it is noteworthy to mention that, the bow wave spray sheet detaching from the hull and merging with the downstream breaking bow wave, is far better captured by the MGDS simulation (see figs.2).

4 ADAPTIVE MESH REFINEMENT STRATEGY FOR FREE-SURFACE FLOWS

4.1 Adaptive grid procedure

The ultimate goal of an automatic adaptive procedure is clearly to reduce, without human interaction, the discretisation error for reaching a solution of prescribed accuracy for a low computational cost. In order to do so, each control volume marked for grid refinement is subdivided into several smaller ones of *the same topology*. As the initial mesh can possibly be too fine in some region for the desired accuracy, it can be coarsened by an *agglomeration algorithm*. This steady adaptive procedure based on an original error estimation has already been successfully applied by the authors to the computation of steady turbulent flows (3). Although the same approach can be retained for multi-fluid flows, once generalized to unsteady problems, it is wiser, for a first step, to use a strategy based on an explicit physical indicator. As indicated before, a free-surface capturing methodology is based on the solution of a transport equation of a contact discontinuity which indicates the location of the interface. Although the compressive discretisation schemes described above guarantee an interface captured over three to five cells, it is crucial to keep as small as possible the characteristic length of the cells on either side of the interface in order to avoid too much a numerical smearing of the discontinuity. Ideally, such an approach should make possible the use of a grid schematically described in Figure 3(a) instead of that shown in Figure 3(b). Moreover, an automatic grid adaption frees the user from a tedious task : the generation of a mesh suited everywhere to the unknown interface since one can start from a uniform grid which will be automatically refined near the interface, thanks to the explicit interface indicator. The solution chosen here is based on an explicit error indicator which is proportional to the gradi-

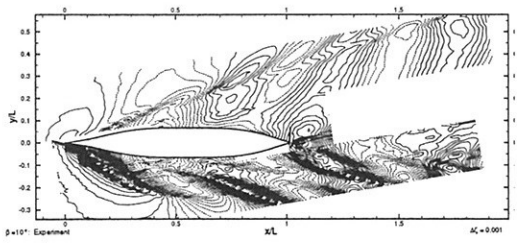

(a) Experiments

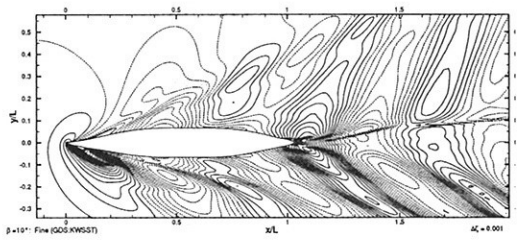

(b) GDS

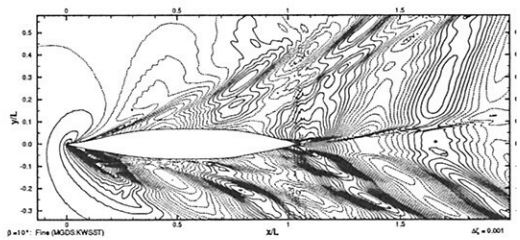

(c) MGDS

Figure 1: Free-surface elevations for a drift angle of 10 degrees. Comparison of GDS, MGDS discretisation schemes and experiments

(a) Experiments

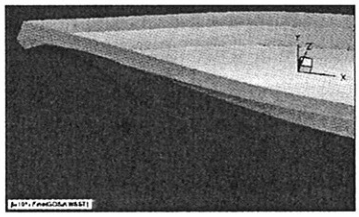

(b) Computations with GDS

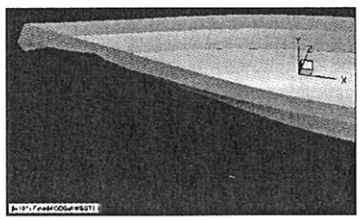

(c) Computations with MGDS

Figure 2: Detailed view of the experimental and computed bow waves for a drift angle of 10 degrees. Comparison of GDS and MGDS discretisation schemes

ent of concentration in order to concentrate the points in the vicinity of the interface.

5 FREE-SURFACE AROUND THE WIGLEY HULL

5.1 Characteristics of the computations

The Wigley hull has a shape which is defined by a mathematical formula given by:

$$z(x,y) = \frac{B}{2}(1-4x^2)(1-(\frac{y}{D}^2) \qquad (2)$$

where B is the maximum thickness of the hull and D is the draft of the hull. These constants are set here to 0.1 and 0.0625 respectively. This hull has been preferred to the more realistic Series 60 hull because its analytical definition facilitates the inclusion of the new grid points on the surface of the body. Computations using slip wall conditions instead of wall-function boundary condition, are performed for a Froude number of 0.289 on grids systematically refined according to an explicit indicator based on the vertical component of the gradient of the concentration C_i. However, to avoid the inclusion of points in regions where the free-surface is not deformed, this criteria is activated only inside a triangular region around the hull. Figures 4 and 5 show the typical grid concentration near the interface after two levels of refinement on

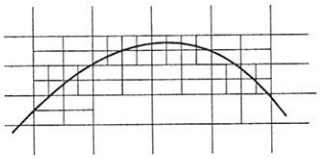

(a) Adapted grid

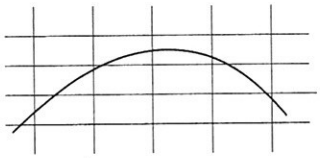

(b) Unadapted grid

Figure 3: Adaption of grids around an interface

a very coarse grid containing 64000 cells. A transversal cut comparing the reference structured grid and the coarse adapted grid. One can notice here that the criteria used in this preliminary study is based on the density discontinuity without considering the shape of the waves. This is the reason why no wave pattern is visible on this figure. It is clear that such a criteria will have to be improved in the future to distinguish between moderate and steeper waves. Such an improvement will require the use of a directional refinement approach instead of the actual isotropic strategy. The results obtained on the adapted coarse mesh (two generations of local refinement) are compared to that obtained on (i) a very fine structured grid made of 1.8 M cells, (ii) a medium structured grid having the same number of cells (300 000) than the adapted coarse grid. The computational costs are listed in Table 1.

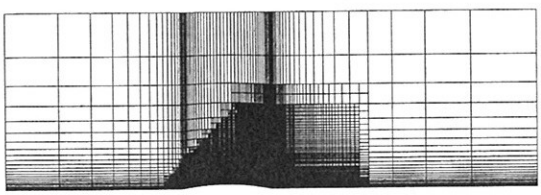

Figure 4: Global view of the region where the adaption criteria is activated

5.2 Free-surface elevation

The respective free-surface elevations are shown in Figs. 7. Although the solution obtained on the adapted

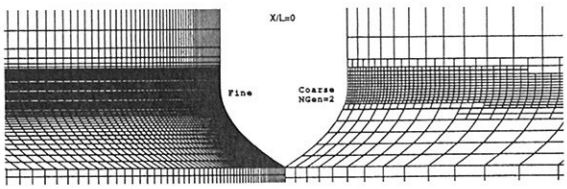

Figure 5: View of the structured and adapted grids at a section X=cst.

Number of generations	Number of cells	Total monoproc. CPU time (hours)
Coarse - Ngen=0	64000	5
Coarse - Ngen=2	307000	70
Medium - Ngen=0	306000	77
Fine - Ngen=0	1 800 000	960

Table 1: Characteristics of the grids used for the computations of the free-surface around the Wigley hull

coarse grid is not as accurate as the one provided on the very fine structured grid (1.8 M cells), one can say that the interface is very well captured since all the waves are visible although slightly damped. The influence of the right positioning of grid points is illustrated by the solution obtained on a structured grid made of the same number of points as the adapted grid (roughly 300 000 cells), but distributed according to the criteria used to build the fine structured mesh. The free-surface elevation obtained on that medium structured grid is obviously far too smeared. Lastly, a global and detailed view of the elevation computed on the adapted grid is given in Figure 6.

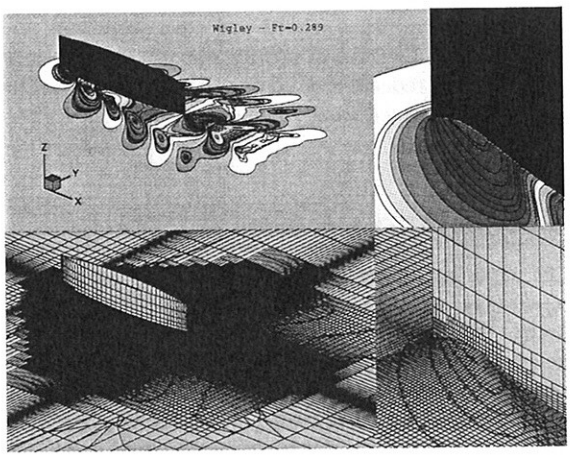

Figure 6: Global and detailed views of the flow and adapted grids

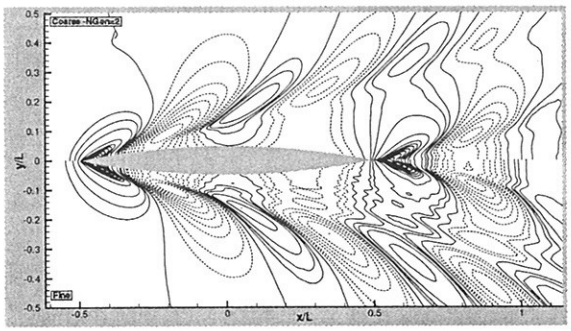

(a) 2 generations of refinement (top) vs a fine structured grid (bottom)

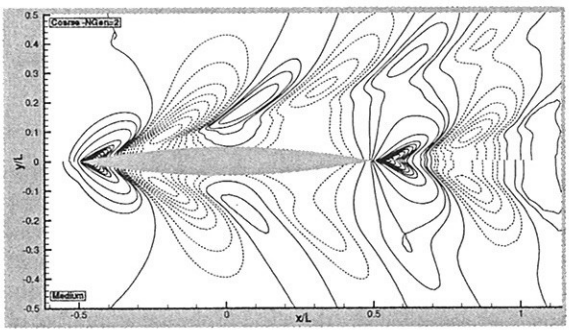

(b) 2 generations of refinement (top) vs a moderate structured grid having the same number of points (bottom)

Figure 7: Comparisons of the free-surface elevation with different grids

By considering these results and other wave cuts not shown here for the sake of brevity, one can evaluate to a a factor 10 the reduction of computational cost related to the use of an adapted locally refined grid.

6 CONCLUSION AND PERSPECTIVES

This paper has described a modern free-surface capturing strategy implemented in an unstructured finite-volume viscous flow solver. It has been established that, despite the relatively fine grids used in this study, the role played by the compressive property of the discretisation schemes is still fundamental to get a reliable simulation of the free-surface. A new adaptive grid refinement strategy has also been described and applied to the free-surface flow around the Wigley hull. Very promising although preliminary results have shown that an approach linking the use of unstructured adaptive grids with several levels of local refinement to a free-surface capturing strategy may be optimal in terms of robustness and accuracy. The first results are very encouraging and indicate that the development of a three-dimensional anisotropic grid refinement will yield even more accurate results by making possible the use of less points along the free-surface and more refinement generations across the interface. Apart from the implementation of anisotropy, the future developments will aim at generalizing this approach to arbitrary (i.e. non analytical) hull geometries and implementing an efficient parallelization with a dynamic load-balancing.

7 ACKNOWLEDGMENTS

The authors gratefully acknowledge the scientific committee of CINES (project dmn2050) and IDRIS (project 1308) for the attribution of CPU time.

REFERENCES

[1] L. Larsson, F. Stern, and V. Bertram, "Summary, conclusions and recommandations of the Gothenburg 2000 Workshop," A Workshop on Numerical Ship Hydrodynamics, L. Larsson, F. Stern, and V. Bertram, eds., Göteborg, Chalmers University of Technology, September 2000.

[2] A. Hay, Etude de stratégies d'estimation d'erreur numérique et d'adaptation locale de maillages non-structurés pour les équations de Navier-Stokes en moyenne de Reynolds. PhD thesis, Université de Nantes, 2004.

[3] A. Hay and M. Visonneau, "Adaptive error control strategy : Application to a turbulent flow." AIAA CFD Conference, Orlando, June 2003.

[4] J. Longo and F. Stern, "Effects of drift angle on model ship flow," Experiments in Fluids, Vol. 32, 2002, pp. 558–569.

[5] H. Jasak and H.G. Weller, "Interface tracking capabilities of the inter-gamma differencing scheme.." Internal Report, Mechanical Engineering Department, Imperial College of Science, London, February 1995.

[6] G.B. Deng, R. Duvigneau, P. Queutey, and M. Visonneau, "Assessment of turbulence model for ship flow at full scale," Comp. Mech., WCCM IV, Beijing, China, September 2004.

Development and Validation of CIP based Cartesian Grid Method for Nonlinear Wave-Body Interactions

Changhong Hu[1], Odd Faltinsen[2] and Masashi Kashiwagi[1]

[1] *RIAM, Kyushu University (hu@riam.kyushu-u.ac.jp)*

[2] *Department of Marine Technology, NTNU*

Introduction

Owing to practical importance in ship and ocean engineering, the strongly nonlinear phenomena such as slamming, water on deck, wave impact by green water, and capsizing due to large-amplitude waves, have attracted a large number of researches. Many investigations have been done in the past to understand the fundamental hydrodynamics of such non-linear wave-body interactions. In recent years rapid progress of computer technology makes it possible to study a practical engineering problem by means of CFD simulation. However, as a practical problem generally contains not only violent free surface motion/deformation, but also bodies with complicated geometries that may be both time and flow dependent, conventional numerical approaches such as the boundary element method for potential flows or the finite difference/volume method using curvilinear grids adapted to both free surface and body surface, are not applicable. We need to develop a new numerical method. This new method should be not only able to handle complicated flow phenomena but also relatively simple in scheme which can perform three-dimensional simulations in an acceptable spatial and temporal resolution at reasonable cost.

In past two years, the authors developed a new numerical model for this purpose [1]. This model is a finite difference method in a stationary Cartesian grid, in which the CIP (Constrained Interpolation Profile) algorithm [2] is adopted as the base scheme. There are two key points of the CIP method: (1) a compact upwind scheme with sub-cell resolution for the advection calculation and (2) a pressure-based algorithm that can treat multi-phase problems. By a series validation computations on solitary wave propagation, dam breaking, et al., this method has been proved to have the capabilities that we expect, e.g., handling the complicated free surface geometries and treating violently moving floating bodies. On the other hand, as the grid does not conform to the body boundaries, to develop a boundary treatment with good precision and conservation property for the flow computation near the body boundaries is still remaining a big challenge. Therefore the emphasis of present study is addressed on the imposition of boundary conditions at the immersed body boundaries for the present CFD method, which is considered to be very essential for accurate calculation of hydrodynamic force on floating bodies. In the current paper, at first some major features of the present model are described. Then two methods of imposing velocity in a computation cell including the solid body boundary to achieve a no-slip condition are introduced and their efficiencies are investigated by several 2D numerical simulations on forced oscillating cylinder in a free surface.

Governing Equations

The governing equations are unsteady, viscous, compressible Navier-Stokes equations.

$$\frac{\partial \rho}{\partial t} + u_i \frac{\partial \rho}{\partial x_i} = -\rho \frac{\partial u_i}{\partial x_i}, \tag{1}$$

$$\frac{\partial u_i}{\partial t} + u_j \frac{\partial u_i}{\partial x_j} = \frac{1}{\rho} \frac{\partial \sigma_{ij}}{\partial x_j} + F_i, \tag{2}$$

where σ_{ij} is the total stress. F_i denotes a body force such as the gravity force. It may also include a forcing term that is non-zero only at the body boundary to describe a no-slip condition, in the case of applying immersed boundary method [3]. If no temperature variation is assumed, the equation of state can be written as $p = f(\rho)$. Then the equation for pressure is derived as

$$\frac{\partial p}{\partial t} + u_i \frac{\partial p}{\partial x_i} = -\rho C_S^2 \frac{\partial u_i}{\partial x_i}, \tag{3}$$

where C_S is the sound speed. Eqs 1-3 are the governing equations, and are solved numerically by a fractional step method in which these equations are divided into an advection phase and a non-advection phase. The coupling of velocities and pressure is treated by using the following Poisson equation in the non-advection phase calculation

$$\frac{\partial}{\partial x_i}\left(\frac{1}{\rho}\frac{\partial p}{\partial x_i}\right) = \frac{p - p^n}{\rho C_s^2 \Delta t^2} + \frac{1}{\Delta t}\frac{\partial u_i^n}{\partial x_i}. \tag{4}$$

Note that this equation is valid for liquid and gas phases, and is computationally possible to apply to solid phase. By solving Eq. 4, the pressure in the whole computation domain can be obtained. The advection phase calculation is performed by CIP method, which is described as follows.

CIP Scheme

Here by CIP we mean the scheme for advection calculation. For advection computation of a variable χ, not only the transportation equation of χ but also the transportation equation of its spatial gradient, $\varphi_i = \partial\chi/\partial x_i$, is used. The value of χ may represent the density, the velocity and the pressure in the governing equations, respectively. We write a general transportation equation of χ in non-conservative form as

$$\frac{\partial \chi}{\partial t} + u_i \frac{\partial \chi}{\partial x_i} = H. \tag{5}$$

By differentiating Eq. 5 with respect to the spatial coordinates, we obtain the transportation equation of φ_i as

$$\frac{\partial \varphi_i}{\partial t} + u_j \frac{\partial \varphi_i}{\partial x_j} = \frac{\partial H}{\partial x_i} - \varphi_j \frac{\partial u_j}{\partial x_i}. \tag{6}$$

Computation of (5) and (6) can be divided into two steps, an advection phase and a nonadvection phase. The advection phase calculation is carried out by a semi-Lagrangian procedure as

$$\chi^*(\mathbf{x}) = \tilde{\chi}^n(\mathbf{x} - \mathbf{u}\Delta t), \qquad \varphi_i^*(\mathbf{x}) = \tilde{\varphi}_i^n(\mathbf{x} - \mathbf{u}\Delta t) \tag{7}$$

where $\widehat{\chi}^n$ is an interpolation approximation to χ^n and $\widehat{\varphi}_i^n = \partial\widehat{\chi}^n/\partial x_i$. The profile at the n+1 step is obtained by shifting the profile at the n step by $\mathbf{u}\Delta t$ to the upwind direction. For one-dimensional case, at a grid point $x_1 = x_{1m}$ the cubic polynomial can be used to approximate $\widehat{\chi}^n$ as

$$\widehat{\chi}^n(x_1) = a_m\left(x_1 - x_{1m}\right)^3 + b_m\left(x_1 - x_{1m}\right)^2 + c_m\left(x_1 - x_{1m}\right) + d_m . \tag{8}$$

We can find an upwind computational cell for the grid point $x_1 = x_{1m}$, e.g., $[x_{1m-1}, x_{1m}]$ for $u_1 \geq 0$, then the 4 unknown coefficients of $\widehat{\chi}^n(x_1)$ can be determined using χ_m^n, χ_{m-1}^n, φ_{1m}^n and φ_{1m-1}^n.

$$a_m = \left(\varphi_{1m}^n + \varphi_{1m-1}^n\right)/\Delta x_1^2 + 2\left(\chi_m^n - \chi_{m-1}^n\right)/\Delta x_1^3 , \qquad b_m = -\left(2\varphi_{1m}^n + \varphi_{1m-1}^n\right)/\Delta x_1 - 3\left(\chi_m^n - \chi_{m-1}^n\right)/\Delta x_1^2 ,$$

$$c_m = \varphi_{1m}^n , \qquad d_m = \chi_m^n . \tag{9}$$

As the advection of spatial gradients in each computation cell can be solved and only the information (value and its spatial gradients) at the grid points of one cell is required for the interpolation function, the CIP scheme has both a sub-cell resolution feature and a compact structure. Therefore, for a multiphase computation in which there are discontinuities or large gradients for physical quantities at the interfaces, the CIP scheme can keep the sharpness better than other upwind schemes.

Treatment of Free Surface and Body Boundary

The moving body boundary and the free surface are distinguished by a density function ϕ_m, which is solved by the following equation.

$$\frac{\partial \phi_m}{\partial t} + u_i \frac{\partial \phi_m}{\partial x_i} = 0 , \tag{10}$$

where, m = 1, 2, 3 denote liquid, gas, and solid phases, respectively.

The free surface is determined by solving Eq. 10 with the CIP method. Like most of the Eulerian methods, the original sharp phase interface may become a layer with finite thickness due to the numerical diffusivity. However, owing to the sub-cell resolution feature of the CIP method, the thickness grows very slowly as the computation proceeds. In the authors' previous paper [1], this treatment has shown to be very efficient by the validation computation on solitary wave propagation and dam breaking problem.

For the floating body boundary, we only consider the rigid body case. Instead of the computation using Eq. 10, a Lagrange method has been developed to directly calculate the density function for the solid phase ϕ_3 and the local velocity of the body $\mathbf{U}_b$ [1]. To achieve a no-slip condition on the body boundary, two methods are implemented in the present CIP code.

The first method, which was adopted in the previous computations, determines the velocity in the cell containing solid phase as

$$\mathbf{U} = \phi_3 \mathbf{U}_b + (1 - \phi_3)\mathbf{u} , \tag{11}$$

where $\mathbf{u}$ is the velocity obtained by Eq. 2. Obviously in boundary cell this is a volume fraction

weighting treatment for velocity interpolation. In the numerical solution procedure, the method of imposing the velocity distribution inside and on the body boundary is equivalent to apply a forcing term f_i to the momentum equation. Therefore this treatment falls into the category of immersed boundary method (IB method) [3]. If Eq. 2 is discretized as

$$\frac{u_i^{n+1} - u_i^n}{\Delta t} = RHS_i + f_i, \tag{12}$$

where RHS_i contains the remaining terms of Eq. 2. The forcing f_i is zero in the fluid cell, and has the following expression in the solid and boundary cell to let $u_i^{n+1} = U_i^{n+1}$ (no-slip condition) on the body boundary.

$$f_i = -RHS_i + \frac{U_i^{n+1} - u_i^n}{\Delta t}, \tag{13}$$

The second method is an interpolation method to determine the velocity **U**, as shown in Fig. 1, by a linear approximation as used by Fadlun et al. [4]. The forcing is given by imposed velocity U_0 which is obtained by the interpolation using the boundary velocity U_b and the neighboring fluid cell velocity U_1.

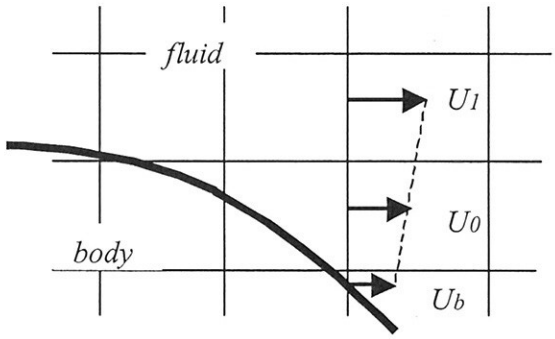

Fig.1. Sketch of velocity interpolation.

In the following we denote the first method using Eq.11 as '*CIPIB1*', and the second method showing in Fig.1 as '*CIPIB2*'. As the outer flow field is essentially independent of the velocity distribution inside the body by the present CIP code, the difference of the two methods lies on the way to determine the imposed velocity at the body boundary.

Numerical Results

The computation example is a forced oscillation in heave with a rectangular cylinder shown in Fig. 2, which is correspondent to the laboratory experiment by Vugts [5]. The width of the cylinder section is $B = 0.4m$ and the ratio is $B/T = 4$. As the main flow structure is symmetric to the vertical centerline of the cylinder in the case of forced heaving, present computation is carried out using a half domain. The grid number is $500(x) \times 205(y)$; the minimum grid spacing is $\Delta x_{\min} = 2 \times 10^{-3} m$ at the body boundary and $\Delta z_{\min} = 2 \times 10^{-3} m$ at the still free surface.

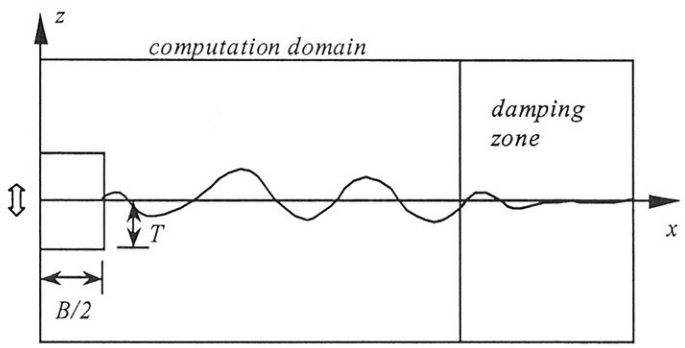

Fig.2. Skematic view of computation domain.

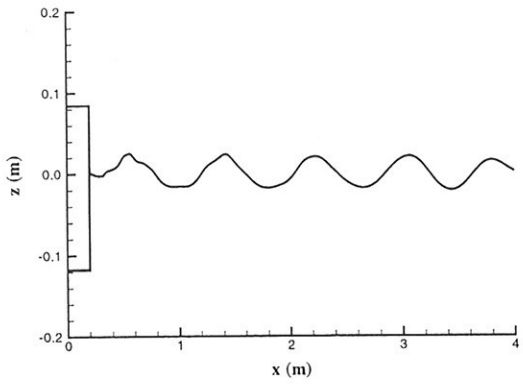

Fig.3. A snapshot of computation.

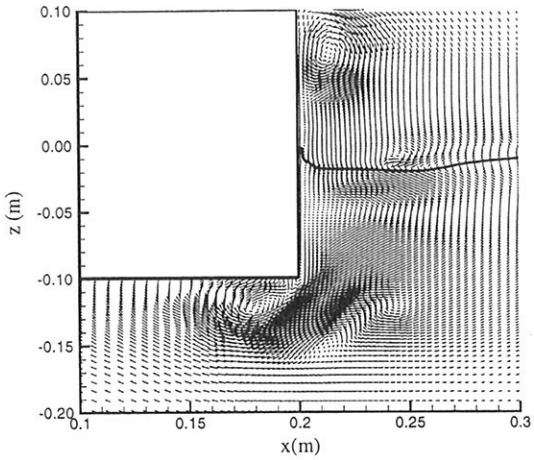

Fig.4. Close-up view of flow around the body.

Figure 3 shows a snapshot for the case of $\omega\sqrt{B/2g}=1.25$ at $t/T_{osc}=9.0$, and Fig. 4 is a close-up view of the flow field around the body for the same case. Vortex shedding can be clearly seen around from the corner. The computation is done by CIPIB2. Figure 5, 6 and 7 are comparisons among different numerical models and the experiments. For the added mass coefficients, both CIPIB1 and CIPIB2 give good results. For damping coefficient in high frequencies, numerical results by present CIP method are larger than the experiments. Part of the reason is considered to come from the sharp edge of the cylinder in computation, while a round corner is used in the experiment. The investigation on the effect of the round corner is under progress. Nevertheless, predictions by CIPIB2 for low frequencies are reasonable well. From the results of generated wave amplitude ratios, it is found that good results are obtained by both methods. The reason for larger computed damping coefficients in the high frequencies by the present model than by the potential BEM is effect of vortex shedding. Then we can obtain the drag coefficients by a analysis method [6], and the results for the computations by CIPIB2 are shown in Fig. 8.

Concluding Remarks

A Cartesian grid approach based on CIP method for computation of nonlinear wave-body interactions has been developed and described in this paper. Validation of the code by numerical simulation on a forced oscillating cylinder in a free surface was carried out. Two methods are applied to obtain no-slip BC on the solid body boundaries: imposition of the velocity in a boundary cell by volume fraction average and by linear interpolation. It is found that the both methods can give reasonable good results of hydrodynamic force. The improvement of the method as well as extension to three-dimension version is now in progress.

References

[1] Hu, C.-H., and Kashiwagi, M., A CIP-Based Method for Numerical Simulations of Violent Free Surface Flows, Journal of Marine Science and Technology (in press)

[2] Yabe T and Wang PY (1991) Unified numerical procedure for compressible and in-compressible fluid. J Phys Soc Jpn 60:2105-2108

[3] Peskin, C.S., Flow patterns around heart valves, J. Comput. Phys. 10 (1972), 252-271,

[4] Fadlun, E.A., Verzicco, R., Orlandi, P., and Mohd-Yusof, J., Combined immersed boundary finite difference methods for three dimensional complex flow simulations. J. Comput. Phys., 161 (2000), 30-60.

[5] Vugts, J. H., The hydrodynamic coefficients for swaying, heaving and rolling cylinders in a free surface. Report 112S, Shipbuilding Laboratory, Technological University Delft. (1968)

[6] Faltinsen, O.M., On seakeeping of conventional and high-speed vessels, JSP, 37,2(1993),87-101.

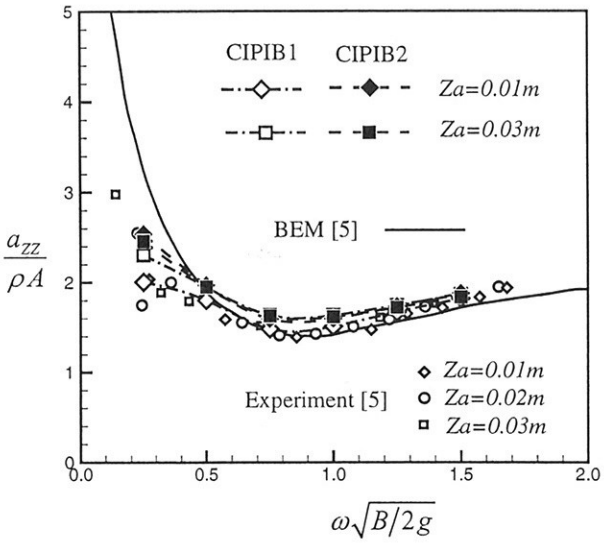

Fig. 5. Added mass coefficient

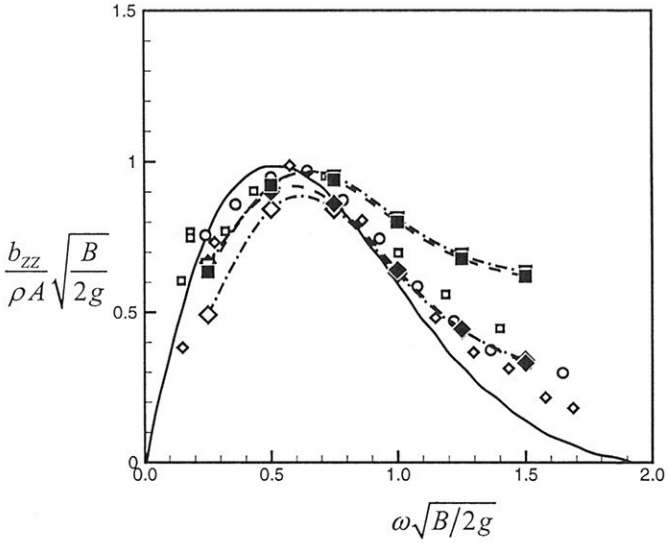

Fig. 6. Damping coefficient

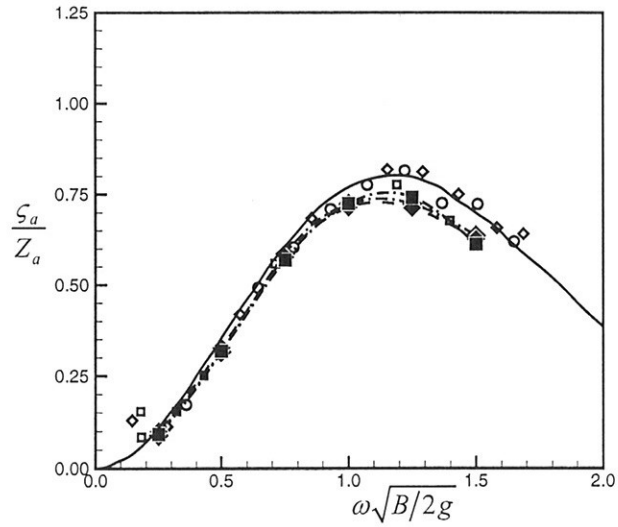

Fig. 7. Wave amplitude ratio

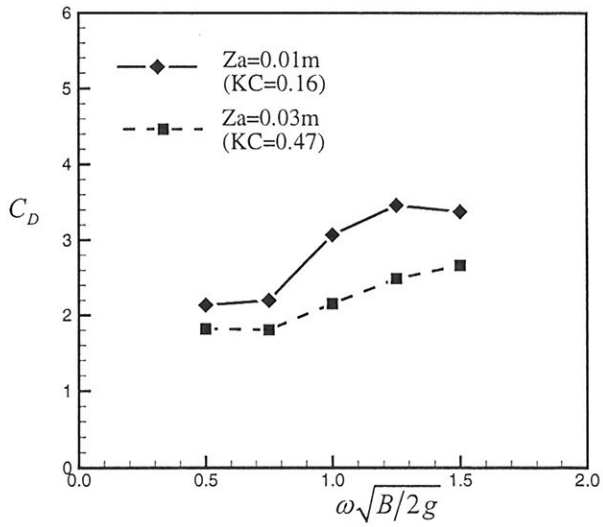

Fig. 8. Drag coefficient

Air entrainment induced by vorticity–free-surface interaction

Alessandro Iafrati and Emilio F. Campana
a.iafrati@insean.it , e.campana@insean.it

INSEAN – The Italian Ship Model Basin, Via di Vallerano 139, 00128 Rome, Italy

1 Introduction

A strong vorticity–free-surface interaction is studied through a two-fluids numerical model. The method is applied to simulate the viscous interaction of a vortex pair rising vertically toward the free surface. This problem has been investigated by Ohring & Lugt (1991) (referred to hereinafter as OL) who used a single fluid model based on a boundary fitted, moving grid approach. In their study, OL performed a parametric study by varying the free surface stiffness and evaluating the effect on the dynamics of the primary vortex. The occurrence of secondary vorticity structures has been found, intensity of which depends on the free surface compliance and can significantly affect the path of the primary vorticity peak. The decay rate of the primary vortex peak and the free surface deformation are evaluated as well. Owing to the adopted numerical approach, results are limited by capability of the numerical method to describe the flow in presence of large free surface deformation.

The above limitation motivated the analysis of the same flow by using a two-fluids approach which can easily handle the occurrence of strong free surface deformations, even beyond the conditions at which air entrainment occurs (Iafrati et al. 2001). The model is based on a Navier-Stokes solver for a single incompressible fluid having density and viscosity smoothly varying across the interface. The formulation is written in curvilinear coordinates and solved with a fractional step approach (Zang et al. 1994). The interface between air and water is captured with the help of a Level-Set technique, as proposed in Sussman et al. (1994) while surface tension effects are introduced in the form of a continuum force as suggested by Brackbill et al. (1992).

As a first step, the two fluid model is carefully verified and validated and comparisons with results presented in OL are established for two sets of governing parameters for which free surface is stiff enough to prevent air to be entrained. Then, the free surface stiffness is reduced and the occurrence of air entrainment. The last result significantly differs from what found in OL for the same parameter set.

2 Two-fluids Navier-Stokes solver

With the aim of describing the free surface flow even when complex topologies of the air and water domains occur, the two-fluids flow is modelled as that of a single fluid with physical properties, like density and viscosity, varying smoothly across the interface. The flow is controlled by the non-dimensional Froude, Reynolds and Weber numbers, defined as:

$$\mathrm{Fr}=\frac{U_r}{\sqrt{ga}} \qquad \mathrm{Re}=\frac{U_r\rho_w}{\mu_w} \qquad \mathrm{We}=\frac{\sigma}{U_r^2\rho_w a}$$

with $U_r=\Gamma/(2\pi a)$ denoting the translation velocity of the vortex pair, Γ and a being the initial values of the circulation and of the distance between them, σ is the surface tension coefficient while ρ_w and μ_w are the density and dynamic viscosity in water. Details of the numerical method are given in Iafrati & Campana (2003) and will not be repeated here.

As originally suggested in Brackbill et al. (1992), surface tension contributions to the momentum equation are modelled with a continuum force, intensity of which comes from the gradient of a smoothed Heaviside function defined as

$$H_{\delta_T}(d)=\frac{1}{2}+\frac{1}{2}\sin\left(\frac{\pi d}{2\delta_T}\right) \qquad |d|<\delta_T\ ,\ H_{\delta_T}(d)=0 \quad d<-\delta_T\ ,\ H_{\delta_T}(d)=1 \quad d>\delta_T$$

where d is the signed normal distance from the interface ($d>0$ in water, $d<0$ in air). The thickness of the region along which surface tension effects are spread is governed by the parameter δ_T. In the calculations this parameter is assumed large enough to include at least five grid cells. At $t=0$ the function d is initialised as the signed normal distance from the interface and the density and viscosity distributions in the domain are assigned according to the equation

$$f(d)=f_a/f_w+\left(1-f_a/f_w\right)H_{\delta_P}(d)$$

where $f(d)$ is the local value of the physical property nondimensionalised by the corresponding value in water f_w, while f_a is the value in air and δ_P is the thickness of the region along with the jumps in physical properties is spread by the smoothed Heaviside function. During the motion, the function d is simply transported by the flow through an evolution equation and the new location of the air-water interface is captured as the level-set $d=0$ (Sussman et al. 1994). But for the fluid particles lying on the free surface, the function d, initialised as the distance, looses its geometrical meaning. In other words, in the new configuration the actual distance from the interface differs from the local value of d. As a result, in order to ensure a uniform

and constant thickness of the transition region, the function d is reinitialised at every time step as the minimum (signed) distance from the interface.

3 Numerical results

The numerical method described in the previous section is used to simulate the flow generated by a viscous vortex pair vertically rising toward the free surface. A similar study has been carried out by OL who used a boundary fitted numerical method which describes the flow in a single fluid by tracking the free surface through a moving-grid approach. In that approach, the interface is sharp and exact boundary condition are applied there. OL performed a parametrical study by varying the Reynolds, Froude and Weber numbers and evaluated the different behavior in terms of free surface deformation, path and decay of the primary vortices and secondary vorticity resulting from the interaction. On the basis of the above considerations, a careful verification and validation of the present two-fluid model is carried out, aimed at understanding the role played by the two parameters δ_P and δ_T governing the interface smoothness. In the calculation shown hereinafter, two grids (400×304 and 800×608) are used to discretize the computational domain $-11 \le x_1 \le 11$, $-6 \le x_2 \le 6$. The coarse one is uniform in the region $| x_1 | \le 3$, $-4 \le x_2 \le 0.5$ with $\Delta x_1 = \Delta x_2 = 0.02$, while a gradually growing grid spacing is adopted outside. It is worth noticing that the grid spacing used for the coarse grid is comparable to that adopted in OL to discretize the fluid domain at t=0, although in the moving grid approach the grid size changes in space and time due to the deformation of the fluid boundary. At t=0, the free surface is assumed to be flat and the centres of the submerged vortices located at (x_1, x_2) = (±0.5,-3). In the vicinity of the vortex centre the Lamb's formula for the decaying vortex is used to assign the initial velocity distribution whereas the potential velocity field is used further. All along the boundary of the computational domain the two velocity components are assigned by a second order extrapolation. More details concerning the initial and boundary conditions are described in OL. In the present two-fluids formulation density and viscosity ratios are assumed as the real ones for air and water. With the aim of investigating the role played by the finite thickness along which the density jump is smeared, a first calculation is performed for the case Re=100, Fr=0.2, We=0. The calculation is done by using the two grids with the same thickness δ_P=0.05, thus implying that five and ten grid cells are within the transition region in the coarse and fine grid computations, respectively. In Figure 1a,b the vorticity contours obtained with the two grids at time t=6.5 are drawn by using the same levels as in OL. Time sequences provided by the two calculations (not shown here) are in quite good agreement between them and compare well with the results by OL. The most relevant difference between the two figures concerns the lack of the vorticity contour at ω=+0.45 in the coarse grid result. In order to investigate if this lack is associated to an excessive numerical diffusion, the dissipation rate of the primary vortex is evaluated and compared with the theoretical law given by Lamb (1932) from which it follows that the vorticity peak decays as $|\omega_{MAX}| = \mathrm{Re}/[2(t+t_L)]$, where t_L=0.25 according to the initial data. The decay of the vorticity peak obtained with the two grids are essentially overlapped and a rather good agreement with the theoretical estimate can be also noted up to $t \approx 6$ (see Figure 2a). After this time the intense free-surface/vortex interaction begins to matter, giving rise to a faster decay rate. On the basis of the above considerations, it can be said that the coarse grid accurately describes the vorticity dynamics while the (weak) underproduction of secondary vorticity is due to the small number of grid cells within the transition region. In Figure 2b the paths of the vorticity peak obtained with the two grids are shown and differences are always smaller than the cell dimension. In order to get a better comprehension of the role played by the thickness of the region along which surface tension effects are smeared, two calculations are performed for the case Re=100, Fr=0.4, We=1 by using the fine grid with δ_P=0.05 and two different values of δ_T (0.05 and 0.025). Also in this case the two time sequences (not shown) are in rather good agreement with the results shown in OL. The vorticity plots at t =5.0, displayed in Figure 3a,b, show that the contour at ω=+1 is missing when using δ_T=0.05. Hence, in order to correctly evaluate surface tension effects, they have to be spread onto a region which is region small compared to the local radius of curvature but still large enough to include at least five grid cells to assure that the continuum model works appropriately.

What presented so far shows that the two-fluids model adopted is rather accurate and allows to face problems where a large free surface deformation can lead to entrainment of air. Hence, the case Re=100, Fr=0.4, We=0 is numerically simulated by using the coarse grid and δ_P=0.1. Some of the most relevant configurations of the time sequence are shown in Figure 4a-l and clearly display the entrapment of an air bubble not found in OL. In order to give an explanation for this difference, we observe that the density contour at $\rho = (\rho_a + \rho_w)/2$ taken at t =3.5 is rather distorted, probably beyond the maximum distortion permitted by the moving grid approach (see comment to figure 3 in OL). In spite of this very remarkable difference, some similarities in terms of the secondary vorticity produced can be found at least until t =4.5 when the air bubble has not yet significantly affected the dynamics of the primary vortex. Successively, the air bubble wraps around the primary vortex and gradually rises due to the buoyancy, eventually approaching the free surface on the top and disappearing.

References

Brackbill, J.U., Kothe, D.B. & Zemach, C. 1992. A continuum model for modeling surface tension. *J.F.M.* 100: 335-354.

Iafrati, A., Di Mascio A. & Campana, E.F. 2001. A level-set technique applied to unsteady free surface flows. *International Journal for Numerical Methods in Fluids* 35: 281-297.

Iafrati, A. & Campana, E.F. 2003. A domain decomposition approach to compute wave breaking. *International Journal for Numerical Methods in Fluids* 41: 419-445.
Lamb, H. 1932. *Hydrodynamics*. New York: Dover.
Ohring, S. & Lugt, H.J. 1991. Interaction of a viscous vortex pair with a free surface. *Journal of Fluid Mechanics* 227: 47-70.
Sussman, M., Smereka, P. & Osher, S. 1994. A level-set approach for computing solutions to incompressible two-phase flow. *Journal of Computational Physics* 114: 146-159.

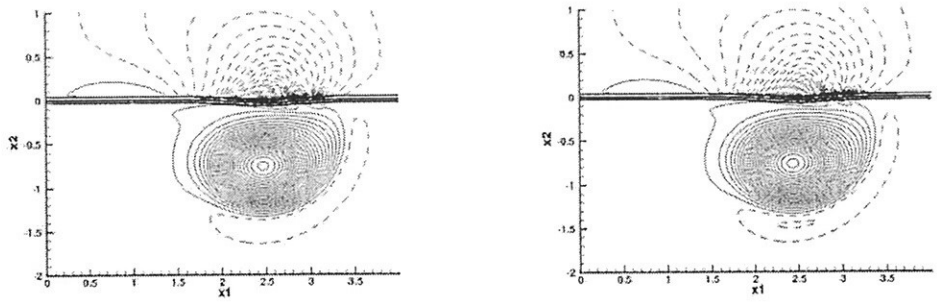

(a) (b)

Figure 1. Coarse (a) (400×304) and fine (b) (800×608) grid computations for Re=100, Fr=0.2, We=0 and same thickness δ_P=0.05. The vorticity contours at t=6.5 show the lack of the contour at ω=+0.45 in the coarse grid result, while fine grid computation exactly recovers the OL contour distribution.

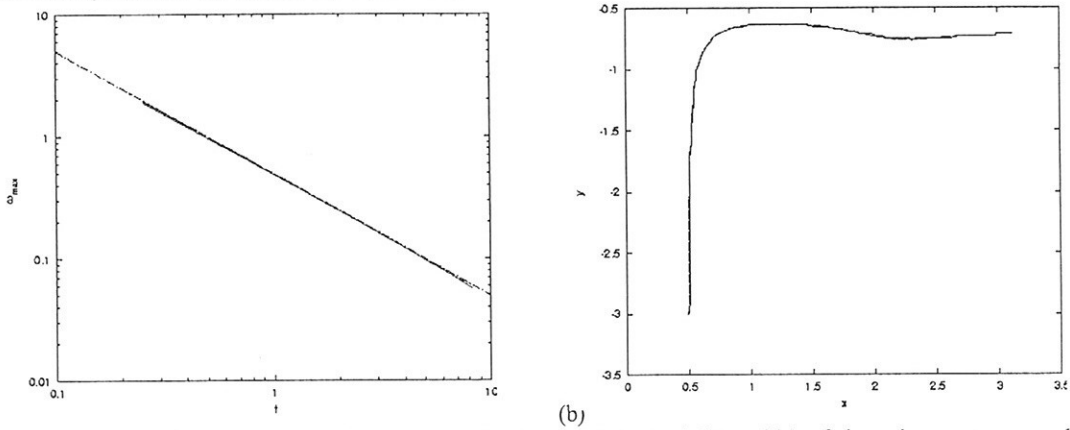

(a) (b)

Figure 2. (a) Comparison between the computed dissipation rate (coarse and fine grids) of the primary vortex and the theoretical law (Lamb) reveals a good agreement up to $t \approx 6$. (b) Paths of the vorticity peak with the coarse and fine grids.

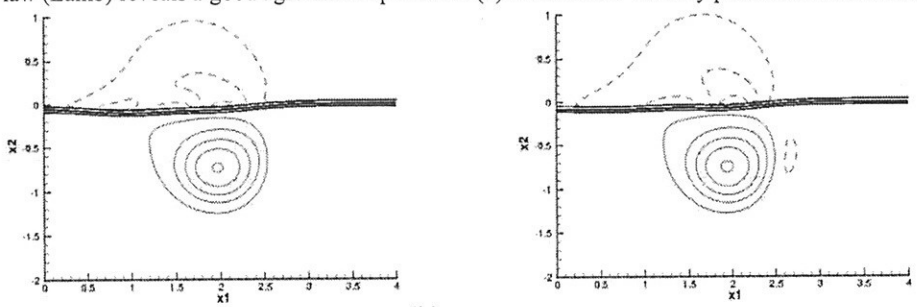

(a) (b)

Figure 3. Effect of the δ_T on the generation of secondary vorticity for the case Re=100, Fr=0.4, We=1. On δ_T = 0.05 and δ_T = 0.025 have been used for the calculation shown in (a) and (b), respectively.

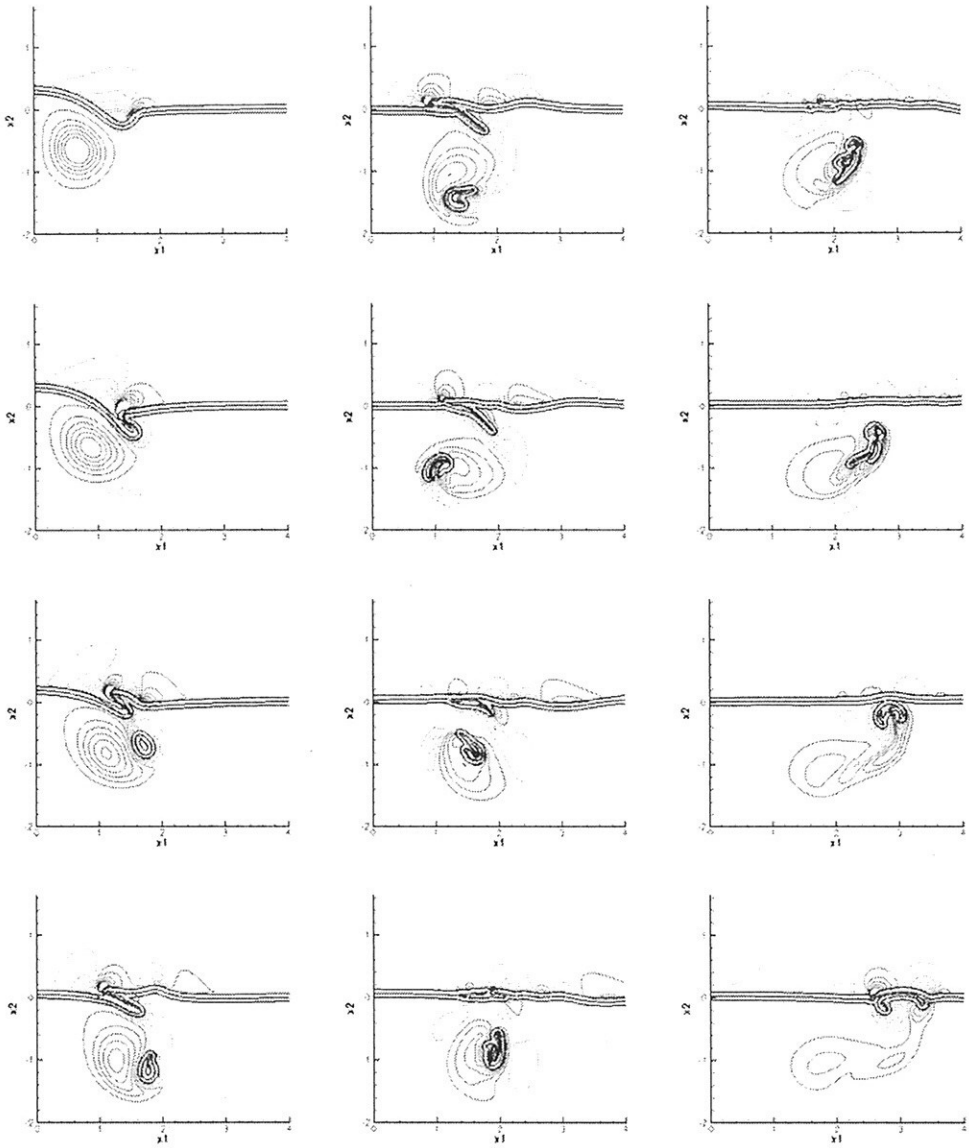

Figure 4 – Time sequence of the rising vortex pair for Re=100, Fr=0.4, We=0 (coarse grid, δ_P=0.1). The entrapped air bubble wraps around the primary vortex and gradually rises due to the buoyancy and eventually approaches the free surface.

VISCOUS CALCULATION OF INTERACTION OF 2D WATER WAVES WITH SUBMERGED BODIES

H. ISSA [(1)], M. BA [(1)] and M. GUILBAUD [(2)]

Laboratoire d'Etudes Aérodynamiques (UMR CNRS 6609)
[(1)] ENSMA – 1, avenue Clément Ader – BP 40109 - 86961 FUTUROSCOPE CEDEX, France
[(2)] CEAT, Université de Poitiers – 43, rue de l'Aérodrome – 86036 POITIERS CEDEX, France
e-mail: issa_fr@yahoo.fr; malick.ba@lea.ensma.fr; michel.guilbaud@lea.univ-poitiers.fr

INTRODUCTION

The study of the interaction between waves and bodies is a difficult problem featuring non linear and purely unsteady characters. For a numerical method, the main difficulty is the choice of a numerical scheme accurate enough to be able to describe the deformation of the free surface along the time.

To determine the location of the free surface, some methods have been studied in the last decades, as the first treatment presented in [1] using the marker and cell (MAC) method. This simple method is widely used. Another method, the volume-of-fluid method (VOF) can be considered as an enhancement of the MAC, using a similar approach but employing only one variable to determine the status of the cell. First introduced in [2], it overcomes important disadvantages of the MAC method, requiring less memory and a shorter computational time but it is unable to deal with multiple free surfaces as wave breaking or merging. Basically, the MAC and VOF methods are connected with the governing equations in the Eulerian formulation, using a fixed mesh. It is also possible to use another fundamental formulation, the Lagragian formulation based on a mesh moving with the fluid. One of the disadvantages of the Eulerian formulation is the difficult treatment on the free surface boundary. The Lagragian formulation enables a more easy treatment of this boundary but unacceptable degrees of mesh distortion may occur and potential entanglements may lead to unsuccessful calculations.

The arbitrary Eulerian-Lagragian (ALE) method, first presented in [3], combines the advantages of the two methods and avoid their impairments. In the past years, this method has been mainly used to solve large deformation problems in the area of solid mechanics and fluid-structure interaction problems. Some examples of application can be found in hydraulic engineering.

The method presented in this paper uses a MAC method with following of markers on the free surface and uses a fixed grid to simulate 2D incompressible and viscous flows with a free surface with submerged bodies. A multigrid technique is used for including submerged or surface-piercing bodies.

PRESENTATION OF THE PROBLEM

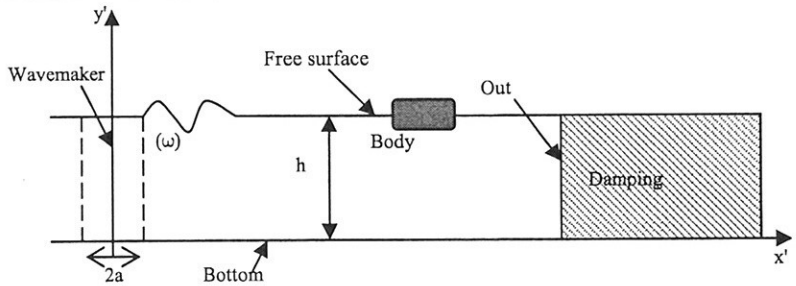

Figure 1 : Description of the towing tank in study

We study the waves in a numerical towing tank, fig. 1, with sinusoidal motions of the left vertical wall, the wavemaker. The motion is given by $x = a(y)\cos(\omega.t)$, x being the instant location of the wavemaker at time t, a is the motion amplitude and ω is the circular frequency. The velocity of the wavemaker is $u'_{bat} = -\bar{u}.\sin(\omega t)$ where $\bar{u} = \max[a(y)]\cdot\omega$ is the maximum velocity of the wavemaker and u'_{bat} is the dimensional velocity at time considered.

The equations to solve are the Navier-Stokes equations for incompressible flow in a 2D domain. We use non dimensional data defined by dividing by the water height h the spatial coordinates, by $\bar{u}$ velocities, by $h/\bar{u}$ time and by $\rho\bar{u}^2$ pressure. The Reynolds and Froude numbers are defined by

$\mathrm{Re} = h\bar{u}/\nu$, $Fr = \bar{u}/\sqrt{gh}$. We use the modified pressure including both the static pressure and the gravity term: $p = \bar{p} + (y-1)/Fr^2$.

The boundary conditions are the body condition with null relative velocity on the solid boundaries, an exit boundary on the right of the tank to suppress the wave reflection, the free surface kinematic boundary condition given by :

$$\frac{Dx}{Dt} = u \quad ; \quad \frac{Dy}{Dt} = v \tag{1}$$

where *(u,v)* are the velocity vector of a particle considered on the free surface at point *(x,y)* and the dynamic condition in [4] :

$$\bar{p} = \frac{2}{\mathrm{Re}}.n_x.n_x.\frac{\partial u}{\partial x} + \frac{2}{\mathrm{Re}}.n_x.n_y.\left(\frac{\partial u}{\partial y} + \frac{\partial v}{\partial x}\right) + \frac{2}{\mathrm{Re}}.n_y.n_y.\frac{\partial v}{\partial y} \tag{2}$$

$$\frac{\partial u}{\partial x}.n_x.m_x + \left(n_y.m_x + n_x.m_y\right).\left(\frac{\partial u}{\partial y} + \frac{\partial v}{\partial x}\right) + \frac{\partial v}{\partial y}.n_y.m_y = 0 \tag{3}$$

where $\vec{n}(n_x, n_y)$ and $\vec{m}(m_x, m_y)$ are respectively the unit normal and tangent vectors to the free surface.

METHOD OF RESOLUTION

By discretising the unsteady term of momentum equations, we obtain the following equation:

$$\vec{U}_{n+1} + \Delta t.\left(\frac{\partial p}{\partial \vec{x}}\right)_{n+1} = \vec{U}_n + \Delta t.\left(\vec{D}_{n+1} - \vec{C}_{n+1}\right) \tag{4}$$

with n and n+1 the considered instants, $\vec{x} = (x, y)$ the position vector, $\vec{U}_n = (u, v)_n$, the velocity vector: $\vec{D}_{n+1} = = \left(\frac{\partial^2 \vec{U}}{\partial x^2} + \frac{\partial^2 \vec{U}}{\partial y^2}\right)_{n+1} / \mathrm{Re}$ and $\vec{C}_{n+1} = \left[\left(\frac{\partial u^2}{\partial x} + \frac{\partial uv}{\partial y}\right)_{n+1}, \left(\frac{\partial uv}{\partial x} + \frac{\partial v^2}{\partial y}\right)_{n+1}\right]$ are respectively the diffusion and convective terms; Δt is the time step. Using then a fictitious velocity field $\vec{U}_* = (u_*, v_*)$, eq. (4) can be transformed in:

$$\vec{U}_* = \vec{U}_n + \Delta t.\left(\vec{D}_{n+1} - \vec{C}_{n+1}\right) \tag{5}$$

$$\vec{U}_{n+1} = \vec{U}_* - \Delta t.\left(\frac{\partial p}{\partial \vec{x}}\right)_{n+1} \tag{6}$$

With eq. (6), the real velocity field can be calculated from the pressure field once the fictitious velocity field is known, using eq. (5). By taking the divergence of eq. (6), we obtain:

$$\nabla \cdot \vec{U}_* = \nabla \cdot \vec{U}_{n+1} + \Delta t.\nabla^2 p_{n+1}, \tag{7}$$

but using the continuity equation, we have:

$$\nabla \cdot \vec{U}_{n+1} = \left(\frac{\partial u}{\partial x} + \frac{\partial v}{\partial y}\right)_{n+1} = 0, \tag{8}$$

so finally, we obtain the following Poisson equation enabling to express the pressure field in term of the fictitious velocity field:

$$\nabla^2 p_{n+1} = \nabla \cdot \vec{U}_* / \Delta t \ . \tag{9}$$

- At each iteration k+1 (on the value of $\vec{U}_*$), the fictitious velocity field is determined from eq. (5), real velocities computed at iteration k being known, terms $\vec{D}_{n+1}$ and $\vec{C}_{n+1}$ can be calculated and real velocities known at time (n).
- Then from the resolution of eq. (9), the pressure field is computed using the boundary conditions at the walls and at the free surface.
- Finally, the velocity field at time n+1 is determined from eq. (6).

GRIDDING AND DISCRETISATION OF THE EQUATIONS

Gridding of the computational domain

We use a 2D cartesian structured by blocks grid, fig. 2, enabling an easy introduction of a submerged or surface-piercing body. The Navier-Stokes equations are discretised and solved for the unknowns (velocities, pressures and free surface elevations). The equations derived of eq. (5) et (6) are discretised at the nodes using a finite difference method of second order in space and the Poisson equation eq. (9) is solved by a finite volume method, in order to improve the accuracy. By integrating this equation on a cell surrounding a point P (fig. 3), we obtain:

$$\int_{cell}\left(\frac{\partial^2 p}{\partial x^2}+\frac{\partial^2 p}{\partial y^2}\right)dxdy=\int_{ab}\left.\frac{\partial p}{\partial x}\right|_e dy-\int_{cd}\left.\frac{\partial p}{\partial x}\right|_w dy+\int_{da}\left.\frac{\partial p}{\partial y}\right|_n dx-\int_{bc}\left.\frac{\partial p}{\partial y}\right|_s dx=\iint_{cell}\nabla\cdot\vec{U}^* dxdy \quad (10)$$

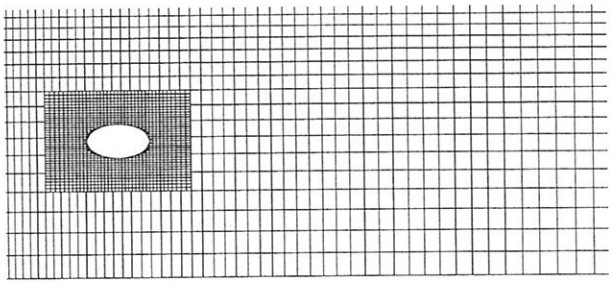

Figure 2 : Grid of the computational domain

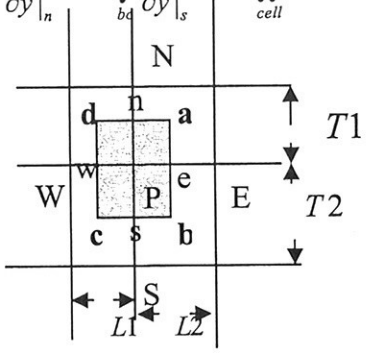

Figure 3 : Definition of inner nodes

Equation (10) written at point P is calculated from pressure at nodes W, S, N and E. We obtain a linear system with a matrix constituted by 5 diagonal strips which is inverted by an iterative method to obtain the pressure field. For nodes closed to the fluid domain boundaries, we use Neumann condition on the pressure (solid walls) directly introduced in eq. (10). For the free surface where a Dirichlet condition has to be satisfied, the derivative of the pressure is calculated using fictitious nodes above the free surface.

Treatment of the free surface boundary condition

We consider a point on the free surface as shown on fig. 4. To calculate the fictitious velocity field in order to compute the pressure, we have to calculate by finite difference the real velocity field. Close to the free surface, the introduction of fictitious nodes above the free surface is required. We use the boundary conditions to determine the values of the variables in these points.

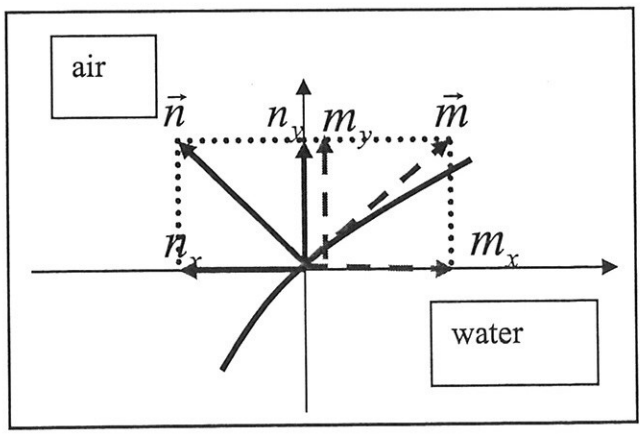

Figure 4 : Representation of the free surface

The shape of the free surface is divided into 3 different cases: the tangent at the free surface makes an angle β=45°, 0° or 90°. From equations (2) and (3), these three different cases lead to the following conditions on the free surface:

	Eq.(11a)	Eq.(11b)	Eq.(11c)
Case 1 β=45°	$\frac{\partial u}{\partial x}=0$	$\frac{\partial v}{\partial y}=0$	$p=\frac{\eta(x)}{Fr^2}-\frac{2}{\mathrm{Re}}.\left(\frac{\partial u}{\partial y}+\frac{\partial v}{\partial x}\right)$
Case 2 β=0°	$\frac{\partial v}{\partial y}=-\frac{\partial u}{\partial x}$	$\frac{\partial u}{\partial y}=-\frac{\partial v}{\partial x}$	$p=\frac{\eta(x)}{Fr^2}+\frac{2}{\mathrm{Re}}.\left(\frac{\partial v}{\partial y}\right)$
Case 3 β=90°	$\frac{\partial u}{\partial x}=-\frac{\partial v}{\partial y}$	$\frac{\partial v}{\partial x}=-\frac{\partial u}{\partial y}$	$p=\frac{\eta(x)}{Fr^2}+\frac{2}{\mathrm{Re}}.\left(\frac{\partial u}{\partial x}\right)$

If we consider only the first case β=45° (fig. 5), the unknowns to calculate are $v_{j+1,i}, u_{j,i-2}, p_{j,i-1}$. So we compute $v_{j+1,i}=v_{j,i}$ by applying equation (11b) to node M_2 and $u_{j,i-2}=u_{j,i-1}$ using (11a) at node M_1 and the pressure is determined by:

$$p_{j,i-1}=\frac{\eta(x)}{Fr^2}-\frac{2}{\mathrm{Re}}.\left(\frac{\left(u_{ji-2}+u_{ji-1}\right)-\left(u_{j-1,i-2}+u_{j-1,i-1}\right)}{2.\Delta y_{j-1}}+\frac{\left(v_{j-1,i}+v_{j,i}\right)-\left(v_{j-1,i-1}+v_{ji-1}\right)}{2.\Delta x_{i-1}}\right)$$

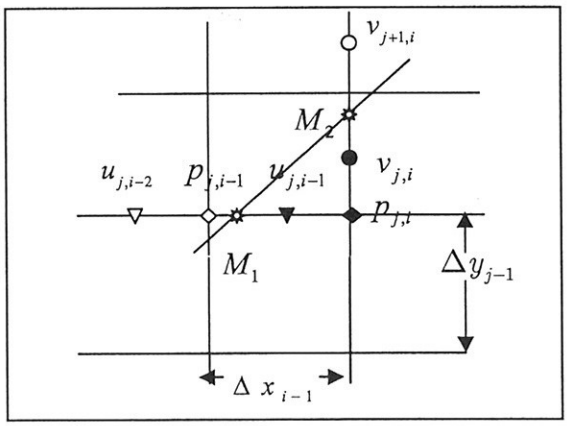

Figure 5 : Definition of the fictitious nodes

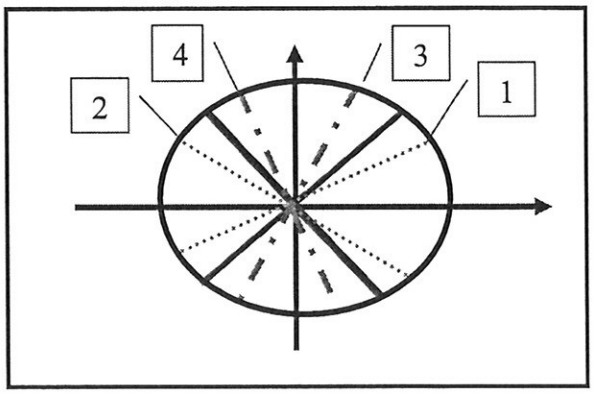

Figure 6 : Intermediary cases

The cases with a horizontal or vertical slope of the free surface are easily computed using a similar calculation. For intermediary cases, the calculation is performed with four extra cases, fig. 6. For $0°\leq\beta\leq+45°$ or $-45°\leq\beta\leq0°$, case 1 and 2 we define the coefficient $\alpha=\left|\partial\eta/\partial x\right|$ (with α=1 if β=±45° or α=0 if β=0°) and $0\leq\alpha\leq1$. The unknowns are calculated using the solutions for 0°, +45° or -45°.

$$u_{(0<\beta<+45°)}=(1-\alpha)u^0+\alpha.u^{+45} \qquad u_{(-45°<\beta<0)}=(1-\alpha)u^0+\alpha.u^{-45}$$

$$v_{(0<\beta<+45°)}=(1-\alpha)v^0+\alpha.v^{+45} \qquad v_{(-45°<\beta<0)}=(1-\alpha)v^0+\alpha.v^{-45}$$

$$p_{(0<\beta<+45°)}=(1-\alpha)p^0+\alpha.p^{+45} \qquad p_{(-45°<\beta<0)}=(1-\alpha)p^0+\alpha.p^{-45}$$

For the cases 3 and 4, similar calculations are performed using the solution for ±45°, ±90°. Knowing the velocity of the free surface markers, the kinematic free surface boundary condition enables to modify the shape of this surface and to determine its variation with time using discretisation of eq. (1).

$$x_{fs}^{n+1}=x_{fs}^{n}+\Delta t.u_{fs}^{n+1} \qquad y_{fs}^{n+1}=y_{fs}^{n}+\Delta t.v_{fs}^{n+1}$$

where subscript « fs » is for markers on the free surface. Once, all the markers on the free surface have been displaced, N polynomial forms of degree 3 are used to smooth the free surface. The equality of the values of the polynomials, and of the first and second derivatives is imposed at the mesh vertical lines, enabling to calculate the coefficients of the polynomial forms.

RESULTS AND VALIDATIONS

Numerical towing tank

To validate the present calculations, we have calculated the free surface elevation for a sinusoidal motion of the wavemaker, with constant amplitude 0.02m and circular frequency $5s^{-1}$ in a tank with length 5m and 1m deep. The mesh has been extended on 6m in order to avoid reflection at the right end. Our results ($Re=10^5$) have been compared to an analytical solution for an inviscid fluid, fig. 7. The agreement is quite good particularly for the phase.

The numerical results have been also compared with some tests performed in the towing tank of Ecole Centrale de Nantes (63m long, 5m width), the water height during the tests being 2.785m. The calculations are performed at the location (x=9.875m from the wavemaker) of one of the transducer L_1. The test presented here, « hb 191 » from [5], has the following parameters:

Test	Period (s)	Wavemaker amplitude (m)	Starting ramp nb of periods	Number of periods
hb 191	2.1	0.15	5	15

Table 1 : Experimental conditions

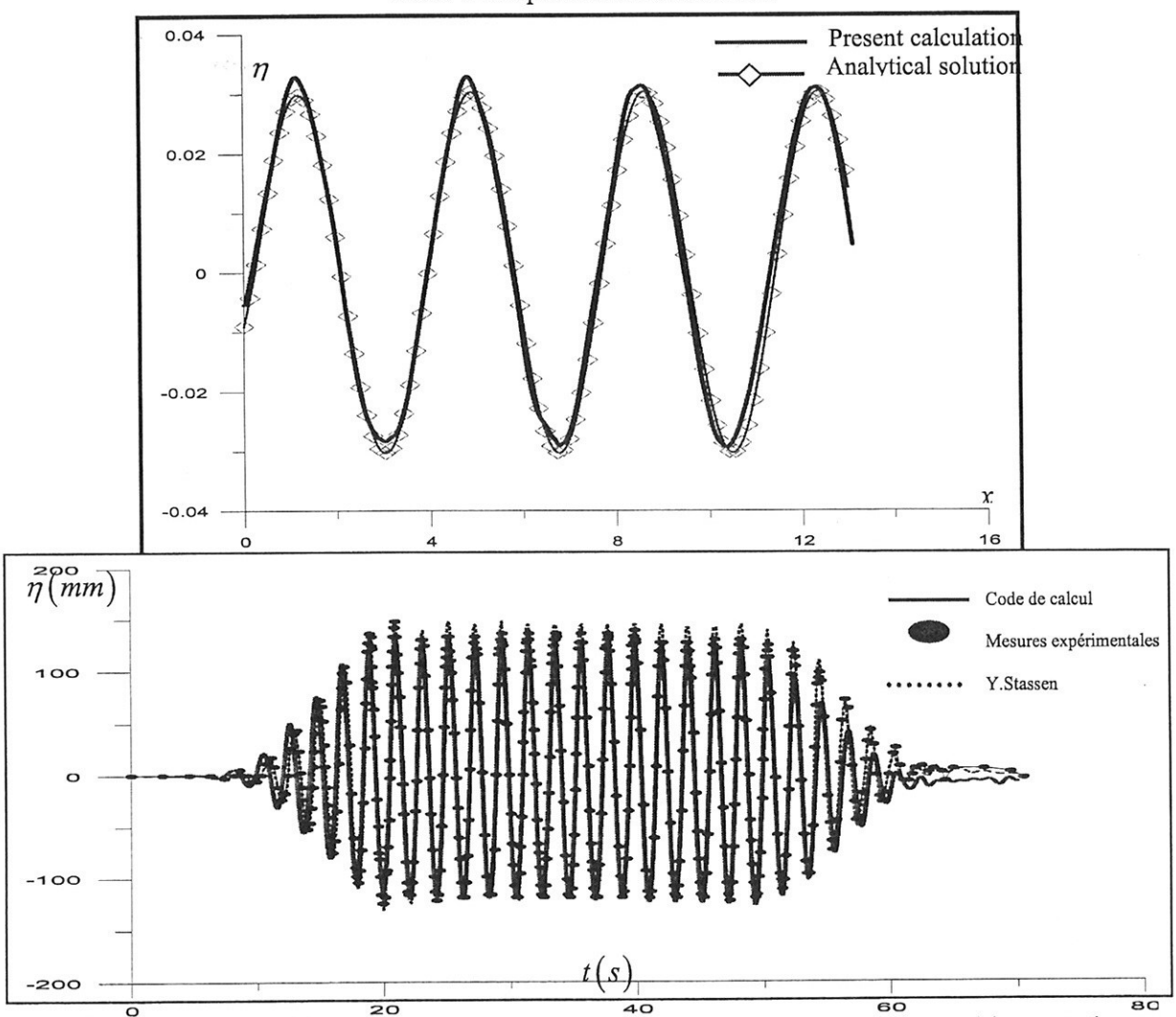

Figure 8 : Test"hb 191", free surface elevations at transducer L_1 Comparison with test and calculations from [5]

The wavemaker is started at time 0s and then stopped at t=50s. In the present calculations, a grid of 40 lines and 360 columns is used (210 in the domain and the rest for the damping zone); the length of the domain is 60m for $h=2.785$m deep and the damping zone is 120.57m long. The results presented on fig.8 are for time step 0.02s and the calculations simulate 80s and require 20 hours of

CPU time on a PC 1.5Ghz. The agreement is excellent between our results (full lines), the test measurements (symbols) and the calculation of [5] (dotted lines). These last calculations have been performed using a higher order panel method with a polynomial interpolation of high degree for the singularity distribution. For the free surface boundary conditions, use of expansion series has been done.

Numerical tank with a submerged body

To show the ability of the method to calculate the flow around a submerged body, we show on fig. 9 a plot of the horizontal velocity distribution on an ellipsoid of 0.32m long with axis ratio 1:4. The main axis is located at 0.53m deep and the bottom is at hm. The tank length is $12h$ and the period of the wave is 2.1s and the amplitude is $2\pi(2.1)h$. We can observed on the plot, the continuity of the horizontal velocity between the outer and inner grids. The time step is Δt=0.02s and the plot is for t=0.94s.

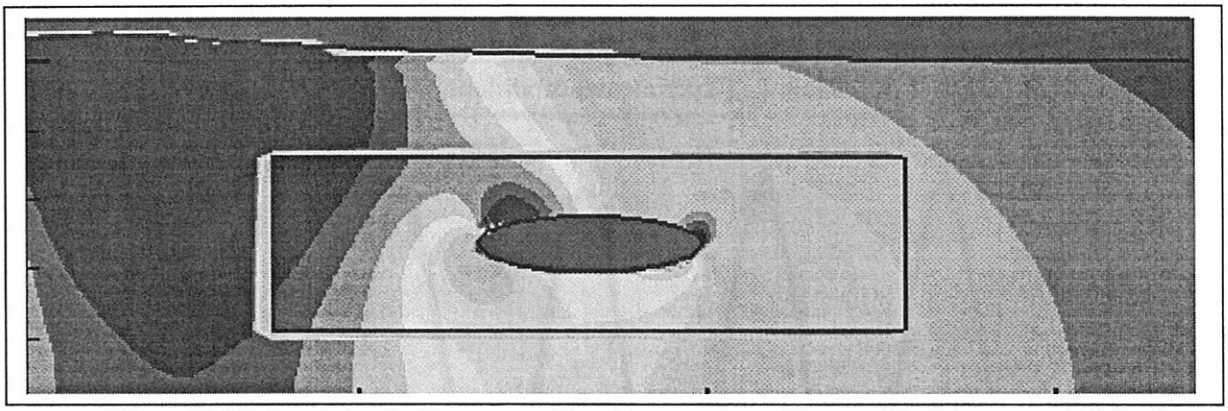

Figure 9: Horizontal velocity on an ellipsoid computes with a multigrid process (t=0.94s)

Conclusion

We have presented in this paper first results obtained with a numerical method enabling to simulate unsteady 2D flows with a free surface of a viscous fluid. The unsteady Navier Stokes equations are discretised by finite differences. The pressure in the domain is obtained by solving a Poisson equation using fictitious velocities with a finite volume method. The free surface is discretised by an interface capturing method (« MAC » method), using interpolation of exact results for three basic positions of the free surface, but with a fixed domain of computation. The treatment of the free surface boundary conditions have been first validated by results obtained by the study of the sloshing of a liquid in a tank under the effect of gravity only (not presented here by lack of place).

Other results for a tank with a wavemaker and a wave damping have been compared with test measurements. They show a good agreement including for the starting and the stopping of the wavemaker. To deal with submerged bodies, a multigrid technique has been used. First results show the continuity of the pressure amplitude across the grids. The method is being extended to a surface piercing body and first results will be presented.

References

[1] Harlow F.H. and Welch J.E. (1965), Numerical calculation of time-dependant viscous incompressible flow of fluid with free surface, *Phys. Fluids* 8 (12), 2182-2189.

[2] Hirt C.W. and Nichols B.D (1974), An arbitrary Lagrangian-Eulerian computing method for all flow speeds, *Journal of Computational Physics,* 14, 227-253.

[3] Hirt C.W. and Nichols B.D. (1981), Volume of fluid method for the dynamics of free boundaries, *Journal of Computational Physics*, 39, 201-225.

[4] Huang and Dong (1998), Numerical simulation of nonlinear water waves propagating, Proc. 8^{th} *Int. Offshore and Polar Ing. Conf.*, Montréal, 313-319.

[5] Stassen Y. (1999), Simulation Numérique d'un Canal à Houle Bidimensionnel au Troisième Ordre d'Approximation par une Méthode Intégral, Ph. D. thesis, University of Nantes (France).

RANSE Simulations of Ships in Waves using Overlapping Grids

Matthias Klemt, Plaza Compositor Miguel Asíns Arbó 16, 46013 Valencia, Spain, klemt@freenet.de
Gerhard Jensen, Technical University of Hamburg-Harburg, Germany, g.jensen@tu-harburg.de
Olaf Lindenau, Technical University of Hamburg-Harburg, Germany, lindenau@tu-harburg.de

1. Introduction

Ship motions and associated loads on a ship hull are usually predicted with methods based on potential flow assumptions. Large errors can be introduced by these assumptions for some practically important cases like ship motions in large amplitude waves, ship responses under a wave impact (slamming), or ship capsizing etc. The need for a numerical tool that can predict the motions and loads in large waves, taking into account inertia, flow separation and wave-breaking phenomena is obvious.
The objective of this research is to develop and validate a computational technique for the coupled analysis of viscous flow and flow-induced body-movements in large waves. For this purpose, some cases are selected to be investigated using this method and compared with experimental results.

2. Numerical Method

The program "Comet", version 2.000, has been used, which employs a finite volume method to predict forces acting on a body and free surface deformations by solving the Navier-Stokes equations, *ICCM (2001)*. The two-fluid system is modelled by a two-phase formulation of the governing equations. No explicit free surface is defined during the computations. The location of the free surface between air and water is obtained by solving an additional transport equation for the volume fraction of one of the fluids (interface capturing). To obtain a sharp interface, the high resolution interface capturing (HRIC) scheme has been used, *Muzaferija et al. (1999)*. Overturning (breaking) waves as well as buoyancy effects of the trapped air is considered automatically by the model. The flow is assumed to be laminar and incompressible.

The Navier-Stokes-Equations and the body dynamic equations are to be solved in a coupled manner. Applying the finite volume method on block structured grids, the viscous flow around a floating-body is predicted. The floating body dynamic has been implemented into the program via the user-coding interface. The body motions are calculated according to the forces and moments obtained by integrating pressure and shear stress over the body surface. The velocity of the floating body is corrected by a Crank-Nicholson-Method after every iteration (fully implicit), taking advantage of the iterative nature of the fluid-flow solver. An approximation for the hydrodynamic masses is used to make the coupled procedure robust. Nonlinear effects like impact loads, *Sames et al. (2001)*, ship responses in large waves and viscous effects are considered.

An approach with overlapping grids has been developed and employed to avoid the difficult grid-management caused by change the body position. There is a space-fixed grid with a hole enclosing to the body and a body-fixed grid overlapping the space-fixed grid. Fig. 1 shows the principle of this approach. The flow solution has to be interpolated on the boundaries of every grid from the other to force a unique solution on both grids in the overlapping area. Finally a correction of the convective velocities makes sure that the mass conservation law will be satisfied, as the interpolation procedure cannot be formulated in a conservative form. This correction is getting smaller with a greater number of iterations.

There are two ways to calculate the flow in the case of body-movement. The first approach is

changing the coordinates of the body-fixed grid in every iteration (moving grid) and after that solving the Navier-Stokes-Equations in the space-fixed coordinate system. The other way, which is employed here, is to keep the coordinates of the body-fixed grid fixed and the Navier-Stokes-Equations will be solved in the body-fixed coordinate system. Considering grid-accelerations and velocities is necessary in this case.

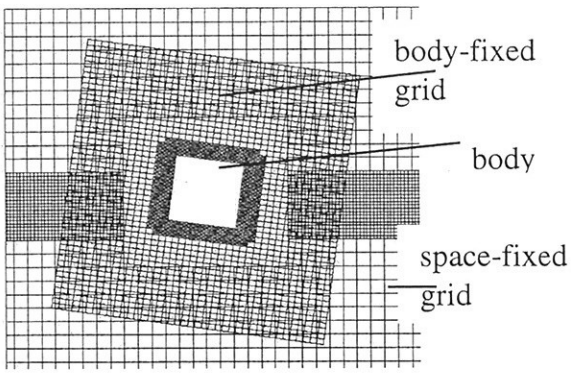

Fig. 1 2-dimensional body with overlapping grids

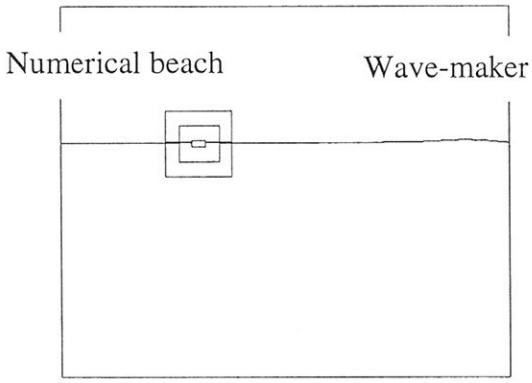

Fig. 2 Numerical tank for body motion

The numerical tank into which the floating bodies are placed consists of a fluid domain with two phases (water and air) bounded by a layer of air on top, a bottom surface in water and four vertical boundaries. Regular waves are generated by giving inlet velocity and water height based on potential theory (Airy, Stokes I-IV) at the inlet boundary, *Clauss et al. (1998)*. At the other side of the tank a numerical beach is defined to avoid reflection of the waves.

Details of the overlapping grid method will be published by *Klemt (2005)*.

3. Application - Motions of a fast conventional passenger ferry in waves

A fast conventional RoRo passenger ferry was selected as reference ship for the study. The ship was designed by IZAR for the European research project *DEXTREMEL (1997)*. Model tests were carried out at a scale of 1/40 in a sea keeping basin by MARIN. Fig. 2 shows the coarse discretisation of the ship and its main particulars are listed there.

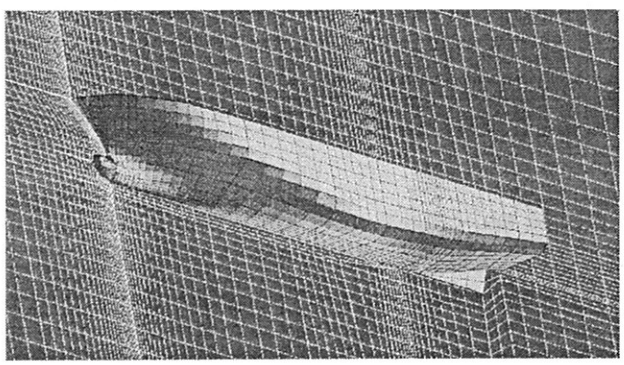

	Symbol	Value	Unit
Length between perpendiculars	Lpp	173.00	m
Beam	B	26.00	m
Draft	T	6.50	m
Displacement	Δ	16800	t
Service Speed	Vs	28	kts

Fig. 2 Discretisation (coarse) and main particulars of RoRo passenger ferry

The coarse grid has about 200.000 cells, the medium grid about 0.5 million cells and the fine grid about 1.2 million cells. For the simulations an average Courant number of 0.01 is realized. The

computation was done for a ship speed of 26 kts (93 % of service speed) in head waves. Only half of the ship at model scale has been discretized and pitch and heave were the degrees of freedom. First results on the coarse grid were presented by *Klemt et al. (2003)*.

At the beginning of the calculation the whole computation domain was initialized with undisturbed waves and the ship was at rest. Fig. 3 shows the calculated heave and pitch motion in waves with ω=0.6, H=7.3 m and a plot of the situation at t=32.1 s is presented in Fig. 4.

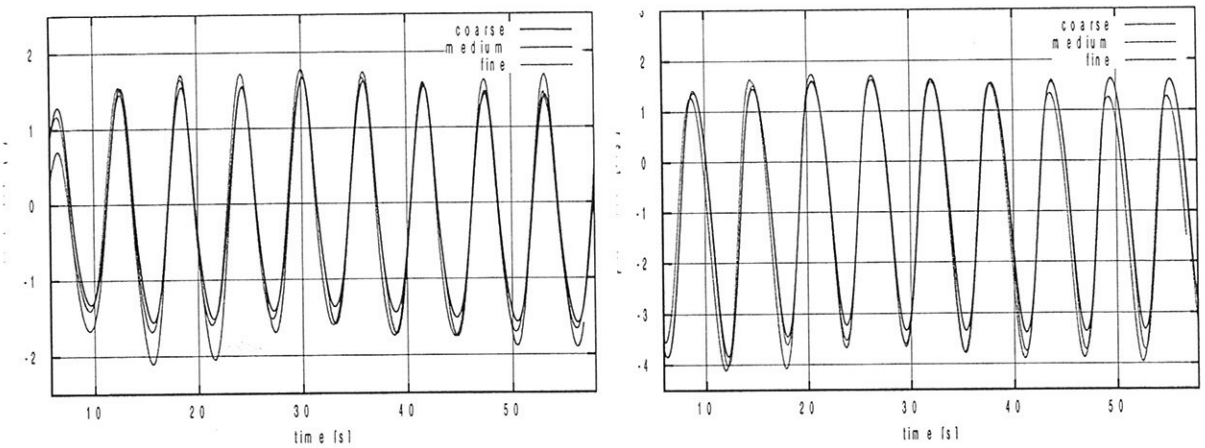

Fig. 3 Calculated heave and pitch motions of RoRo passenger ferry

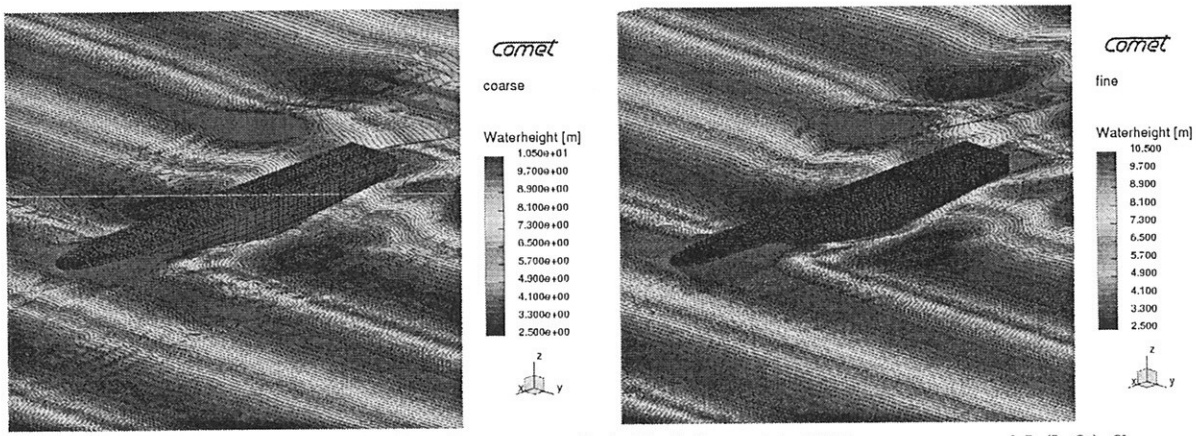

Fig. 4 RoRo passenger ferry in head waves, ω=0.6, H=7.3 m at t=32.1 s; coarse grid (left) fine grid (right)

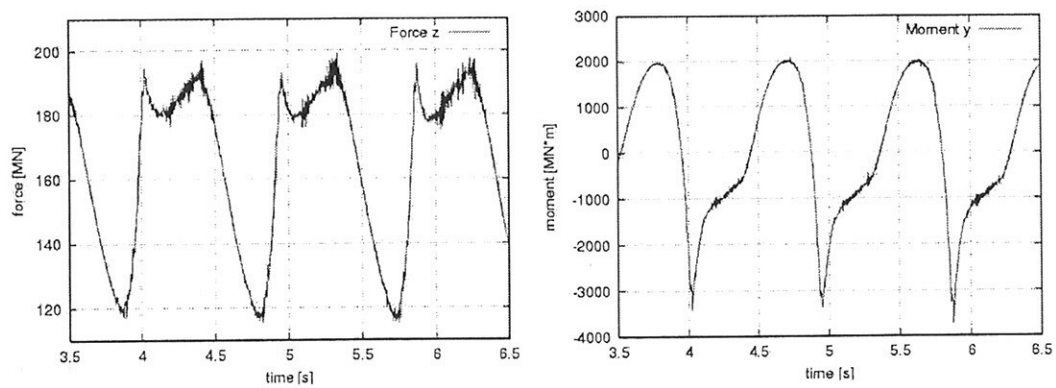

Fig. 5 Calculated heave force and pitch moment of RoRo passenger ferry

Note that the magnitude of negative pitch angle (trim by stern) is much higher than the positive one caused by bow flare effects and impact loads. The corresponding force and moments acting on the hull are shown in Fig. 5. The time histories of the forces have a nonlinear appearance due to the impact loads during the water entry. Fig. 6 presents the comparison of calculated and measured response amplitude operators (RAO) of heave and pitch motion.

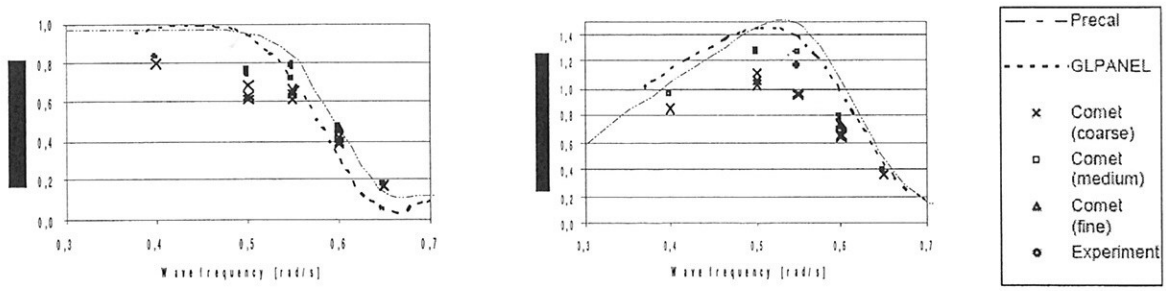

Fig. 6 Comparison of RAOs of heave and pitch motion of RoRo passenger ferry

The heave and pitch response are a bit under predicted by the computational method compared to the experiments and methods based on potential theory. This effect might be caused by numerical damping due to the generally coarse discretisation of the ship, as grid refinement produces higher amplitudes of motion.

An approach using the "Virtual Reality Modeling Language" (VRML) for CFD post-processing is presented by *Klemt et al. (2004)*. There also simulations for a sailing yacht are published.

References

CLAUSS, G.; LEHMANN, E.; ÖSTERGAARD, C. (1998), *Meerestechnische Konstruktionen*, Springer-Verlag Berlin Heidelberg New York

DEXTREMEL (1997), *Design for Structural Safety under Extreme Loads*, BriteEuRam project, contract BPPR-CT97-0513, http://research.germanlloyd.org/Projects/DEXTREMEL/index.html

ICCM (2001), *Comet user manual*, ICCM (Institute of Computational Continuum Mechanics GmbH), Hamburg

KLEMT, M.; PERIC, M.; JENSEN, G. (2003), *Simulation of floating-body motions in viscous flow*, Int. Conf. On Fast Sea Transportation (FAST 2003), Ischia, Italy, Vol. 2 Session C1

KLEMT, M.; JENSEN, G.; LINDENAU, O. (2004), *CFD Simulation and Virtual Reality Visualization for a Fast Monohull in Waves*, HIPER 2004, Rom

KLEMT, M (2005), *Simulation of floating-body motions in viscous flow*, Ship Technology Research, Hamburg

MUZAFERIJA, S.; PERIC, M. (1999), *Computation of free-surface using interface-tracking and interface-capturing methods,* Chap. 2, O. Mahrenholtz and M. Markiewicz, eds., *Nonlinear Water Wave Interaction*, WIT Press, Southampton, pp. 59-100

SAMES, P.C.; KLEMT, M.; SCHELLIN, T.E. (2001), *Prediction of Wetdeck Slamming Loads for a Catamaran*, HIPER 2001, Hamburg

CFD Modeling of Hydrodynamic Interaction of Bodies in a Fluid

Stefan Kyulevcheliev, Bulgarian Ship Hydrodynamics Centre, stefan.q@bshc.bg

Introduction

The hydrodynamic interaction of ships moving in close proximity to one another is difficult to investigate experimentally due to sophisticated experimental equipment needed (e.g. two independent towing carriages). That is why experimental data are fairly scarce. That makes numerical modeling an indispensable means to tackle the problem.

The numerical studies of hydrodynamic interaction known to the author employ potential-flow, wing/lifting surface or slender-body theories.

Some initial results are presented here of the attempts to apply a RANSE solver to the problem of hydrodynamic interaction.

Tasks and tools

Two groups of tasks have been set:

A. Parametric studies of the hydrodynamic forces experienced by bodies moving along straight parallel paths. This is the problem usually considered by many authors in the past using various approaches.

B. Simulation of the motion of the bodies affected by the hydrodynamic interaction between them.

The flow solver used is FLUENT v. 6.1.18.

The hydrodynamic interaction between bodies is inherently unsteady process even when they move with constant speeds due to changing their relative positions (except for the case of equal speeds in one direction). So the time-dependent solution option have been used (specifically, with first-order time stepping in all cases reported here).

The relative motion of the bodies calls for application of moving and deforming computational domains.

The cases of group A have been tackled with the sliding meshes technique incorporated in FLUENT. It features sliding of adjacent non-conformal grid zones relative to one another along the grid interface. The fluxes across the grid interface are computed using the faces resulting from the intersection of the two interface zones determined at each new time steps.

The dynamic mesh model in FLUENT has been used for the simulation of the free motion of the interacting bodies. Since this motion is unknown initially and may be quite arbitrary in direction two of the available mesh motion methods could be used: spring-based smoothing and local remeshing.

In the spring-based smoothing method, the edges between any two mesh nodes are idealized as a network of interconnected springs. A displacement at a given boundary node will generate a force proportional to the displacement along all the springs connected to the node. Knowing the displacements at the boundaries (after boundary node positions have been updated), the equation of equilibrium of the mesh is solved using a Jacobi sweep on all interior nodes. The method necessitates the use of tetrahedral (triangular in 2D) cells.

The local remeshing method is applied to cells violating preset skewness and/or size criteria with the solution being interpolated from the old cells.

Only 2D cases have been studied so far and shall be presented here.

Parametric study of the hydrodynamic interaction of bodies moving along parallel paths

Elliptic cylinders moving along parallel paths have been considered in the parametric studies. This shape is a benchmark case, first studied theoretically by Dr. Collatz [1], tested at the HSVA [2] and used also by other authors for validation.

The following nomenclature and conventions apply to all figures presented below:

a, b – half-length and half-breadth of body

l – longitudinal spacing between bodies

h – lateral spacing between bodies

(l > 0: approach, l < 0: departure)

Forces are rendered non-dimensional by $\rho b U^2$ and yaw moment by $\rho b^2 U^2$, with ρ- water density and U – body speed.

Positive side force means attraction and positive yaw moment ="bow inwards" (towards the other body).

Fig 1. shows comparison with Collatz's result for the case of two identical cylinders moving head-to-head with equal speeds. The forces and moment are close in the approach stage of the maneuver but differ in the departure stage due to the effect of the viscous wake.

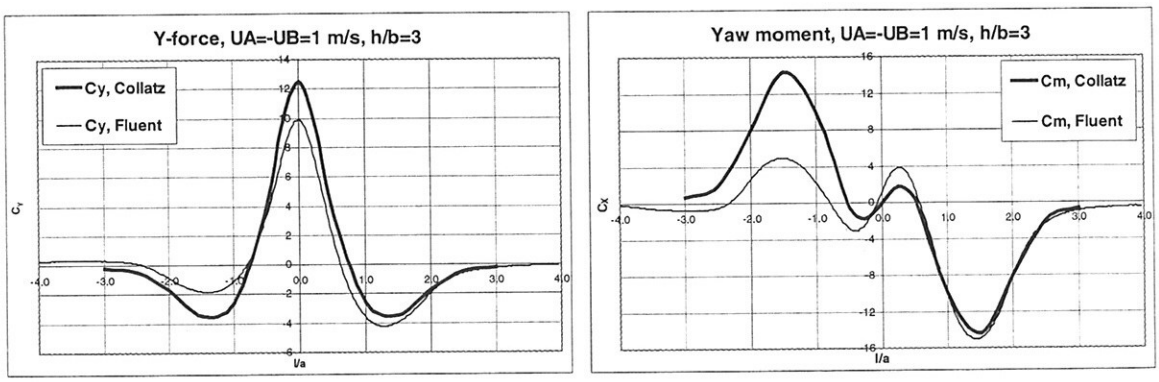

Fig 1. Comparison with potential flow results

The parameters, affecting most significantly the interaction loads, have been studied, some sample results being presented below.

- **Hull separation**

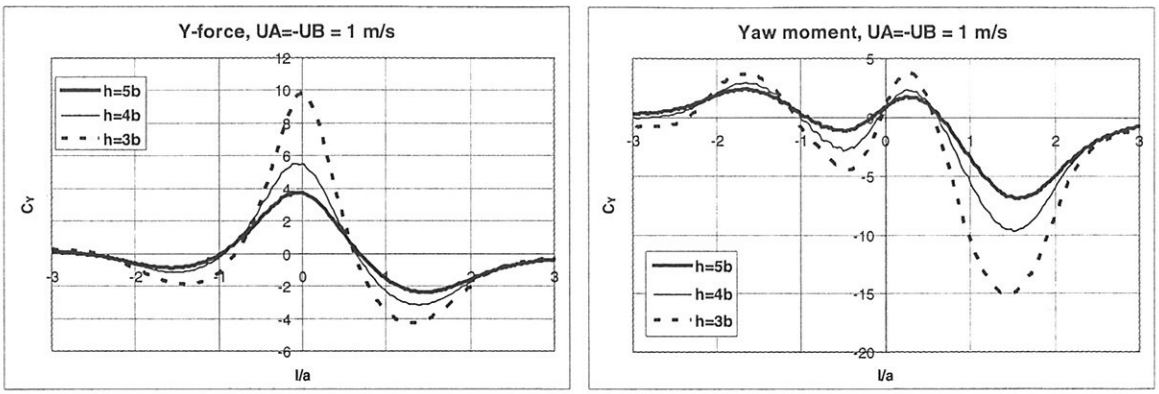

Fig 2. Two identical elliptic cylinders in head-to-head motion

- **Relative speeds**

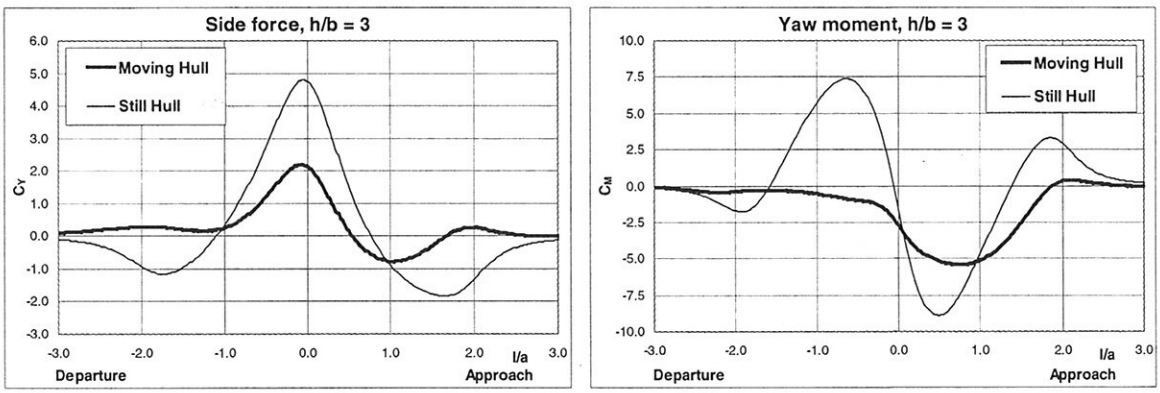

Fig 3. Elliptic cylinder passing by an identical stationary one

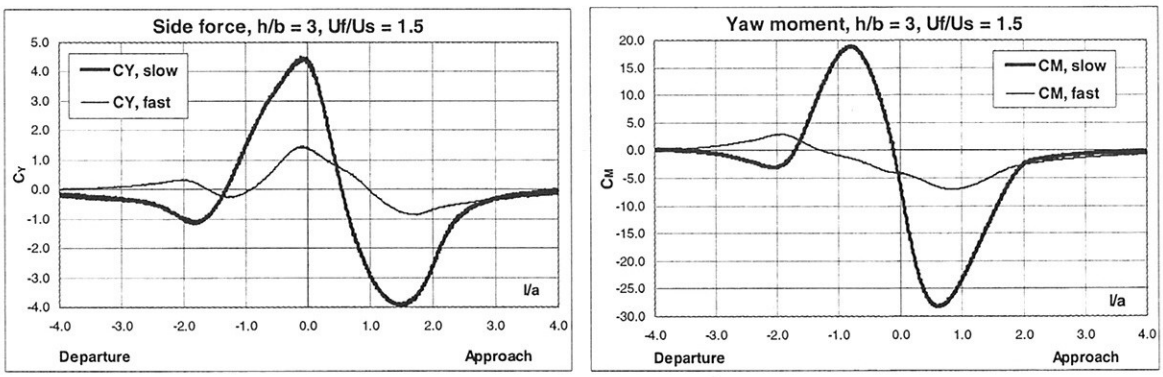

Fig 4. Two identical elliptic cylinders in overtake motion

- **Size ratio**

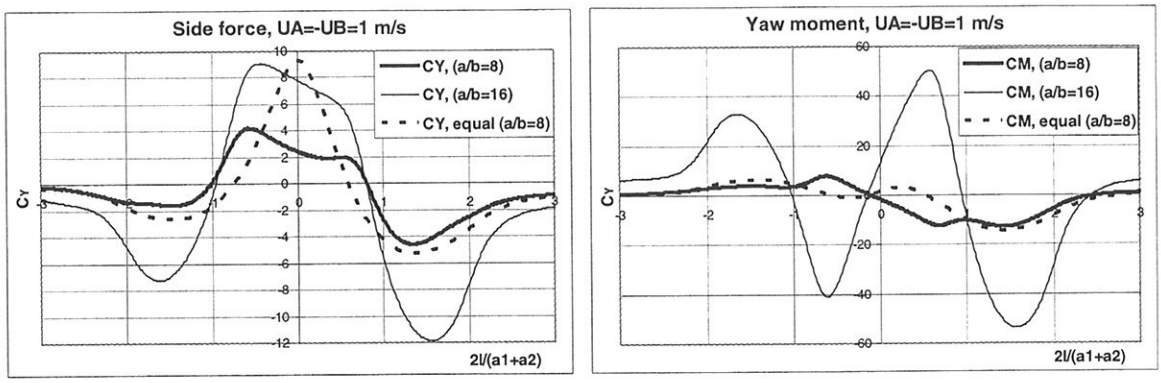

Fig 5. Head-to-head motion of two cylinders with equal b and a1/a2=2

- **Body shape effect**

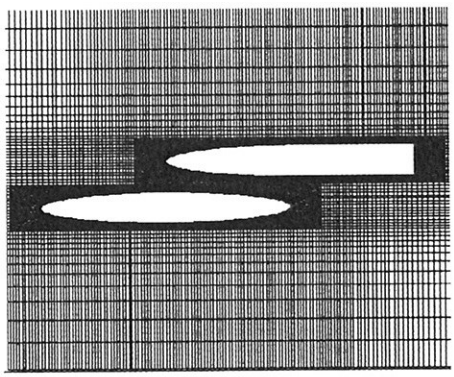

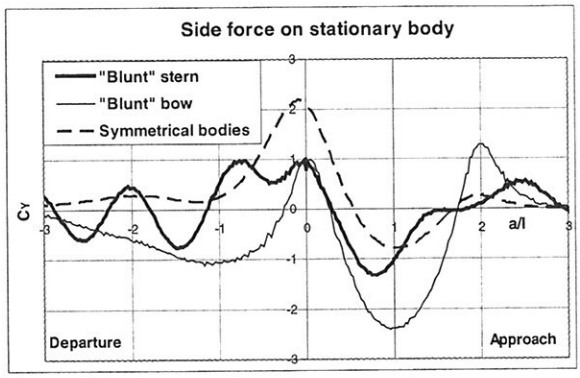

Simulation of the body motion affected by the interaction

A more interesting and challenging task is the simulation of the motion of bodies affected by the hydrodynamic interaction between them. That requires coupled solution of the fluid flow equations and the equations of motion of the body(ies). The first part is performed by FLUENT supplying the RHS of the ODE's of motion, which are integrated numerically with the time step of the solver. This is done by means of a user-defined function. FLUENT offers a macro (called DEFINE_CG_MOTION) to specify the motion of a dynamic zone by providing the linear and angular velocities at every time step. FLUENT uses these velocities to update the node positions on the dynamic zone based on solid-body motion. As mentioned earlier, the updated node positions on the boundaries determine the fluid zone mesh deformation and remeshing.

The simplest and straightforward way to integrate the ODE of motion seems to be the application of an explicit scheme with the time step of the flow simulation, i.e. (for 1 DOF translation) a one-step Euler scheme:

$$V^{(n+1)} = V^{(n)} + \frac{F^{(n)}}{m}\Delta t$$

However, in contrast to the usual approach in maneuverability and seakeeping, the forces and moments evaluated by the solver are the total forces and moments including the components due to acceleration. That makes the equation of motion non-linear. As Prof. Söding has rigorously proved and explained in [3], in cases of an added mass larger than the corresponding mass of the body the explicit schemes do not converge, when applied to non-linear equations, and implicit schemes converge slowly, needing a strong relaxation. Prof. Söding suggests a method for approximate evaluation of the added mass in the process of flow simulation.

Both implicit schemes and this method, however, use data from the internal iterations within a single time step. No way is known to this author so far to access the necessary solver data at each internal iteration (DEFINE_CG_MOTION runs only between time steps).

That is why a more trivial approach has been adopted. The added masses are considered constant and known (from reference data or evaluated by preliminary computations of the individual components by prescribing the corresponding motions). Then we calculate (e.g. for 1 DOF translation):

$$V^{(n+1)} = V^{(n)} + \frac{F^{(n)} + \lambda.(\Delta V / \Delta t)^{(n)}}{m+\lambda}.\Delta t$$

,where $\lambda$is the estimated added mass.

Thus the algorithm of the UDF developed for determining the motion of a body comprises the following steps:

1. Initialize mass, moments of inertia and estimated added masses.
2. Read data from previous time step: linear and angular velocity, linear and angular accelerations, Euler angles.
3. Get CG position
4. Get hydrodynamic forces and moments
5. *[Optional]* Add other external forces (driving, steering, …)
6. Calculate velocity of CG and its new position
7. Using Euler angles calculate the transformation matrix for the body orientation
8. Using Euler angles calculate the matrix relating angular velocities to Euler angle rates.
9. Transform moments to body-oriented coordinate system
10. Calculate angular accelerations and new angular velocities in body coordinate system
11. Transform angular velocities to global CS to return to Fluent
12. Calculate Euler angle rates and new Euler angles
13. Write data to be used in the next time step.

Several maneuvers of 2 elliptic cylinders (a/b=8) with length ratio 2 have been simulated using this approach.

In all cases the bodies are driven only by a constant force corresponding to their steady straight line movement, i.e. no steering is applied. The bodies are first let to move along fixed straight line for several time steps and the calculated forces with an opposite sign are taken as driving forces further throughout the maneuver. The initial paths are separated by a distance of 3b.

The figures below show the pressure distributions at several characteristic positions of each maneuver.

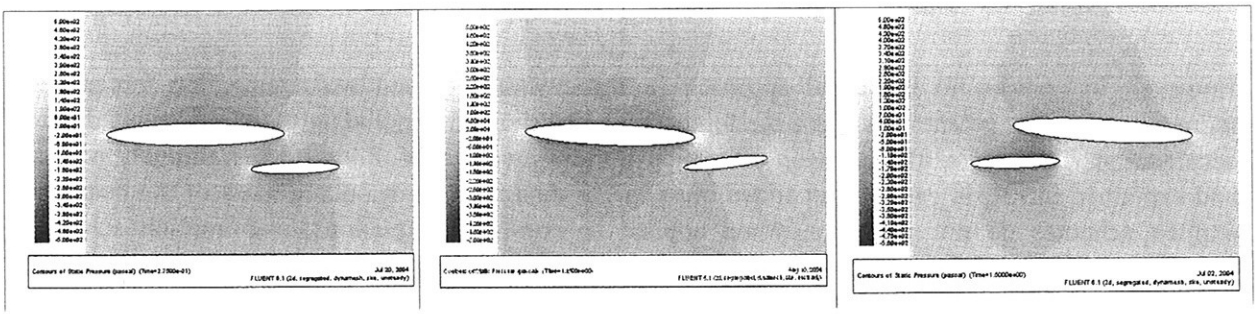

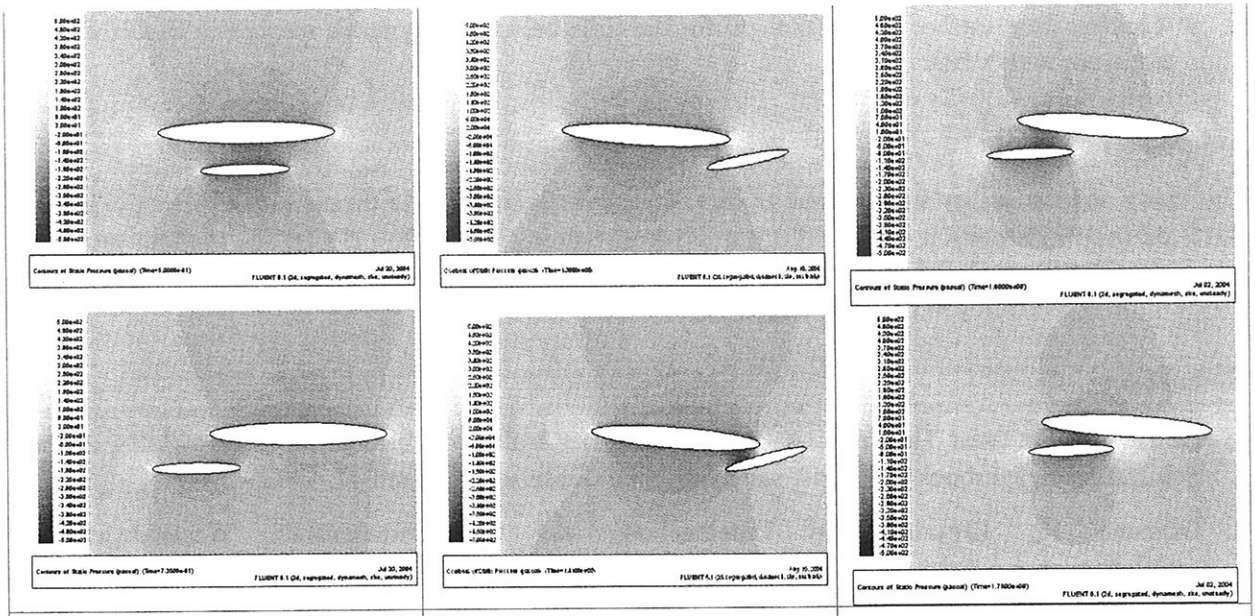

Bodies moving in opposite directions with equal speeds	The big body overtaking the small one (speed ratio = 1.5)	The small body overtaking the big one (speed ratio = 1.5)

In the encounter maneuver, due to the initial repulsion, the bodies pass by each other safely, only slightly deviating from their original straight paths. In both cases of overtaking, the bodies have eventually collided. This generally confirms the practical observation of navigators that overtaking maneuver is more dangerous than encounter.

Obviously, the correct and steady prediction of hydrodynamic forces and moments is of crucial importance for the adequate simulation of the body trajectory. It has been observed that the used mesh deformation and remeshing methods may produce quite irregular meshes, which leads to numerical oscillations of the computed forces. The situation can be improved by proper setting of the parameters governing the spring-based smoothing and that needs a more systematic parametric investigations.

Another remedy has been tried and found useful. The body has been "dressed" with a boundary-layer-like structured mesh zone, which is not deformed but moves as a rigid body with the velocities calculated for the body boundary. Figure 6 below shows an irregular mesh generated by deformation and remeshing and the proposed non-deforming zone around the body.

Fig. 6. Application of non-deforming structured grid around the body

Tests have shown that this technique largely damps the irregularities in pressure and, consequently, of the hydrodynamic forces.

Conclusions

The computations with 2D cases presented here demonstrate the feasibility of using CFD for both studying the features of hydrodynamic interaction of bodies moving in fluids and for coupling the flow analysis with body motion equations to simulate the actual motion of bodies subject to interaction.

That gives confidence to pursue the problem further to:

- Incorporating motion control (steering devices) and motion control optimization
- Solution of 3D cases

- Tackling free surface flows (though, for the time being, the dynamic meshes in FLUENT do not work with VOF)

Acknowledgements

This study and the author's attendance of this event have been possible thanks to the project G3MA-CT-2002-04040 Promotion of High-Tech in Hydrodynamics Research – HYTECH, implemented by the Bulgarian Ship Hydrodynamics Centre with the financial support of the Fifth Framework Programme of the European Community.

References

1. Collatz G., Potential Theoretische Untersuchung der hydrodynamischen Wechselwirkung zwier Schiffskörper, Jahrbuch der Schiffbautechnischen Gesselschaft, Band 47, 1963.
2. Oltmann P., Experimentelle Untersuchung der hydrodynamischen Wechselwirkung schiffsähnlicher Körper, Schiff und Hafen, Jahrgang 22, Heft 8, 1970
3. Söding H., How to Integrate Free Motions of Solids in Fluids, 4th Numerical Towing Tank Symposium, Hamburg, 2001
4. FLUENT 6.1 User's Guide
5. FLUENT 6.1 UDF Manual

Numerical Simulation of Sheet Cavitation Effects on the Hydrodynamic Performance of Foils and Propellers

Jean-Marc Laurens (Ensieta) ; Surasak Phoemsapthawee(Ensieta)
(laurenje@ensieta.fr)

Nomenclature

Unless specified otherwise, the symbols and terminology used in this document comply where possible with the ITTC Symbols and Terminology Group (1997).

Introduction

From a propeller design point of view, cavitation is obviously an unpleasant phenomenon, since it causes many undesirable effects such as erosion, noise, vibrations, etc. Propellers are generally designed not to cavitate. Some advanced design tools have been developed for this purpose, Raulo. J. (1997). However, in recent times, mostly due to an increasing demand for higher propeller loadings and the limited propeller installation space, propellers have to be designed with acceptable cavitation side effects. Therefore, the current propeller design tools which can only calculate hydrodynamic forces and propeller performance in subcavitating conditions are no longer sufficient. Cavitation simulation is required as well.

There are many types of propeller cavitation such as bubble, tip vortex, hub vortex, cloud and sheet cavitation. Among these cavitation types, sheet cavitation, as well as cloud cavitation which often occurs downstream of sheet cavitation, have a considerable effect on performance loss since sheet cavitation attaches to the lifting surface and modifies the flow on this surface. Sheet cavitation can also be divided into two types: partial sheet cavitation where the cavitation starts and ends on the lifting surface and supercavitation where the cavitation does not end on the lifting surface. Moreover, apart from tip vortex cavitation, sheet cavitation is the most frequent type of cavitation that occurs in the flow around a propeller. The tip vortex cavitation generates noise but, unlike sheet cavitation, it does not induce performance loss.

Some full Navier-Stokes simulations of cavitation have been presented these past two years by several teams, Streckwall H. and Hympendahl O. (2003), but so far nobody claims to be capable of using such simulations in an industrial project. In this project, an existing program using the Boundary Element Method to calculate the hydrodynamic forces and performance of propellers is used. There is nothing fundamentally new about the idea of adding a sheet cavitation module to a BEM code.

The literature contains numerous studies that have been performed to develop such tools, generally with a certain success, although for some reason, few authors are concerned by the effects of sheet cavitation on global performance.

On the other hand, there are a lot of detailed measurements available. Cavity detachment point criteria are heavily discussed in the available literature. An important point is that the pressure upstream of the cavity is usually found to be lower than the vapor pressure. When the flow is laminar, the cavity normally detaches downstream of the laminar boundary layer separation point, La Cavitation (1995). However, according to the experiments carried out at the *Laboratory For Hydraulic Machines, Swiss Federal Institute of Technology,* , partial sheet cavitation can also occur without a laminar boundary layer separation. In this case, the pressure inside the cavity can be equal (non-burst type) to or higher (burst type), than the vapor pressure. Downstream the cavitation sheet is a highly turbulent two-phase flow. Therefore, the pressure downstream oscillates and is difficult to measure. In order to model

partial sheet cavitation, apart from the solving method, we should concentrate on two important points, namely the cavity detachment criteria and the cavity closure model.

There are many criteria to determine the cavity detachment point. Pellone C., Maître T. and Briançon- Marjollet L. (2000), in the first section of their paper, provide a concise summary of these criteria : from the smooth detachment criterion or Brillouin-Villat's criterion used by most scientists including Lee H. and Kinnas S. (2004) , where both the slip condition and vapor pressure condition are satisfied, to the laminar boundary layer criterion introduced by Franc J-P. (1986) which imposes a laminar flow separation. The other models mentioned are the minimum pressure criterion and finally the leading edge criterion used for instance in Vaz G., Bosschers J. and DeCampos J.F. (2003). In the same article the former divide the cavity closure models into two categories: closed and open models. As defined by Rowe A. and Blottiaux O. (1993) , a closed model is a model in which the cavity or streamline originating from the rear of the cavity closes onto the foil, and an open model is a model in which the streamline does not close on the foil. They describe some models : Closed model without a cavity wake, Closed model with a near cavity wake, Closed model with an algebraic cavity wake, Kinnas S. and Fine N. (1993), and the Re-entrance jet model which is totally inadequate for BEM codes and should be left for full Navier-Stokes simulations.

The solving methods based on the potential theory depend strongly on the available potential flow code. Hoeijmakers, H.W.M. (1992) summarized the different methods. According to Kinnas S. and Fine N. (1993) and Salvatore F., Testa C. and Greco L. (2003) , the unknown elements are the source strengths, however in our case it is the exact opposite. Krasilnikov V-I., Berg A. and Oye I-J. (2003) implemented an open cavity model within a lifting surface code. Finally, the method developed by deserves to be mentioned. The authors have proposed an adaptation method to predict partial sheet cavitation within some Navier-Stokes solver. However, the adaptation process is carried out separately from the flow calculation. Therefore, this method has the advantage that it can be used with any available code. The initial premise is taken from the Rayleigh-Plesset solution. Subsequently, the free-surface is adapted in terms of the difference between the pressure coefficient and cavitation number.

Model

The BEM code we use belongs to what Hoeijmakers, H.W.M. (1992) refers to as "second generation" panel methods involving the Dirichlet condition (Φ=0 in the inner body). The body surfaces are discretised into first order panels carrying constant source and doublet distributions. The wake developing behind the propeller or the rudder is formed with a sheet of first order panels carrying constant doublet distributions and it is generated over time in a Lagrangian manner. Using the Dirichlet condition which imposes the slip condition on the body surface, the sources can be directly determined from the inlet velocity and the normal vectors. Hence, the unknown elements are the dipoles. The locations of the vertices of the sheet panels are recalculated at each time step but not the dipoles they carry.

Non-lifting bodies such as the hub are discretised using first-order panels carrying constant source distributions. The propeller hub can be easily modelled this way but in most cases it does not influence the hydrodynamic coefficients, therefore we do not simulate its presence in the results presented here. The code allows for unsteady flow simulation and the body thickness representation leads to an accurate distribution of the pressure coefficients (Cp) on the rudder and blade surfaces. A brief description of the code can be found in Laurens, J.-M. (1993). The document also reports the results of the verification and mesh sensitivity analysis.

As mentioned previously, the unknowns in our code are the dipoles. Therefore, methods where the doublets are computed from the cavitation sheet theory and imposed as a condition on the cavity surface while the sources are to be computed, cannot be applied without drastic

changes and without practically rewriting the potential flow code. The propeller blade thickness which is explicitly modeled within our code, a method where the blade is considered as a lifting surface is also ruled out.

Several years ago a procedure was developed at the Bassin d'Essais des Carènes to model sheet cavitation within this BEM code. The potential code has been modified since, but the main solver is still based on the same method described at the beginning of this section. The method involved a relatively complex procedure to couple the BEM code with a bi-dimensional code. The following procedure was used. Firstly, the tri-dimensional BEM code is run. Each blade section is then transformed in order to match the pressure coefficients (Cp) curves in both 2D and 3D simulations. When the section is symmetrical and the wing operates in a uniform flow, the transformation is simply obtained by changing the angle of attack as the lifting line theory indicates. Nevertheless, when it comes to propeller blade sections, the transformation is far from being trivial. After the transformation, the 2D code is run in order to obtain the cavity shape. The profile with the cavity is then transformed using the inverse transformation. A new profile is obtained showing a hunchback for this section. The procedure is repeated for all sections and a new blade geometry which shows the cavity as a hunchback is obtained. The new geometry is then used directly within the 3D BEM code without any additional modifications or boundary conditions. Despite the complexity of the procedure, a perfect match between 2D and 3D simulations was obtained as reported in the RSTD (1999) presenting the activities of the Bassin d'Essais des Carènes.

We decided to abandon this tedious procedure. However, there is still a way to intervene within the code using the transpiration velocity technique. Therefore, the cavitation effect can be taken into account by modeling the cavity form using transpiration velocity. The technique was originally used to model the boundary layer effect, Laurens, J.-M. (1993). The transpiration velocities, v*, are normal to the panels and deviate the flow streamlines. Using the v* is equivalent to using a geometrical modification although it is much more convenient since no re-meshing procedure is needed. Furthermore, within the BEM code, specifying a transpiration velocity for a particular panel is equivalent to adding a source strength $\sigma^*=v^*$ to the actual source strength σ. We therefore know from previous studies how to intervene within the potential flow solver. The question remaining is how can we define the v* distribution.

We first considered imposing the shape since the cavity length for a closed model depends on the cavitation number (Fine and Kinnas 1993). A verification showed that changing the cavity length moves the average Cp up and down and changing the cavity thickness adjusts the distribution mean slop. Therefore, when the Cp mean at the suction side matches the target value of σ the cavitation number, iterating on the thickness allows us to obtain the flat Cp distribution we seek. After some other trials we went for the simplest idea. We simply assume v* to follow P-k.Pv. The first non-zero v* value will then naturally start where -Cp reaches the cavitation number. The values of v* are given by the following :

$$v^*(p) = \pm \sum_{Start}^{End} \alpha \sqrt{\frac{2|P - k.Pv|}{\rho}} \qquad \text{(Eq. 1)}$$

When –Cp reaches the cavitation number for the second time, v* becomes negative. We keep adding for the value of v* until the cavity thickness reaches zero, that is when :

$$t_c(p) = \int_{Start}^{End} \frac{v^*}{u(s)} ds = 0 \qquad \text{(Eq. 2)}$$

or if the trailing edge is reached before. At present, we have not performed enough tests to talk about the super-cavitation model but finally the idea is not very different from Krasilnikov V-I., Berg A. and Oye I-J. (2003) .

The tuning factors within this formulation are of course the proportionality coefficient α and the factor k. We realized that the best results are obtained if α starts from a small value. This was also shown by the study reported in Laurens, J.-M. (1993). At present α is specified in the input file with a recommended value. On the next iteration, v* is increased in the same manner using the new value of the pressure obtained by solving the potential problem within the presence of v*. We then have to define a criterion to stop the iterations, i.e. when a reasonably flat distribution of P is obtained at the cavity surface. We compute both the average and the standard deviation. As long as the standard deviation decreases, the distribution is improving toward our target. Eventually, the iteration will reach a point where the standard deviation increases. In this case we keep the previous iteration. The fact that P presents a flat distribution on the cavity surface does not mean that P is equal to Pv. The factor k is here to adjust the level of P on the cavity surface. In fact, sometimes, k is only adjusted on the first time step and remains to 1 for the rest of the computation.

Results

Some test cases are presented hereunder. The potential flow code can be used to either simulate the propellers or the wings. There is apparently no difference in the manner in which the cavitation model is implemented, except for the output format.

We first start with the hydrofoil case presented in RSTD (1999). The conditions are the same, a rectangular three-dimensional foil of constant section NACA0004 and of aspect ratio, $A=3$. The cavity number, σ is 0.45. The results are compared to those previous results in Figure 1.

Although the finer mesh gives better looking results, the hydrodynamic coefficients remain the same. These values are given in Table 1. Since the tool will be used to assess the performance of the cavitating propeller, it would be unproductive to consider a very high number of panels in order to obtain a nicer picture.

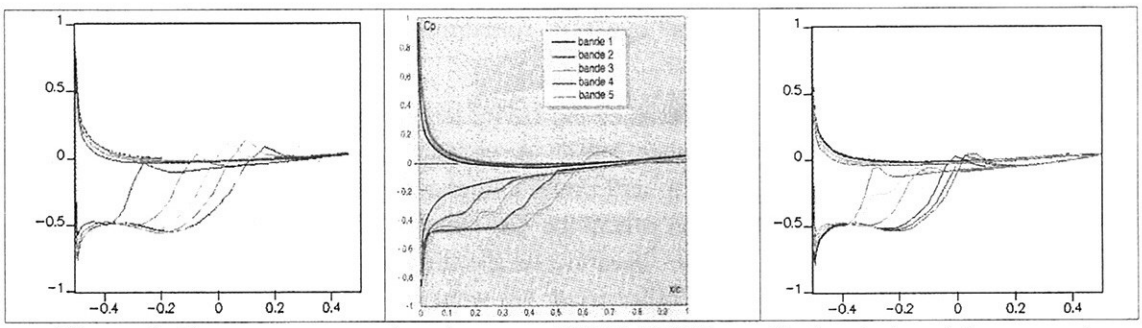

Figure 1. Cp curves comparison between RSTD (1999) results (center) and the present simulations with a coarser grid (left) and a finer grid (right).

	C_L	C_D
Sub-cavitating	0.19	0.0064
Cavitating	0.23	0.011

Table 1. Hydrodynamic coefficients for the cavitating and non cavitating foil.

The results of Table 1 show that the lift, for this case, increases in cavitating conditions. The drag also increases in such a way that a significant loss is observed for the fin finesse (lift-to-drag ratio). Most papers tend to present qualitative results rather than quantitative results. In the book by Carlton, JS. (1994), some effects of cavitation on the hydrodynamics coefficients are reported. They were taken from Balhan J. (1951). The report presents the Cp curves and the hydrodynamic coefficients for four different foils with different angles of attack and

cavitation numbers. All results were obtained experimentally. For a given foil at a given angle of attack, the C_L and the C_D increase in partial (or closed) sheet cavitation conditions as σdecreases. They decrease in super-cavitation conditions as σdecreases.

We then used a rather standard propeller with a diameter of 5.75 m, four blades and a slightly lower advance parameter, J=0.7346 has been considered than the design parameter. We set a target cavitation number slightly above the maximum –Cp obtained for the sub-cavitating computation. Table 2 shows the Kt and Kq for the steady state case.

σ	Kt	Kq	η	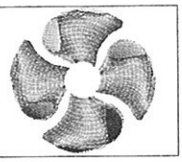
1.6	1.91E-01	3.12E-02	0.7182	
2.0	1.80E-01	2.74E-02	0.7675	
Subcavitating	1.79E-01	2.73E-02	0.7667	

Table 2. Loss of propeller efficiency due to sheet cavitation.

The same type of results is obtained in Table 3 when the propeller is working at 7° angle of inclination.

	Kt	Kq	η
Cavitating	1.86E-01	3.00E-02	0.724
subcavitating	1.82E-01	2.77E-02	0.769

Table 3. Cavitating and subcavitating results for Kt and Kq when the propeller is working in an incoming flow with an inclination angle of 7°, σ=2.

More interesting is the unsteady behavior. Figure 2 shows the evolution of each of the 4 blades Kt during the propeller revolution. Finally, we implemented the necessary elements to take the hydrostatics into account. As a final remark, writing a Graphical User Interface is a tedious exercise. We made the code output compatible to Fieldview, a very powerful CFD post-processor.

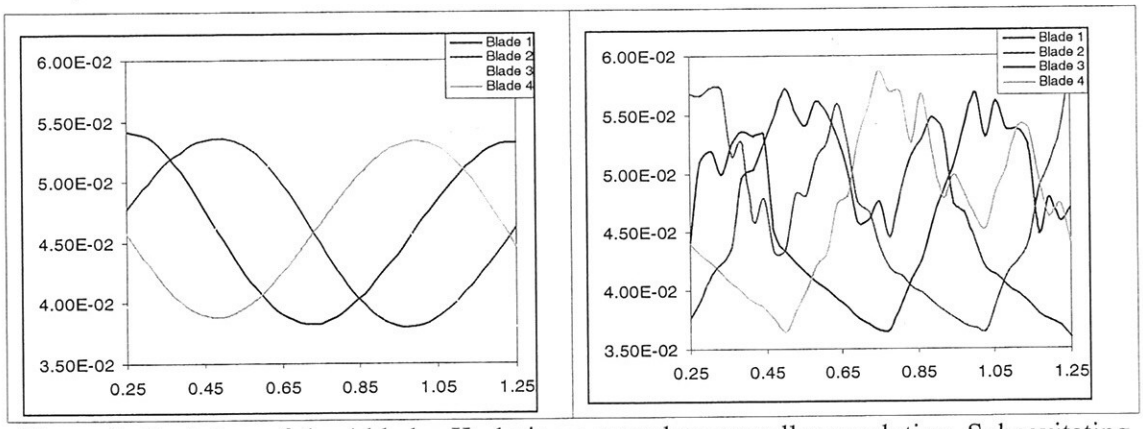

Figure 2. Evolution of the 4 blades Kt during a complete propeller revolution. Subcavitating (left), cavitating (right).

Conclusion and scope for future work

A method using transpiration velocities has been implemented within a BEM code to model partial sheet cavitation. Results were obtained for a hydrofoil already used for a previous development of cavitation model with the same BEM code. As far as we can tell, the results of the present method are practically similar to those of the previous study. The procedure was then applied to simulate partial sheet cavitation on propeller blades in both steady and

unsteady state conditions. We report some effects on the hydrodynamic coefficients which are compatible with some existing experimental data.

We cannot claim that the code and its new module are now fully operational but reasonable results are obtained. Some questions remain and a better criterion for convergence is needed. Considering the number of attempts we made to find a better one, we can tell that it won't be an easy task. We do not pretend to be able to simulate supercavitation but if we do not close the cavity, we have to check what happens to the Kutta condition and maybe we can find something that resembles open cavity.

References

Ait-Bouziad Y., Guennoun F., Farhat M. and Avellan F. (2003) *Numerical Simulation of Leading Edge Cavitation*, Proceeding of FEDSM 2003, 4th ASME_JSME Joint Fluids Engineering conference, Honolulu, USA

Balhan J. (1951) Metingen aan Enige bij Scheepsschroeven Gebruikelijke Profielen in Vlakke Stroming met en zonder Cavitatie, N.S.P.W. *(now MARIN)*, report N°99.

Carlton, JS. (1994) . Marine Propellers and Propulsion. Ed. Butterworth HeineMann.

Fine N. and Kinnas S. (1993) *A Boundary Element Method for the Analysis of the Flow Around 3D Cavitating Hydrofoils*, Journal of Ship Research, Vol.37, N°3, pp.213-224.

Franc J-P. (1986) *Etude Physique d'Ecoulements Cavitants*, Thèse de Docteur d'Etat ès Sciences, Université de Grenoble.

Hoeijmakers, H.W.M. (1992) *Panel Methods for Aerodynamic Analysis and Design,* AGARD Report 783, pp.5.1-5.47.

Kinnas S. and Fine N. (1993)*A numerical Nonlinear Analysis of the Flow around Two- and Three- dimensional Partially Cavitating Hydrofoils*, Journal of Fluid Mechanics, Vol. 254, p.151-181

Krasilnikov V-I., Berg A. and Oye I-J. (2003) *Numerical Prediction of Sheet Cavitation on Rudder and Podded Propellers Using Potential and Viscous Flow Solutions*, CAV2003.

La Cavitation (1995) JP. Franc, F. Avellan, B. Belahadji, J.Y. Billard, L. Briançon, D. Fréchou, D.H. Fruman, A. Karimi, J-L. Kueny and J-M. Michel., La Cavitation : Mécanismes physiques et Aspects industriels, Presses Universitaires de Grenoble.

Laurens, J.-M. (1993) Couplage code de calcul fluide parfait, code de calcul couche limite 3D, Rapport DCN/Bassin d'Essais des Carènes, Etude 2524 pièce 3.

Lee H. and Kinnas S. (2004) Application of a Boundary Element Method in the Prediction of Unsteady Blade Sheet and Developped Tip Vortex Cavitation on Marine Propellers, Journal of Ship Research, Vol. 48, p.15-30

Pellone C., Maître T. and Briançon- Marjollet L. (2000) *Partially Cavitating Hydrofoils: Experimental and Numerical Analysis*, Journal of Ship Research, Vol. 44 p. 40-58

Raulo. J. (1997) *Optimisation des Sections de Pales d'Hélice.* Thèse de Doctorat, Université de Rouen.

Rowe A. and Blottiaux O. (1993) Aspects of Modeling Partially Cavitating Flows, Journal of Ship Research, Vol. 37, p.34-48

RSTD (1999) Le Bassin d'Essais des Carènes, RSTD N°43.

Salvatore F., Testa C. and Greco L. (2003) *A Visous/Inviscid Coupled Formulation for Unsteady Sheet Cavitation Modeling of Marine Propellers*, CAV2003

Streckwall H. and Hympendahl O. (2003) *Simulation of cavitating flows around propellers with a RANSE code,* 6th NuTTs, Rome.

Vaz G., Bosschers J. and DeCampos J.F. (2003) *Two-Dimensional Modeling of Patial Cavitation with BEM. Analysis of Several Models*, CAV2003

7th Numerical Towing Tank Symposium
Hamburg, Germany, 3-5 October 2004

Validation of CFD Results Behind the Working Propeller of a Ship Model

Lars Ole Lübke (luebke@sva-potsdam.de)
Klaus-Peter Mach (mach@sva-potsdam.de)

Potsdam Model Basin

Introduction

Laser Doppler Velocimeter (LDV) wake field measurements of the propelled KRISO container ship (KCS) are presented. The angular based measurements were carried out 0.15 propeller diameter behind the propeller plane under propulsion conditions. The obtained flow field offers insight into the flow and enables a detailed validation of computational results. In general a very satisfactory agreement between calculation and experiment has been found.

The propeller behind a single screw ship operates in highly inhomogeneous flow conditions, characterised by the wake peak and the bilge vortex of the ship hull. The flow towards the propeller blades and their performance becomes a function of the angular position of the propeller, due to different axial, tangential and radial velocities. The propeller accelerates the flow depending on the radial load of the blades. Behind the propeller a complex flow field arises, where the effects of both ship and propeller superimpose. The knowledge of the flow behind the propeller is of particular importance with respect to rudder performance and cavitation.

For the calculation of the propelled ship it is of particular importance that the numerical method is able to simulate the interaction between propeller and ship, in order to obtain accurate results. Ships under propulsion conditions are yet in most applications calculated with body forces in order to reduce the computational effort. The effect of the (not present) propeller on the flow is approximated by distributing fictive forces, which yield the thrust and the torque, in a disk located at the propeller plane. Only few publications deal with calculations considering the real turning propeller in the wake of the ship [1]. This approach simulates the true transient interaction between ship and propeller but also requires more computational resources. However increasing effort is being made to establish this approach in practice.

Geometry

The ship and propeller model of the KCS were manufactured at the Potsdam Model Basin, according to the data provided by KRISO. The main particulars of ship and propeller model are given in Tab. 1, with the scale ratio being λ=31.5994. The propeller plane is located x/L_{PP}=0.0175 upstream of the aft perpendicular.

Length perpendiculars	L_{PP}	[m]	7.2786
Breadth	B	[m]	1.0190
Draught	T	[m]	0.3418
Propeller diameter	D	[m]	0.250
Pitch ratio	P/D	[-]	0.996
Area ratio	A_E/A_0	[-]	0.800
Number of blades	z	[-]	5

Table 1: Ship and propeller model geometry

Experimental setup

For the LDV measurements a traversing unit was mounted on the ship, according to Fig. 1 and 2. The experimental setup allowed to move the LDV probe to the desired measuring position. A dual beam two-color backwards scattering LDV system from TSI was used, which allows to measure two orthogonal velocity components simultaneously. In order to measure the three dimensional velocity field each point had to be measured twice. Therefore the points were measured from below and from the side.

The measurements were carried out in the towing tank of the Potsdam Model Basin with additional seeding. With this approach it was possible to increase the data rate considerably during the measurements, achieving a speed up of the initial data rate of up to approximately 20 times. For the tests the KCS model was fixed to the carriage, suppressing dynamic sinkage and trim.

During the angular based measurements a total of

12,000 values were collected. The collected data at each measuring point was sorted depending on the angular position of the propeller blades, in order to obtain the velocities for the same occasion. The data was measured in a cylindrical co-ordinate system according to Fig. 3. In total 186 points were measured for the ship with turning propeller. The measurements were carried out 0.15D behind the propeller plane.

Calculation setup and grid generation

To calculate the viscous flow around ship and propeller the RANS equations were solved numerically using the commercial software package CFX5. For details on the numerical method see [2]. The k-ω SST model of Menter [3] was used to model turbulence.

Block-structured numerical grids have been generated with the commercial software ICEM-CFD.

The unpropelled KCS was investigated on a medium sized mesh with approximately 700,000 grid cells on one ship side only, taking advantage of the symmetry at the ships center line. Dynamic sinkage and trim was not taken into account. The surface elevation was previously calculated with the panel code KELVIN (Potsdam Model Basin) and used to prescribe the upper boundary for the RANS calculations. For the grid a dimensionless wall distances $y^+=u_\tau y/\nu$ of about 1 was obtained, with ν being the kinematic viscosity, $u_\tau=\sqrt{\tau_w/\rho}$ the shear velocity and τ_w the shear stress at the wall. In Fig. 4 the numerical mesh on the bare hull is shown. The grid blocks in the propeller region were generated such, that they could be substituted with blocks containing the propeller mesh.

For the calculation of the propeller open water performance a steady approach considering one propeller blade with periodic side boundaries was used. The numerical mesh was divided into an inner and an outer part, considering the propeller geometry in full detail. The grid topology was chosen such, that the inner part, surrounding the propeller blade, could also be used for the unsteady simulation of the flow around the ship with propeller. For the inner mesh 150,724 grid cells were employed. Fig. 5 shows the surface grid on one propeller blade.

For the calculations of the flow around the ship with rotating propeller an unsteady approach was chosen. The ship flow is calculated in a stationary, while the propeller in a rotating frame of reference. For the calculation of ship with propeller approximately 2.15 million grid cells were used. The surface meshes on ship and propeller are shown in Fig. 6. During the simulation the propeller was rotated by 4° in every time step, employing 5 inner iterations.

Results

The KCS model was investigated for the operation point given in Tab. 2, corresponding to V_S=24kts in full-scale. Prior to the calculation of ship with turning propeller the wake field of the bare hull and the open water curves of the propeller were calculated.

Velocity model	V_m	[m/s]	2.196
Rate of revolution	n	[1/s]	9.5
Froude number	F_N	[-]	0.260
Reynolds number	R_N	[-]	$1.4 \cdot 10^7$

Table 2: Operation point

In Fig. 8, 9 and 10 the axial, tangential and radial velocities of the KCS hull are plotted over the circumference for different dimensionless radii (r/R=0.4, 0.7 and 1.0). The computational results are compared with the experimental data and a good general agreement can be found. However some discrepancies can be observed in the region of the bilge vortex and at inner radii, while the quantitative agreement at the outer radii is considered to be satisfactory for the calculation of the propeller performance in the behind ship condition.

Propeller open water tests were conducted at the Potsdam Model Basin with the KCS propeller. The open water curves from KRISO and Potsdam agree well. In Fig. 7 the experimental (Potsdam Model Basin) and the computed propeller curves are shown. In the advance coefficient range of interest between 0.7 and 0.8, the calculated thrust coefficient is about 10% to small, while for the torque coefficient the error is less than 1%.

For the simulation of the propelled KCS model the measured and the computed results are compared in a plane located 0.15 propeller diameter behind the propeller plane.

In Fig. 11, 12, 13 and 16 the time histories of the measured and computed axial, tangential and radial velocity components on radius r/R=0.7 at four different positions are shown for one propeller revolution. The considered circumferential positions are φ=0°, φ=90°, φ=180° and φ=270° respectively, with the 0° position being defined above the propeller shaft. The data has been made dimensionless with the ship speed (V_m=2.196m/s) and provides a detailed insight into the flow field behind the working propeller. The unsteady behavior of the flow depending on the passing blades can be observed. In general the agreement between measurements and calculation is very good, in particular for the angular position φ=180° and φ=270°.

A snapshot of the flow field behind the propeller

for the blade position ϑ=220° is shown in Fig. 14 for the measurements and in Fig. 17 for the simulation. Please note, that the measured velocities in Figs. 14 and 15 are interpolated in time and space, thus showing a denser vector field than was actually measured. The thrust generation is eccentric since the propeller rotates on the port side against and on the starboard side with the rising flow. For this reason the propeller blades operate with varying inclination angles. The largest velocities can be seen at roughly the 90° position. Although the tip vortices of the five bladed propeller are not accurately resolved in space, the position of the vortices can clearly be identified. The largest axial velocity gradients in space can be observed in the wake peak amidships above the propeller shaft. Both bilge vortices (port and starboard side), although not as pronounced with operating propeller as without, do influence the velocity field in this region considerably. This can be observed on basis of the downwards pointing velocity vectors amidships above the propeller shaft which are a superposition of the bilge vortex and the tangential velocity component imposed by the rotating propeller. In the wake of the propeller blades the velocity field is disturbed, with a decrease in the axial and an increase in the transversal components of the velocity vector. In Fig. 15 and 18 the comparison is carried out for the blade position ϑ=240°. The agreement between measurements and calculation is very satisfactory.

Concluding remark

LDV measurements and RANS calculations for a single screw container vessel (KCS) in propelled condition were carried out at the Potsdam Model Basin in a plane located 0.15 propeller diameters behind the propeller plane. The experimental results were used to validate the CFD calculations. In general very encouraging results were obtained with good agreement between measurements and calculations. For further details please refer to the proceedings of the 25th Symposium on Naval Hydrodynamics [5].

The authors would further express their gratitude towards the "Bundesministerium für Bildung und Forschung" for funding this project.

References

[1] ABDEL-MAKSOUD, M., MENTER, F., RIECK, K.
Unsteady numerical investigation of the turbulent flow around the container ship model (KCS) with and without propeller,
Proceedings of Gothenburg 2000, A Workshop on Numerical Ship Hydrodynamics

[2] CFX5 Manual Version 5.7,
July 2004

[3] MENTER, F.
Two-equation eddy-viscosity turbulence models for engineering applications,
AIAA-Journal, 32(8), 1994

[4] ITTC Quality Manual
ITTC 1960, 9th pp237-258, 21st p413

[5] LDA Measurements in the Wake of the Propelled KCS Model and its use to Validate CFD Calculations
25th Symposium on Naval Hydrodynamics, 8-13 August, St. Johns, Canada

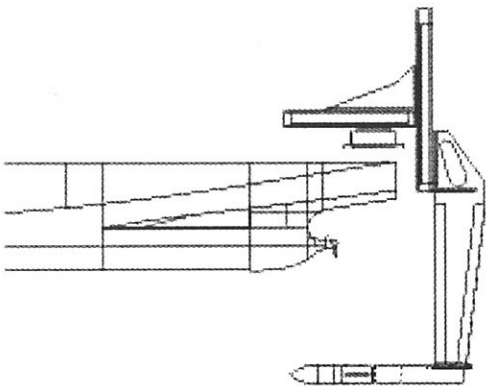

Figure 1: Experimental setup for LDA measurements, side view

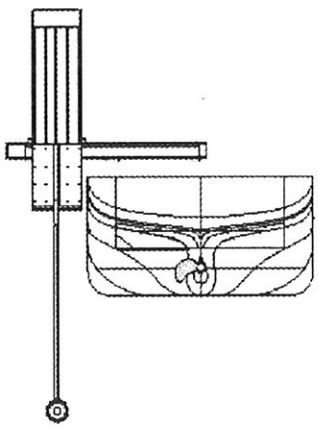

Figure 2: Experimental setup for LDA measurements, aft view

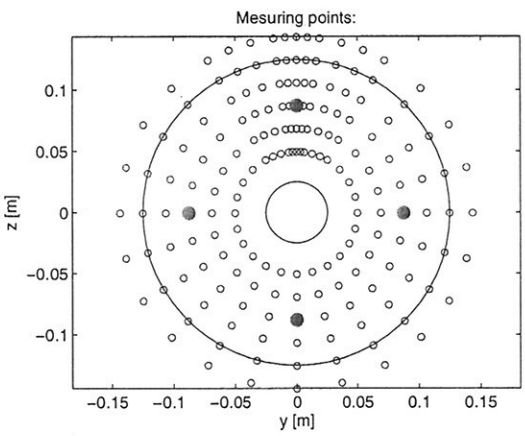

Figure 3: Measuring points

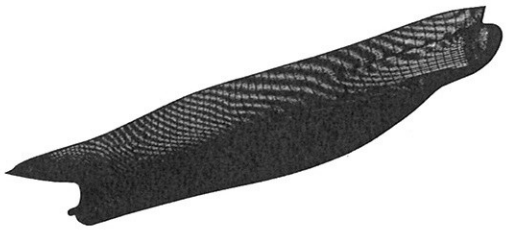

Figure 4: Numerical mesh, KCS hull

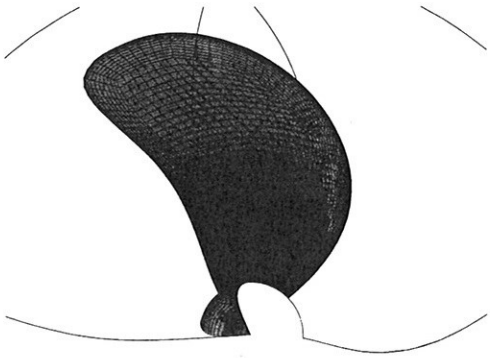

Figure 5: Numerical mesh, propeller

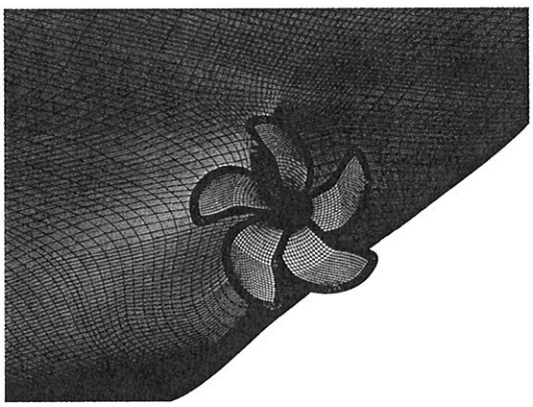

Figure 6: Numerical mesh, ship and propeller

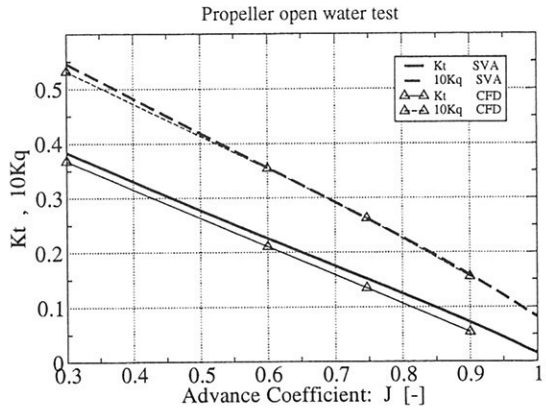

Figure 7: Measured and computed propeller open water test

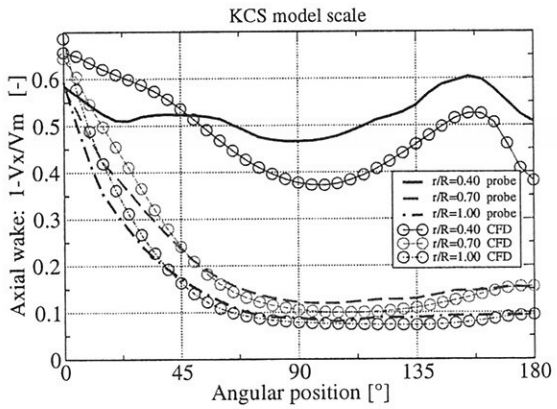

Figure 8: Measured and computed axial velocities in propeller plane

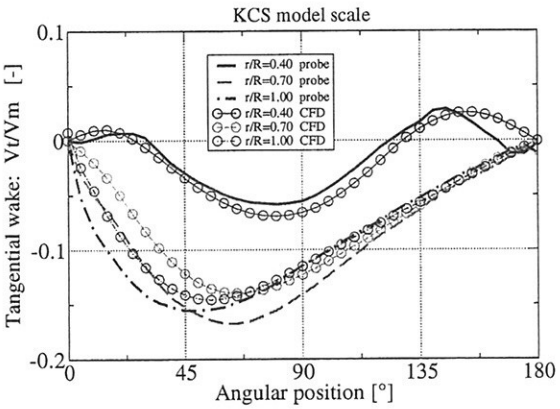

Figure 9: Measured and computed tangential velocities in propeller plane

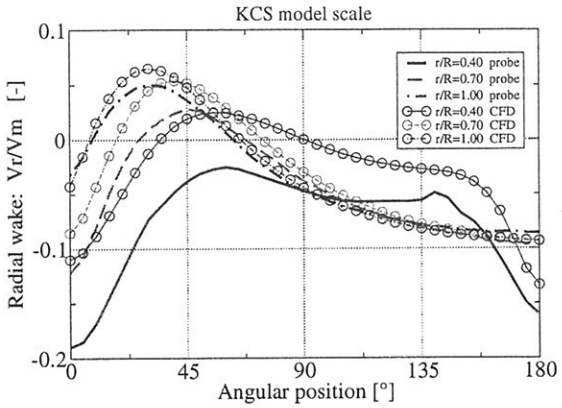

Figure 10: Measured and computed radial velocities in propeller plane

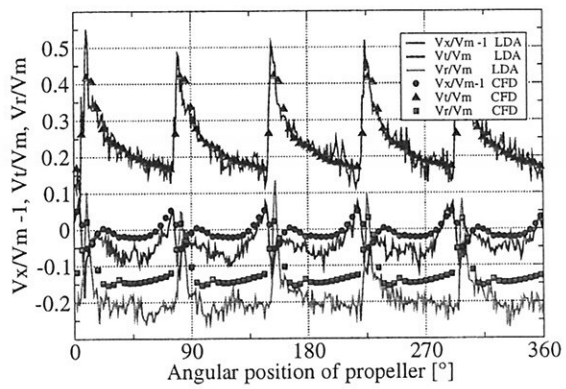

Figure 11: Velocity components, position φ=0°, r/R=0.7, 0.15D behind propeller plane

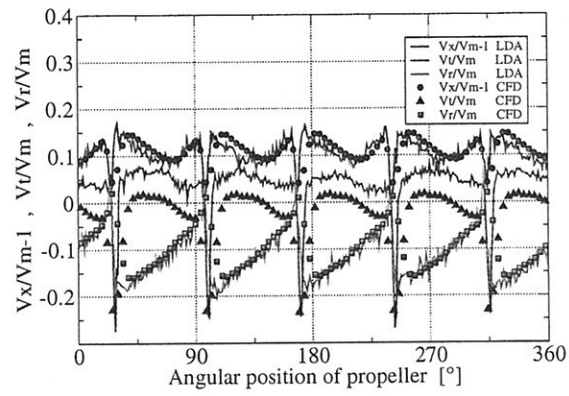

Figure 12: Velocity components, position φ=90°, r/R=0.7, 0.15D behind propeller plane

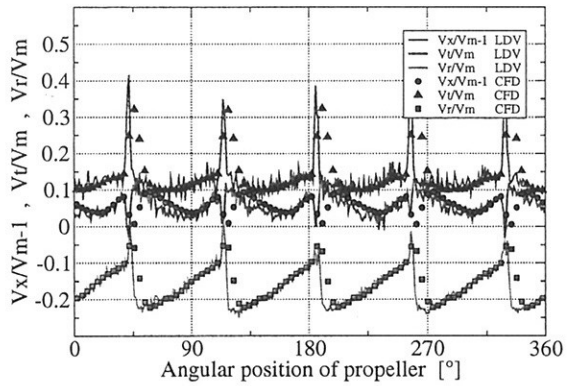

Figure 13: Velocity components, position φ=180°, r/R=0.7, 0.15D behind propeller plane

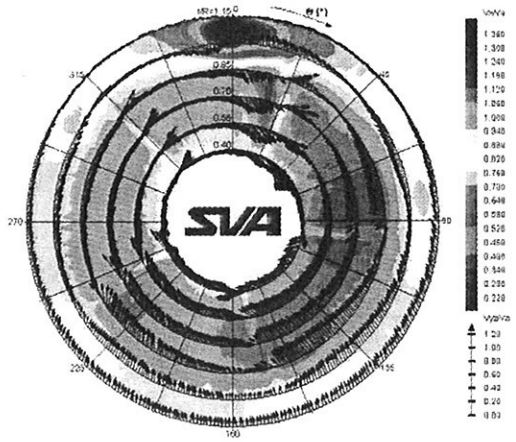

Figure 14: Velocity field 0.15D behind propeller plane for position ϑ=220° of blade1, LDV

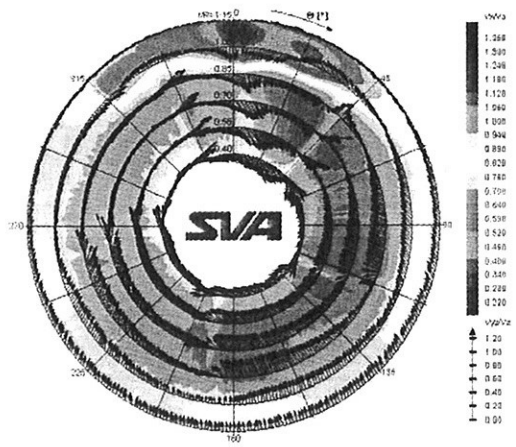

Figure 15: Velocity field 0.15D behind propeller plane for position ϑ=240°, LDV

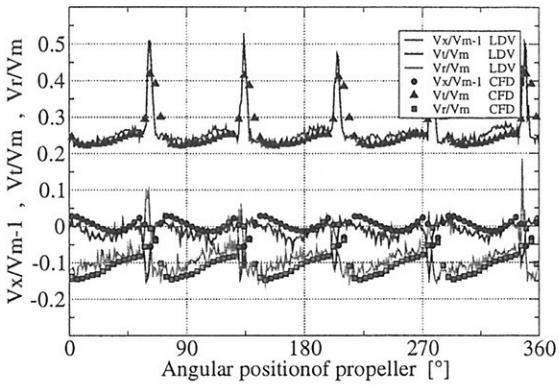

Figure 16: Velocity components, position φ=270°, r/R=0.7, 0.15D behind propeller plane

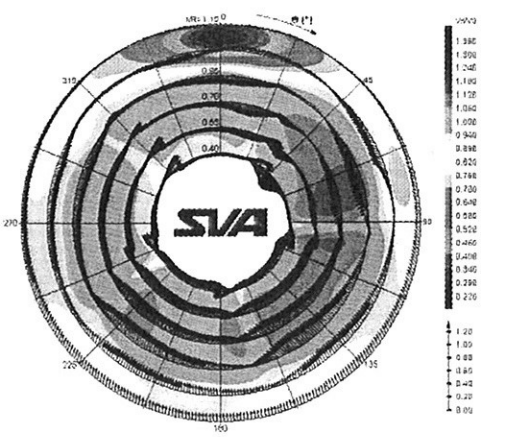

Figure 17: Velocity field 0.15D behind propeller plane for position ϑ=220° of blade1, CFD

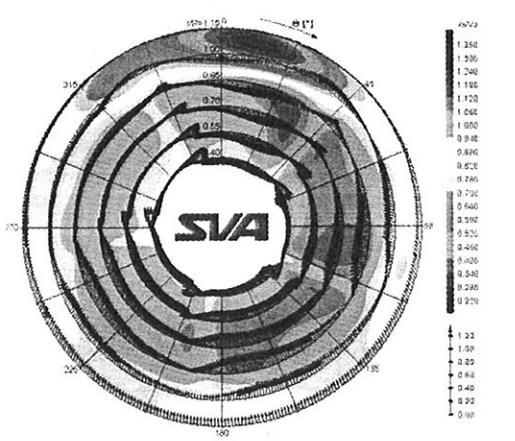

Figure 18: Velocity field 0.15D behind propeller plane for position ϑ=240° of blade1, CFD

TIME ACCURATE SIMULATION OF FREE SURFACE FLOWS IN 2D USING UNSTRUCTURED GRIDS

Tommi Mikkola[1]
Ship Laboratory, Helsinki University of Technology

1 INTRODUCTION

Within the field of computational marine hydrodynamics, there is a growing interest in time dependent flows. Several examples of such flows exist, e.g. unsteady flows around blunt bodies, wave generation of bodies in motion as well as motions and loads of bodies due to waves to name just a few. At the same time, the complexity of the geometries and motions considered is also increasing, setting limits to the applicability of some of the current methods.

A few years ago, a long term basic research on unstructured FVM for the simulation of complex, time dependent free surface flows was started at the Ship Laboratory. First phase of the project focused on the development of a basic 2D flow solver for steady flows without free surface. [7] In the second phase, the emphasis was on the inclusion of the free surface. [9] Recently, the method has been extended for unsteady free surface flows. At the same time, a possibility to model boundaries following a predefined movement was implemented in the solver. This included some necessary improvements to the free surface and boundary geometry treatments as well. The abstract discusses these recently added features, namely the implementation of time accurate solution of the bulk flow and free surface problems as well as the current grid updating routine.

In addition to the discussion on the numerical method, some results for a swaying cylinder submerged to a relatively shallow depth are presented. A more complete set of results for this and other test cases will be presented at the symposium.

2 NUMERICAL METHOD

The numerical method is based on 2D unstructured FVM with triangular control volumes. A collocated SIMPLE-type pressure correction scheme is used for the solution of the bulk flow, with velocities and pressures stored at the cell centres. Free surface flows are simulated using a surface tracking approach. For the present the updating of the grid is based on point movement by spring analogy using linear [1] and torsional springs [2].

Details of the implementation of the bulk flow solver and the general free surface approach can be found in e.g. [7], [8], [9].

2.1 Implementation of time dependency

The simulation of time dependent flows is based on a three level fully implicit scheme (3-LFI) [3]. The method is implemented using dual time stepping, i.e. two time steps – a physical and a pseudo one – are used. This is done by including the physical time derivative terms into the appropriate steady state equations and keeping the pseudo time derivative terms. Within each physical time step, the problem is considered as a steady state problem and is iterated until the pseudo time derivative terms vanish.

For the bulk flow we start with the implicit steady state momentum equations

$$\frac{V\Delta u_i^n}{\Delta\tau} = R_i^{n+1} \,, \tag{1}$$

where V is the volume of the control volume, u_i are the velocity components, τ is the pseudo time, n is the pseudo iteration step and R_i are the residuals of the momentum equations. By including a three level difference approximation for the physical time derivative [3] on the left hand side of this equation, we get

$$\frac{3/2V^{k+1}u_i^{k+1} - 2V^k u_i^k + 1/2V^{k-1}u_i^{k-1}}{\Delta t} + \frac{V^n\Delta u_i^n}{\Delta\tau} = R_i^{n+1} \,, \tag{2}$$

[1]Ship Laboratory, Helsinki University of Technology, Tietotie 1, FIN-02015 Espoo, Finland – E-Mail: Tommi.Mikkola@hut.fi
This work has been funded by the Academy of Finland (project 49846) and the Graduate School in Computational Fluid Dynamics

where t is the physical time and k is the physical iteration step. By approximating the solution at the physical iteration $k+1$ in the future by the solution at the next pseudo iteration, i.e $u_i^{k+1} = u_i^{n+1}$, and by approximating the volume at that time instant by the current volume $V^{k+1} = V^n$, we can write Eq. (2) as

$$\frac{3/2V^n\left(u_i^n + \Delta u_i^n\right) - 2V^k u_i^k + 1/2V^{k-1}u_i^{k-1}}{\Delta t} + \frac{V^n \Delta u_i^n}{\Delta \tau} = R_i^{n+1} \,. \tag{3}$$

Here u_i^{n+1} has been written as $u_i^n + \Delta u_i^n$. Rearranging the terms leads to

$$V^n\left(\frac{3}{2\Delta t} + \frac{1}{\Delta \tau}\right)\Delta u_i^n = R^{n+1} - \frac{3V^n u_i^n - 4V^k u_i^k + V^{k-1}u_i^{k-1}}{2\Delta t} \,. \tag{4}$$

As can be seen from Eq. (4), from the theoretical point of view the changes to Eq. (1) are minor and the implementation of time accuracy in the steady state version is rather straightforward. It is enough to add a single term dependent on the physical time step into the diagonal terms of the momentum equation system and subtract the physical time derivative from the residuals. Of course, in addition to these changes, one has to add storage for the solution at the previous time levels as well as update these values after completion of a physical time step.

Similar treatment applies for the solution of the free surface deformation as well. In the current version of the method, calculation of the wave height is based on the partially coupled kinematic approach [9], [8]. Here the change of wave height is solved from the kinematic boundary condition

$$\frac{\partial h_i}{\partial \tau^{fs}} = u_n n_i \,, \tag{5}$$

where h_i are the components of the wave height defined at the centres of the free surface faces, τ^{fs} is the pseudo free surface time step, u_n is the normal component of the velocity on the free surface and n_i are the components of the outward directed normal vector on the free surface. This can be written in an alternative form:

$$\frac{\partial h_i}{\partial \tau^{fs}} = u_i - u_t \frac{\partial h_i}{\partial s} = R_i^{fs} \,. \tag{6}$$

Here u_t is the tangential velocity on the free surface and s the distance along the free surface.

Similarly to what was done with the solution of the bulk flow, we include the physical time derivative on the left hand side of Eq. (6). This gives us

$$\frac{\partial h_i}{\partial t} + \frac{\partial h_i}{\partial \tau^{fs}} = R_i^{fs} \,. \tag{7}$$

The physical time derivative is again approximated by the three level difference scheme and the pseudo time derivative with a simple two level approximation leading to

$$\frac{3/2\left(h_i^n + \Delta h_i^n\right) - 2h_i^k + 1/2h_i^{k-1}}{\Delta t} + \frac{\Delta h_i^n}{\Delta \tau^{fs}} = R_i^{fs} \,, \tag{8}$$

with the solution at the future physical time approximated similarly to the bulk flow case. By rearranging the terms we get

$$\left(\frac{3}{2\Delta t} + \frac{1}{\Delta \tau^{fs}}\right)\Delta h_i^n = R_i^{fs} - \frac{3h_i^n - 4h_i^k + h_i^{k-1}}{2\Delta t} \,. \tag{9}$$

Previously the free surface solution was based on an explicit Euler scheme, i.e. the residual R_i^{fs} in Eq. (9) was taken as $R_i^{fs,n}$. In the current method, however, a semi-implicit approach [6] is used. Here the spatial derivatives in the residuals

$$R_i^{fs,n+1} = u_i - u_t \frac{\partial h_i^{n+1}}{\partial s} \tag{10}$$

are linearized relative to the previous pseudo iteration, i.e.

$$R_i^{fs,n+1} = u_i - u_t \frac{\partial h_i^n}{\partial s} - u_t \frac{\partial \Delta h_i^n}{\partial s} \,. \tag{11}$$

The last term is approximated with a first order upwind scheme and transfered on the left hand side of Eq. (9). The first and second term on the right hand side are treated as

$$u_i - u_t \frac{\partial h_i^n}{\partial s} = u_n n_i^n \,. \tag{12}$$

The normal vectors n_i^n are calculated at the beginning of each iteration with all the other grid properties. The accuracy of the free surface solution depends on, how the wave height components are transfered into grid point locations for the calculation of these surface normals. This is discussed in more detail later.

The equation system is created by the inclusion of the residual (11) into Eq. (9) in place of R_i^{fs}. The resulting system is solved with a predefined number of Gauss-Seidel iterations. The semi-implicit free surface treatment is not restricted to time dependent simulations, but can be used for steady state simulations as well.

2.2 Grid updating

The steps for the update of the grid at each iteration are listed below.

1. Update the boundary geometry.
    a. At the start of every pseudo iteration, the free surface geometry is updated by adding the change of wave height components to the previous values.
    b. At the start of every physical time step, time dependent boundaries are updated by updating the respective geometry definitions.
2. Search for the new intersections of each boundary based on the updated geometry definitions.
3. Redistribute the grid points on the updated geometries based on the new intersection points and the original point distribution.
4. In case of rigid movement (rotation or translation), move all boundary grid points in the opposite direction (only at the start of a physical time step).
5. Update the grid by solving the equilibrium equations for the linear/torsional spring system.
6. In case of rigid movement, perform the movement for the whole grid (only at the start of a physical time step).
7. Check the quality of the updated grid and try to perform diagonal swap for "bad" elements if necessary.

Because of steps 4 and 6, rigid transformations are actually performed in a coordinate system fixed to the body. This ensures, that the grid points close to the moving body are not translated or translated only slightly by the spring system and helps to preserve the original quality of the grid close to the body even in cases of large body movements. However, the approach as such only applies to cases, in which there is just a single body. In case of several bodies, some kind of weighting could be applied (see e.g. [4]). It should also be noted, that transformations are performed only at the start of each physical time step. During the pseudo iterations, from the point of view of grid updating, moving boundaries are stationary and only free surface boundaries are deforming.

The implementation of step 3 for free surface boundaries differs from the treatment for all the other boundaries. For the other boundaries the approach is straigthforward. The geometry definition of a particular boundary is traversed through from the intersection point at the start to the intersection point at the end of the patch inserting grid points on the boundary based on the original point distribution. For free surface points, additional steps are required. This is due to the fact, that the accuracy and the stability of the free surface solution depends on the way the free surface grid points are determined.

Free surface treatment is started by defining the free surface as a set of cubic splines based on current wave height coordinates. After this, the wave heights are redistributed on the splines based on the original distribution at the start of the calculation. The actual grid points are then determined by upwinding in the normal direction and averaging in the tangential direction of the surface. For a particular grid point this means, that the neighbouring wave heights (two on both sides) are first transfered to a coordinate system fitted to the surface. The normal coordinate of the grid point is determined with a MUSCL [12] scheme and the tangential coordinate by taking a weighted average of the tangential components of the closest two wave heights. As a last step, the grid point coordinates are transfered to the original coordinate system.

The quality of the deformed grid is checked by calculating the ratios of the circumradius and inradius of each element and comparing these to a threshold value. If the ratio is above the threshold value, the element is marked for further processing. After all the elements are checked, a diagonal swap [5] (see Fig. 1) is performed for those sides of the grid, which have a marked element on either or both sides, if it improves the quality of the elements.

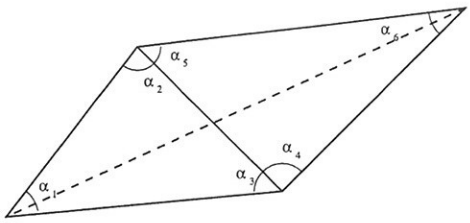

Figure 1: Diagonal swapping between neighbouring elements.

Grid velocities are calculated at the start of each iteration from the geometrical conservation law based on the areas swept by the edges of the triangles during the movement. To be consistent with the momentum equations, a three level scheme derived from the same equations is used. [3] The velocities obtained are then used for the calculation of the convection velocities in the momentum equations.

3 TEST RESULTS

As a simple test case a submerged cylinder swaying close to the free surface [11] is considered. The cylinder has a diameter D of 30.5 cm and is submerged to a depth $h/D = 0.75$, where h is the distance from the free surface to the axis of the cylinder (see Fig. 2). The amplitude to diameter ratio A/D of the swaying motion is 0.033. The motion of the cylinder is defined by

$$x(t) = A\sin(\omega t) \ , \tag{13}$$

where ω is the angular frequency. The results are shown for two frequencies, where the non-dimensional frequency parameter $\omega^* = \omega\sqrt{D/(2g)}$ is 1 and $\sqrt{2}$. The density of the water is taken as 1000 $\mathrm{kg/m^3}$ and the molecular viscosity as 1.13×10^{-6} $\mathrm{m^2}/s$.

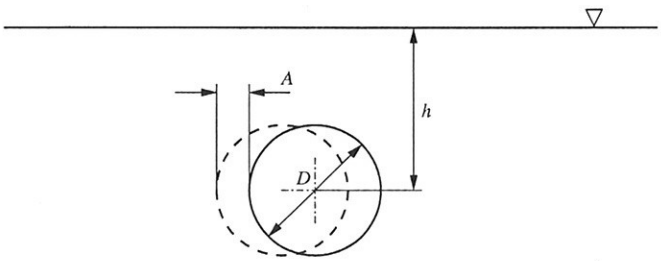

Figure 2: Schematic of the test case.

For the simulations, a grid with approximately 18 700 elements is used. The grid has 384 elements of equal size on the cylinder and 471 elements on the free surface. The size of the smallest free surface element, located directly above the cylinder is 0.01 m. The free surface grid size is increased linearly towards the external boundaries in two intervals. At 4.0 m from the cylinder the size of the element is approximately 0.04 m and 2.0 m at the boundaries. The external boundaries are located at 30.0 m. From 4.0 m onward, MUSCL upwinding in the free surface treatment is replaced with first order upwinding. The physical time step $\Delta t = T/50$, where T is the period of the motion.

Fig. 3 shows the non-dimensional time histories of the horizontal and vertical forces on the cylinder for the two frequencies. These are defined as $F/(\rho g r^2)$, where r is the radius of the cylinder. A start-up transient can be seen at the beginning of both cases and a quasi-steady state is reached during the third period. By performing Fourier analysis for the quasi-steady part of the horizontal force history, we get the added mass coefficient μ_{11} and the linear damping coefficient λ_{11}. In the following, non-dimensional coefficients, defined as $\mu^*_{11} = \mu_{11}/(\rho\pi r^2)$ and $\lambda^*_{11} = \lambda_{11}\sqrt{r/g}/(\rho\pi r^2)$, are used.

For the lower frequency the added mass coefficient is around 0.49. For comparison, Yeung's and Wu's vorticity-diffusion theory [13] gives approximately 0.49 and Seah's and Yeung's free surface random vortex method (FSRVM) [11] approximately 0.60. The latter one of these is supposed to be more accurate and thus the current results seem to underpredict the added mass coefficient. For the linear damping coefficient at the lower frequency the computation gives 0.34, compared to 0.35 and 0.29 for the vorticity-diffusion theory and FSRVM respectively. Damping is thus overpredicted slightly compared to FSRVM.

For the higher frequency, the added mass coefficient is 0.62. The coefficient lies again between the ones for

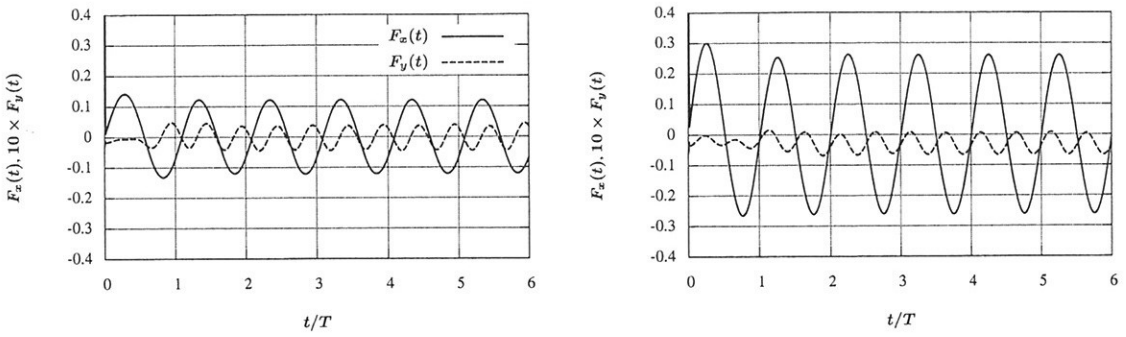

Figure 3: Horizontal and vertical force histories: left $\omega^* = 1$, right $\omega^* = \sqrt{2}$.

vorticity-diffusion theory and FSRVM as they give 0.61 and 0.65 respectively, showing slight underprediction compared to FSRVM. For the linear damping term both the vorticity-diffusion theory and FSRVM give a value between 0.04 and 0.05. The average for the current method is 0.055, and linear damping is thus overpredicted marginally compared to both methods.

Fig. 4 compares wave profiles at two time instants, namely at the beginning of the sixth period and halfway through it. Close to the cylinder, the wave profiles should be mirror images of each other. The computed results agree well with this assumption. It can also be seen, that higher frequency results into a shorter wave length and a smaller amplitude of the waves.

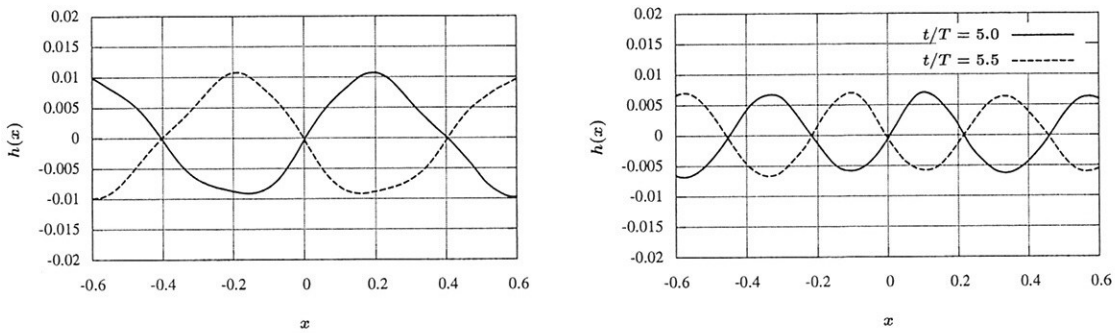

Figure 4: Wave profiles at two time instants: left $\omega^* = 1$, right $\omega^* = \sqrt{2}$.

Further testing of the method is required before drawing any far reaching conclusions on the accuracy of the method. Currently tests are being run for an FPSO with bilge keels in forced roll motion [10], [11]. However, preliminary results for this case suggest, that compared to FSRVM results by Seah and Yeung linear damping is overpredicted also in this case. Another potential test case is the heaving wedge benchmark case of the ISOPE 2nd Numerical Wave Tank Workshop for its extensive set of reference data.

REFERENCES

[1] BATINA, J. T. Unsteady euler algorithm with unstructured dynamic mesh for complex-aircraft aerodynamic analysis. *AIAA Journal 29*, 3 (1991), 327–333.

[2] FARHAT, C., DEGAND, C., KOOBUS, B., AND LESOINNE, M. Torsional springs for two-dimensional dynamic unstructured fluid meshes. *Computer methods in applied mechanics and engineering 163* (1998), 231–245.

[3] HOFFREN, J. Unsteady Navier-Stokes simulations of airfoil flows. In *Numerical Methods in Laminar and Turbulent Flow*, C. Taylor, Ed., vol. VIII. Pineridge Press, 1993, pp. 1065–1076.

[4] LEROYER, A., AND VISONNEAU, M. Moving bodies in viscous flow simulation. In 6^{th} *Numerical Towing Tank Symposium* (Rome, Italy, 2003), V. Bertram, Ed.

[5] MAVRIPLIS, D. J. Adaptive Mesh Generation for Viscous Flows Using Delaunay Triangulation. *Journal of Computational Physics 90*, 2 (1990), 271–291.

[6] MIKKOLA, T. Implementation of an implicit scheme into a free surface RANS solver in order to improve the convergence. Tech. Rep. M-257, Helsinki University of Technology, Ship Laboratory, 2000. Master's Thesis.

[7] MIKKOLA, T. Development of an unstructured pressure-correction solver based on triangle meshes. In 5^{th} *Numerical Towing Tank Symposium* (Pornichet, France, 2002), G. Delhommeau and M. Visonneau, Eds., Ecole Centrale de Nantes.

[8] MIKKOLA, T. Development and application of an unstructured finite volume solver for free surface flows in 2D. In 6^{th} *Numerical Towing Tank Symposium* (Rome, Italy, 2003), V. Bertram, Ed.

[9] MIKKOLA, T. Numerical simulation of free surface flows in 2D with unstructured finite volume based pressure correction method. In *VIII Finnish Mechanics Days* (Espoo, Finland, 2003), P. Råback, K. Santaoja, and R. Stenberg, Eds.

[10] NA, J. H., LEE, W. C., SOO, S. H., AND KYU, P. I. A design of bilge keels for harsh environment FPSOs. In *Proceedings of The Twelfth (2002) International Offshore and Polar Engineering Conference* (Kitakyushu, Japan, 2002), pp. 114–117.

[11] SEAH, R. K. M., AND YEUNG, R. W. Sway and roll hydrodynamics of cylindrical sections. *International Journal of Offshore and Polar Engineering 13*, 4 (2003), 241–248.

[12] VAN LEER, B. Towards the Ultimate Conservative Difference Scheme V: A Second-Order Sequel to Godunov's Method. *Journal of Computational Physics 32* (1979).

[13] YEUNG, R. W., AND WU, C.-F. Viscosity effects on the radiation hydrodynamics of horizontal cylinders. *International Journal of Offshore Mechanics and Arctic Engineering 113* (1991), 334–343.

Grid Generation for Ships and Propellers

Christian Nienhüser
ANSYS Germany GmbH
Christian.Nienhueser@ansys.com

Marco Schneider
ANSYS Germany GmbH
Marco.Schneider@ansys.com

Introduction

Various marine CFD-applications involve complex geometries like ship hulls, propellers, rudders etc. Usually for these applications viscosity effects play an important role and very fine meshes near the walls are required to resolve the boundary layer sufficiently.
These requirements together with the complex geometries make the grid generation for marine CFD-applications a time consuming task that is usually the bottleneck within the simulation-process. Furthermore an experienced user is required to assure the required grid-quality.
In this paper mesh generation techniques will be presented that simplify the mesh generation process for marine CFD-applications and at the same time assure the quality that is necessary to achieve reliable results.

Meshing Approaches

There are several different meshing approaches. Block structured grids are widely used since they combine the possibility to use cells with high aspect ratios together with good flexibility for complex geometries. ICEM CFD Hexa provides a block structured interactive top-down tool that is very flexible and powerful. However for complex geometries this tool requires an experienced user. To make the tool also available for occasional users a Ship-Topology Library was created within the framework of a BmBF project of Hamburgische Schiffbau-Versuchsanstalt and ANSYS Germany GmbH (former CFD & Structural Engineering GmbH). The library is presented in the next chapter. Figure 1 shows the block structured mesh of a single screw ship including the rudder and propeller.

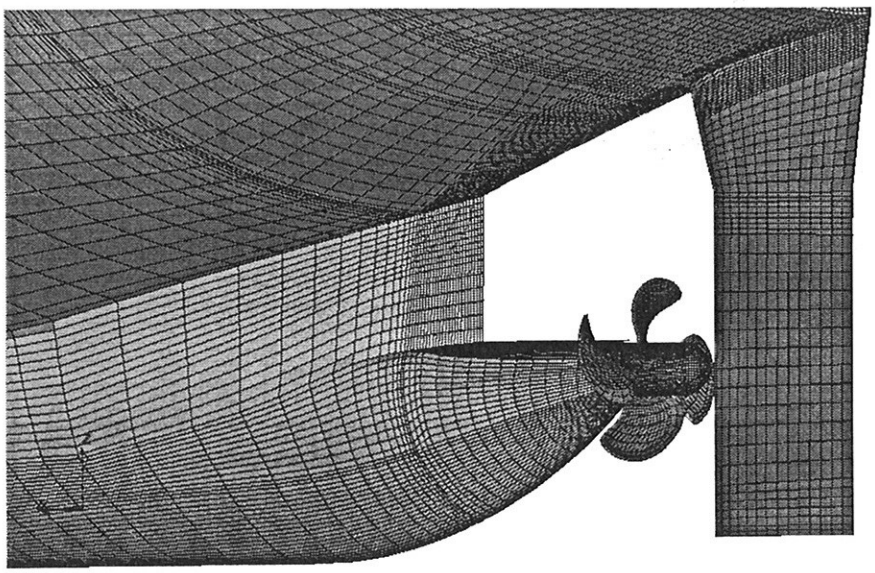

Figure 1: Block structured grid of a ship

Unstructured meshes are more flexible for complex geometries and require far less user input.
ICEM CFD Tetra divides the solution domain into tetrahedral elements that are cut and projected to the surface afterwards. This method is very flexible and robust to bad CAD-Data. The resolution of the boundary layer, which requires high aspect ratio cells, is achieved by prismatic layers at the walls.

Quad and tetra surface meshing together with the possibility to extrude the surface-meshes into the volume provides another meshing tool for complex geometries. The remaining volume can be meshed with tetrahedral or a combination of tetrahedral and hexahedral elements.

Ship-Topology Library

Within a BmBF project of Hamburgische Schiffbau-Versuchsanstalt and ANSYS Germany GmbH (former CFD & Structural Engineering GmbH) blocking templates were created that can be used to mesh a large number of ship-types. These templates are designed for single-screw ships with and without bulbous bow, twin-screw ships with skeg and bulbous bow and can be extended to other ship-types.
In order to makes the templates suitable for a large number of ships the rudder, pod and the propeller are meshed with separate templates stored in sub-topologies. The different parts get later connected with general grid interfaces (GGI). This approach also enables the user easily to change the propeller and rudder and to modify the rudder angle.

The propeller itself is a cyclic periodic part and only one blade is meshed. Copying and rotating the original topology template generates the complete topology. A picture of a propeller template is shown in Figure 2.

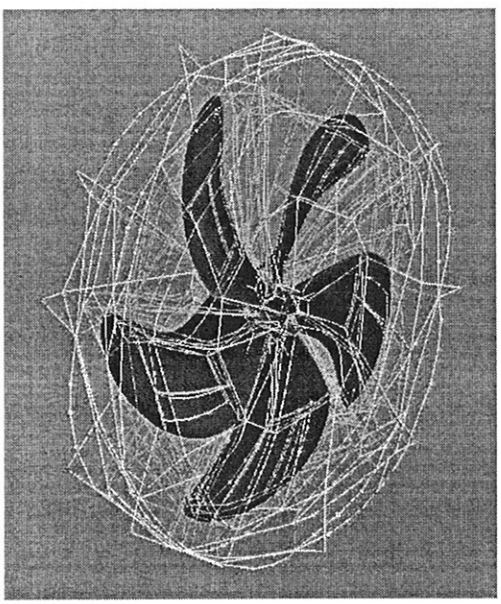

Figure 2: Complete blocking for propeller

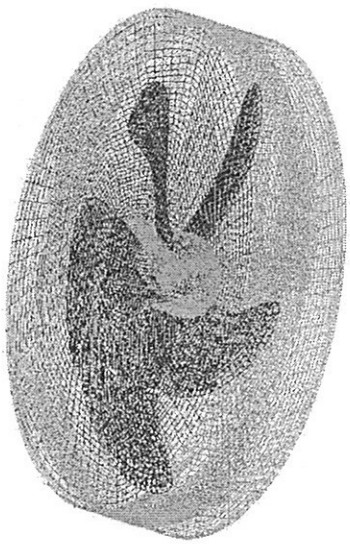

Figure 3: Propeller grid

Mesh Smoothing

The quality of the generated mesh can be improved with mesh-smoothing algorithms. These efficiently enhance the mesh quality with few user input and can be used to obtain better grid angles and smooth transitions.

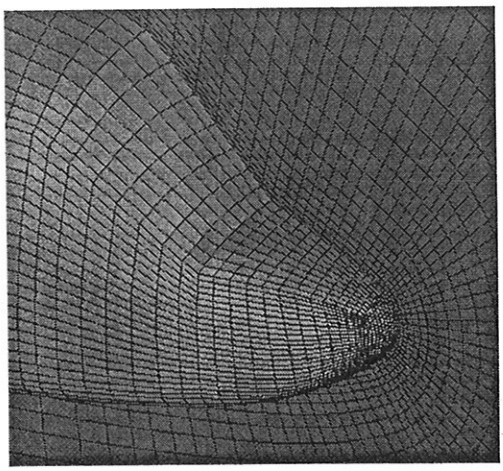

Figure 4: Grid before smoothing

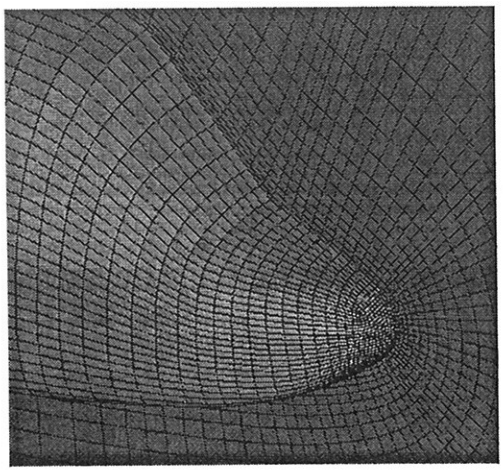

Figure 5: Grid after smoothing

CAD-Repair

The quality of the CAD data frequently doesn't satisfy the requirement of grid generation tools. Often the user has no access to the original CAD-date or the CAD-tool. With repair tools the geometry can be simply modified, holes and small buttons or features removed and surfaces re-approximated.

References

[1] D. Hafermann, R. Steberl, B. Brasas, "*Effiziente Gittererzeugung für maritime RANSE-Berechnung mit hohen Ansprüchen an die Gitterqualität*", HSVA Bericht Nr. CFD 25/02

Numerical Investigation of Scale Effects of the Wake Equalizing Duct

Jil-Pyo Ok *
Technical University of Hamburg-Harburg

2nd September 2004

1 Introduction

Schneekluth's wake equalizing duct (WED) is a ring-shaped nozzle fitted to a single-screw ship hull in front of the upper half of the propeller in order to reduce the required propulsion power and the propeller-induced vibrations [3, 9] (See Fig. 1).

With the exception of Grim's vane wheel, the concept and the layout of various energy saving devices in ships, including Schneekluth's duct, is largely a matter of experience based on model tests. Often the reason for the energy saving is not clearly understood. The accuracy of full-scale tests is, normally, not high enough to show unequivocally the difference in required power for the ship with and without such devices. Thus one has to rely on model experiments. However, because the Reynolds number of ship model experiments is, typically, two orders of magnitude smaller than that of the full scale ship, the scale effect has to be estimated. A prerequisite for this is to understand the reason for any power saving: Whereas effects of flow viscosity are strongly influenced by Reynolds number, potential flow effects are not.

An extensive experimental test of a so-called E3 tanker hull [11] with and without Schneekluth's duct was performed in the HYKAT (Hydrodynamics and Cavitation Tunnel) in HSVA by Johannsen [2, 6]. Also resistance and propulsion tests in HSVA's towing tank were performed for the same model. Due to the limits of the (quite large) test facility the experiments were performed only in a narrow range of relatively low Reynolds numbers.

Much larger Reynolds numbers can be applied in numerical flow computations. This was the main reason for using numerical flow computations for this investigation, which concentrates on scale effects in Schneekluth's ducts. Another reason is the hope that computations which differ only in small details, e.g. flow around hulls with and without a duct, will show very similar errors, so that the difference between the conditions with and without duct will be resolved better by computations than by model experiments, even if the total error of computations may be larger than that of model experiments.

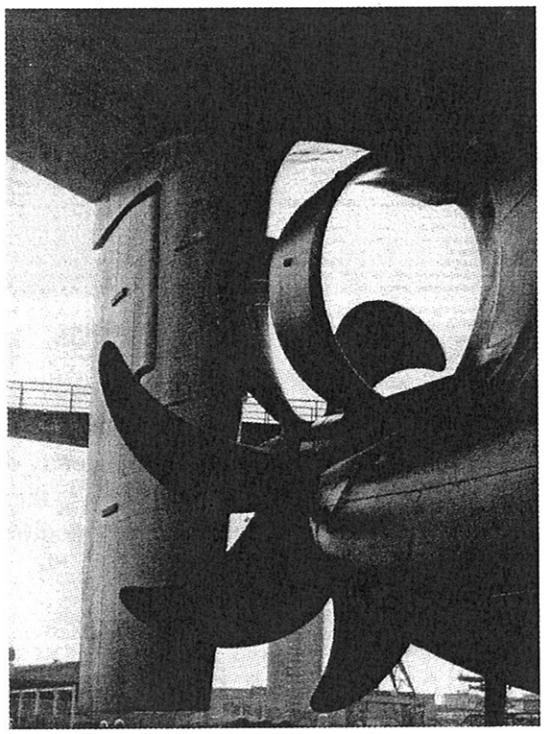

Figure 1: Schneekluth's Duct (Photo from HDW)

In this investigation the forces and the flow fields around the ship hull with and without Schneekluth's duct are computed and compared with each other for 7 different Reynolds numbers (ship speeds). For the computations the viscous-flow code Comet, which solves the Reynolds-averaged Navier-Stokes equations (RANSE) by means of a finite-volume-method, is used. Wave-making is suppressed in the computations by applying a symmetry condition at the undisturbed free water surface. This corresponds to the experiments in the HYKAT were a rigid plate was used to suppress any waves.

The ship is simulated in steady forward motion. The propeller is not modeled as a rotating body; its effect on the flow is taken into account by applying appropriate, time-invariant forces in x-direction on the fluid cells within the propeller disc.

*jil-pyo.ok@tuhh.de

2 Numerical Methods

Here the RANSE-solver Comet [5] was used, which was developed by Peric and his collaborators (see Muzaferija *et al.* [4]). Comet uses the finite-volume method with control volumes (cells) having an arbitrary number of faces. For each cell the scalar continuity (mass conservation) equation, a vector momentum equation and two scalar turbulence equations have to be satisfied. The fluid is assumed here to be incompressible. For more details about the RANS equations, the finite volume method and the turbulence model see Ferziger and Peric [7].

The Ship Model

E3 Tanker As mentioned above the E3 tanker is chosen as example. It has a block coefficient $C_B = 0.83$. The hull form is typical for a modern VLCC (very large crude carrier). Table 1 gives the principle dimensions.

	unit	Full Scale	Model Scale
Length L_{PP}	m	318.0	6.989
Breadth	m	57.0	1.253
Draft	m	20.9	0.459
Displacement	m^3	314,000	3.333
Wetted Surface	m^2	27711	13.385
D_{PROP}	m	9.8	0.215
Design Speed	m/s	8.025	1.19
R_n	-	$0.255 \cdot 10^{10}$	$0.832 \cdot 10^7$
$log_{10}(R_n)$	-	9.407	6.920

Table 1: Principle Dimensions of the E3 Tanker

The Froude number of the ship F_n at design speed is 0.143. As shown in Fig. 2 the ship has a bulbous bow with elliptical cross-sections and a transom stern.

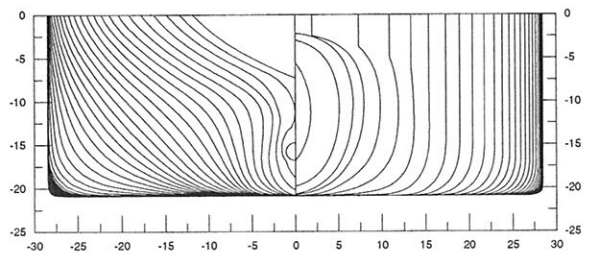

Figure 2: Lines Plan of the E3 Tanker

Geometrical Properties of Duct Variants To investigate effects of the geometrical parameters of the duct on the propulsion performance of the ship, 6 duct variants are considered. The geometrical parameters of each variant are shown in Table 2. Fig. 3 explains the symbols R_{IN}, R_{OUT} and d_{SFT}. The length of all ducts is 2.9m.

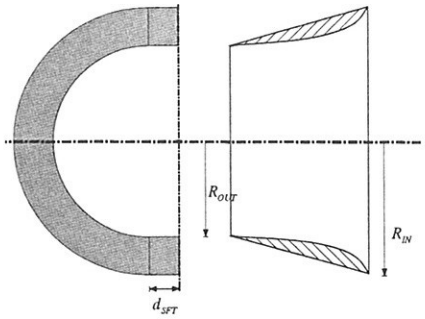

Figure 3: Geometric Parameters of Duct Variants

Duct	D1	D2	D3	D4	D5	D6
R_{IN} [m]	2.6	2.6	2.8	2.8	3.0	3.8
R_{OUT} [m]	2.1	2.1	2.1	2.1	2.1	2.8
d_{SFT} [m]	0.0	1.65	0.0	1.65	1.65	2.0

Table 2: Geometric Parameters of Duct Variants

Numerical Propulsion Model

To reduce the required CPU time to values suitable for investigating numerous alternatives, the propeller had to be modeled in a simplified manner by applying external longitudinal forces on the fluid volumes within the propeller disk. This allows a stationary computation confined to one half of the symmetrical flow field.

The force distribution over the propeller disc was assumed constant in circumferential direction; in radial direction the distribution function $F_B(r)$ used by Starke [1] was applied also here:

$$F_B(r) = T \cdot f_B(r) \tag{1}$$

where,

$$f_B(r) = \alpha \frac{r}{R_P} \sqrt{1 - \frac{r}{R_P}} \tag{2}$$

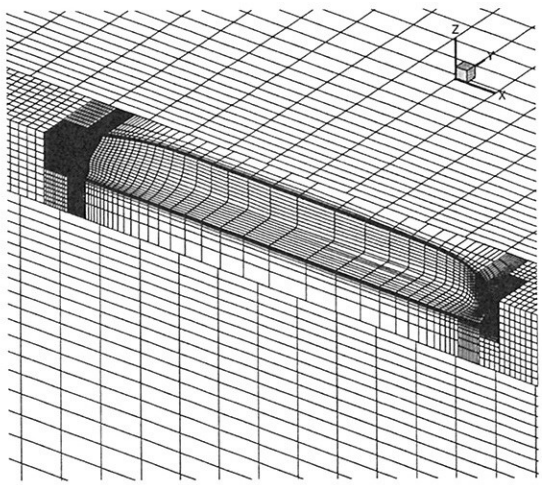

Figure 4: Numerical Grids

such that

$$\int_{A_P} f_B(r) dA_P = 1 \tag{3}$$

Here α_T is a constant which is adapted to obtain the required total force. R_P is half the propeller diameter, and r is the radial coordinate. The number of cells within the propeller disc was $N_\theta \cdot N_r \cdot N_x = 25 \cdot 15 \cdot 3$.

Grid Generation

The commercial grid generating program GridGen [10] was used here to generate block-structured three-dimensional grids. Grid fairness was achieved by using a Poisson solver [8, 12]. Also for the grids on the boundary surfaces the Poisson solver was applied. The tolerance for solving (by iteration) the Poisson equations was 10^{-3}. Normally about 30 to 40 iterations were required. In the resulting grid the spacing between cells changes smoothly. The number of fluid cells was about 1.8×10^5 for cases without a Schneekluth duct, and 2×10^5 for cases with duct. Except for the blocks surrounding the duct the block structure and geometry were identical for all variants investigated.

3 Computational Results

3.1 Simulation of Resistance Tests

Resistance Coefficient

The resistance of the E3 tanker was computed for 7 Reynolds numbers (speeds) for the model without duct called "Model-0" and with each of the 6 duct variants called "Model D1" to "D6". In Fig. 5 the resistance coefficient of Models D1 to D6 is compared with that of Model-0 (without duct). The figure shows:

- For all duct variants, the ducts cause an additional resistance of up to 10% (often $\approx 3\%$). The larger values correspond to the larger duct entrance diameter.
- The absolute difference of the resistance coefficients with and without duct increases a little with increasing R_n; the relative difference increases noticeably.

The frictional resistance of the models with and without duct is practically the same; the additional resistance of the duct is thus a pressure resistance. The surface of the duct is negligible ($\approx 0.2\%$) compared to the wetted surface area of the ship. The larger duct resistance coefficient for higher R_n is held to be due to the fact that, for higher R_n, less of the duct is immersed within the hull boundary layer.

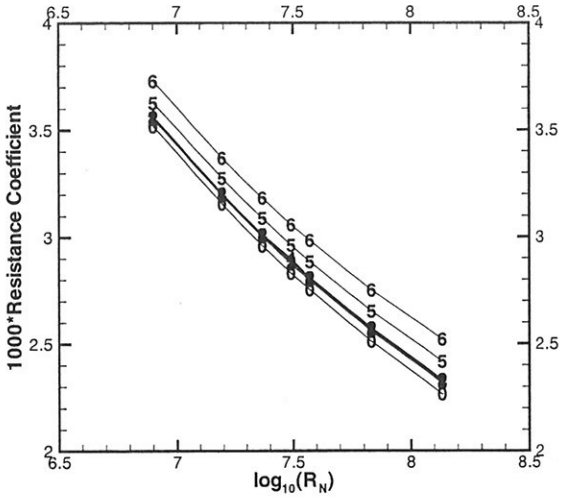

Figure 5: Resistance Coefficient

Nominal Wake Fraction

To compare the flow in the propeller disc with and without duct, the average relative axial speed of the fluid in the propeller disc can be considered. It is defined as

$$\bar{u} = \frac{1}{A_P} \int_{A_P} \frac{u(r,\theta)}{U} dA = 1 - w_n \tag{4}$$

A_P denotes the area of the propeller disc excluding the nozzle.

In Fig. 6 the average relative axial speed of all duct variants is shown. As results, Model-0 (without Duct) has the highest $\bar{u}$. This may seem unexpected: The duct is intended to produce an *in*crease in axial flow velocity behind it, which would necessarily be associated with a decrease of axial flow velocity farther outward. The water flowing through the duct passes also through the propeller disk and is thus accounted for in the wake fraction, whereas of the water flowing outside of the duct only a certain part flows through the propeller disc and has thus influence on the wake fraction. Thus the expected velocity increase behind the duct should dominate, producing a higher $\bar{u}$ for the ship with duct. But Fig. 6 shows just the opposite duct effect.

This contradiction is due to a wrong estimation of the duct effect. Looking to the profile of a duct with its axis in the direction of the flow, one notices that the pressure side of the profile is the interior side, and owing to the higher interior than exterior pressure the flow velocity is lower inside and higher outside of the duct. The same result is observed if one substitutes the duct by a ring vortex: To account for the smaller aft than forward diameter of the duct, the vortex must move the fluid radially outside in front of the duct and

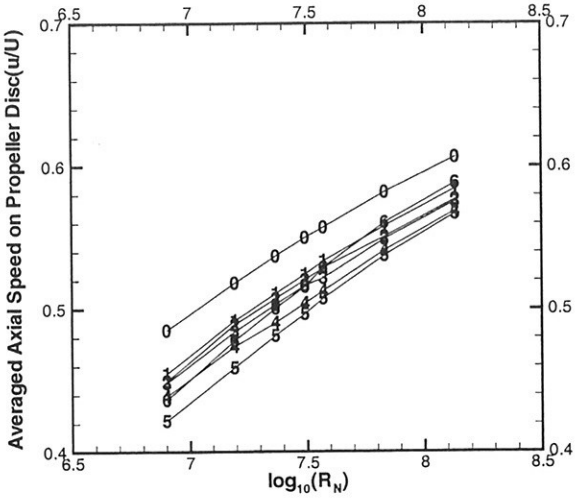

Figure 6: Average Relative Axial Speed on Propeller Disc

inward behind the duct. Inside the duct the velocity induced by the ring vortex is opposite to the inflow velocity. Thus the duct has just the opposite effect as expected by its inventor Prof. Schneekluth. Because it is fitted in the range of the propeller disc where the inflow velocity is small, it decreases this small velocity even more, acting thus not as a *wake equalizing duct*, but oppositely.

The error may be due to the expectation that, at the inlet of the duct, the inflow velocity is assumed to be, approximately, the same as without a duct. Then, due to the smaller duct diameter at its aft end, the flow would be accelerated behind the duct. However, in reality the inflow to the duct is substantially decreased compared to the case without duct; this more than compensates the flow acceleration within the duct.

3.2 Simulation of Self-Propulsion Tests

Procedure of Simulation of Self-Propulsion Tests

The propeller thrust T required to move a ship is generally larger than the resistance R_T of the ship, i.e. the fluid force in $-x$ direction determined for the model without propeller. The required thrust is calculated here by integrating the pressure and friction forces acting on the ship hull and its appendages. Because especially the pressure in the afterbody depends on the propeller action, the self-propulsion condition was attained in the following way (see Fig.7);

1. A calculation with no propeller force applied gave the resistance.

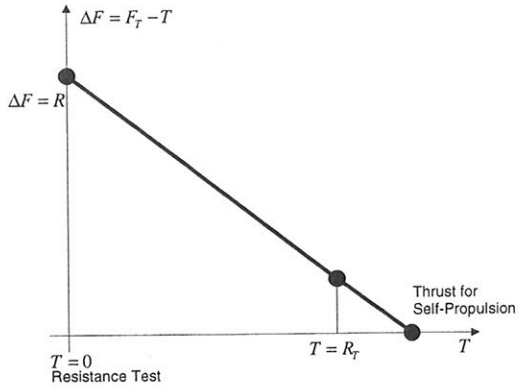

Figure 7: Extrapolation Approach to find the Thrust for Self-Propulsion

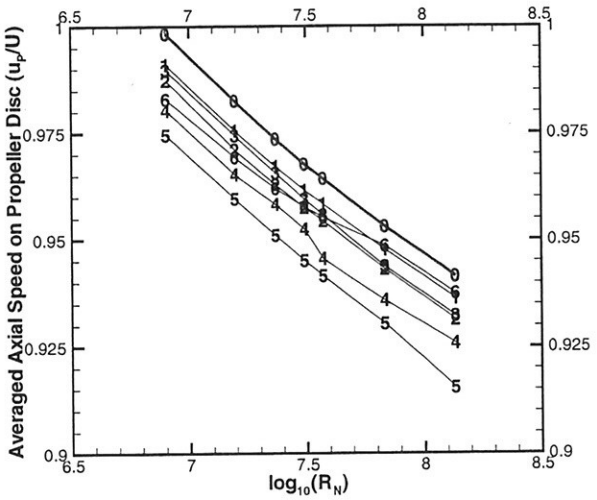

Figure 8: Comparison of Axial Relative Flow Speed

2. A calculation with a propeller force equal to the resistance gave a larger hull longitudinal force F_T.

3. The difference between hull longitudinal force and applied propeller force was extrapolated linearly over the applied propeller thrust. The difference becomes zero at the propeller thrust T in he self-propulsion condition.

For some cases, test calculations have been performed with the propeller force T as determined under 3 above. They showed that the hull longitudinal force was equal to T with errors much smaller than 1%. Thus T corresponds indeed to the self-propulsion condition. This linear relation between the thrust and the rest force is also found in model experiments [2].

Axial Relative Flow Speed and Velocity Distribution under Self-Propulsion

To characterize the average longitudinal flow speed within the propeller disc area A_P excluding the hub

area, the average relative speed of flow in the propeller disc $\bar{u}_P$ is used. It is defined as

$$\bar{u}_P = \frac{1}{A_P} \int_{A_P} \left(\frac{u_P(r,\theta)}{U} \right) dA \tag{5}$$

with U = ship speed, u_P = axial component of flow speed, including the propeller induced flow, in the centers of the central sheet of fluid cells within the propeller volume.

- The average axial speed $\bar{u}_P$ decreases with increasing Reynolds number due to the smaller nondimensional propeller thrust required for higher R_n. This result is opposite to that of the resistance test simulations.
- The ducts decrease the average axial flow speed like in the resistance test simulations.

Figures 9(a) (for the low R_n) and 9 (b) (for the high R_n) show the flow velocity distribution in the propeller plane for the model without duct and with duct D4. Also here the effect of the duct is visible: it decreases the axial velocity behind the duct, and increases it outside of (especially below) the duct.

3.2.1 Power Requirement

The main purpose of Schneekluth's ducts is to reduce the required propulsion power. To compare the propulsion power requirement of the variants, the power exerted by the thrust force on the fluid is considered:

$$P_{RQ} = \int_{A_P} F_B(r) \cdot u_P(r,\theta) dA \tag{6}$$

where $u_P(r,\theta)$ is the axial component of the flow speed in the central sheet of propeller cells. u_P includes the propeller-induced velocity. For the thrust distribution function $F_B(r)$ see Eq. 1. The actual power requirement will be higher than P_{RQ} because the latter does not include frictional losses of the propeller, losses due to circumferential variations in induced speed, and losses due to the rotational energy transferred to the propeller slipstream. Because these effects are hardly influenced by the presense or absense of a duct, P_{RQ} appears as a nearly perfect quantity to compare the propulsion power requirements of the various duct alternatives.

Again, to obtain a non-dimensional quantity, P_{RQ} is divided by the effective power P_E^0 (= resistance times speed) of the variant without a duct. This ratio is called nondimensional power requirement K_{RQ}:

$$K_{RQ} = \frac{P_{RQ}}{P_E^0} \tag{7}$$

where

$$P_E^0 = R_T^0 \cdot U \tag{8}$$

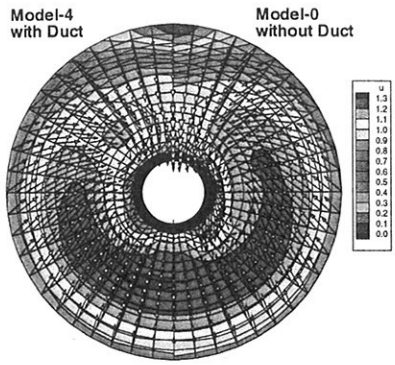

(a) Low R_n

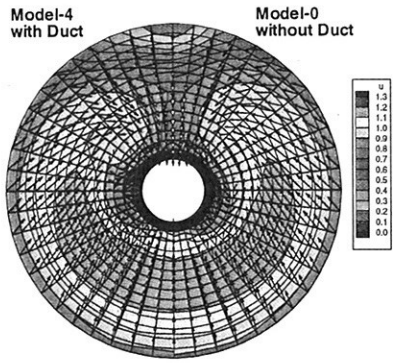

(b) High R_n

Figure 9: Comparison of Velocity Distribution

In Fig. 10 K_{RQ} is plotted for all variants. The figures show:

- The nondimensional power requirement decreases with increasing R_n. This is caused by the decreasing frictional resistance coefficient which leads to a lower propeller loading and, thus, higher propeller efficiency for larger R_n.
- Ducts 5 and, even more, 6 have a severe unfavourable effect. Duct 4 appears best.
- Whereas for low R_n duct 4 reduces the power requirement by about 1% compared to the model without duct, the other ducts have no effect, or they *increase* the required power.
- For higher R_n all ducts are disadvantageous: If the bad duct models 5 and 6 are excluded, the ducts increase the required power by 2 to 3% for the largest R_n investigated.

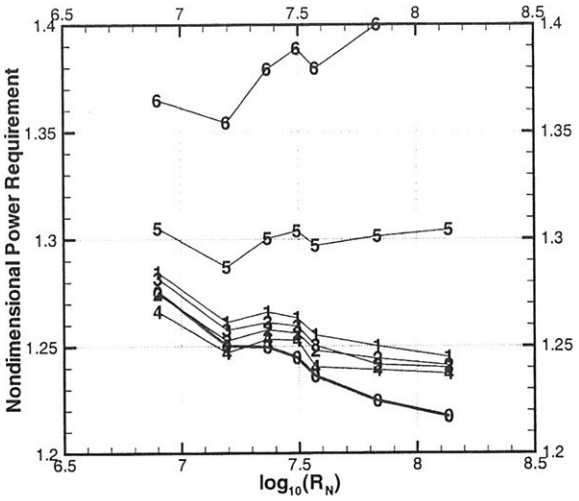

Figure 10: Comparison of Nondimensional Power Requirement

4 Summary and Concluding Remarks

Using a full tanker (block coefficient $C_B = 0.83$) as an example, the effects of 6 different Schneekluth's ducts on the ship resistance and propulsion were numerically investigated using the RANSE code Comet. The free surface was substituted by a symmetry plane, and the propeller was substituted by longitudinal forces acting on the fluid cells within the volume swept by the propeller. The required propulsion power was estimated indirectly by comparing the energy flow transferred to the fluid by the propeller longitudinal forces.

- The duct has hardly any effect on the ship resistance ($\ll 1\%$ resistance increase). Contrary to the expectations of Schneekluth and some other authors dealing with these ducts, the duct *decreases* the longitudinal flow velocity of the water flowing through it, while the water flowing outside of the duct is accelerated by a small amount.

- The lower flow speed and the higher required thrust cause an increase in the nondimensional propeller loading and, accompanied with the higher loading, a lower propeller efficiency. Thus, in the absence of viscous effects the duct, producing a smaller average flow speed in the propeller circle, is expected to *increase* the required propulsion power.

- For the lowest Reynolds number investigated, duct 4 produces a small reduction ($\approx 1\%$) of the required propulsion power compared to the ship without duct.

- Beyond $R_n > 20 \cdot 10^6$, however, the duct has the opposite effect: For the highest $R_n = 130 \cdot 10^6$ the ship with duct requires about 2% more power than that without a duct. Obviously the non-viscous flow effects dominate for higher R_n. Because a real tanker operates at still higher $R_n \approx 2000 \cdot 10^6$, the duct will not reduce but increase the required propulsion power.

References

[1] Starke; A validation study of wake-field predictions at model and full scale reynolds numbers. In *4th Numerical Towing Tank Symposium Hamburg*, 2001.

[2] Johannsen; Untersuchung der Masstabseffekte an Anhaegen voeller Schiffe im Modellversuch im HYKAT. Technical Report 1585, HSVA, 1994.

[3] Schneekluth; Die Zustromduese - alte und neue Aspekte. *HANSA*, (21):2189, 1985.

[4] Muzaferija, Peric, Demirdzic; *Computation of turbulent flows in complex geometries, calculation of complex turbulent flows.* WIT Press, 1999.

[5] ICCM; *Comet User Manual Version 2.00.*

[6] Johannsen, Friesch; Propulsion optimization tests at high reynolds numbers. *Transactions of SNAME*, 102, 1994.

[7] Peric, Ferziger; *Computational Methods for Fluid Dynamics.* Springer Verlag, 2nd edition, 1999.

[8] Steger, Sorenson; Automatic mesh point clustering near a boundary in grid generation with elliptic partial differential equations. *Journal of Computational Physics*, 33(3):405–410, Dec 1979.

[9] Stein N., Die Zustromausgleichsduese - eine neue Kompontnente zur Verbesserung der Arbeitbedingungen des Propellers. *Hansa*, (20):1953, 1983.

[10] Pointwise. *GridGen User Manual Version 13.3.*

[11] Gutierrez-Fraile, Rosemberg; The European E3 tanker: Development of an ecological ship. *Transaction of SNAME*, 102:237–264, 1994.

[12] Sorenson; A computer program to generate two-dimensional grids about airfoils and other shapes by use of poissons equation. Technical Report TM-81198, NASA, 1980.

Flow around a Circular Cylinder at Re=3900 and 140,000

T. Persson[1], R.E. Bensow[1], C. Fureby[1,2], U. Svennberg[2]
([1]Chalmers University of Technology, [2]Swedish Defense Research Agency, FOI)

1 Introduction

Many of the structures in marine vehicles can be characterized as bluff bodies and the flow around marine vehicles is often at very high Reynolds number. This gives a very complicated flow with many interesting properties. To be able to resolve properties such as structural dynamics, acoustic wave generation and propagation, and magnetohydrodynamics, the full unsteady flow must be taken into account. The flow around simpler bluff bodies can in general also be very complicated, especially if the geometry of the bluff-body is such that the separation line(s) are not fixed, as is the case for the flow past a circular cylinder that will be addressed here. Such flows typically involve boundary-layer separation, flow regime transition, transition to turbulence, vortex-shedding motion and coherent structure dynamics. All properties that exists in flow past marine applications, e.g. at chimneys, periscopes, masts, cables and antennas. The wake behind a bluff-body is usually spatially complex, often consisting of curved shear layers enclosing a region of extreme complexity characterized by the presence of intense vortices, but also including the entrainment of irrotational flow elements into the wake from the surroundings. The vortices are generated by shear around the obstacle and are shed and advected down the wake. The second effect of the vortex shedding is the generation of intense fluctuating forces on the obstacle in the streamwise and spanwise directions. During the last two decades there has been an increasing interest in bluff-body flows, in particular for flow past a circular cylinder.

2 The circular cylinder

The flow around a circular cylinder is, in addition to the Reynolds number, $Re_D = D \cdot v_0/\nu$, usually characterized by the surface pressure distribution in terms of the pressure coefficient, the skin friction coefficient, the drag coefficient and the Strouhall number, $St = f_s \cdot D/v_0$. Here, v_0 denotes the free-stream flow speed, p the time-averaged pressure, D the diameter of the cylinder, ν the kinematic viscosity and f_s the shedding frequency. At Re_D numbers less than about 150 the flow is laminar. The boundary layer separates at about $Re_D = 5$, whereafter a pair of steady symmetric vortices are formed downstream of the cylinder. At $Re_D = 40$ the flow becomes unsteady and is dominated by vortex shedding and transition to turbulence occurs at between $Re_D = 150$ and 200. At $300 < Re_D < 2 \cdot 10^5$, the so called sub-critical regime, the flow around the entire cylinder is laminar and transition to turbulence occurs in the separated free-shear layers, Beaudan & Moin [2]. For increasing Re_D the flow becomes fully turbulent further downstream, and for $Re_D > 10^4$ the shear layer transition occurs very close to the separation points. The critical regime occurs when $2 \cdot 10^5 < Re_D < 3 \cdot 10^6$ which in turn can be sub-divided into two regimes: (i) the lower transition regime $2 \cdot 10^5 < Re_D < 5 \cdot 10^5$, and (ii) the upper transition regime $5 \cdot 10^5 < Re_D < 3 \cdot 10^6$. In the lower transition regime the separation point moves from the front to the downstream side of the cylinder, which in turn causes the width of the near wake to decrease to less than 1D. In the upper transition the separation point moves forward, but remains on the downstream side of the cylinder and the near wakes widens, but stays smaller than 1D. In the post critical regime, $Re_D > 3.5 \cdot 10^6$, the boundary layer of the cylinder becomes turbulent prior to separation, and therefore the separation-reattachment bubble, present in the critical regime, virtually disappears.

3 LES techniques

The governing equations for the large scale motions of the flow are derived from the continuity and momentum equations. A low pass filter operation is applied to the equations, see e.g. Sagaut [13], giving the filtered equations as

$$\begin{cases} \partial_t \overline{v} + \nabla \cdot (\overline{v} \otimes \overline{v}) &= -\nabla \overline{p} + \nabla \cdot (\overline{S} - B) + m, \\ \nabla \cdot \overline{v} &= m, \end{cases} \tag{1}$$

Here is $\overline{v}$ the filtered velocity, $\overline{p}$ the filtered pressure, $\overline{S} = 2\nu\overline{D}$ is the viscous strain tensor,

$\overline{\boldsymbol{D}} = \frac{1}{2}(\nabla\overline{\boldsymbol{v}} + \nabla\overline{\boldsymbol{v}}^T)$ is the rate of strain tensor, and ν is the kinematic viscosity. In equation 1, there arise two new terms, the subgrid stress (SGS) tensor $\boldsymbol{B} = \overline{\boldsymbol{v}\otimes\boldsymbol{v}} - \overline{\boldsymbol{v}}\otimes\overline{\boldsymbol{v}}$ and the commutation error $\boldsymbol{m} = [G\star, \nabla](\boldsymbol{v}\otimes\boldsymbol{v} + p\boldsymbol{I} - \boldsymbol{S})$, where $[G\star, \nabla]f = \overline{\nabla f} - \nabla\overline{f}$ is the commutation operator.

The effects of the unresolved scales, or subgrid scales, SGS, is described by $\boldsymbol{B}$, which has to be modeled. The commutation error terms m and $\boldsymbol{m}$, is an effect of the fact that filtering and differentiation in general do not commute. At the present there is no trustworthy model for these terms. Here, the commutation terms is included in the the wall model.

3.1 SGS models

3.1.1 Eddy viscosity model

A common way to model the sub-grid stress (SGS) tensor $\boldsymbol{B}$ is to use the Boussinesq hypothesis in a similar way as in RANS modeling. We introduce an eddy viscosity ν_{SGS} and the sub-grid kinetic energy k, and model the deviatoric part of $\boldsymbol{B}$ as,

$$\begin{cases} \boldsymbol{B}_D = \boldsymbol{B} - \frac{2}{3}k\boldsymbol{I} \approx -2\nu_{SGS}\overline{\boldsymbol{D}}\,, \\ k = \frac{1}{2}\mathrm{tr}\boldsymbol{B}. \end{cases} \tag{2}$$

To close the model, we need expressions for ν_{SGS} and k which can be derived assuming scale separation. In this paper, we use the One-Equation-Eddy-Viscosity-Model (OEEVM) Scaumann [14], where a modeled transport equation for k is solved,

$$\begin{aligned} \partial_t(k) + \nabla\cdot(k\boldsymbol{v}) &= 2\nu_{SGS}||\overline{\boldsymbol{D}}||^2 + \\ &+ \nabla\cdot((\nu + \nu_{SGS})\nabla k) - \epsilon \end{aligned} \tag{3}$$

and the eddy viscosity is computed as,

$$\nu_{SGS} = c_k\Delta k^{1/2}, \tag{4}$$

where $\epsilon = c_\epsilon k^{3/2}/\Delta$ is the dissipation and c_ϵ and c_k are model parameters. The value of the model parameters $c_\epsilon \approx 1.03$ and $c_k \approx 0.07$ are derived from the assumption that $|\boldsymbol{k}|^{-5/3}$ extends to infinity.

3.1.2 Scale-similarity model

A severe drawback of the eddy-viscosity models is the alignment of $\boldsymbol{B}$ with $\overline{\boldsymbol{D}}$. The correlation between these two quantities have been shown to be low, see e.g. Liu *et al.* [9]. The Scale-Similarity Model (SSM) by Bardina *et al.* [1] is a *structural model* that does not rely on the Boussinesq hypothesis and shows a much better correlation compared with experiments and DNS, McMillan [11],

$$\boldsymbol{B} \approx \overline{\overline{\boldsymbol{v}}\otimes\overline{\boldsymbol{v}}} - \overline{\overline{\boldsymbol{v}}}\otimes\overline{\overline{\boldsymbol{v}}}\,. \tag{5}$$

This model originates from the fact that since the sub-grid scale field is given by

$$\boldsymbol{v}' = \boldsymbol{v} - \overline{\boldsymbol{v}}\,, \tag{6}$$

the filtered sub-grid velocities can be computed as

$$\overline{\boldsymbol{v}'} = \overline{\boldsymbol{v}} - \overline{\overline{\boldsymbol{v}}}\,. \tag{7}$$

The energy of the parts of the sub-grid scales that interact with the resolved scales can thus be estimated as,

$$\frac{1}{2}\mathrm{tr}\boldsymbol{B} \approx \frac{1}{2}(\overline{\overline{\boldsymbol{v}}^{\,2}} - \overline{\overline{\boldsymbol{v}}}^{\,2}), \tag{8}$$

which then can be expanded to give a model of the components of the sub-grid stress tensor that interacts with the smallest resolved scales.

3.1.3 Mixed model

While the SSM does not suffer from the alignment of the principal axes of the SGS-tensor with those of the stress tensor, it may however not be numerically stable since it only models the largest unresolved scales and may thus not be dissipative enough. A linear combination of a structural model, like the SSM, to model the interaction between the resolved scales and the sub-grid scales, and a functional model, like the OEEVM, to model the energy transfer between the scales, is referred to as a Mixed Model (MM).

In the mixed model used in this paper, the sub-grid stress tensor is modeled as,

$$\begin{aligned} \boldsymbol{B}_D \approx &\overline{\overline{\boldsymbol{v}}\otimes\overline{\boldsymbol{v}}} - \overline{\overline{\boldsymbol{v}}}\otimes\overline{\overline{\boldsymbol{v}}} - \frac{1}{3}(\overline{\boldsymbol{v}^2} - \overline{\boldsymbol{v}}^{\,2})\boldsymbol{I} + \\ &- 2\nu_{SGS}\overline{\boldsymbol{D}}\,, \end{aligned} \tag{9}$$

where ν_{SGS} is computed using OEEVM.

3.1.4 MILES

In Monotone Integrated LES (MILES) the discretization effectively filters the Navier-Stokes Equations across the grid using an anisotropic kernel. When founding MILES on concepts like the Flux Corrected Transport (FCT), the functional reconstruction of the convective fluxes is done using a flux-limiting method combining a high-order flux-function with a low-order dispersion-free flux-function using a non-linear flux-limiter Γ. Moreover, the functional reconstruction of the viscous fluxes is typically performed using linear or cubic interpolation. The implicit subgrid model may be formulated,

$$\boldsymbol{B} = \boldsymbol{C}(\nabla\overline{\boldsymbol{v}})^T + (\nabla\overline{\boldsymbol{v}})\boldsymbol{C}^T + \chi^2(\nabla\overline{\boldsymbol{v}})\boldsymbol{d}\otimes(\nabla\overline{\boldsymbol{v}})\boldsymbol{d}, \tag{10}$$

where $\boldsymbol{C} = \xi(\overline{\boldsymbol{v}} \otimes \boldsymbol{d})$, $\chi = 0.5(1-\Gamma)(\beta^- - \beta^+)$ and $\beta^{\pm} = 0.5(\boldsymbol{v}_f \cdot d\boldsymbol{A} \pm |\boldsymbol{v}_f \cdot d\boldsymbol{A}|)/|\boldsymbol{v}_f \cdot d\boldsymbol{A}|$. This is done in a in a finite volume context, where d$\boldsymbol{A}$ is the face-area vector, $\boldsymbol{d}$ is is the topology vector connecting two neighboring control volumes and $()_f$ is the integrated value on face f. In particular, it is noted that in smooth regions, $\Gamma = 1$ implies that $\chi = 0$ and $\boldsymbol{C} = 0$, and $\boldsymbol{B} = 0$. The implicit subgrid stress tensor can be decomposed into $\boldsymbol{B}^{(1)} = \boldsymbol{C}(\nabla\overline{\boldsymbol{v}})^T + (\nabla\overline{\boldsymbol{v}})\boldsymbol{C}^T$ and $\boldsymbol{B}^{(2)} = \chi^2(\nabla\overline{\boldsymbol{v}})\boldsymbol{d} \otimes (\nabla\overline{\boldsymbol{v}})\boldsymbol{d}$, in which the former is a tensor-valued eddy-viscosity model with $\boldsymbol{C}$ the eddy viscosity tensor, while the latter is of a form equivalent to the first part of the mixed model, equation 9. For more information see e.g Saguat [13] or Fureby *et al.* [8].

3.2 Near-wall treatment

LES of wall bounded flows becomes prohibitively expensive at high Re_D if one attempts to resolve the small but dynamically important eddies in the near-wall region. The classical remedy to this problem is to modify the subgrid model, by means of damping functions, that provides the correct scaling of ν_{SGS} with y^+ as the wall is approached. We here instead use an explicit wall model together with the SGS-models. Following Wikström [15], we determine (locally) the friction velocity u_τ from the law-of-the-wall,

$$v^+ = \begin{cases} y^+ & \text{if } y^+ \leq 11.225, \\ \frac{1}{\kappa}\ln(y^+) + B & \text{if } y^+ > 11.225. \end{cases} \quad (11)$$

The approximate wall boundary condition can be implemented by adding a subgrid wall-viscosity ν_{BC} to the kinematic viscosity ν on the wall so that the sub-grid viscosity becomes,

$$\nu_{Eff} = \nu + \nu_{SGS} = \frac{\tau_w}{(\partial v/\partial y)|_P} = \frac{u_\tau y_P}{v_P^+}, \quad (12)$$

where the subscript P denotes that the quantity is to be computationally evaluated at the first grid point away from the wall.

4 Computational setting

The flow past a circular cylinder is examined at sub-critical Reynolds number of $Re_D = 3900$ and $1.4 \cdot 10^5$, respectively, using two LES models for $Re_D = 3900$ and three for $Re_D = 1.4\Delta 10^5$. For both cases, the computational domain is of rectangular form with a spanwise extent of $1.5\pi D$. The cylinder (of diameter D) is positioned 10D downstream of the inflow plane and 20D upstream of the outflow plane. Moreover, the total vertical extent of the computational domain is 20D. The angular position at which separation occurs is defined clockwise from the upstream side of the cylinder. A block-structured H-grid has been used with an O-grid with radius 3D around the cylinder, see figure 1.

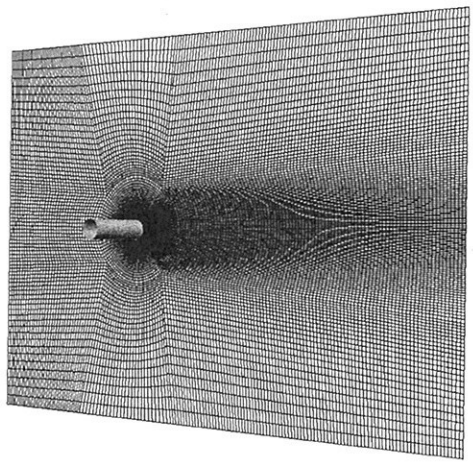

Figure 1: The grid.

The height of the first cell at the cylinder surface is about $3 \cdot 10^{-3} D$, which, at $Re_D = 3900$, is about 20% larger than the value used by Breuer [3], but is still small enough for $y+$ being about 1 at this Reynolds number. At $Re_D = 1.4 \cdot 10^5$ this corresponds to y+ of about 50, which is far larger than what can be used in a wall resolved LES, but should be appropriate for a wall-modeled LES calculation. The grid is then stretched in the normal direction of the cylinder wall. The number of grid cells in the spanwise direction is 48 and the number of grid points in each of the planes is about 22,000, giving a total number of grid cells of about 1,000,000 for the baseline grid. At the inlet boundary, a normal inflow boundary condition is used, at the outlet, a standard outflow boundary condition, at the sides, periodic boundary conditions are set, at the top and bottom we use slip boundary conditions and and on the cylinder wall, noslip boundary conditions. Initially, one simulation at each Re-number is initiated with quiescent conditions, and these initial simulations are continued until the first order statistical moments of velocity and pressure have converged. This occurs after about $80 \cdot D/v_0$. After this, all simulations, using different subgrid models, for each Re-number are started in sequence in which velocity and pressure statistics is sampled under another $200 \cdot D/v_0$.

5 Result

The sampled statistics is averaged over time for comparison with measurements. Here, the work by Lourenco & Shih, data taken from Ma *et al.* [10], and Ong & Wallace [12] have been used for validation of the calculations at $Re_D = 3900$, and the work by Cantwell & Coles [6], data taken from Agard [16], for validation of the calculations at $Re_D = 1.4 \cdot 10^5$. For comparison with DNS at $Re_D = 3900$, see Ma *et al.* [10]. Due to the capability of LES to capture the largest fluctuating scales, it is possible to study a snapshot of the instantaneous flow. As expected from experiments, the calculation shows the well known von Kármán vortex street, see figure 2 for $Re_D = 3900$ and figure 3 for $Re_D = 1.4 \cdot 10^5$.

Figure 2: Magnitude of the vorticity at $Re_D = 3900$

Figure 3: Magnitude of the vorticity at $Re_D = 1.4 \cdot 10^5$.

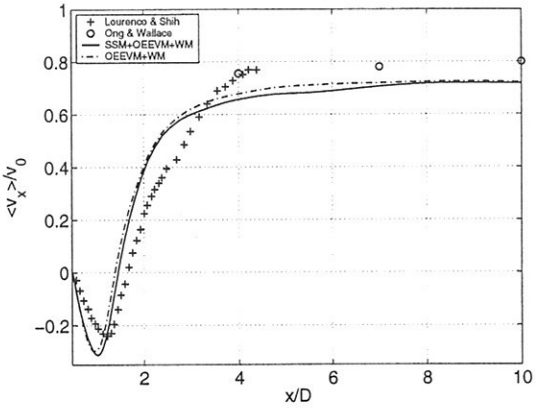

Figure 4: Mean velocity along centerline at $Re_D = 3900$.

are there no data measured on the recirculation velocity.

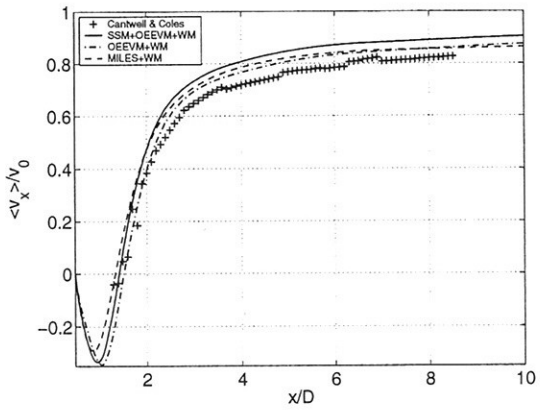

Figure 5: Mean velocity along centerline at $Re = 1.4 \cdot 10^5$.

From the snapshots in figure 2 and 3, one can also see the difference in thickness of the two wakes. Time averaged profiles is taken both along the centerline and at streamwise stations. The streamwise results are taken at $x/D = 1.06, 1.54, 2.02, 4, 7, 10$ for $Re_D = 3900$ and $x/D = 1, 1.5, 2, 4, 7$ for $Re_D = 1.4 \cdot 10^5$. Results are shown at all or some of these stations.

Figure 4 displays the comparison of the centerline velocities between measurements and calculated results with different SGS models at $Re_D = 3900$. The calculated profiles show some deviation from the measurement, the recirculation bubble is slitly to short and with slightly too high recirculation velocity.

Figure 5 displays centerline velocities at $Re_D = 1.4 \cdot 10^5$. This profile shows a good length of the recirculation bubble, unfortunately

The streamwise velocity profiles for $Re_D = 3900$ is displayed in figure 6. The predictions of the velocity profiles show that the calculated wake has a correct width and that it flattens out and gets wider and wider. A detailed view of the last stations shows that the calculated velocities is slightly to high in the far wake.

In figure 7, the corresponding prediction of the streamwise velocity profiles at $Re_D = 1.4 \cdot 10^5$ is plotted. These profiles show the same tendencies as the $Re_D = 3900$ case, but with slightly better velocity prediction in the far wake.

For comparison with other LES calculations on $Re_D = 3900$, see Beaudan & Moin [2], Breuer [3], [4] and Franke & Frank [7], and Breuer [5] for $Re_D = 1.4 \cdot 10^5$.

As a consequence of LES capability of pre-

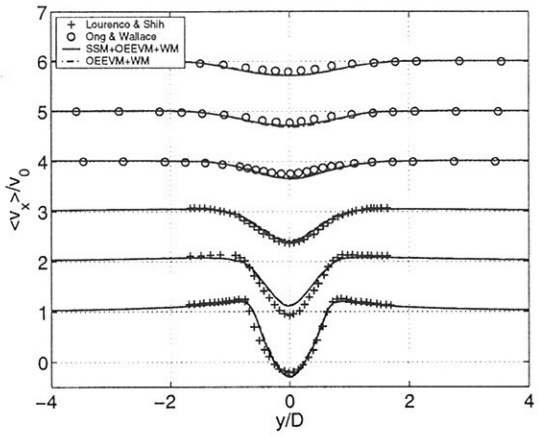

Figure 6: Streanwise velocity profiles at $x/D = 1.06, 1.54, 2.02, 4, 7, 10$ at $Re_D = 3900$.

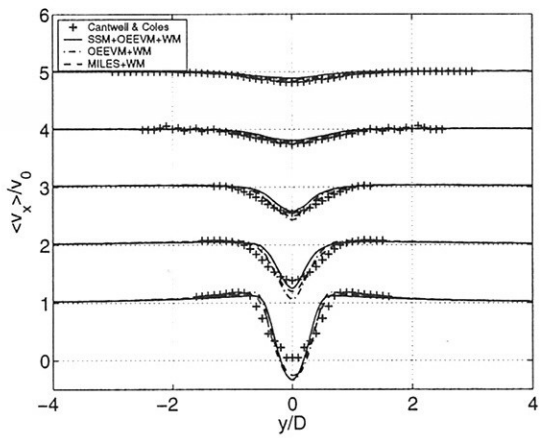

Figure 7: Streanwise velocity profiles at $x/D = 1.06, 1.54, 2.02, 4, 7$ at $Re_D = 1.4 \cdot 10^5$.

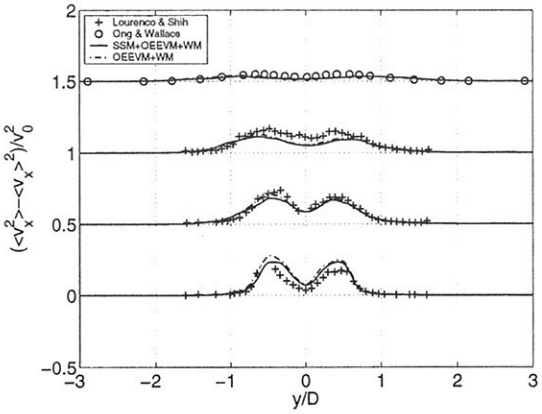

Figure 8: Reynold stresses at $x/D = 1.06, 1.54, 2.02, 4$ at $Re_D = 3900$.

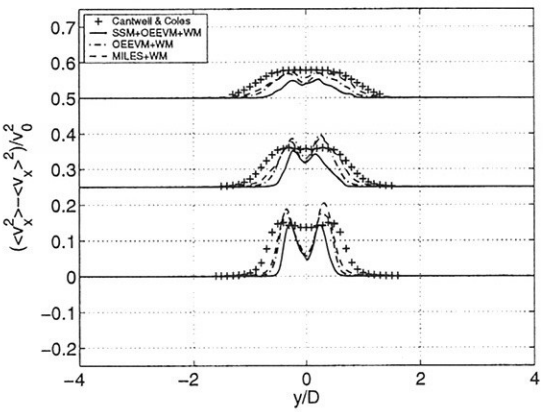

Figure 9: Reynold stresses at $x/D = 1, 1.5, 2$ at $Re_D = 3900$.

dicting some of the fluctuating velocities, the calculated Reynolds stresses can be compared with measurements. These give a qualitative indication of how well the solution has converged as well as it is good test of the capability of the SGS-models to reproduce a correct turbulent kinetic energy. To be able to tell the difference between a bad statistical convergence and a bad SGS-model, one has to check the convergence in another way, e.g. by studying the time evolution of the Reynold stress in one point. The Reynold sheer stress for $Re_D = 3900$ is in figure 8 and for $Re_D = 1.4 \cdot 10^5$ in figure 9.

6 Conclusions

LES calculations have been performed at two well known and well tested cases, the circular cylinder at $Re_D = 3900$ and $Re_D = 1.4 \cdot 10^5$. The calculations have been performed to test the different SGS models on a well known case. The results from the different models are hard to separate, but it might be so that the mixed model and MILES are slightly better. This is very hard to say from these results, but this indication has been seen on other test cases. The biggest discrepancies between the models are in the Reynolds stresses at $Re_D = 1.4 \cdot 10^5$, but this is probably due to lack of convergence of the statistics. This has not yet been checked, but an indication can be that the OEEVM model and the MILES model are close together and the mixed model are a bit lower in value. It is expected that MILES and the mixed model have more equal properties to each other than to the OEEVM model. All models have been sampled for an equal amount of time, but there are indications in earlier cases that the mixed model needs more statistics then the other two to converge. The discrepancy in recirculation

bubble length can be due to several things, one likely cause is the difference in outer geometry. The experiments have been performed on a finite length cylinder in a wind tunnel and the calculations have been performed on cylinder with infinite length without the exact geometries of the wind tunnel, for further discussion see e.g. Ma *et al.* [10].

6.1 Further work

There are several areas of this work that has to be further investigated. The most important part is to get the results from the MILES model for the $Re_D = 3900$ case. This will be done within a short time. Other important parts is to sample more statistics from the $Re_D = 1.4 \cdot 10^5$ case and check that the statistics has converged. Then properties such as the pressure coefficient, the skin friction coefficient and the drag coefficient will be calculated for all cases. More possibilities for enhancement of the work is to try higher Reynolds number, use unstructured grid for better grid quality, do RANS calculations on the same grid for comparison and use more advanced SGS and wall models.

7 Acknowledgments

This work is supported by the Swedish Defence Material Administration (FMV) under the grant 'MarinLES'. High Performance Computing (HPC) resources are provided by the Swedish Defence Research Agency (FOI).

References

[1] Bardina J., Ferziger J.H. and Reynolds W.C.; 1980, "Improved Subgrid Scale Models for Large Eddy Simulati-ons", AIAA Paper No. 80-1357.

[2] Beaudan P. and Moin P.; 1994, "Numerical experiments on the flow past a circular cylinder at sub-critical Reynolds number", Tech. Rep. TF-62, Stanford University, Stanford, CA 94305

[3] Breuer M.; 1998, "Large eddy simulation of the subcritical flow past a circular cylinder: numerical and modeling aspects", Int. J. num. met. in Fluids 28 1281-1302

[4] Breuer M.; 1998, "Numerical and modeling influence on large eddy simulations for the flow past a circular cylinder", Int. J. Heat and Fluid Flow 19 512-521

[5] Breuer M.; 2000, "A challenging test case for large eddy simulation: high Reynolds number circular cylinder", Int. J. Heat and Fluid Flow 21 pp. 648-654

[6] Cantwell B. and Coles D.; 1983, "An experimental study of entrainment and transport in the turbulent near wake of a circular cylinder", J. Fluid Mech, vol 136, pp. 321-374

[7] Franke J. and Frank W.; 2002, "Large eddy simulation of the flow past a circular cylinder at $Re_D = 3900$", J. of Wind Eng. and Ind. Aerodynamics 90, pp. 1191-1206

[8] Fureby C., Alin N., Wikström N., Menon S., Svanstedt N. and Persson L.; 2004,"On large eddy simulation of high Reynolds number wall bounded flows", AIAA J., vol 42, pp. 457

[9] Liu S., Menevau C. and Katz J.; 1994, "On the Properties of Similarity Sub-Grid Scale Models as Deduced from Measurements in a Turbulent Jet", J. Fluid Mech., 275, p 83.

[10] Ma X., Karamanos G.-S. and Karniadakis G. E.; 2000,"Dynamics and low-dimensionality of a turbulent near wake", J. Fluid Mech., vol 410, pp. 29-65

[11] McMillan O.J. and Ferziger J.H. and Rogallo R., 1980, Direct Testing of Sungrid Scale Models, AIAA paper 80-1339

[12] Ong L. and Wallace J.; 1996, "The velocity field of the turbulent very near wake of a circular cylinder", Experiments in Fluids 20, pp. 441-453

[13] Sagaut, P.: Large Eddy Simulation for Incompressible Flows, Springer Verlag, Heidelberg, 2001.

[14] Schumann U.; 1975, "Subgrid Scale Model for Finite Difference Simulation of Turbulent Flows in Plane Channels and Annuli", J. Comp. Phys.,18, p 376.

[15] Wikström N., Svennberg U., Alin N. and Fureby C.; 2003, "Large Eddy Simulation of the Flow past an Inclined Prolate Spheroid", To appear in the proceedings of TSFP 3, Sendai, Japan.

[16] Working group 21 Nasa, "A selection of test cases for the validation of large-eddy simulations of turbulent flows", Agard-AR-345

Numerical Simulation of Free Surface Flow around a Surface Piercing NACA0024 Hydrofoil

S.H. Sadathosseini, S.M. Mousaviraad, Mohammed S. Seif
Dept. of Mechanical Engineering, Sharif University of Technology, Tehran/Iran
Email: sadathosseini@mehr.sharif.edu

NOMENCLATURE

Fr= Froude number, $\frac{U_\infty}{\sqrt{gL}}$
g = acceleration of gravity
L= foil chord length
Re= Reynolds number, $\frac{U_\infty L}{\upsilon}$
U_∞ = freestream velocity
$\overline{u_i' u_j'}$ = Reynolds stress
v= velocity vector
X, Y, Z= Cartesian coordinates
λ = wave length
υ = kinematic viscosity
α_w= volume fraction of water
α_a= volume fraction of air
ρ = density
μ = viscosity

INTRODUCTION

Free surface wave induced separation, i.e. separation solely due to wave induced effects, is very important in ocean and marine engineering. It involves the complexities of free surface deformations, vorticity, and turbulence along with the already formidable subject of three dimensional boundary layer separation. The boundary layer becomes complicated when there is a free surface due to the effect of gravity waves and the free surface boundary condition. Such effects are a unique and poorly understood problem of ship and platform hydrodynamics due to wave making, wave breaking and/or incident waves and are important with regard to ship performance, wake signatures, and platform stability. The NACA0024 foil is a simplified geometry that has insignificant separation at large depths, thus making an ideal geometry by isolating the wave induced separation.

The wave induced separation was first identified by Chow (1967) using vertical (surface piercing) and horizontal (submerged) foils, designed for insignificant separation at large depths. Chow observed regions of separated flow originating just beyond the wave trough and in some cases beyond the trailing edge. It was also studied by Stern et al. (1989) using a surface piercing flat plate with attached wave generating upstream horizontal submerged foil (foil-plate model). As with Chow, separation initiated just beyond the wave trough and extended to the following wave crest. These studies showed the dependence of the streamwise and depthwise extent of the separation region on Froude number and wave steepness and that the transverse extent is wedge shaped with significant free surface vorticity and turbulence. Choi and Stern (1993) performed laminar and turbulent CFD calculations for a surface piercing flat plate with an external Stokes wave, which simulates the Stern et al. experimental geometry. In comparison to the experimental data, the extent was grossly over/under predicted for the laminar/turbulent solutions. Zhang and Stern (1996) studied the problem through RANS simulation with exact nonlinear kinematic and approximate dynamic free surface boundary conditions. The nature of the flow in the separation region was qualitatively similar as Choi and Stern, but described in detail using a topological rule derived for free surface wave induced separation in which free surface streamlines are treated similarly as skin friction lines. Zhang and Stern also remarked that the flow is naturally unsteady for high Froude numbers and both further CFD study and experimental data are needed to obtain accurate wave breaking solutions and validate the CFD results. Pogozelski et al. (1997) performed ex-

perimental study of free surface wave induced separation, but with different foil geometry. Metcalf et al. (2001) provided detailed experimental data documentation of the wave elevations and surface pressures for surface piercing NACA0024 hydrofoil. Kandasamy et al. (2001) using CFDSHIP-IOWA (a general purpose research code for ship hydrodynamics) performed RANS simulation to study wave induced separation. They also studied the effects of blockage considering four different solution domains.

For free surface modeling, the present simulation uses VOF (Volume of Fluid) which takes the effect of outer air into consideration and solves RANS equations simultaneously for both water and air, while all previous calculations used surface tracking methods. As a result, the present study shows better agreement with the experimental data.

Wave breaking phenomenon, occurring at high Froude numbers, is an intricate subject when numerical simulation is concerned and needs robust modeling schemes to get accurate results. This paper represents wave breaking at Fr=1, but unfortunately there is no experimental data or previous numerical study to compare the results with.

COMPUTATIONAL METHOD

The CFD (Computational Fluid Dynamics) results were obtained solving RANS (Reynolds Averaged Navier Stokes) equations based on the finite volume method. The treatment for the two phase flow uses an interface capturing method, volume of fluid (VOF). In this method, an additional transport equation is solved for the volume fraction of water in each cell. If the volume fraction of water and air in each cell is denoted as α_w and α_a, the tracking of the interface between the phases is accomplished by the solution of a continuity equation for the volume fraction of water. This equation has the following form:

$$\frac{\partial \alpha_w}{\partial t} + \vec{v}.\nabla \alpha_w = 0 \qquad (1)$$

The volume fraction equation will not be solved for air; the volume fraction of air will be computed based on the following constraint:

$$\alpha_w + \alpha_a = 1 \qquad (2)$$

The properties appearing in the transport equations are determined by the presence of the component phases in each control volume. The density in each cell, for example, is given by:

$$\rho = \alpha_w \rho_w + \alpha_a \rho_a \qquad (3)$$

All other properties (e.g., viscosity) are also computed in this manner.

A single momentum equation is solved throughout the domain, and the resulting velocity field is shared among the phases. The momentum equation is dependent on the volume fractions of all phases through the properties ρ and μ.

Turbulence is modeled using the Reynolds Stress Model (RSM). This model involves calculation of the individual Reynolds stresses, $\overline{u_i' u_j'}$, using differential transport equations. A single set of transport equations is solved, and the Reynolds Stresses are shared by the phases throughout the field. The individual Reynolds stresses are then used to obtain closure of the Reynolds averaged momentum equation.

NUMERICAL MODLING

A NACA0024 foil having a chord length of 1.2 m, a span of 2 m (75% in water), and a thickness of 0.29 cm is considered as model problem. Fig.1 shows the solution domain.

Three conditions simulated are based on the experimental data, i.e., Fr= (0.19, 0.37, 0.55) and the corresponding Re= (0.822, 1.52, 2.26) $\times 10^6$. Additionally, Fr=1 solution is obtained to simulate wave breaking.

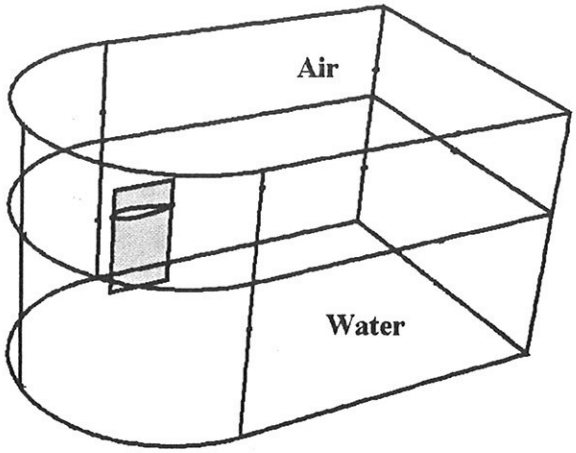

Fig.1 Solution domain

Using symmetry plane, only half domain which consists of hexahedral structured grid with 215000 cells is solved. The cells near free surface in both fields (air and water) are considered to have very small sizes (2 mm height) in order to catch the water waves precisely. Fig.2 shows the grid generated for the foil, free surface and boundaries.

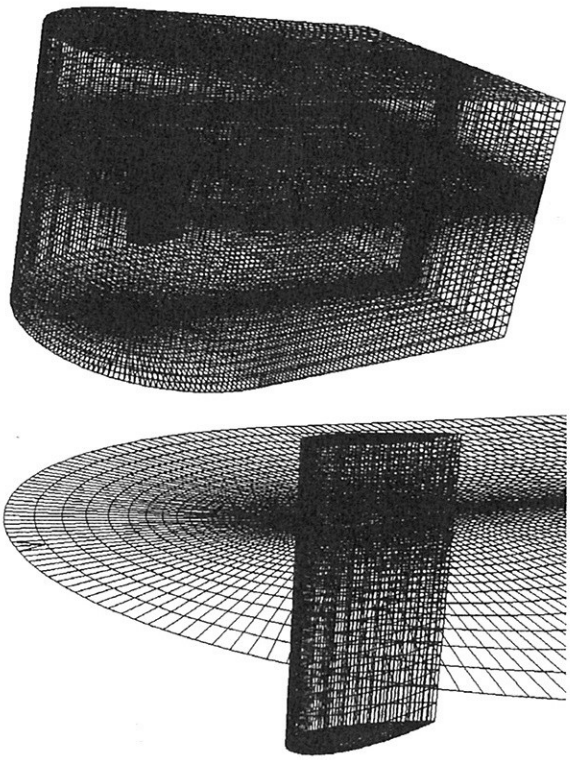

Fig.2 Computational grid

RESULTS AND DISCUSSIONS

Fig.3 shows the wave profile along the body and comparison with Zhang & Stern experimental and numerical data for Fr=0.19. The wave profile is similar to a typical ship wave profile and the wave length is slightly greater than the wave length given by Kelvin wave theory ($\lambda = 2\pi Fr^2$). The results are nearly as accurate as Zhang & Stern numerical results, indicating that the effect of air is less significant at low Froude numbers.

Figs. 4 and 5 show the wave profiles for Fr=0.37 and 0.55, respectively. At these Froude numbers separation occurs for $X < \lambda$ and the wave profiles are different from those of ships. The wave profiles are relatively flat in the separation regions due to constant pressure and the flat region is smaller for Fr=0.55 than Fr=0.37. The bow wave peak for Fr=0.37 and 0.55 are 6.2 and 14 percent of L, respectively.

Fig.6 compares the wave profiles from the present calculation. For Fr=0.19, the wave pattern is similar to ship flow. For Fr=0.37, it shows a different wave system from that of the low Fr cases. The bow wave becomes more significant; the wave steepness is larger; and the free surface is relatively flat in the separation region. For Fr=0.55, the free surface has an even more complicated wave system, with increases in bow wave peak, wave steepness and distortion of the free surface in the separation region.

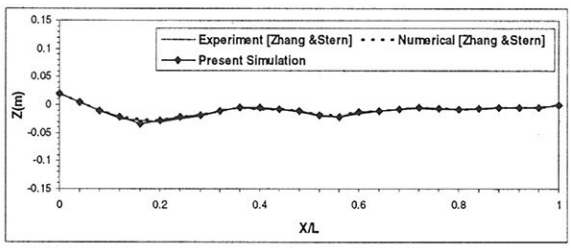

Fig.3 Wave profile for Fr=0.19

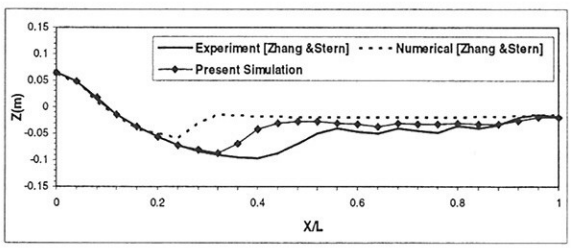

Fig.4 Wave profile for Fr=0.37

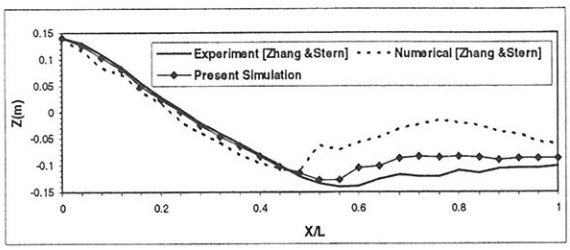

Fig.5 Wave profile for Fr=0.55

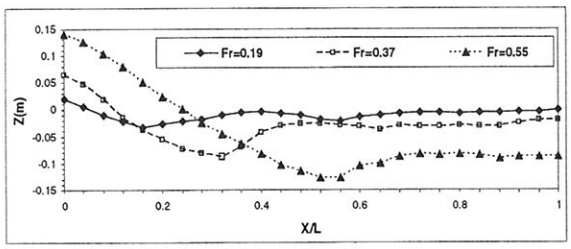

Fig.6 Wave profiles comparison

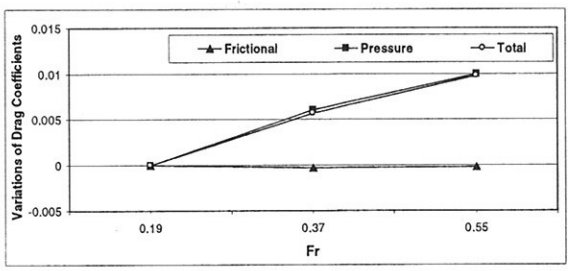

Fig.7 Variations of drag coefficients

Fig.7 presents the variations of pressure, frictional and total drag coefficients versus Froude number. All values are subtracted from the corresponding values for Fr=0.19. As Fr increases, the pressure drag coefficient increases due to the effects of the bow wave. The frictional drag coefficient, on the other hand, decreases as Fr increases from 0.19 to 0.37 and then increases a little as Fr increases further to 0.55, which is consistent with the size changes of the separation region.

Fig.8 shows the pressure contours in symmetry plane so as to show the free surface elevations near the hydrofoil. At low Froude numbers, the waves are found to be trivial far from the body due to its slenderness. However, water deformations are slightly extended after the trailing edge for Fr=0.55. The wave patterns around the foil are also shown in Fig.9.

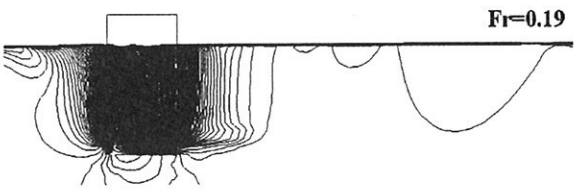

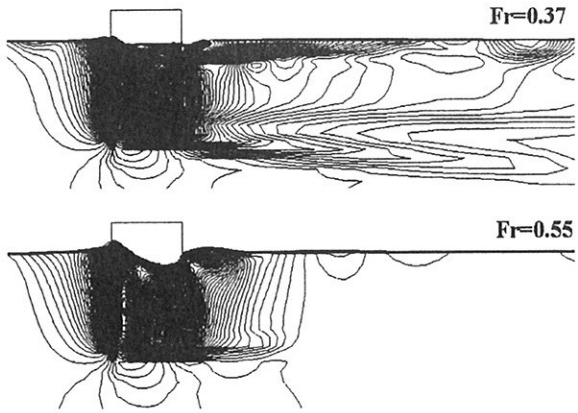

Fig.8 Pressure contours

The wall shear stress contours are presented in Fig.10, in which the separation regions distinguished by the negative wall shear stress values are marked. For Fr=0.19, the wave effects are limited to a region very close to the free surface and the separation region is very small. The flow recovers to 2D at about Z=-0.3 m. For Fr=0.37, the wave effects become strong, extend to about Z=-1 m, and the separation region at free surface is about 68 percent L. For Fr=0.55, the wave effects become even stronger and extend to about Z=-1.15 m. The separation region is about 45 percent L, which is smaller than Fr=0.37 since the point of separation is pushed down stream.

The wave breaking flow at Fr=1 is shown for some time steps in Fig.11. The phenomenon is extremely complicated due to the effects of unsteadiness, turbulence and air trapping. Though the present calculation was able to cope with these intricacies, further developments seem to be vital in order to elucidate the details of the issue.

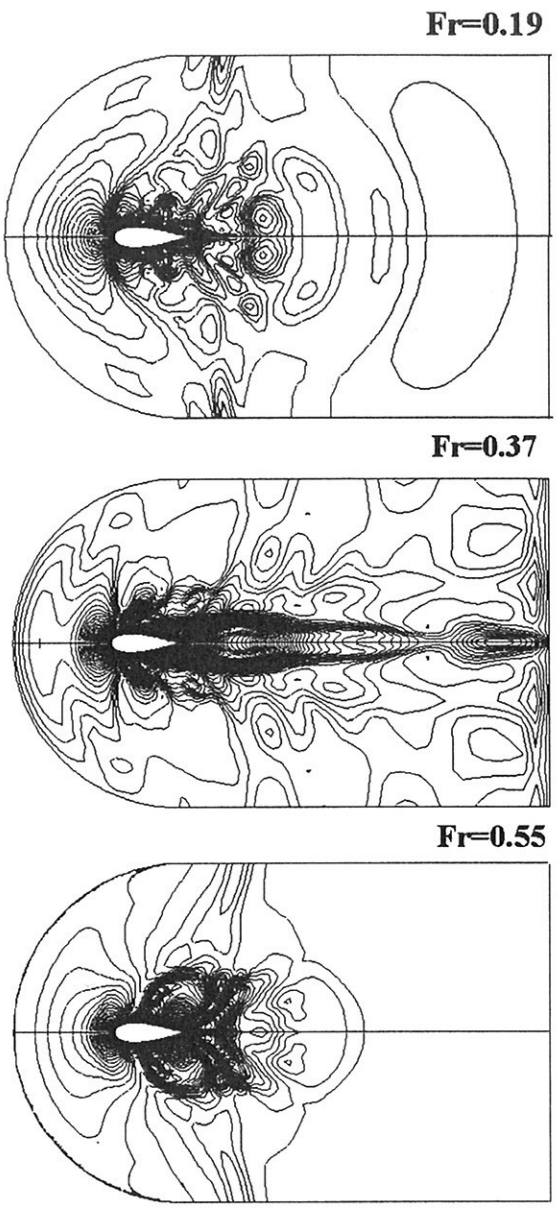

Fig.9 Wave patterns

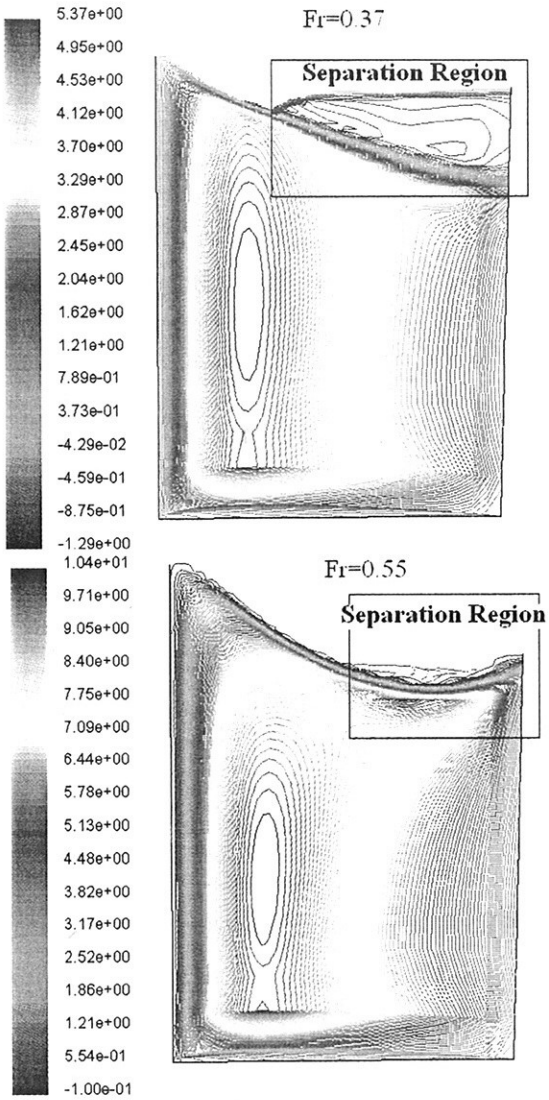

Fig.10 Wall shear stress contours

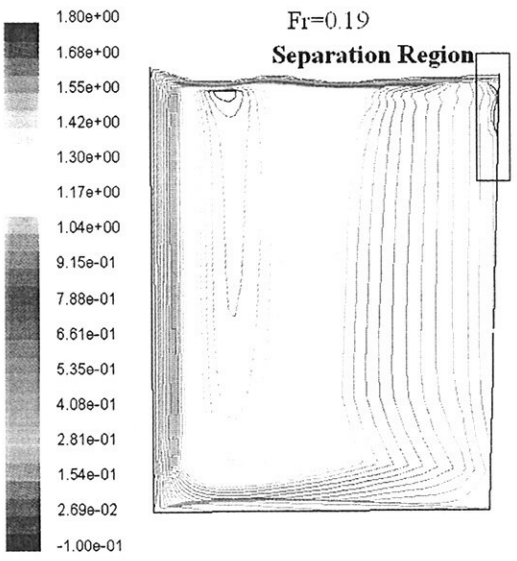

CONCLUSIONS

Free surface flow simulation is performed for a surface piercing NACA0024 foil over a range of Fr solving RANS equations. Flow results are presented and analyzed with regard to the wave and viscous flow, nature of the separation, and weave breaking.

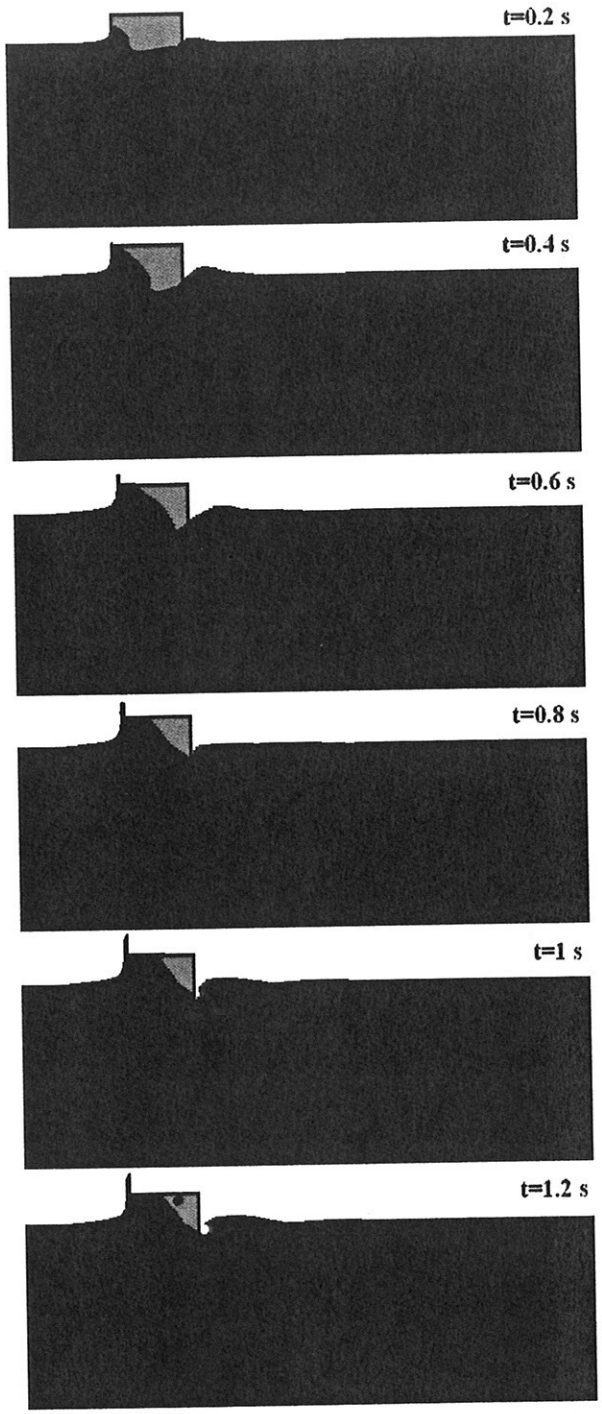

Fig.11 Wave breaking at Fr=1

The study indicates that the drag coefficients, free surface waves, and the separation patterns are all Fr dependent. The bow wave peak increases with Fr and the separation region increases as Fr increases from small (0.19) to medium (0.37) and then decreases as Fr increases further to high (0.55). Associated with the wave pattern, the pressure drag coefficient increases with Fr. The frictional drag coefficient increases and then decreases with Fr in agreement with the separation region. The separation region is relatively flat at medium Fr (0.37) and becomes highly distorted at high Fr (0.55).

This study also proves that the effect of air is significant, especially for medium and high Fr, and can have a considerable influence on the numerical results.

The flow is intensely unsteady for very high Fr and the waves generate and break repeatedly. Therefore, the simulation is possible only with a robust surface capturing free surface method (e.g. VOF) that can deal with air trapping. Moreover, fine grid and strong turbulence model are absolutely necessary.

The study is useful both in providing insight on this complicated problem which is important for ship and platform hydrodynamics and for being an implement of design and optimization. However, more study is needed to evaluate the performance of turbulence models, to study the effect of Reynolds number and to assess the critical Fr at which the wave breaking flow begins.

REFERENCES

CHOI, J.E.; STERN, F. (1993), *Solid-fluid juncture boundary layer and wake with waves*, 6th Int. Conf. Num. Ship Hydrodynamics, Iowa City, pp. 215-238

CHOW, S.K. (1967), *Free-surface effects on boundary-layer separation on vertical struts*, PhD Thesis, University of Iowa

KANDASAMY, M. (2001), *RANS simulation of free-surface wave-induced separation on a surface–piercing NACA0024 hydrofoil*, University of Iowa Thesis, Iowa City

METCALF, B. (2001), *Experimental investigations of wave-induced separation on a surface-piercing NACA0024 hydrofoil*, University of Iowa Thesis, Iowa City

POGOZELSKI, E.; KATZ, J.; HUANG, T. (1997), *The flow structure around a surface-piercing strut*, Physics of Fluids 9/5, pp.1387-1399

STERN, F.; HWANG, W.S.; JAW, S.Y., 1989, *Effects of waves on the boundary layer of a surface–piercing flat plate: Experiment and theory*, J. Ship Research 33/1, pp.63-80

ZHANG, Z. (1995), *Wave-induced separation*, M.S. Thesis, University of Iowa

ZHANG, Z.; STERN, F. (1996), *Free-surface wave-induced separation*, J. Fluids Eng. 118, pp.546-554

7th Numerical Towing Tank Symposium
Hamburg, GERMANY, 3-5 October 2004

The prediction of scale effects on ship wave systems using a steady iterative RANS method

Bram Starke
Maritime Research Institute Netherlands (MARIN), P.O. Box 28, 6700 AA Wageningen, Netherlands.
e-mail: b.starke@marin.nl

INTRODUCTION

Model testing of ships is usually performed at equivalent Froude numbers to obtain equal wave patterns at model scale and at full scale. However, once the Froude number is fixed, one can not also obtain equivalent Reynolds numbers. Typically, in ship design projects the Reynolds number at model scale is a factor one hundred smaller than at full scale. To account for the so-called *scale effects* caused by the difference in Reynolds number, extrapolation procedures are used. The primary scale effect on the flow is a decrease of the boundary-layer thickness on the hull and a corresponding decrease of the width of the wake behind the stern with increasing Reynolds number. This results in a considerable change of the velocity distribution in the propeller plane. A secondary, and therefore less pronounced, scale effect is caused by the interaction between the viscous flow and the wave pattern. Wave effects on the viscous flow around the hull may be significant for all cases with substantial wave making, as the wavy surface affects the development of the boundary layer all along the hull. On the other hand, viscous effects on the wave pattern are generally insignificant and only substantial in the stern region, as is confirmed by many validations of non-linear panel methods. Viscous effects are expected to result in a reduction of the height of the stern wave system and an upstream shift of the first wave crest behind the stern. The level of this reduction depends on the amount to which the flow itself is affected by viscosity. Since the width of the boundary layer and the wake decrease with increasing Reynolds number, so does the reduction of the stern wave system. This secondary scale effect on the wave system is not specifically accounted for in extrapolation procedures. However, with the development of solution methods for the free-surface viscous-flow problem, it has now become possible to calculate these effects, which is the subject of this paper. Results will be presented for a full-block tanker, sailing at a relatively low Froude number. Attention will be given to the grid dependency of the solution and the results will be validated against available experiments.

COMPUTATIONAL METHOD

The viscous-flow computations are carried out with the computer code PARNASSOS, (Hoekstra, 1999) which solves the three-dimensional Reynolds-averaged Navier-Stokes equations for a steady, incompressible fluid, supplemented by a turbulence model. In the present computations single-block, body-fitted, HO-type meshes are used, which are strongly stretched towards the hull to capture the gradients in the boundary layer. The governing equations are integrated down to the wall, i.e. no wall-functions are used, not even in the full-scale computations.

The free-surface boundary conditions are imposed using an unconventional steady iterative approach, first published in (Raven & Van Brummelen, 1999) and (Van Brummelen & Raven, 2000). This approach has been developed to reduce the long computation times needed by current time-dependent methods. A more detailed discussion of our method and earlier results that have been obtained for, e.g., the Series 60 hull can be found in (Raven & Starke, 2002) and (Raven, Van der Ploeg and Starke, 2004).

COMPUTATIONAL DOMAIN

The computational domain extends from $0.5L_{pp}$ in front of the bow to $1L_{pp}$ behind the stern. The domain is approximately $0.6L_{pp}$ wide and $0.4L_{pp}$ deep. Due to symmetry considerations (zero drift angle) only one side of the ship is taken into account. The computational mesh for the model-scale case consists of 553 grid nodes in the streamwise direction, 121 grid nodes in wall-normal direction and 45 grid nodes in girthwise direction. For the full-scale case the number of grid nodes in wall-normal direction has been increased to 161, to resolve the stronger gradients in a boundary layer at full scale. To study the effect of discretisation errors in the solution, these grids are three times coarsened in the streamwise direction by a factor two. The resulting grids therefore have 70, 139, 277 and 533 nodes in streamwise direction and will be referred to as *istep8*, *istep4*, *istep2* and *istep1*, respectively.

FREE SURFACE UPDATES

In our method, a surface-fitting approach is used to compute the free surface. The computations start on the coarsest mesh beneath an undisturbed water surface. Then, the RANS/FS equations are solved until the maximum changes in the pressure coefficient anywhere in the flow field drop beneath $5x10^{-5}$, followed by an update of the free surface. This process is repeated several times, until the changes in the free surface have become sufficiently small. Next, the computation is continued on the following finer mesh using the previous result as an initial solution, with an appropriate interpolation of the flow quantities to the stations that are not present in the coarser mesh. This is followed by the same procedure to solve the RANS/FS equations as described above and continued until a solution on the finest mesh has been obtained. Typically only 3 to 8 free-surface updates are required on each mesh. The final results obtained on each of the meshes can be used to study the grid dependency of the solution.

APPLICATION

Results are presented for the Dyne tanker, a ship with a cylindrical bow and a block coefficient C_b=0.87. It has been used as a test case in (Larsson et al., 1991). At model scale the Reynolds number of the flow is equal to $Rn=8.5x10^6$, and at full scale $Rn=1.8x10^9$. The Froude number is equal to Fn=0.165.

Convergence of the free-surface

The convergence history of the waterline in the model-scale computation is shown for two of the meshes in Fig. 1. As discussed earlier, the calculation starts on the coarsest mesh assuming an undisturbed water surface. Hence the "0^{th}" free-surface update corresponds to the line $z/L_{pp}=0$.

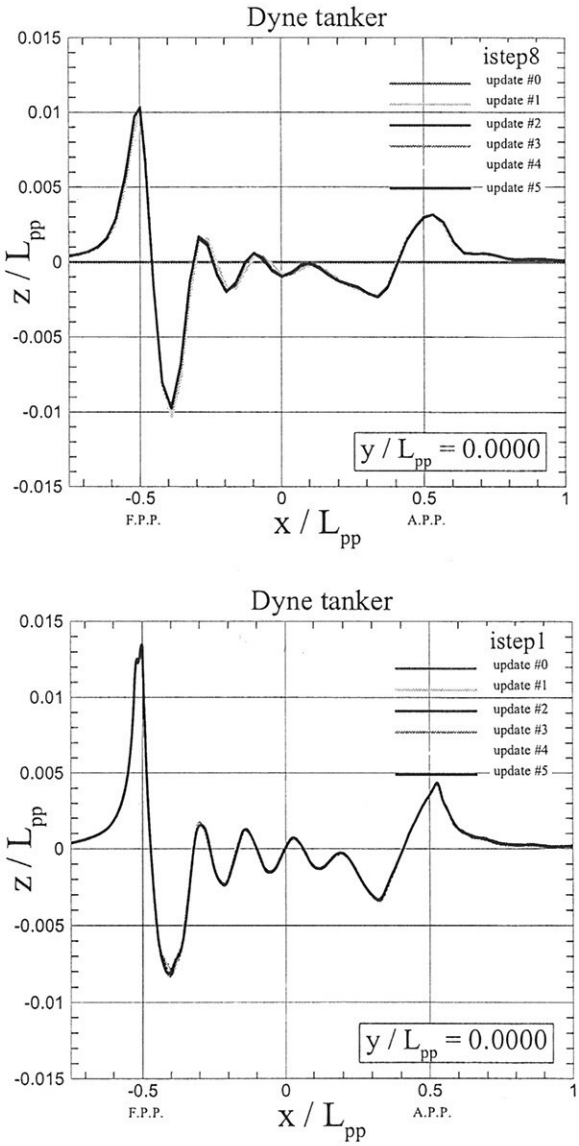

Figure 1: Convergence of the model-scale waterline at the coarsest mesh (top) and the finest mesh (bottom).

Although results are shown for the waterline only, the first free-surface update returns practically the entire wave system that will be obtained on this mesh. Between the first and the second free-surface update only a small upstream shift of the wave crests and the wave troughs along the hull is noticeable. The waterlines in all subsequent free-surface updates practically coincide on the scale shown in this figure. Quantitatively, the maximum change in the waterline in the second free-surface update equals $dz/L_{pp}=9.5x10^{-4}$, which is approximately one per cent of the maximum wave height. This value rapidly decreases and at the fifth update the maximum change in the waterline on the coarsest mesh equals $dz/L_{pp}=6.8x10^{-6}$.

A similar fast convergence is found on the finest mesh, as shown in the bottom part of Fig 1. It is recalled that the "0^{th}" update on this mesh corresponds to the (interpolated) converged solution obtained on the second finest mesh. The predicted waterline both in this solution and in all following free-surface updates on the finest mesh practically coincide in the figure. The largest changes in the solution occur near the bow wave and the first wave trough and, to a lesser extent, at the centerline behind the stern of the ship. The maximum change in the free-surface in the final update of the finest mesh equals $dz/L_{pp}=1.6x10^{-4}$.

Grid dependency of the solution

To study the effect of discretisation errors, solutions obtained after the final free-surface updates on each of the four meshes are compared. The results for the waterline are shown in Fig. 2, both for the model scale and for the full-scale computation. In each case the solution on the coarsest mesh is affected by a substantial amount of numerical damping and dispersion, which manifests itself in an under-estimation of the wave height and an over-estimation of the wave length, respectively. On the three finer meshes more pronounced wave profiles are predicted and differences between the solutions on each of the meshes have reduced considerably. At model scale the maximum change in the waterline between the coarsest and the second coarsest mesh equals $dz/L_{pp}=2.9x10^{-3}$. This change corresponds to an increase of the height of the bow wave. Between the second coarsest and the second finest mesh the maximum change in the waterline decreases to

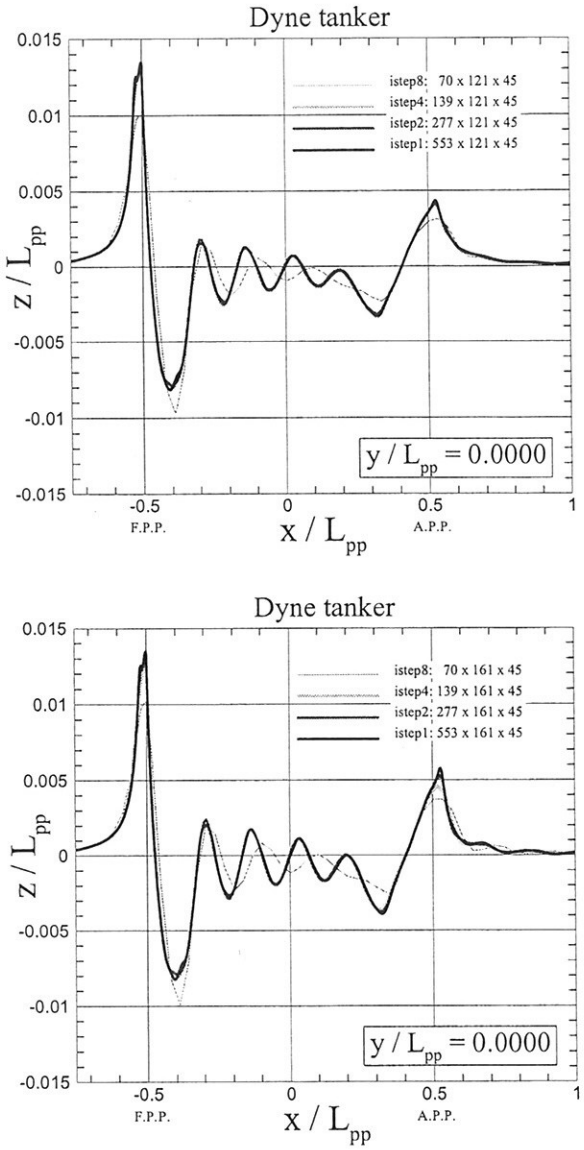

Figure 2: Grid dependence of the waterline at model scale (top) and full scale (bottom).

$dz/L_{pp}=9.3x10^{-4}$ and finally to $dz/L_{pp}=4.2x10^{-4}$ between the second finest and the finest mesh. Comparable values are found for the level of grid independence at full scale. There, the largest changes along the waterline decrease from $dz/L_{pp}=2.9x10^{-3}$ to $9.8x10^{-4}$ and $4.4x10^{-4}$ between the successively refined meshes.

The grid dependence of the solution for a wave cut at $y/L_{pp}=0.2181$ is shown in Fig. 3. As in the case of the waterline, the wave height on the coarsest mesh is under-predicted. On the second coarsest mesh the wave height has improved considerably and the solutions of the second finest and the finest mesh show good agreement, although small differences can still be found in the solution.

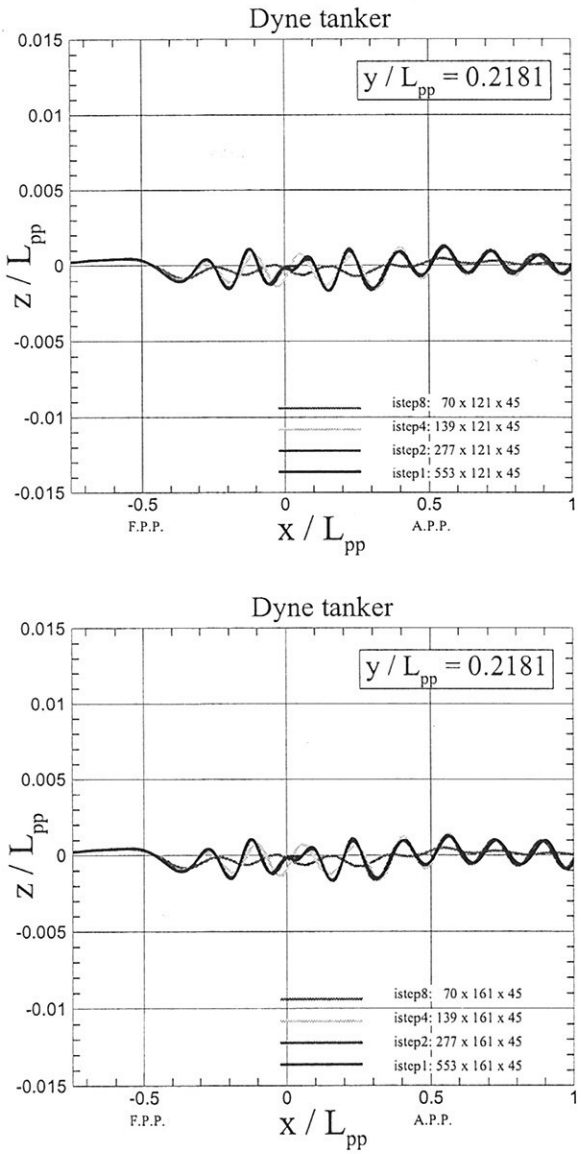

Figure 3: Grid dependence of a longitudinal wave cut at $y/L_{pp}=0.2181$ at model scale (top) and at full scale (bottom).

Comparison with experiments

In order to validate the numerical results, the predicted model-scale wave heights are compared to experiments available from Lundgren & Åhman (1994). Their experiments include several longitudinal wave cuts, two of which are shown in Fig. 4. The top part of the figure corresponds to the location closest to the hull where an experimental wave cut is available, while the bottom part of the figure corresponds to the location furthest away from the hull. Both longitudinal wave cuts show good agreement between the prediction and the experiments. In the top part of the figure several short diverging waves can be observed in the computational results near the first wave trough, which are less pronounced in the experiments. Furthermore it appears that the waves along the entire wave cut are located slightly more upstream in the computations compared to the experiments.

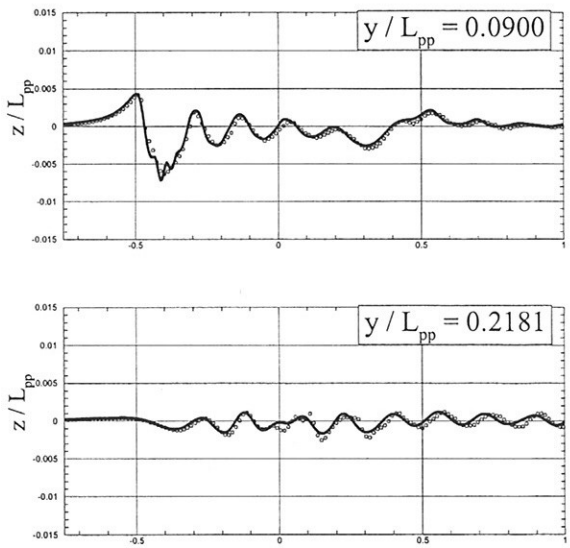

Figure 4: Validation of the model-scale wave pattern at two longitudinal wave cuts. Solid lines: computation, open circles: experimental values.

Scale effects on the wave system

To illustrate the Reynolds scale effect on the wave system, consider Fig. 5. In this figure the following results are simultaneously shown for two longitudinal wave cuts; the experimental

model-scale values, the RANS/FS predictions both at model and at full scale, and finally the corresponding wave cuts obtained with the non-linear panel method RAPID (Raven, 1996). Several observations can be made from these results. Concentrating on the stern wave system, i.e. beyond $x/L_{pp}=0.5$, it is found that the model scale RANS/FS computation gives the right reduction of the stern wave system to the experimental values, in comparison with the non-linear panel method.

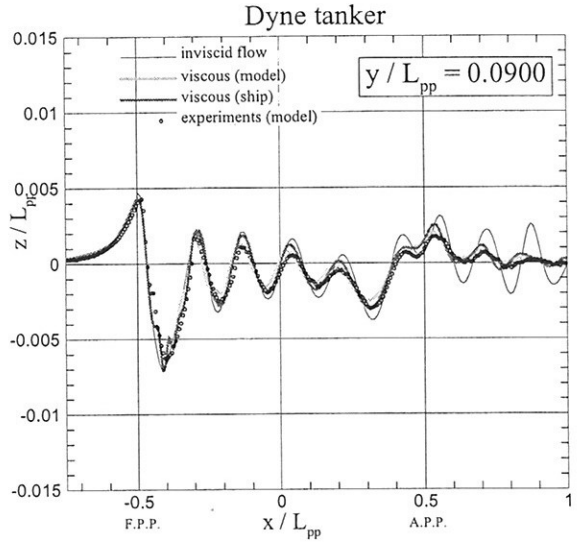

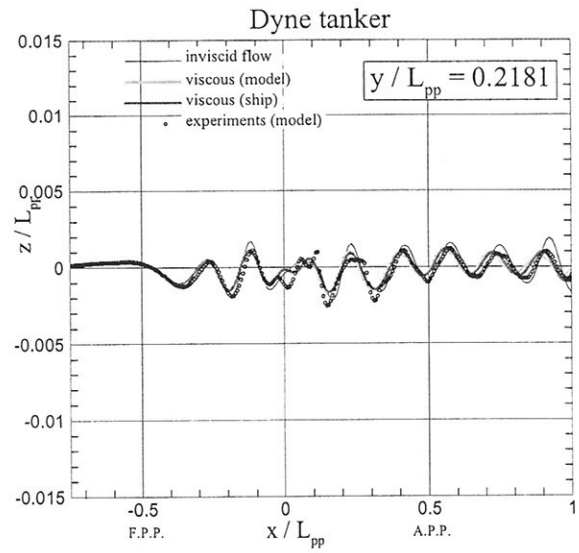

Figure 5: The Reynolds scale effect on the wave pattern of the Dyne tanker.

This is especially clear in the wave cut closest to the hull. At full scale the wave amplitudes behind the stern are somewhat higher compared to both the model scale computation and the experiments, while they are smaller than in the prediction with the non-linear panel method. This result is consistent with our earlier observation that the viscous damping of the stern wave system decreases with increasing Reynolds number.

It can also be observed, however, that the scale effect on the stern wave system is relatively small in this case. Especially further away from the hull, the predicted scale effects are of the same order of magnitude as the level of grid independence claimed in the previous section. This is illustrated in more detail in Fig. 6. Here, the predicted model-scale waterlines at the finest and second finest mesh (the light-grey lines) are shown together with the corresponding full-scale predictions (the dark-grey lines). Close to the stern, around $x/L_{pp}=0.5$, both model-scale solutions are visibly located below the full-scale solutions. Further downstream, however, all four lines practically coincide and there the scale effect is of the same order of magnitude as the level of grid independence of the solution, which of course limits a further analysis of the scale effect.

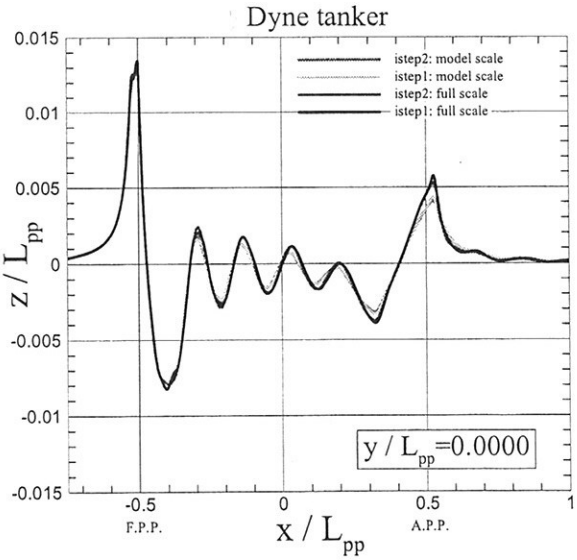

Figure 6: Scale effect on the waterline in relation to the grid dependence of the solution.

CONCLUSION

With the development of a solution method for the problem of viscous flow around ship hulls, including wave making, a tool has become available to study and quantify the Reynolds scale effect on the wave system. The results may be used to verify or improve extrapolation methods used in model testing. In cases such as the Dyne tanker, however, this still requires a significant computational effort. First, because the relatively low Froude number of this test case requires a rather high mesh density in the main stream direction. And second, because for this specific test case the Reynolds scale effect on the wave system is relatively small. Nevertheless, we have shown that it is indeed possible to solve the RANS/FS problem with sufficient accuracy to quantify the moderate differences between the wave systems at model scale and at full scale.

REFERENCES

Hoekstra, M., "Numerical simulation of ship stern flows with a space-marching Navier Stokes method", Thesis, Delft University of Technology, October 1999.

Larsson, L., Patel, V.C. and Dyne, G. (Eds.), "SSPA-CTH-IIHR workshop on viscous flow", Flowtech Research Report 2, Flowtech Int. AB, Gothenburg, Sweden, 1991.

Lundgren, H. and Åhman, M., "Experimentell och numerisk bestämning av vågmotstand för ett tankfartyg (Dynetankern)", Report No. X-94/58, Dept. Naval Architecture and Ocean Engineering, Chalmers Univ. Techn., Gothenburg, Sweden, 1994. (In swedish).

Raven, H.C., "A solution method for the nonlinear ship wave resistance problem", Thesis, Technical University of Delft, June, 1996.

Raven, H.C. and Starke, A.R., "Efficient methods to compute ship viscous flow with free surface", 24th Symp. Naval Hydrodynamics, Fukuoka, Japan, 2002.

Raven, H.C., Van der Ploeg, A. and Starke, A.R., "Computation of free-surface viscous flows at model and full scale by a steady iterative approach", 25th Symp. Naval Hydrodynamics, St. John's, Canada, 2004.

Raven, H.C. and Van Brummelen, E.H., "A new approach to computing steady free-surface viscous flow problems", 1st MARNET-CFD Workshop, Barcelona, Spain, 1999.

Van Brummelen, E.H. and Raven, H.C., "Numerical solution of steady free-surface Navier-Stokes flow", 15th Int. Workshop on Water Waves and Bodies, Ceasarea, Israel, 2000.

Yet another coupled Navier-Stokes solver

Arthur Stück, arthur.stueck@tu-harburg.de
Gerhard Jensen, g.jensen@tu-harburg.de
Daniel Schmode, d.schmode@tu-harburg.de
AB 3-13 of TU Hamburg-Harburg, Lämmersieth 90, 22305 Hamburg

1 Introduction

Navier-Stokes solvers, based on segregated *SIMPLE*-like algorithms, are widely used in maritime industry. In this paper a completely different approach is presented—i.e. assembling the linearised momentum equations and the continuity equation in one linear equation system (LES). The method uses a cell-centered, collocated grid approach and the Picard iteration scheme to linearise the convective terms.

In contrast to common segregated algorithms, implicit pressure-velocity coupling is ensured for every step right from the beginning of the iteration process, as the Navier-Stokes equations are solved simultaneously for pressure and velocities. Therefore the method is expected to show increased robustness, especially facing awkward grids of high cell skew and aspect ratio.

Validation and performance studies are carried out on the base of a steady 2D lid-driven cavity flow at Reynolds number $Re = 1000$.

2 Governing equations

Incompressible, steady flow is described by the Navier-Stokes equations, consisting of the continuity equation

$$\int_S \rho\, \vec{v} \cdot \vec{n}\, dS = 0$$

and the momentum equations

$$\int_S \rho\, u_i \vec{v} \cdot \vec{n}\, dS = \int_S \mu\, \mathrm{grad}\, u_i \cdot \vec{n}\, dS - \int_S p\, \vec{i}_i \cdot \vec{n}\, dS$$

This investigation is restricted to 2D problems, while the flow is assumed to be entirely laminar.

3 Discretisation

The solution algorithm uses a collocated grid approach, storing all variables (velocities and pressure) in the middle of each control volume (CV).

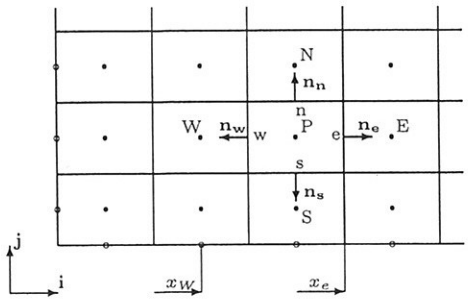

Figure 1: Collocated grid arrangement

As linear solvers are to be applied, linearisation is performed according to the Picard iteration: On Cartesian grids the convective flux through the east CV face is interpreted as

$$F_e^c \approx (\dot{m}\, u_x)_e$$

calculating the mass fluxes $\dot{m}$ with the velocities of the previous iteration u_i^{old}. On behalf of stability, the CV face velocities are determined implicitly by upwind schemes (UDS)—to increase accuracy, a deferred central difference (CDS) correction is made explicitly with the velocities of the previous Picard step.

Diffusive velocity gradients on the CV face centres are determined by CDS.

Volume and cell face integrals are calculated according to the mid-point rule.

Velocity coefficients of the momentum equations are assembled within sub-matrix $\mathbf{A}$ (fig. 2), which has a penta-diagonal structure for the 2D case.

Discretisation of the pressure terms within the momentum equations (sub-matrix $\mathbf{B}$) is a crucial issue in terms of the collocated grid alignment. According to Ferzinger and Peric [1], CDS pressure discretisation can cause oscillations on equidistant grids. In that case the central pressure coefficients drop out and allow a checkered pressure distribution to come up. The vanishing central coefficients are indicated by dashed matrix diagonals within sub-matrix $\mathbf{B}$.

A third order polynomial pressure approximation would contain the central coefficients; but it would

not be symmetric and violate elliptical pressure propagation.

Alternatively, a fourth order polynomial approximation is implemented. The central coefficients drop out again on equidistant grids. The additional outer coefficients (EE, NN, WW, SS) are only 1/10 the magnitude of the inner ones and might be too weak to rid the chequerboard. Generally, high order approximations are costly to implement and tend to cause oscillations—so just increasing the approximation order is not considered very promising.

For *SIMPLE*-like algorithms [6] these oscillations are typically overcome by a correction term in the discrete pressure correction equation, originally proposed by Rhie and Chow [7]. This approach is adopted to our *coupled* code, applying the correction term to the discrete continuity equation

$$(u_e^* - u_w^*)\,\Delta y + (v_n^* - v_s^*)\,\Delta x = 0$$

containing the Rhie-Chow corrected CV-face velocities

$$u_e^* = \overline{(u)}_e - (\Delta V)_e \overline{\left(\frac{1}{A_P^u}\right)}_e \left[\frac{p_E - p_P}{\Delta x} - \overline{\left(\frac{\partial p}{\partial x}\right)}_e\right]$$

and

A_P^u	central velocity coefficient from momentum equation
ΔV	volume of staggered CV

Over-lined expressions denote CV-face values which are interpolated linearly from the nodal values.

This correction term makes out oscillations within the pressure field and restricts its variations to be quadratic at most. Here Rhie and Chow's term (RCT) is included implicitly within the continuity equation (sub-matrix $\mathbf{C}$), extending the pressure molecule to the neighbouring EE, WW, NN and SS nodes. This way a smooth pressure distribution is ensured while the pressure approximation within the momentum equations can be second order again. The suggested RCT addenda to the continuity equation are also plotted in dashed lines.

If second order approximations are used for the pressure terms within the momentum equations and the discretisation of the continuity equation, the diagonal matrices within $\mathbf{B}^*$ are equal to the diagonal matrices of $\mathbf{B}$.

4 Solvers

To solve the linearised Navier-Stokes equations (fig. 2) we use the PETSc software package, provided by the the Argonne National Laboratory [5]. Owing

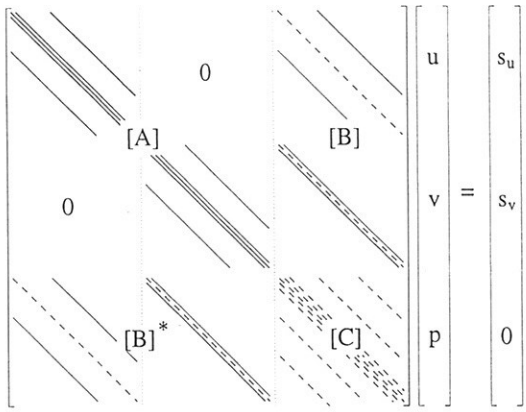

Figure 2: *Coupled* equation system

to the unsymmetry of the coefficient matrix, GMRes, BiCGSTAB and BiCG solvers are used, combined with ILU preconditioning.

Results are returned by the solver once a demanded inner residual has been reached. Then the next Picard iteration follows and the solver is called once again.

Preconditioning and solver parameters have not been investigated in detail. So far the default settings are used, so that a certain acceleration of the code should be possible.

5 Results

A 2D lid-driven cavity flow at $Re = 1000$ (fig. 3) is used to validate the code.

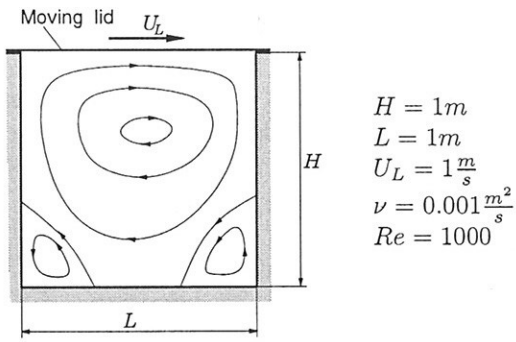

Figure 3: Lid-driven cavity flow case

As described above, the collocated grid arrangement requires special pressure treatment to avoid oscillating pressure fields. Fig. 4 shows the grid-dependency of these oscillations, caused by second order discretisation without RCT: The lower left quarter shows a smooth pressure distribution due to the two-dimensional grid expansion. Upper left and lower right quarters use one-dimensional grid expansion,

causing growing oscillations. Top right the equidistant mesh suffers from severe oscillations. This shows the influence of the central pressure coefficient, which is zero for equidistant grids. The picture also demonstrates the local character of the oscillations.

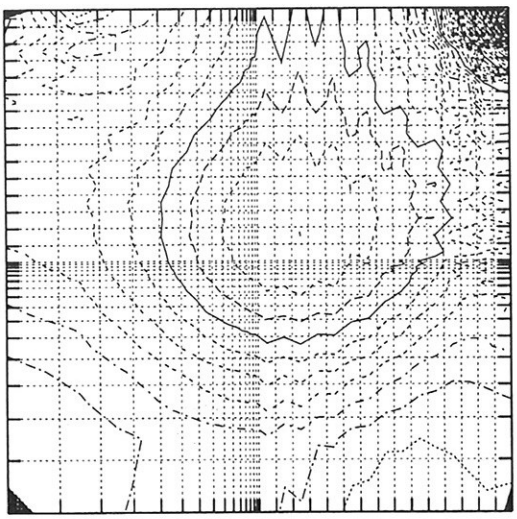

Figure 4: Grid dependent pressure oscillations, 2nd order prs. discr. without RCT

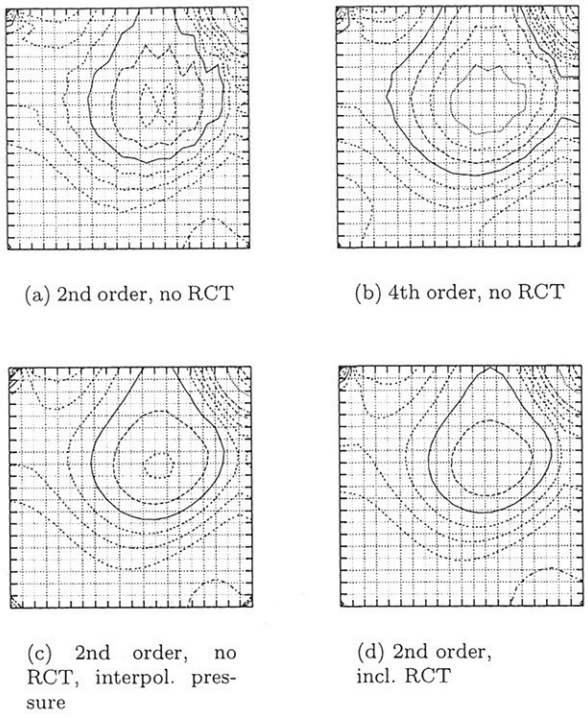

(a) 2nd order, no RCT

(b) 4th order, no RCT

(c) 2nd order, no RCT, interpol. pressure

(d) 2nd order, incl. RCT

Figure 5: Different pressure discretisations

The outcome of different pressure treatments, which have been applied during the project to eliminate the oscillations, is presented in fig. 5:

- The second order pressure discretisation shows the well-known oscillations on equidistant collocated grids (fig. 5(a)).
- The fourth order pressure discretisation can reduce oscillations, but as expected its coupling effect is too weak to provide a smooth pressure field (fig. 5(b)).
- In fig. 5(c) the oscillating pressure field of fig. 5(a) has been smoothed in postprocessing by linear interpolation. This crude procedure will only work as long as convergence can be obtained in spite of oscillations.
- Eventually, implementation of RCT, combined with second order pressure discretisation in the momentum equations, yields smooth pressure fields (fig. 5(d)).

The following results are obtained by RCT correction within the continuity equation and second order pressure discretisation in the momentum equations. Output is compared against Peric and Schreck's *SIMPLE* algorithm [6]. A 30×30 grid is chosen, using double-sided expansion ($r = 1.1$) in x and y direction. The velocity field is plotted in fig. 6.

Fig. 7 shows the influence of UDS-CDS blending on the velocity profiles. The UDS case suffers from numerical diffusion, showing flattened velocity profiles and smeared gradients. The *SIMPLE* profiles for the 0.7 UDS case are included in fig. 7—they are hardly recognisable as they are matching with the referring *coupled* curves very well. For all cases results showed excellent agreement.

6 Assessment of algorithm

Only a few selected parameters have been investigated as presented in the following, exhaustive performance and optimisation studies have not been undertaken yet.

Over- and under-relaxation have been applied to the mass fluxes within the momentum equations. According to fig. 8, relaxation does not accelerate the solver for the current test case. The demanded accuracy (inner residual), the Picard steps are solved with, is varied for every relaxation factor. Over the whole range of inner accuracy the minimum CPU time is required for $\beta_{ur} = 1$. Neither a higher inner accuracy for over-relaxation, nor a lower accuracy for under-relaxation are justified.

Subsequently, the consumption of CPU time over the grid size is investigated, which is crucial when

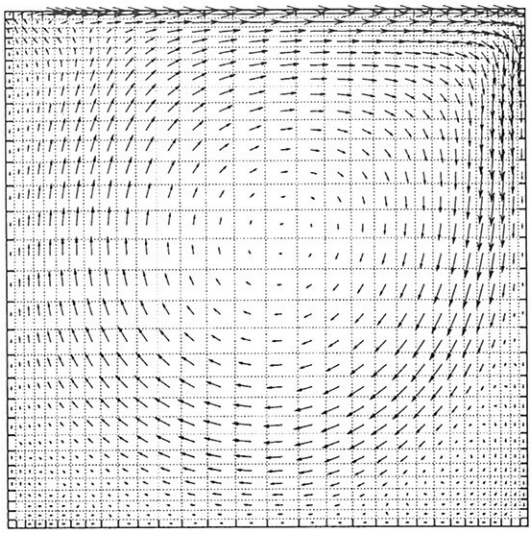

Figure 6: *Coupled* velocity field, pure CDS

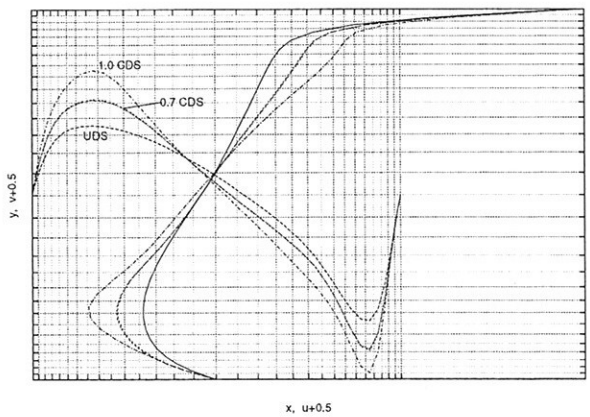

Figure 7: *Coupled* and *SIMPLE* velocity profiles, variation of CDS-UDS blending

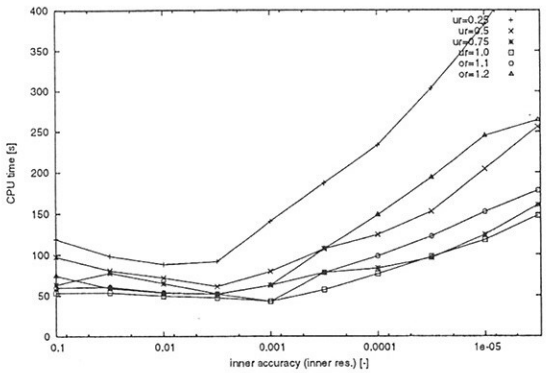

Figure 8: Relaxation of mass fluxes, *coupled* (GMRes with ILU)

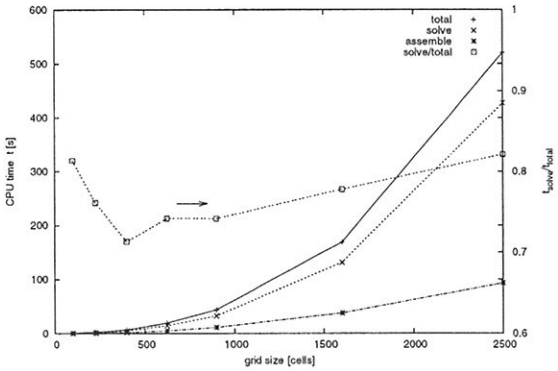

Figure 9: CPU time over gird size, *coupled* (GMRes with ILU)

it comes to practical CFD analysis. This has been investigated for the GMRes solver with ILU preconditioning. Fig. 9 subdivides the *total* CPU time into *assembling* time for the iteration matrices and *solving* time for the LES. For small cases the ratio t_{solve}/t_{total} is relatively low; for a 100×100 test case it becomes 96%. The CPU time for solving increases with the grid size to the power of 2.5. The assembling time should grow almost linearly as the iteration matrices have a diagonal structure; here it grows faster, indicating that the assembling routine could be a little slimmer.

To get a first impression of the robustness of the algorithm, the grid quality is worsened systematically by creating cells of high aspect ratio $\Lambda = l/b$. As shown in fig. 4, expansion ratios $r < 1$ go out from the lower and the left cavity wall, refining cells towards the middle of the domain; from there on the grid is equidistant. The maximum cell aspect ratio is controlled by decreasing the expansion ratio r. Both, *coupled* (ILU preconditioning and GMRes solver) and *SIMPLE* algorithm (SIP solver) are confronted with these awkward grids. In either case residuals are to be reduced for five orders of magnitude. Fig. 10 shows the consumed CPU time over the maximum aspect ratio Λ of the used grid. When the cells get stretched, *SIMPLE* is slowed down as it requires heavy underrelaxation (particularly for the pressure correction equation). The *coupled* code can profit relatively, shown by the ratio $t_{coupled}/t_{simple}$.

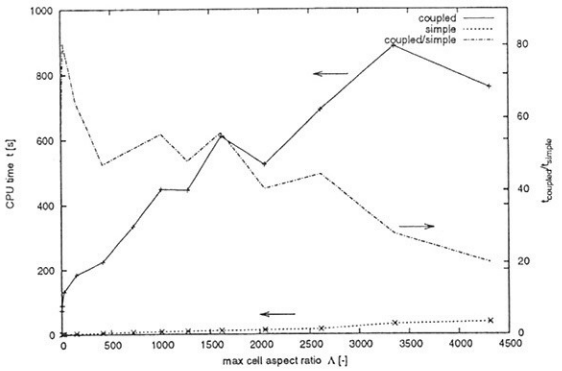

Figure 10: Performance over grid quality

7 Conclusions and outlook

As far as the first investigations have indicated, the *coupled* algorithm can be regarded an accurate and robust Navier-Stokes solver. The code has not been systematically optimised yet, so that a certain speedup should be possible. In its current version, it is clearly outpaced by the *SIMPLE* algorithm. But its potential is believed to lie in its robustness due to direct pressure-velocity coupling. This is backed by the brief performance study on awkward grids. So far the code can only deal with Cartesian, structured grids—but particularly when it comes to unstructured arrangements, with cells of high skew and aspect ratio, its advantages are expected to be more distinct.

In contrast to segregated solvers, simultaneous variable treatment inflates the equation systems: In case of 2D laminar Navier-Stokes this is about thrice the volume *SIMPLE*-like algorithms require; for more sophisticated turbulent 3D CFD, it will of course become more costly. But as today's computers provide economically priced memory, the coupled approach becomes more attractive.

This investigation has been restricted to steady, laminar 2D flow. For future studies the coupled approach could be extended to further variables, e.g. for transport of turbulence or free surfaces, to simulate more sophisticated problems.

References

[1] J.H. FERZIGER, M. PERIC
Computational Methods for Fluid Dynamics
Springer (1997)

[2] G.B. Deng, J. Piquet, P. Queutey and M. Visonneau
A new fully coupled solution of the Navier-Stokes equations
International journal for numerical methods in fluids, vol. 19, 605-639 (1994)

[3] C. Vuik and A. Segal
Solution of the coupled Navier-Stokes equations
Report 95-28, Delft University of Technology (1995)

[4] J. Fischer, W. Mackens
Anwendung eines approximativen Newtonverfahrens auf Finite-Volumen-diskretisierte Navier-Stokes Gleichungen
Diplomarbeit, Institut für angewandte Mathematik der Universität Hamburg (1997)

[5] *PETSc Users Manual*
Mathematics and Computer Science Division, Argonne National Laboratory
http://www.mcs.anl.gov/petsc

[6] M. Peric, E. Schreck
program comet (parp.f)
Institut für Schiffbau der Universität Hamburg (1994)
ftp://ftp.springer.de/pub/technik/peric

[7] C.M. Rhie and W.L. Chow
A numerical study of the turbulent flow past an isolated airfoil with trailing edge separation
AIAA J., 21, 1525-1532 (1983)

7th Numerical Towing Tank Symposium
Hamburg, GERMANY, 3-5 October 2004

Simulation and Validation of the Viscous Flow around the Series 60 Hull Form at 10° Drift Angle

Serge Toxopeus
Maritime Research Institute Netherlands (MARIN), P.O. Box 28, 6700 AA Wageningen, Netherlands.
e-mail: S.L.Toxopeus@MARIN.NL

INTRODUCTION

In order to optimise the flow in the aft region of ships, viscous-flow calculations are increasingly used. For studies into the manoeuvrability of ships, however, only limited use is made of viscous-flow calculations. One of the major reasons for this is that these calculations involve substantial computing requirements. Another reason is that validation material is sparse and only a few successful demonstrations of the practical application of these calculations are available. Furthermore, in order to study the manoeuvrability of a ship, either time-domain viscous-flow calculations for the ship with active propulsion and steering appendages should be made, or a dedicated mathematical model should be derived from viscous flow calculations for steady yaw and drift conditions.
At MARIN, viscous-flow computations are used frequently for the optimisation of hull forms from a resistance and powering point of view. Currently, studies are conducted to extend the capabilities of this solver to also simulate the flow around ships in oblique flow. Besides the possibility to study the detailed flow around the ship in various conditions, this is the first step towards using the viscous flow solver as a tool to predict the forces and moments on manoeuvring ships.

Extensive flow field measurements on the well-known Series 60 hull form were conducted at Iowa Institute of Hydraulic Research (IIHR) and the results were made available to the public. Therefore, this case is very suitable for validation studies of viscous-flow calculations. Various researchers have already reported such validation studies. Some of these are Alessandrini and Delhommeau [1], Cura Hochbaum [2], Di Mascio and Campana [3] and Tahara et al. [4].
This paper presents viscous-flow calculations conducted on the Series 60 hull form sailing at a drift angle. In order to examine the reliability of the predicted flow fields and integrated quantities derived from the solution, the discretisation error in the result is studied based on grid refinement. To validate the results, detailed comparisons are made between model measurements conducted at IIHR and simulations of the viscous flow around the model.

PARTICULARS OF THE SHIP AND VALIDATED CONDITIONS

The hull form under consideration is the Series 60 with a block coefficient C_B of 0.6. The particulars of this hull form are presented below, taken from Longo [5]:

Main particulars of Series 60

Designation	Model scale (1:40)	Full scale
Length L_{pp}	3.048 m	121.92 m
Beam B	0.406 m	16.26 m
Draught T	0.163 m	6.502 m
Block coefficient C_B	0.6	0.6
Wetted area S	1.579 m^2	2526.4 m^2

Bilge keels, rudder and propeller were not present during the model tests and are therefore not modelled in the calculations.

As a first step, the calculations are conducted with an undisturbed water surface, i.e. neglecting the generation of waves. The measurements were conducted at two different Froude numbers, i.e. Fn=0.16 and Fn=0.316. For the validation study of the flow fields presented in this paper, the Fn=0.16 results are used.

The measurements of the mean velocities and pressure fields were conducted with the model restrained from moving in any direction relative to the carriage. For the measurements of the forces and moments, however, the model was free to heave, roll and pitch.

Because of the definition of the coordinate system used in the calculations for the present study, the data of the IIHR measurements have been mirrored to allow for easier comparison with the numerical results. This means that in this study, the starboard side is the pressure side and the port-side the suction side.

The origin of the right-handed system of axes used in this study is located at the intersection of the water-plane, midship and centre-plane, with x directed aft, y to starboard and z vertically upward. Note that all coordinates given in this paper are made non-dimensional with L_{pp} unless otherwise specified. All velocities are made non-dimensional with the undisturbed velocity U_0.

NUMERICAL PROCEDURES

Boundary conditions

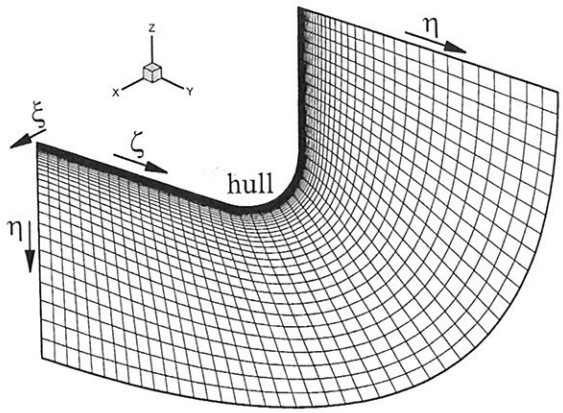

Figure 1: Definition of curvilinear coordinate system

At the hull surface, no-slip and impermeability boundary conditions are used. The velocities are set to zero ($\overline{u}=0$) while the pressure is extrapolated from the interior. Symmetry conditions are used on the water surface:

$$u_\zeta = 0, \frac{\partial u_\xi}{\partial \zeta} = 0, \frac{\partial u_\eta}{\partial \zeta} = 0, \frac{\partial p}{\partial \zeta} = 0$$

Because the velocity and pressure behind the ship are unknown, Neumann boundary conditions are applied on the outflow plane:

$$\frac{\partial u_i}{\partial \xi} = 0, \frac{\partial p}{\partial \xi} = 0$$

The velocity components in the inflow plane and off-body plane are taken from a potential flow calculation while the pressures in both planes are calculated using the Bernoulli equation. During the viscous-flow calculation however, the velocity normal to the off-body plane is updated to allow for the displacement effect of the viscous boundary layer.

Solver set-up

Use was made of the in-house solver PARNASSOS [6]. It solves the discretised Reynolds-averaged Navier-Stokes equations for a steady, three-dimensional incompressible flow around a ship hull, supplemented by a turbulence model. For all calculations, Menter's one-equation turbulence model [7] extended with the correction for longitudinal vorticity of Dacles-Mariani [8] was used. The governing equations are integrated down to the wall, i.e. no wall-functions are used. The latest developments in the solver are described in a recent paper by Raven, Van der Ploeg and Starke [9].

In the solver grid-sequencing is automatically conducted in order to accelerate convergence on the final grid. This technique starts the calculation on a coarse grid (istep=8) obtained by taking every 8th stream-wise plane and converges until the maximum changes in the pressure are below a certain limit. Then the grid is refined (istep=4) and the calculation is continued until the required convergence. This procedure is conducted until the solution satisfies the specified convergence criterion on the finest grid (istep=1). For the present study, all solutions were converged until the maximum variation of the pressure coefficient dropped well below $5 \cdot 10^{-5}$.

COMPUTATIONAL DOMAIN AND GRID

Grid generation

For each calculation, separate blocks are used for the port side and starboard side of the computational space. Each block consists of an inner block and an outer block. The inner block is the same for all yaw angles and the outer block can deform to allow for the drift angle of the ship. Therefore grids for various drift angles can be made efficiently. Due to the division of the computational domain in an inner and outer block, control of the quality of the grid near the hull is obtained. Use is made of body-fitted, non-orthogonal HO-type grids, which are strongly stretched towards the hull to capture the strong gradients in the boundary layer.

The inner block is generated with a number of cells corresponding to normal MARIN practise in resistance and powering optimisation calculations, see Hoekstra [6] or Eça et al. [10]. The size (length, depth and width) of this domain is based on experience with simulations of the viscous flow around a ship sailing with zero drift angle.

During the grid generation, first a base-grid is generated using a 3D elliptic grid generator, with a reasonably stretched grid node distribution in the normal direction, j, and the desired node distributions in stream-wise, i, and girth-wise, k, directions. By varying the control parameters in the grid generation process, the deviation from orthogonality is reduced as much as practically possible. Then grid stretching along the surface-normal grid lines is applied to arrive at the desired grid spacing at the hull surface.

To incorporate the drift angle of the ship, the inner block is rotated around the z-axis over the desired yaw angle. Then the outer block is generated around the inner block. The interfaces between the blocks are matching to allow for subsequent merging of the inner and outer blocks. The stretching used in the inner block is automatically applied to the outer block as well. The size of the outer blocks is chosen such that the rotated inner block can smoothly be incorporated in the outer grids. This means that increasing drift angles will result in wider domains. The size of the domain is based on the assumption that a solver for potential flow is used to calculate the velocities in the inflow and off-body planes. Before starting the calculations, the separate blocks are merged into one block on the port side of the ship and another block on the starboard side of the ship.

The grid used in this study incorporates the hull form of the Series 60 for 10 degrees of drift angle. The port-side and starboard blocks together had for the finest grid 289×81×90 nodes in stream-wise, wall-normal and girth-wise direction respectively, resulting in a total of over 2 million nodes. Compared to similar studies presented in literature this number of grid nodes is relatively large. The maximum deviation from orthogonality in this grid was 45°. The inflow plane was located at $0.65 \cdot L_{pp}$ forward of midship and the outflow plane $0.82 \cdot L_{pp}$ aft of midship. The width and depth of the domain were $0.88 \cdot L_{pp}$ and $0.27 \cdot L_{pp}$ respectively.

In the figure below, a top view of the grid (coarsed for presentation purposes) used for this study is presented. The bow is directed to the left of the figure.

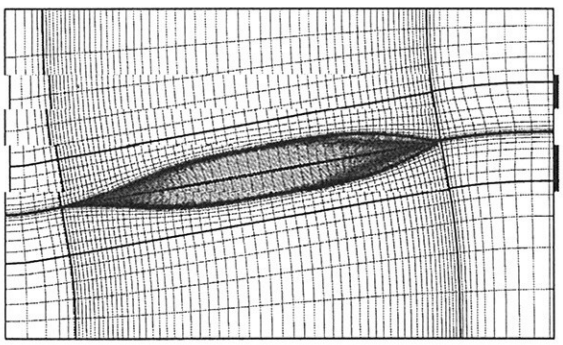

Figure 2: Series 60, computational grid, 10° drift

Discretisation of the hull form

Due to the grid sequencing technique, changes in the discretised representation of the geometry of the ship occur. In Figure 3, an example is given of the changes in the geometry at the bow. The location chosen for this example is just above the lowest part of the bow. The small black squares in this figure represent the grid nodes according to the finest grid. The first point in stream wise direction on the hull is located at i=27. When coarsening the grid to istep=2, it is seen that the nodes at i=28 are removed. This sharpens the bow at this location. However, since i=27 is still the first grid node to represent the hull form, this will probably have only a small influence on the flow around the ship.

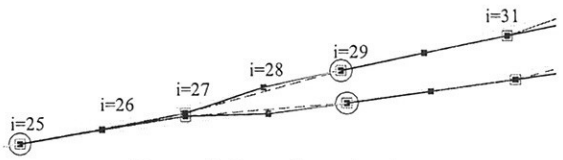

Figure 3: Bow discretisation, top view of k = 5/40, j=1 lines istep=1: black, 2: dashed grey/square, 4: light grey/circle

Coarsening even further to istep=4, the nodes at i=27 are removed and the nodes at i=29 become the first hull nodes. This means that a considerable change in the effective geometry is introduced. The distance between the nodes at i=27 and i=29 is 0.675 m, or $0.6\% \cdot L_{pp}$. For istep=8, the first hull nodes are at i=31, introducing an even larger change in the discretised geometry. The distance from i=25 to i=31 is 1.38 m or $1.1\% \cdot L_{pp}$. It is expected that these changes in the discretisation of the hull form have influence on the flow around the bow and especially on the forces generated at the fore ship.

REVIEW OF THE CALCULATIONS

The following calculations were conducted for the Series 60 at 10° drift angle:

istep	ni	nj	nk	nodes	Δp_{max}	y+
1	289	81	90	$2107 \cdot 10^3$	$9.4 \cdot 10^{-6}$	0.38
2	145	81	90	$1057 \cdot 10^3$	$5.9 \cdot 10^{-6}$	0.33
4	73	81	90	$532 \cdot 10^3$	$4.1 \cdot 10^{-6}$	0.34
8	37	81	90	$270 \cdot 10^3$	$9.3 \cdot 10^{-6}$	0.30

The reference velocity U_0 for the calculations corresponded to a model scale value of 0.875 $m \cdot s^{-1}$. With a kinematic viscosity ν of $1.138 \cdot 10^{-6}$ $m^2 \cdot s^{-1}$ this results in a Reynolds number of $2.34 \cdot 10^6$. All calculations were conducted with undisturbed water plane.

GRID DEPENDENCY STUDY

Based on the results of the calculations using different grid densities, the discretisation error in the solution can be examined. In Figure 4 and Figure 5, the value of the longitudinal velocity u is presented against the transverse position with respect to the centreline.

Figure 4 contains the results for a transverse cut close to the water surface and is located at x=0.3 (i.e. aft of midship) and z=-0.015. Figure 5 shows the results of a cut close to the bilge, for x=0.3 and z=-0.048.

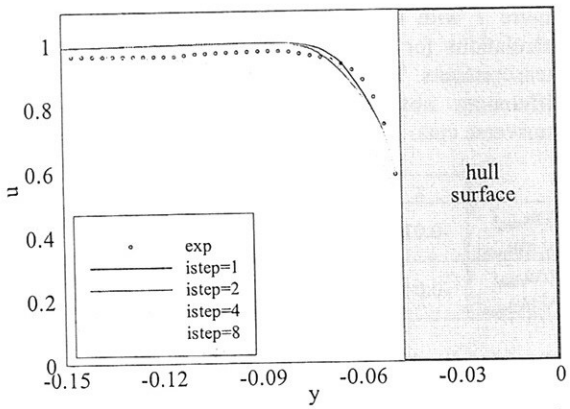

Figure 4: Comparison grid density and experimental data, x=0.3, z=-0.015, longitudinal velocity

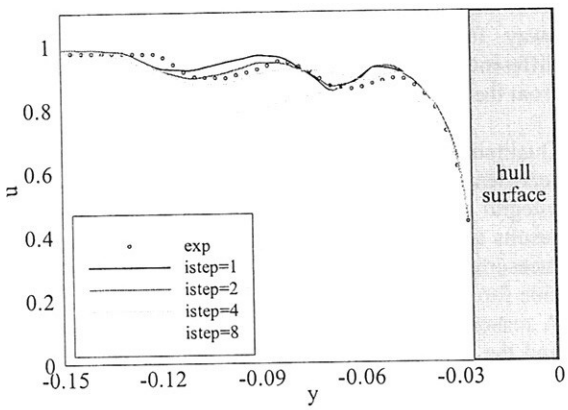

Figure 5: Comparison grid density and experimental data, x=0.3, z=-0.048, longitudinal velocity

Both figures show that the results on the finest grid are not yet grid-independent. But it is encouraging that the differences between successive numerical solutions decrease with increasing mesh density (within 2.6% for the cut close to the water plane and 3.3% for the cut close to the bilge).

In Figure 6 and Figure 7 the differences between the calculated longitudinal velocity and the experimental values are given for the four grids. Especially in the results for the transverse cut at z=-0.048, which is placed directly through the vortex originating from the bilge, the solution still changes with increasing mesh density. However, once again the differences between successive solutions decrease with increasing mesh density.

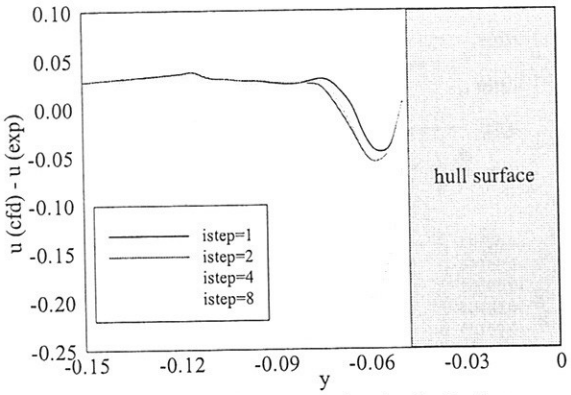

Figure 6: Difference in longitudinal velocity between calculations and experiments, x=0.3, z=-0.015

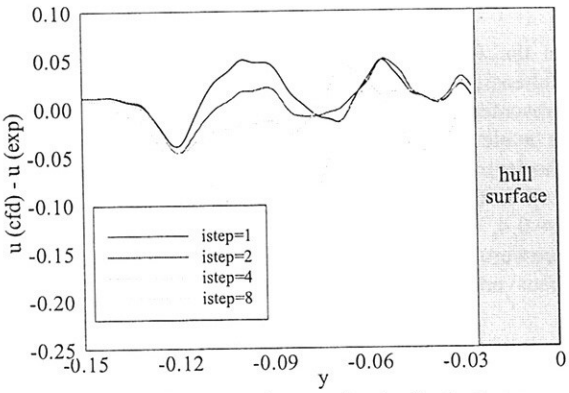

Figure 7: Difference in longitudinal velocity between calculations and experiments, x=0.3, z=-0.048

Also the dependency of the integrated forces on the ship for the various grids has been studied. In Figure 8, the non-dimensional transverse force Y and yawing moment N for the different grid densities are given. Y is made non-dimensional with $0.5 \cdot \rho \cdot U_0 \cdot S$ and N with $0.5 \cdot \rho \cdot U_0 \cdot L_{pp}^3$. The relative step-size indicates the coarseness of the grid with respect to the finest grid. Theoretically, the discretisation error disappears if the solution is extrapolated to the y-axis. The extrapolated value is the value that should be compared to the experiments. The figure illustrates that for the transverse force as well as the yawing moment the difference in the results for progressively finer grids reduces to less than 2.5%. However, work by Eça and Hoekstra [11] has shown that extrapolation of the results from grid dependency studies to zero relative step size for this type of computations is not trivial. For a reliable extrapolation only four grids are insufficient. Figure 8 can therefore only be used as an indication of the reliability of the solution.

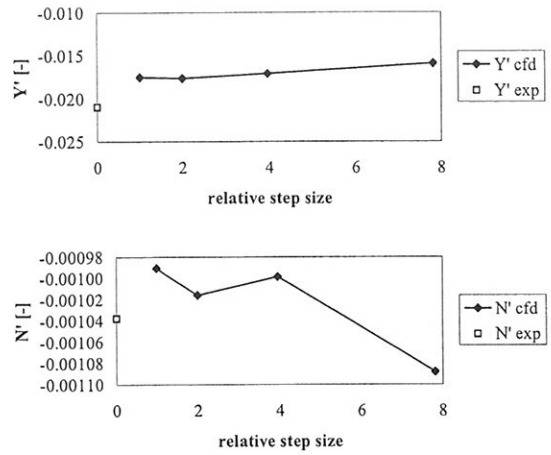

Figure 8: Grid dependency of integrated variables

In the following figure, the distribution of the non-dimensional transverse force along the length is presented for the different grids. In this case, the force is made non-dimensional using the wetted surface of the segment instead of the total hull wetted surface. The hull is divided into ten segments with boundaries on x=-0.4, -0.3, ... 0.3 and 0.4. For each segment, the total pressure and friction are integrated to arrive at the transverse force for that segment.

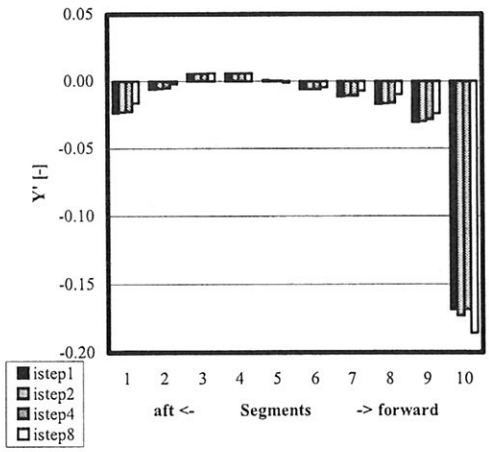

Figure 9: Longitudinal distribution of transverse force

This distribution complies with the distribution normally found when conducting model tests with segmented models at a drift angle. Examining the results, it is clearly seen that istep=8 differs from the three other grids. The largest difference between istep2 and istep1 is 4 kN in segment 10. This is a difference of 2.6%. Segment 10 is the foremost segment and this is also the segment that generates the largest side force, as is often seen in segmented model test results.

COMPARISON WITH EXPERIMENTS

Already in the previous sections, the results of the calculations have been presented along with results of the experiments. As can be seen in Figure 4 through Figure 7 with the transverse cuts, the results of the calculations for the finest grid are quite close to the measurements. The table below presents the maximum differences obtained from the comparison of the transverse cuts:

	z	istep=1	istep=2	istep=4	istep=8
$\|\Delta u_{max}\|$	-0.015	0.046	0.056	0.055	0.120
y $\|\Delta u_{max}\|$		-0.056	-0.058	-0.058	-0.062
$\|\Delta u_{max}\|$	-0.048	0.049	0.049	0.047	0.132
y $\|\Delta u_{max}\|$		-0.099	-0.054	-0.119	-0.084

These results show that for istep=1, the maximum error in the longitudinal velocity at the two transverse cuts at x=0.3 is less than 5%. For the results for z=-0.015 it is seen that the largest differences occur close to the hull surface. The results for z=-0.048 show that the vortex from the bilge in the calculations is slightly shifted away from the hull, resulting in relatively large differences when subtracting the experimental results from the calculations.

Qualitatively, the physics of the flow are well represented. Quantitatively, the comparison of the integral forces in Figure 8 shows that for the istep=1 results a good correlation of the yaw moment with the measurements is found. However, a deviation of the side force from the experimental values is also present. A reason for the discrepancy between the simulations and the experiments can be that the experiments were conducted with the model free to trim and sink while the calculations were done with the ship on even keel. Furthermore, differences may be introduced because in the calculations an undisturbed water plane was assumed. The influence of this assumption has to be examined in further studies.

In Figure 10 through Figure 12, the calculated longitudinal velocity fields based on the finest grid for several transverse planes are given together with the velocity field obtained from the experiments. Note that the calculated results have been projected on the measurement points and therefore some irregularities that are present in the measurement data are introduced in the simulation results. The dashed lines represent the measurements and the continuous lines represent the calculations.

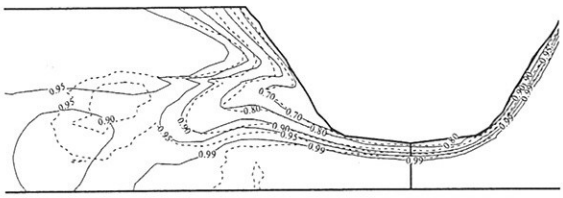

Figure 10: Axial velocity contours, x=0.3, 10° drift

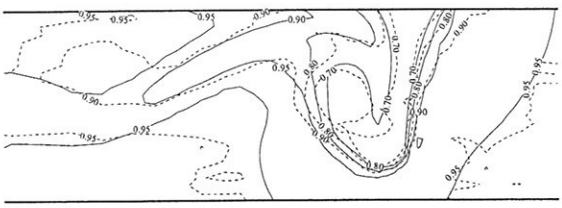

Figure 11: Axial velocity contours, x=0.5, 10° drift

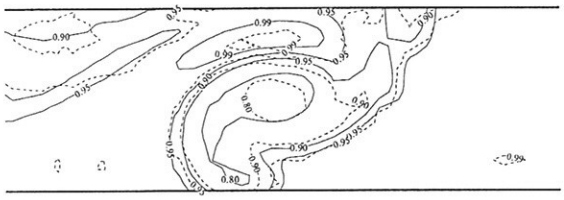

Figure 12: Axial velocity contours, x=0.7, 10° drift

The correspondence between the measurements and the simulations is very promising and most calculated contour lines follow the contours from the experiments closely. The calculated velocity profile at the keel is very close to the measured profile while the position and magnitude of the vortex developing at the keel is well predicted. The strength of the vortex from the bow area is slightly less than found during the measurements and the location is somewhat shifted downward and further away from the ship.

CONCLUSIONS

Simulations have been conducted of the viscous-flow around the Series 60 hull form at 10° drift angle for several grid densities. Although still notable differences between the two finest meshes were found, detailed comparisons with experimental data show that the physics of the flow are well predicted even when looking at discrete positions in the flow field. Qualitatively, promising results are obtained. For practical purposes however, the accuracy of the results should be improved. For the current calculations, the predicted yaw moment is close to the measurements but the side force is under-predicted. Reasons for these discrepancies might be the neglect of trim and sinkage and of the water surface deformation. This should be studied in future research.

REFERENCES

[1] B. Alessandrini and G. Delhommeau. "Viscous free surface flow past a ship in drift and in rotating motion". *22nd Symposium on Naval Hydrodynamics*, pages 491–507, August 1998.

[2] A. Cura Hochbaum. "Computation of the turbulent flow around a ship model in steady turn and in steady oblique motion". *22nd Symposium on Naval Hydrodynamics*, pages 550–567, August 1998.

[3] A. Di Mascio and E.F. Campana. "The numerical simulation of the yaw flow of a free surface ship". *7th International Conference on Numerical Ship Hydrodynamics*, pages 6.1–1–10, July 1999.

[4] Y. Tahara, J. Longo, and F. Stern. "Comparison of CFD and EFD for the Series 60 CB=0.6 in steady drift motion". *Journal of Marine Science and Technology*, pages 7:17–30, 2002.

[5] J.F. Longo. *Effects of Yaw on Model-Scale Ship Flows*. PhD thesis, University of Iowa, May 1996.

[6] M. Hoekstra. *Numerical Simulation of Ship Stern Flows with a Space-Marching Navier-Stokes Method*. PhD thesis, Delft University of Technology, Faculty of Mechanical Engineering and Marine Technology, October 1999.

[7] F.R. Menter. "Eddy viscosity transport equations and their relation to the k-ε model". *Journal of Fluid Engineering*, Vol. 119, pp. 876-884, 1997.

[8] J. Dacles-Mariani, G.G. Zilliac, J.S. Chow and P. Bradshaw. "Numerical / experimental study of a wingtip vortex in the near field". *AIAA Journal*, Vol. 33, pp. 1561-1568, September 1995.

[9] H.C. Raven, A. Van der Ploeg, and A.R. Starke. Computation of free-surface viscous flows at model and full scale by a steady iterative approach. *25th Symposium on Naval Hydrodynamics*, August 2004.

[10] L. Eça, M. Hoekstra, and J. Windt. Practical grid generation tools with applications to ship hydrodynamics. *7th International Conference on Grid Generation and Computational Field Simulations*, February 2002.

[11] L. Eça and M. Hoekstra. "An evaluation of verification procedures for CFD applications". *24th Symposium on Naval Hydrodynamics*, July 2002.

Towards a CFD validation test case - wind tunnel test of a winglet keel

Sofia Werner[1], Lars Larsson[1], Björn Regntröm[2]

[1]Chalmers University of Technology, Sweden, sw@na.chalmers.se
[2]Flowtech International AB, Sweden

1 Introduction

CFD is an increasingly important component in the design of advanced sailing yachts, in particular in the America's Cup, where the result of the race is highly dependent on the success of the design team [1],[2]. One of the important issues in the design process is the optimisation of the keel configuration. The keel normally consists of a fin that generates side force, a large streamlined bulb for the righting moment, and two winglets fitted on the bulb to decrease the induced drag and increase the effective draft when the yacht is heeled. This complex flow case presents a great challenge to the CFDer in the design team. Due to the nature of the highly competitive racing world, very few details on how to succeed in this challenge have been published, and it is difficult to obtain any experimental or computational data for comparison.
The first goal of our work is to produce a public validation case of a fin-bulb-winglet configuration. We also aim at increasing the understanding of how this flow case works, e.g. how the lift-induced vortices develop and interact, how the winglet geometry affect this vortex system and what effect this have on the induced drag. Our final goal is to learn what is required from CFD/panel code simulations for successful simulations of this complicated case. We define success in this context as the ability to correctly predict trends in a keel design and reproduce effects of geometrical changes on the flow. For this reason, the validation model has to consist of several geometrically different cases.
The current paper describes the first wind tunnel test session. The objectives of the test was to increase the understanding of the flow, and also to check how well the measuring technique could capture the effects of the geometrical variations and the features of the flow.
This test session will be succeeded by extensive CFD work, before the actual validation data will be collected in a final round.

2 Test model

Bulb and fin. The test model is a 1:4 model of an America's Cup yacht keel with a bulb and two winglets, as shown in Figure 1. The fin and the bulb were originally used for towing tank tests and they were borrowed from a research institute. The fin is a Naca 0012 wing of aspect ratio 2.4 with a trim tab at 75% of the chord. The bulb has a flat bottom and a fish tail tip. The complete geometrical description can be provided by the author on request.

Winglets. The existing towing tank model did not include any winglets. Therefore, a pair of winglets were designed and manufactured. In order to be able to produce several geometrically different cases, the winglets can be fitted to the bulb at two different longitudinal positions and they can rotate around their longitudinal axis (i.e. variable pitch).

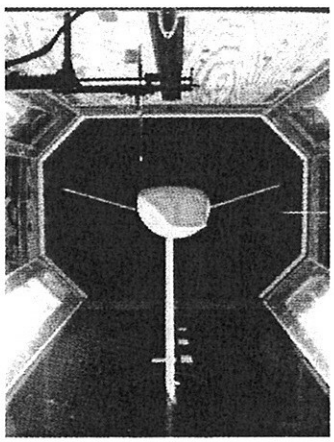

Figure 1: Wind tunnel set-up.

The design of the winglets was a compromise between a "typical" America's Cup design and what was suitable for the wind tunnel and the testing conditions. The span, 3 m full scale, is quite short in order to fit into the wind tunnel. This is compensated by a larger winglet chord length. This results in small aspect ration winglets (2.5) and possibly unrealistically bad efficiency of the winglets themselves, but on the other hand they will create a decent level of lift and produce large effects to study.
The winglet trailing edge is perpendicular to the yachts centreline and the leading edge is swept backwards. This plan form was chosen because it captures some average features seen in real designs, and it is still simple to model. The profile is a Naca 0012, which is well behaved with respect to stall. The dihedral angle is 18 degrees, which leaves the winglet tips on the same vertical position as the lowest point of the bulb.
Winglet longitudinal positions. The designers

from the last Americas Cup seemed to opt for either placing the winglet just behind the trailing edge of the fin or as far aft as possible. With the first option the chord wise lift distribution will continue from the fin over to the winglets without a jump, which could be an advantage. In the aft position, the vortex on the bulb is stronger due to the reduced diameter of the bulb, so the effect of the winglets could be more pronounced. On the other hand, with a smaller bulb diameter the geometrical span of the winglets will be smaller for the same wetted surface, compared to the forward position. It is not obvious which one of those two positions is the most advantageous. Studying the differences, not only in the drag but also in the flow details of those two situations would be interesting. Therefore, these two alternative positions were selected for the ranking tests. The model has winglet fitting arrangements for both alternative positions, as shown in Figure 2. The vacant position is filled with clay.

Pitch. In order to determine a suitable range of pitch angels the test case was analysed with the inviscid code KK-AERO. This showed that a few degrees pitch up or down results in noticable changes in the overall performance. Therefore the model was constructed so that the pitch can be varied from -3° to 3°.

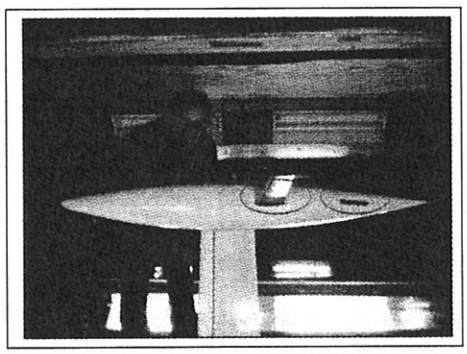

Figure 2: Two longitudinal positions.

3 Testing parameters and set-up

It is desirable to make the test resemble the full scale case as much as possible. However, in some aspects it was necessary to compromise between good testing premises and a realistic set-up. To ensure a sufficient clearance to the wind tunnel walls, no heel angle could be applied. Also, because of the difficulties to accurately set the model trim tab, it was decided to use zero trim tab angle in the tests. By testing at zero heel and zero trim tab angle, the test case deviates from the realistic situation. However, this will not decrease its value as a validation test. The missing trim tab can be somewhat compensated by testing at 4° of yaw angle, which is larger than what is typical for upwind sailing. Obviously, this will affect the profile drag, but here the main interest is the lift-induced tip vortex from the fin. Hence, it is more interesting to have a realistic lift force than a realistic profile drag.

The maximum speed in the wind tunnel with a model of this size is 40 m/s. The resulting Reynolds numbers (Re) are given in Table 1, together with the corresponding Re of the full scale keel. The testing Re is 1/7.5 of the full scale. This means that a number of important viscous effects will not be correctly represented, the main ones being:

- friction drag
- transition
- separation - trailing edge separation
- separation - laminar leading edge bubble

The *friction drag* is not a great problem, since the CFD calculations that will follow the testing will be carried out in model scale.

The *transition* positions will not be representative for a full scale yacht, not only because the Reynolds number is not correctly scaled, but also because the full scale keel might have a different section. Bearing in mind that the test case is a CFD validation test and that the transition position is not an issue of research in this project, it is sensible to use forced transition on the model.

The *separation* is a serious effect, since it changes the whole flow case. If we know that the full scale wings will not experience separation or laminar leading edge bubbles, then it is desirable that the model wings do not present this behaviour either.

Trailing edge separation can be avoided by not overloading the wings. Inviscid simulations of the test case with the panel code KK-AERO gave an idea about the load level to be expected on the winglets. A check with the 2D boundary layer code XFOIL P4 showed that the expected local lift is smaller than what is required for causing separation for both the full scale and model scale winglets. This result is valid only as long as the flow is two-dimensional. Unfortunately, we have no tool for investigating the separation in the junctions and close to the tips, where three-dimensional effects will be dominating.

Testing resources. The wind tunnel is situated at the Department of Thermo and Fluid Mechanics, Chalmers. The tunnel has a closed, atmospheric pressure test section of 1.8 m x 1.25 m x 2.7 m. The free stream turbulence intensity is 0.3%.

	Full scale	Model scale
U (m/s)	5.14	40
Fin chord (m)	1.0	0.25
Fin Re (10^6)	5.14	0.68
Winglet chord (m)	0.25	0.0625
Winglet Re (10^6)	1.29	0.17

Table 1: Reynolds numbers based on chord length.

4 Transition control

The existing fin and bulb model was equipped with studs of diameter 3 mm and height 2.5 mm. We were concerned about their size, and worried that they would disturb the flow and affect the lift behaviour too much. The main interest in this project is in the lift and the lift induced drag more than the profile drag. Therefore, we opted for thin tape strips rather than studs. The disadvantage of tape compared to studs is that it is more difficult to estimate the extra profile drag. It has not been possible to find anything in the literature on the extra drag that a tape strip produces.

An efficient way to trip the transition is to use zig-zag shaped tape [3]. This shape allows thinner layers of tape, which means less disturbance. There are some semi-empirical formulas for determining the minimum tape thickness required to cause turbulence for a given Re. However, we decided to test the different options that we had available in the testing conditions on the actual model. Several types of tape were tested. The thickest was a 0.5 mm zig-zag tape, premanufactured for gliders. Thinner tapes were home made by cutting 0.15 mm adhesive plastic film in one, two or three plies with a pair of tailors zig-zag scissors, or normal scissors for the straight tape. The test was performed using coloured glycerine oil. One of the results is shown in Figure 3. The picture shows that with no strip and for the 0.30 mm straight strip there is a laminar zone until about mid-chord. For the other devices transition occurs at the stimulator position. Thinner zig-zag strip, 0.15 mm, was also tested and was found not able to force transition.

The wakes from the studs and the zig-zag-tape peaks are visible for the whole chord length. The wakes from the studs are larger and there are larger differences in the friction (differences in colour) behind the studs, compared to the zig-zag-tape.

Out of the tested strips, we could choose between the 0.3 mm zig-zag and the 0.45 mm straight strip. The 0.45mm straight will have a larger drag due to its thickness, whereas the friction is more even behind it. It was decided to use the 0.3 mm zig-zag strip for this test. The same result was found for the winglets. For the bulb, only the 0.5 mm zig-zag tape was able to force transition.

The wakes behind the studs and the zig-zag tape are interesting. How much does this affect the result? Is the boundary layer pure turbulent, as we expect? What does it mean for the towing tank tests where they are used? These issues would be interesting to investigate further!

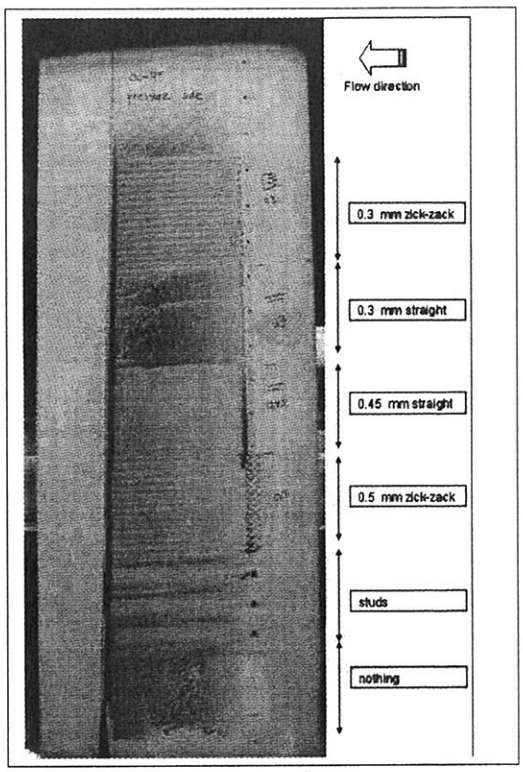

Figure 3: Paint test of trip tape.

5 Experimental method

The measurements in this test consists of wake surveys using a 5-hole pressure probe. The advantage of wake surveys is that it enables estimation of the vortex drag and the profile drag separately by integration of the three velocity components and the pressure in the viscous wake [4]. The disadvantage is that it is time consuming. Therefore, only three configurations were tested:

1. Winglets in the middle of the bulb, positive winglet pitch 2° (nose down in the wind tunnel).
2. Winglets in the middle of the bulb, negative winglet pitch 3° (nose up in the wind tunnel).
3. No winglets.

Unfortunately, there was no time to test the other longitudinal position in this test session.

The measurements were taken in a plane perpendicular to the free stream at a distance of 165 mm behind the bulb tip. For each configuration, around 2200 points in the wake were measured. In each point 10000 samples were taken with a sampling frequency of 1kHz, which gives a sampling time of 10 sec for each spatial point. Pre-tests showed that this sampling time was required in order to have max 1% error of the mean.
The probe was moved automatically between the measuring points. Unfortunately, the traversing mechanism was not optimal for the high speed and the large measuring domain in this experiment, which resulted in large executing times and low accuracy in the position. This is an issue that must improved before the next test session.
Figure 4 indicates the distribution of measuring points. The points are separated by 2.5 mm in the vertical and 2.5 mm in the horizontal direction in the vortex wakes. In the wake of the fin and the winglets between the main vortices measurements are taken at every 20 mm in the span wise direction and 2 mm in the profile thickness direction.

6 Results

Figure 5 display the differences in the viscous wake of the three configurations. (The wake is shown as measured in the wind tunnel, i.e. upside down compared to the real keel, and only a part of the fin wake is included.) With 3° negative pitch the winglet lift is directed downwards (upwards in the wind tunnel) and the lift level is considerably larger on the winglet at the fin pressure side. With positive pitch the opposite is true. The effects on the main vortex are shown in Figure 6, which clearly displays differences between the configurations. The main vortex, anti clockwise in the figure, has pushed up the winglet wakes in the fin pressure side and pushed them down on the suction side. We note that the side wash, which moves the fin wake sideways, is stronger for the configuration without winglets, which probably means that the bulb vortex is stronger. This could indicate that the induced drag is larger. Whether this is true or not can only be confirmed by applying wake integration to the cross flow components, shown in Figure 7. The shape of the vortex in this figure is interesting and hard to interpret. It is probably a result of several converging vortices. We observe that differences between the two winglet configurations are noticeable.

7 Conclusions and Discussion

The wake survey measurements carried out in this test session could detect differences in the flow between alternative configurations. The distribution of measuring points was fine enough for resolving the winglet tip vortices and the main vortex. Hence, this method will be suitable for collecting data for the ranking validation test. However, the measuring technique has to be improved in order to obtain data with a satisfactory accuracy.

8 Further work

Analysing the test result. The next step will be to program a routine for extracting the induced and profile drag from the wake survey data and apply this to the test result. The error due to the limited number of measuring points should be estimated, followed by an assessment of the required number of points to be used in the final test.
CFD simulations. The test case, including the wind tunnel boundaries, will be simulated with Fluent. The goal is to repeat the flow features seen in the experiments, and also to identify new interesting areas and questions for the succeeding wind tunnel tests. Furthermore, the possibility of estimating the induced drag by applying wake integration to the computed wake in the same way as for the experimental wake will be studied.
Further wind tunnel tests. The next experimental test session will include measurements with the 5-hole probe in the wake and in points around the model. A few more winglet pitch angles and the other winglet longitudinal position will be tested. The goal will be to collect the final validation data.
Further CFD simulations The last step in this project will be to simulate the validation cases again and hopefully to learn what is needed from the computations in order to find the same trends and ranking between the cases as in the experiments.

References

[1] Wolf. E. Graf K. CFD investigations and design integration for iacc yachts. In *High Performance Yach Design Conference, Auckland*, 2002.

[2] Sawley M. L. Cowles G., Parolini N. Numerical simulation using rans-based tools for america's cup design. In *The 16th Chesapeake sailing yacht symposium*, 2003.

[3] Hame F. R. An efficient tripping device. *Journal of the aeronautical sciences*, 226:229–361, 1956.

[4] Maskell E. C. Progress towards a method for the measurement of the components of the drag of a wing of finite span. *R.A.E. Tech. Report 72232*, 1972.

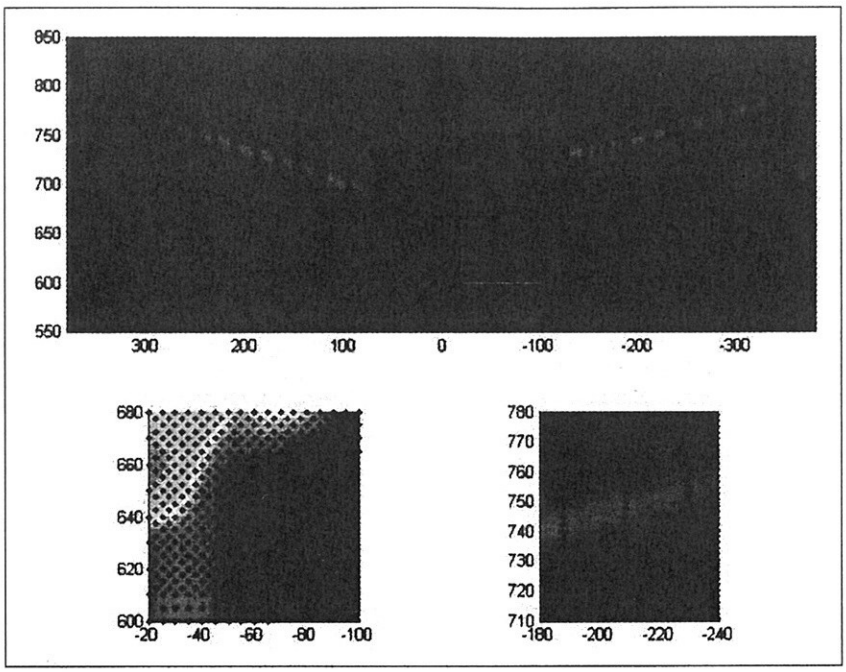

Figure 4: Measuring points.

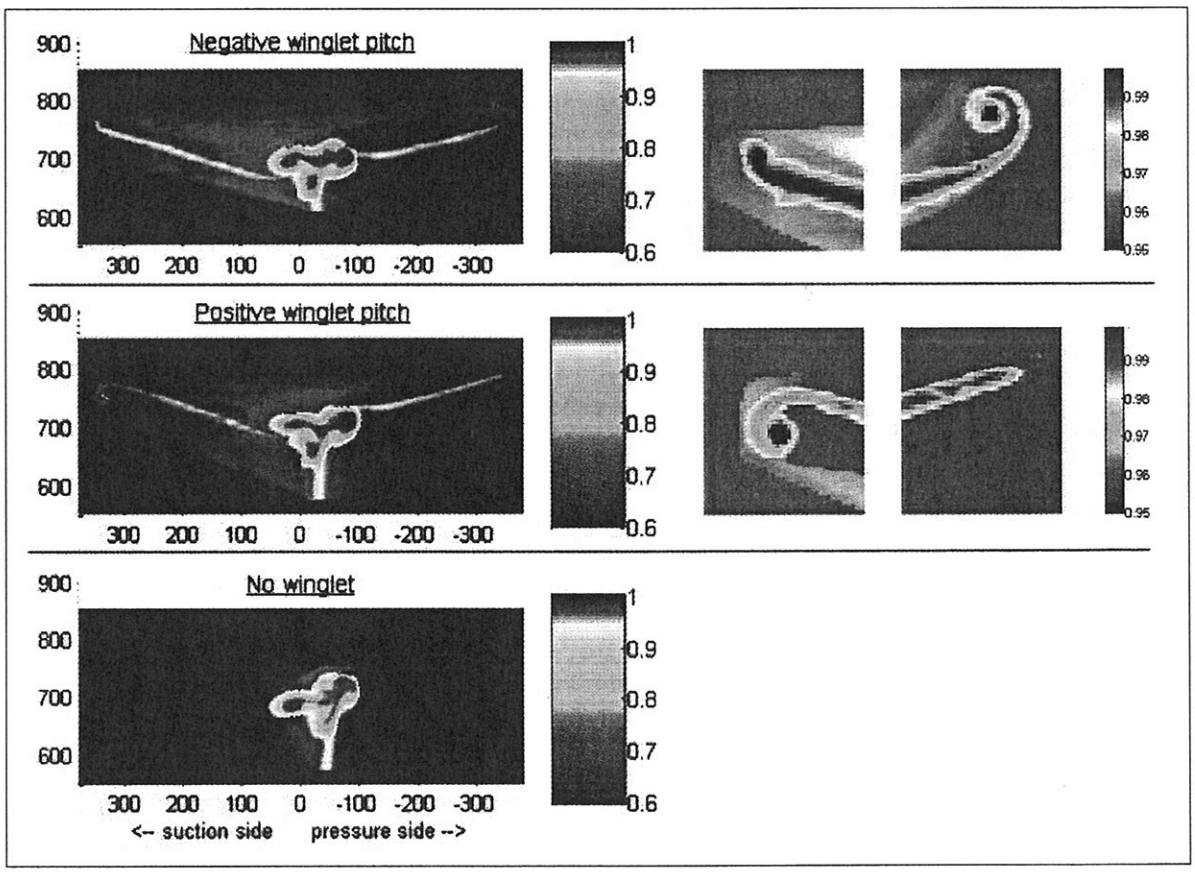

Figure 5: u/u_∞. Wake cut seen from aft. Zoom wakes of winglet tips to the right.

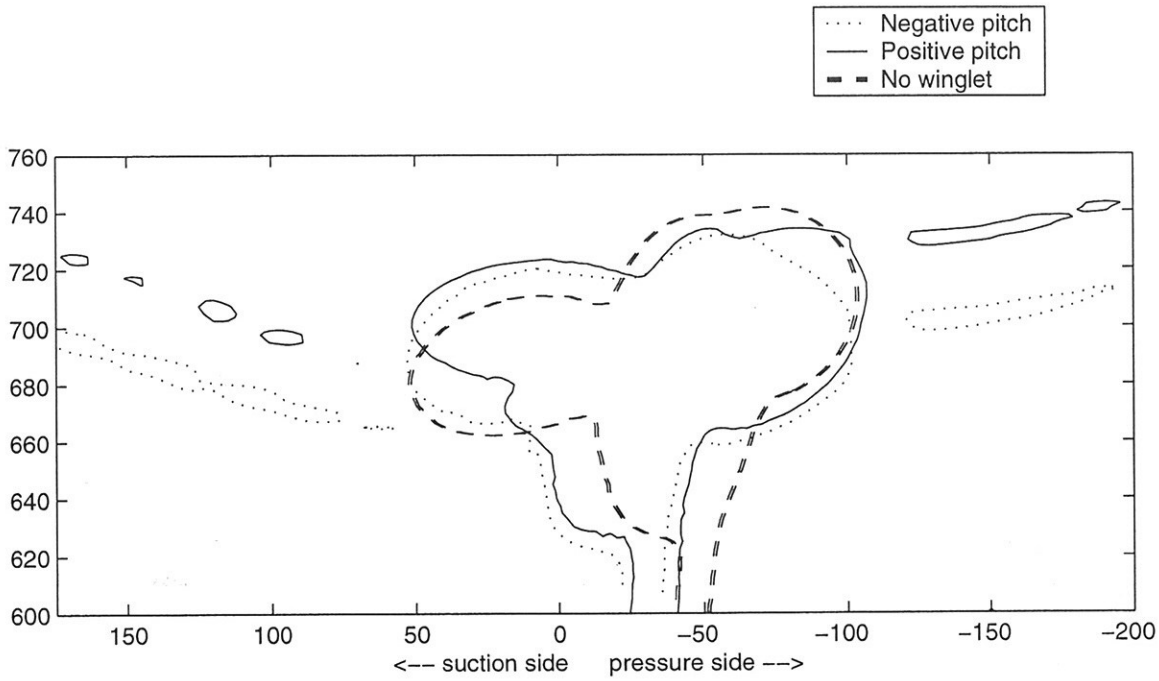

Figure 6: Contour of $u/u_\infty = 0.95$

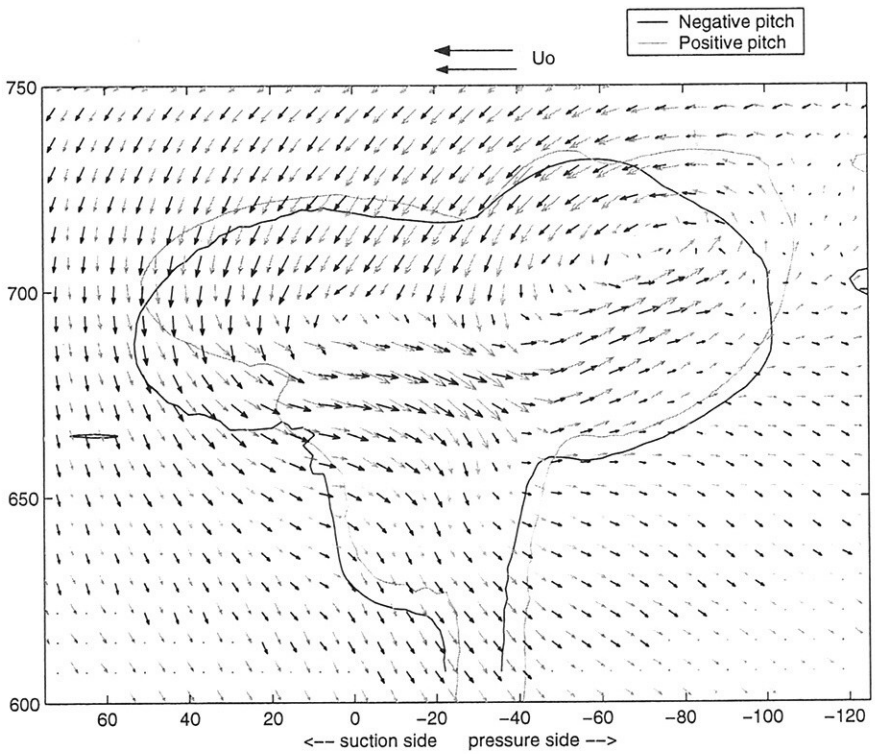

Figure 7: Cross flow components.

RANSE Simulation of Flow and Ship Motion in Manoeuvring Applications

Y. Xing-Kaeding & G. Jensen
Fluid Dynamics and Ship Theory Section, TU Hamburg-Harburg, Germany
Email: yan.xing@tu-harburg.de, g.jensen@tu-harburg.de

1 INTRODUCTION

With the growing concern on the performance based ship safty criteria, the importance of the simulation of ship manoeuvring motions in waves is increasing steadily. The traditional role of model tests is underlined by newbuildings of large seakeeping and manoeuvring basins. At the same time numerical simulation tools are continuously developped and increasingly used. Manoeuvring simulations based on coefficient models are routinely used. However, such simulations suffer from the problems in estimating the coefficients, which are best determined from model tests. More advanced simulations integrate motions in time using hydrodynamic forces which are either based on empirical formulae or special calculations for individual force components. The program SIMPLE (see Pereira 1988) is one example, which computes the hydrodynamic forces on the ship hull based on a strip theory approach beforehand for a variety of frequencies and section immersions. These methods, however, offer no full coupling of the flow field to the motions and ignore wave breaking and three-dimensional effects. Additionally, empirical assumptions especially with respect to flow seperation on the hull have a strong influence on the results.

In this paper, the authors show a fully coupled solution of the motion of the ship with appendages and the Reynolds-Averaged Navier-Stokes Equations (RANSE). A variety of verification and validation on flow-induced motion of both simple-geometry bodies and complex-geometry ships can be found in Hadzic et al. (2000, 2002) and Xing et al. (2001a, 2001b, 2004). Some preliminary results of manoeuvring applications such as turning-circle manoeuvres and Z-manoeuvres in planar motion can be found in Xing et al. (2002, 2003). In this paper further manoeuvring simulations are performed for a container ship CBOX with appendages to demonstrate the potential and robustness of the method. Steady drift motion is first computed to validate the computed forces on the ship hull and on the rudder. Then, a rudder-controlled turning-circle manoeuvre is performed for the self-propelled container ship in calm water.

2 NUMERICAL METHOD

Incompressible viscous flows with free surface are solved here by a finite volume method incorporated in the "Comet" code (CD adapco Group). The conservation equations for mass, momentum, and scalar quantities (e.g. energy or chemical species) are written in their integral form. The so-called *space conservation law* (SCL) is employed for moving-grids. The velocity and pressure fields are coupled using SIMPLE-algorithm, see Patankar & Spalding (1972). Interface-capturing method and High-Resolution Interface Capturing (HRIC) scheme have been used to model the free surface, more details are given in Muzaferija & Peric (1999). Turbulent effects are taken into account by the standard k-ε model. Due to space restriction, these basic equations will not be introduced here; for more detail, see Demirdzic et al. (2000).

The ship motion is computed simultaneously with the flow motion. The body dynamics module is incorporated into the flow solver (Comet) via its user-coding interface. The forces and moments acting on the ship are integrated from the fluid flow around the ship hull. A predictor-corrector procedure is used to predict the ship motion. This procedure is readily coupled with the iterative procedure of the flow solver. For more details about body dynamics,

integration scheme and body-flow coupling, see Xing et al. (2001a, 2001b) and Hadzic et al. (2002).

To avoid further complication of the geometry and reduce the computing effort, the propeller has been simulated by applying body forces distributed to a layer of finite-volume cells in the propeller plane, see Stern et al. (1988). Here, only the thrust and torque are considered while no side forces are taken into account.

3 NUMERICAL GRID AND BOUNDARY CONDITION

Blocks of surface-fitted grid around the ship hull together with its rudder block have been generated in an unstructured manner. The block of surface-fitted grid surrounding the ship has a shape of a rectangle and is made of a finite number of control volumes, which can have more than 6 faces. All variables are stored at the centre of each control volume. Sliding interfaces, which allow a random rudder angle, have been taken between the rudder block and the blocks surrounding it. Numerical beaches have been generated at some boundaries of the domain, which are far away from the ship, to avoid unexpected reflection of the waves at the boundaries.

For the moderate roll, pitch and heave motions of the ship, a block around the ship (including the block with the rudder) can be moved together with the ship and the grid far away from the ship is kept unchanged; the blocks in between have to be smoothed or regenerated in three dimensions. For large yaw motion (e.g. in the case of turning circle), either the whole computational domain can be moved following the yaw motion of the ship or additional body forces corresponding to the rotation should be applied to the whole domain instead of grid moving. The first alternative is used in this paper.

Great care should be taken to set boundary conditions correctly since the fluid could be flowing in or out from the same border of the domain at different stages during manoeuvring motion. Here a inlet boundary is used whenever the flow velocity is known, otherwise a pressure boundary is applied at the end of a numerical beach. No-slip wall condition has been applied to the ship hull as well as the surface of the rudder. At the bottom of the domain, slip wall condition or symmetry condition can be applied if it does not exist physically. At the top of the domain, static air pressure can be applied or other corresponding conditions can be set up if wind is considered.

4 RESULTS AND DISCUSSION

4.1 *Steady drift motion*

The container ship "CBOX", designed by FSG, is taken as one of the test models in the ROLL-S project sponsored by the Germany Ministry of Education and Research (BMBF). The model tests with CBOX are carried out in a model scale of 1/29 at the Hamburg Model Basin (HSVA). The full-scale ship has the length of 145.75 m (L) between perpendiculars and the draught of 9.0 m. The captured ship model has been run with constant forward speed (Fn = 0.23) and propeller revolution ($n = 12.3\ s^{-1}$) at several drift angles β = -10°, -5°, -2.5°, 2.5° and 5° respectively. The rudder angle has been kept zero all the time. The side forces on the hull and the rudder were measured for each drift angle.

The numerical computations are peformed also at model scale to validate the results with the experiments. The computational domain extends to 1.5 L in front of the ship, 2.5 L beside the ship and 3 L behind the ship prolonged by a numerical beach to avoid reflected waves. The top and bottom boundaries are 1.0 L above and below the still water level to simulate a deep-water condition and minimize the air flow effect. The computational grid consists of several blocks resulting in 1,200,000 cells. Figure 1 shows half of the symmetrical grid around the ship hull, the rudder and the rudder fin and the position of the sliding interfaces.

The computation has been started at a drift angle $\beta = 0°$ and a constant velocity corresponding to Fn = 0.23. The body forces simulating the effects of the propeller are added right after the start. The total thrust and torque of the propeller are determined by the instant

inflow condition (calculated by averaging fluid velocities at the propeller disk) with the help of the momentum theory and the propeller diagram. The distribution of the body forces follows the assumptions given by Stern et al. (1988). The fluid in front of and behind the propeller is such accelerated by the imposed body forces and the interations have to continue until a steady state of the fluid flow and the propeller forces is reached and residuals of both are below a prescribed value. Next, the boundary conditions are varied with different drift angles and the computations continue until flow field and forces on the hull and the rudder do not vary any more.

The predicted side forces on the hull and the rudder are compared between computation and experiment in Fig. 2. The agreement is rather satisfactory especially for the forces on the ship hull. The larger differences of the rudder lift forces are assumed to be consequences of the simplified model of the propeller since the propeller slipstream has a strong influence on the rudder inflow and such on the rudder forces. The computed free surface deformation is shown in Fig. 3 for different drift angles β = 0°, 5°, 10°. Stronger asymmetry and less dominant wave systems can be observed as the drift angle increases.

The pressure distribution on the ship hull and the rudder surface together with the free surface position and the shear stress distribution on the ship hull are shown in Fig. 4. As can be seen, the maximum pressure appears at the front of the rudder due to the propeller slipstream. High pressure appears on the ship bow at starboard while the bow at portside is subjected to large shear stress. The axial velocity contour and tangential velocity vectors at the cross section x = -0.45 L viewed from the stern are shown in Fig. 5. As can be seen, the flow becomes strongly asymmetric in this case and a small vertex is developped at the portside of the stern.

4.2 *Turning-circle manoeuvre in calm water*

A turning-circle manoeuvre has been performed for the container ship on its own spade rudder. The same grid mentioned above has been used here.

The computation has been started from a self-propelled ship in steady straight motion with a constant velocity corresponding to Fn = 0.23. Once the steady state is reached, the rudder is turned starboard by a turning rate of 13.5°/s until the maximum rudder angle (δ=35°) is reached.

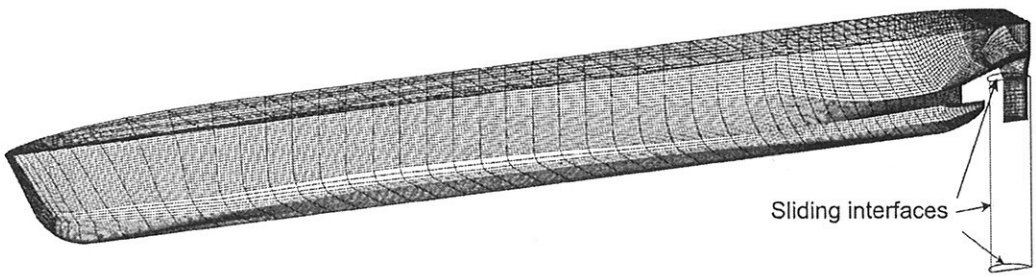

Figure 1. Numerical grid around ship hull, rudder fin and rudder together with the sliding interfaces

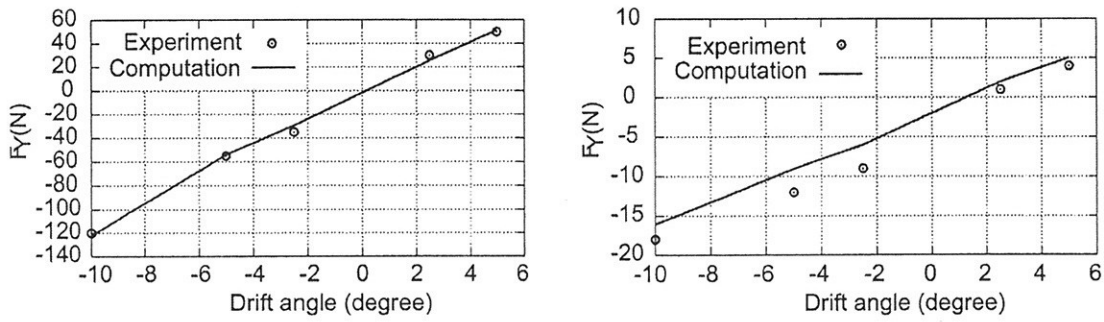

Figure 2. Comparison of side forces on ship hull (left) and rudder (right) between computation and experiment

This rudder angle is then kept until the ship has performed a turning-circle of 540°. The ship is expected to turn dramatically at the initial turning before the steady state of turning is reached. Free surface deformations can be seen from Fig. 6 during the turning-circle manoeuvre at yaw angles ψ = 0°, 30° and 60° respectively. The rudder block surrounded by sliding interfaces can also be seen from Fig. 6 at δ = 35°.

The computed yaw rate and the horizontal velocity of the ship are given in Fig. 7 against time. The non-dimensional yaw rate r' approaches the value of 0.3 at the steady turning state. The speed of the ship has also been decreased dramatically at the beginning of the turning-circle and then reached a steady state at half of the initial speed. The computed tactical diameter is about 2.98 L, which is in the range of typical values for a container ship.

Figure 8 shows the pressure distribution on the ship hull and the rudder surface as views from portside and starboard. As can be seen, the pressure on the ship stern is larger at starboard than on portside of the ship and the maximum pressure appears on the leading edge of the rudder (from starboard view). The axial velocity contour and tangential velocity vectors at the cross section x = -0.45 L viewed from bow are shown in Fig. 9 together with distorted mesh and free surface position. As can be observed, the ship has slightly heeled toward starboard (φ = 2°) as expected.

5 CONCLUSIONS

The instantaneous interaction between viscous free surface flow and flow-induced body motion has been computed using the finite volume method. Rigid body dynamics for six degrees of freedom has been integrated into the fluid solver to compute the body motion. The RANSE code proved to be capable to predict the response and hydrodynamics of the real-geometry ship, showing good agreement with experiments. Despite its shortcoming of large computational effort, the method has been seen as a robust tool to be able to cope with further complicated applications in maritime hydrodynamics. As one example, approaches to ship manoeuvring have been shown using the present method. Steady drift motions and a turning circle manoeuvre of a self-propelled container ship have been presented in this paper considering the free-surface effects. The rudder has been modelled geometrically in addition to the ship hull. The propeller has been simulated by a body force model. The model needs further refinement to better account for in-plane forces of the peopeller in manoeuvring. A Z-manoeuvre of the container ship will also be performed and compared with available experiments in the near future.

REFERENCES

Demirdzic I., Muzaferija S. & Peric, M. 2000. Computation of turbulent flows in complex geometries, chap. 7 in G. Tzabiras et al. (eds.), Calculation of Complex Turbulent Flows. WIT press, Southampton/UK. pp. 249-299.

Hadzic I., Muzaferija S., Peric M., Xing Y. & Kaeding P. 2000. Predictions of Flow-Induced Motions of Floating Bodies. Proc. 3th Numerical Towing Tank Symp. Tjaernoe/Sweden.

Hadzic I., Xing Y., Muzaferija S. & Peric M. 2002. Numerical Simulation of Interaction of a Floating Body and a Free-Surface Flow with Waves. 5th World Congress on Computational Mechanics, Vienna/Austria.

Muzaferija, S. & Peric, M. 1999. Computation of Free Surface Flow Using Interface-Tracking and Interface-Capturing Methods, chap. 2 in O. Mahrenholtz and M. Markiewicz (eds.), Nonlinear Water Wave Interaction, pp. 59-100, WIT Press, Southampton/UK.

Patankar, S. V. & Spalding, D. B. 1972. A calculation procedure for heat, mass and momentum transfer in three-dimensional parabolic flows. Int. J. Heat and Mass Transfer, 15:1787-1806.

Pereira, R. 1988. Simulation nichtlinearer Seegangslasten. Schiffstechnik, 35:173-193.

Stern F., Kim H.T., Patel V.C. & Chen H.C. 1988. A viscous-flow approach to the computation of propeller-hull interaction. J. Ship Research. 32: 246-262.

Xing Y., Hadzic I., Muzaferija S. & Peric, M. 2001a. CFD Simulation of Flow-Induced Floating-Body Motions. Proc. 16th Int. Workshop on Water Waves and Floating Bodies, Hiroshima/JAPAN. pp. 169-172.

Xing Y., Hadzic I. & Peric M. 2001b. Predictions of Floating-Body motions in Viscous Flow. Proc. 4th Numerical Towing Tank Symp., Hamburg/Germany.
Xing Y., Jensen G., Hadzic I. & Peric M. 2002. An approach to ship maneuvering by simultaneous computation of viscous flow and ship motion. Proc. 5th Numerical Towing Tank Symp. Pornichet/France.
Xing-Kaeding Y., Jensen G., Hadzic I. & Peric M. 2003. Simulation of Ship Maneuvering in Viscous Flow with Free Surface. Proc. 5th Numerical Towing Tank Symp. Rome/Italy.
Xing-Kaeding Y., Jensen G. & Peric M. 2004. Simulation of Flow-Induced Ship Motions in Waves using a RANSE Method. J. Ship Technol. Research. 51:56-68.

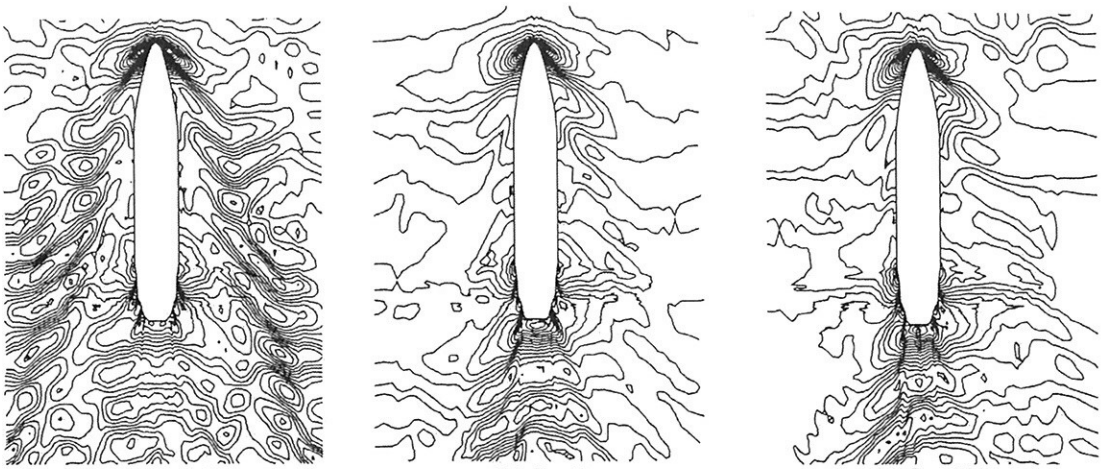

(a) $\beta = 0^o$ (b) $\beta = 5^o$ (c) $\beta = 10^o$

Figure 3. Free surface deformations during steady drift motion of a container ship

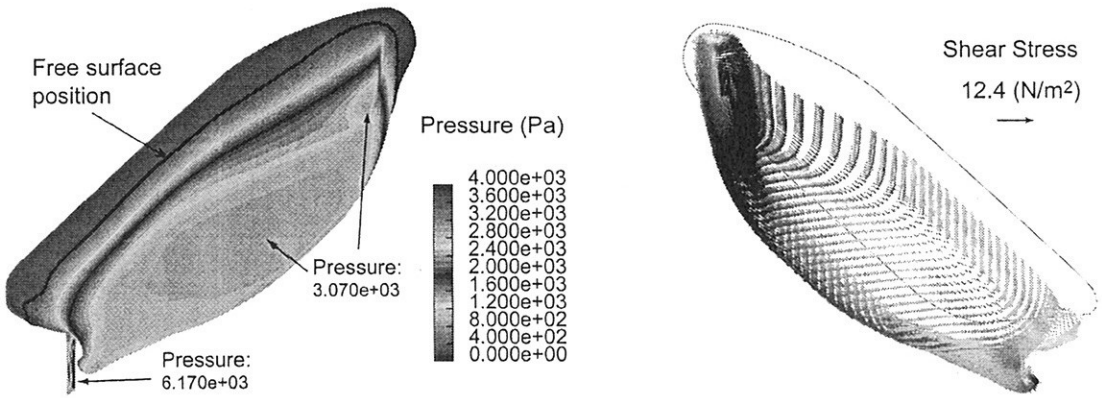

Figure 4. Pressure distribution on ship hull and rudder ($\beta = 10^o$) from starboard view (left) and shear stress distribution on ship hull from portside view (right)

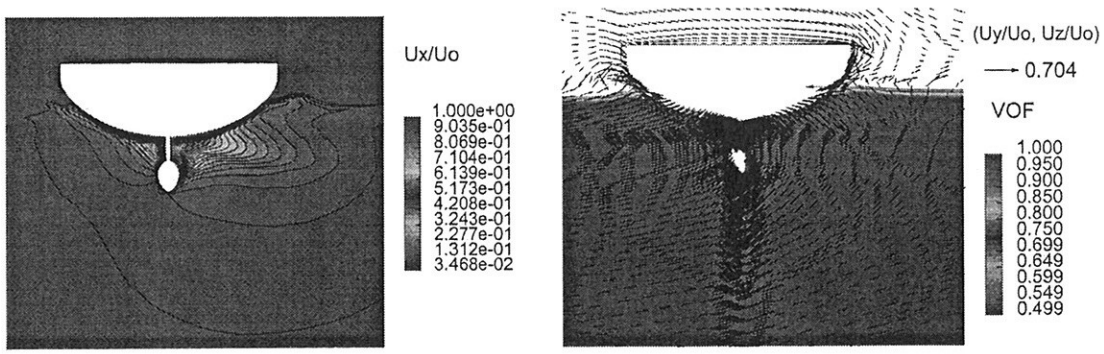

Figure 5. Axial velocity contours (left) and tangential velocity vectors (right) at plane x = -0.45L ($\beta = 10^o$)

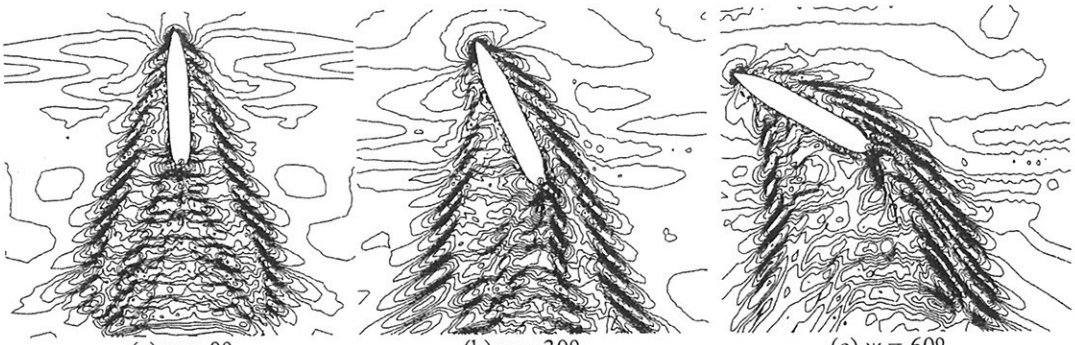

(a) $\psi = 0^o$ (b) $\psi = 30^o$ (c) $\psi = 60^o$

Figure 6. Free surface deformations during a turning-circle manoeuvre of a container ship

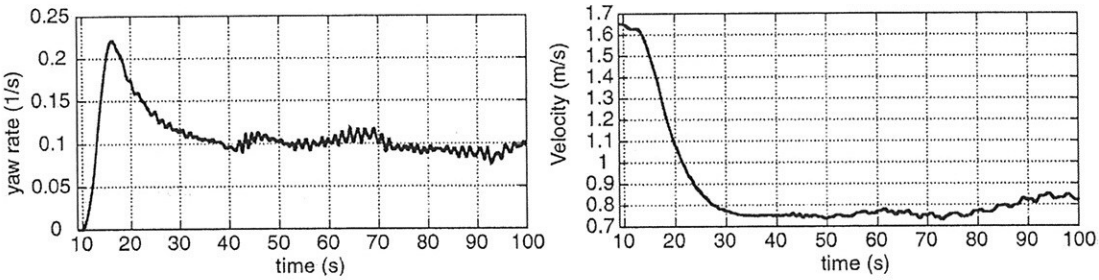

Figure 7. Yaw rate (left) and absolute velocity (right) for a turning circle manoeuvre of a container ship with operating rudder

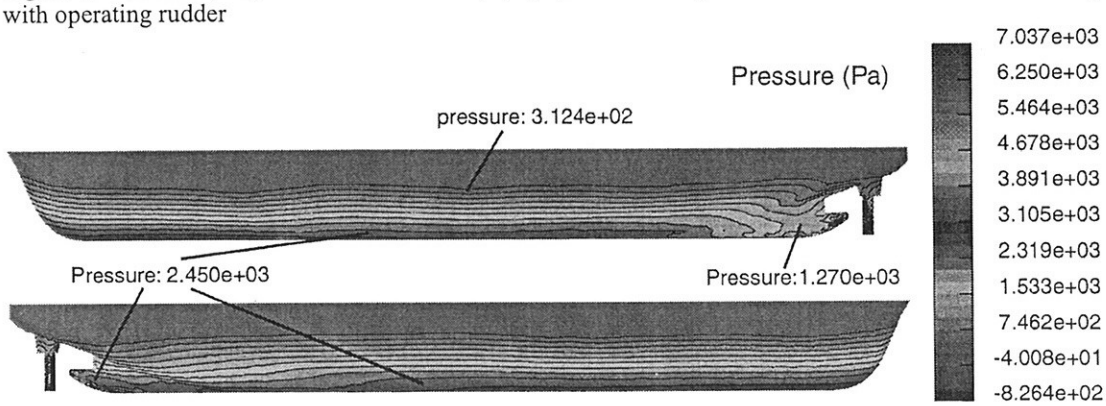

Figure 8. Pressure distribution on the ship hull and the rudder at portside (top) and starboard (bottom)

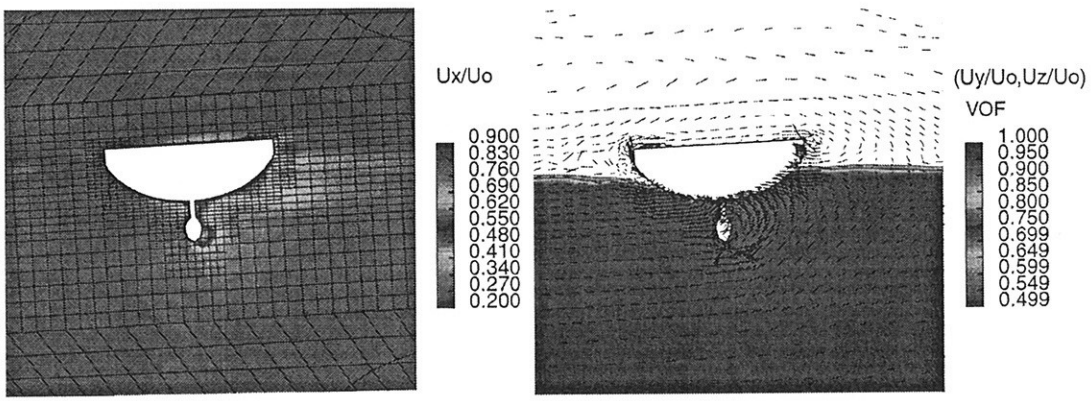

Figure 9. Axial velocity contour with distorted mesh (left) and tangential velocity vectors with free surface position (right) at the cross section x = -0.45 L (view from bow)

Comparison of Alternative Boundary-Integral Representations

Chi Yang[1], Francis Noblesse[2], Rainald Löhner[1]

[1] School of Computational Sciences, George Mason University, Fairfax, VA 22030-4444

[2] NSWC-CD, 9500 MacArthur Blvd, West Bethesda, MD 20817-5700

Introduction

Within the framework of potential-flow theory considered here, the flow in a domain is determined explicitly in terms of the flow at the boundary surface of the flow domain by means of a classical boundary-integral representation that is based on one of Green's classical integral identities. This classical boundary-integral representation defines the flow potential in terms of boundary distributions of sources and normal dipoles, and involves a Green function G and its gradient ∇G. An alternative representation of the velocity potential is given in [1]. This alternative potential representation involves a Green function G and a related vector Green function $\mathbf{G}$. The vector Green function $\mathbf{G}$ satisfies the relation $\nabla \times \mathbf{G} = \nabla G$. Thus, $\mathbf{G}$ is comparable to G and, in particular, is no more singular than G. The alternative potential representation given in [1] therefore is weakly singular in comparison to the classical potential representation, which involves ∇G. A related property of the weakly-singular boundary-integral representation is that it defines a potential that is continous at the boundary surface of the flow domain, whereas the potential defined by the classical boundary-integral representation (which involves a boundary distribution of dipoles) is discontinuous at the boundary surface.

The classical potential representation and the alternative weakly-singular representation are given in [1] for 3D wave diffraction-radiation with forward speed (ship advancing in regular waves), and the particular cases corresponding to zero forward speed (wave diffraction-radiation by an offshore structure) or zero wave frequency (ship advancing at constant speed in calm water). These alternative boundary-integral representations are compared here for the particular case of steady flow about a ship advancing at constant speed in calm water. The classical and weakly-singular potential representations express the potential as the sum of a local-flow component and a wave component. In the farfield, the wave components associated with these alternative boundary-integral representations are identical, as one expects. Farfield waves are considered here, for the particular case of steady flow as already noted.

Farfield waves are defined by a one-dimensional Fourier superposition of elementary waves. The amplitude of the component elementary waves in this Fourier representation is defined by distributions of elementary waves over the mean wetted ship hull Σ_B and the intersection curve Γ of the hull surface Σ_B with the mean free surface. Thus, the wave-spectrum (or wave-amplitude) function S that defines farfield waves is given by the sum of a surface component S^B and a curve component S^Γ, i.e.

$$S = S^B + S^\Gamma = \int_{\Sigma_B} d\mathcal{A}\, A^B e^{kz} E + \int_\Gamma d\mathcal{L}\, A^\Gamma E \quad \text{with} \quad E = e^{i(\alpha x + \beta y)} \tag{1}$$

Here, $d\mathcal{A}$ and $d\mathcal{L}$ stand for the differential elements of area and length of the surface Σ_B and the curve Γ, respectively. The amplitude functions A^B and A^Γ in (1) that correspond to the classical and weakly-singular potential representations are given in [1]. Thus, the classical and weakly-singular potential representations yield different surface and curve components S^B and S^Γ, although the sum $S^B + S^\Gamma$ is identical for these alternative potential representations. The dispersion relation $F^2\alpha^2 = k$ for steady free-surface flows defines the wavenumber $k = \sqrt{\alpha^2 + \beta^2}$ and the Fourier variable α in terms of the Fourier variable β by the relations

$$k = (1/2 + \sqrt{1/4 + (F^2\beta)^2})/F^2 \qquad \alpha = \sqrt{k}/F \tag{2}$$

Thus, the spectrum functions S^B, S^Γ and S are functions of the Fourier variable β.

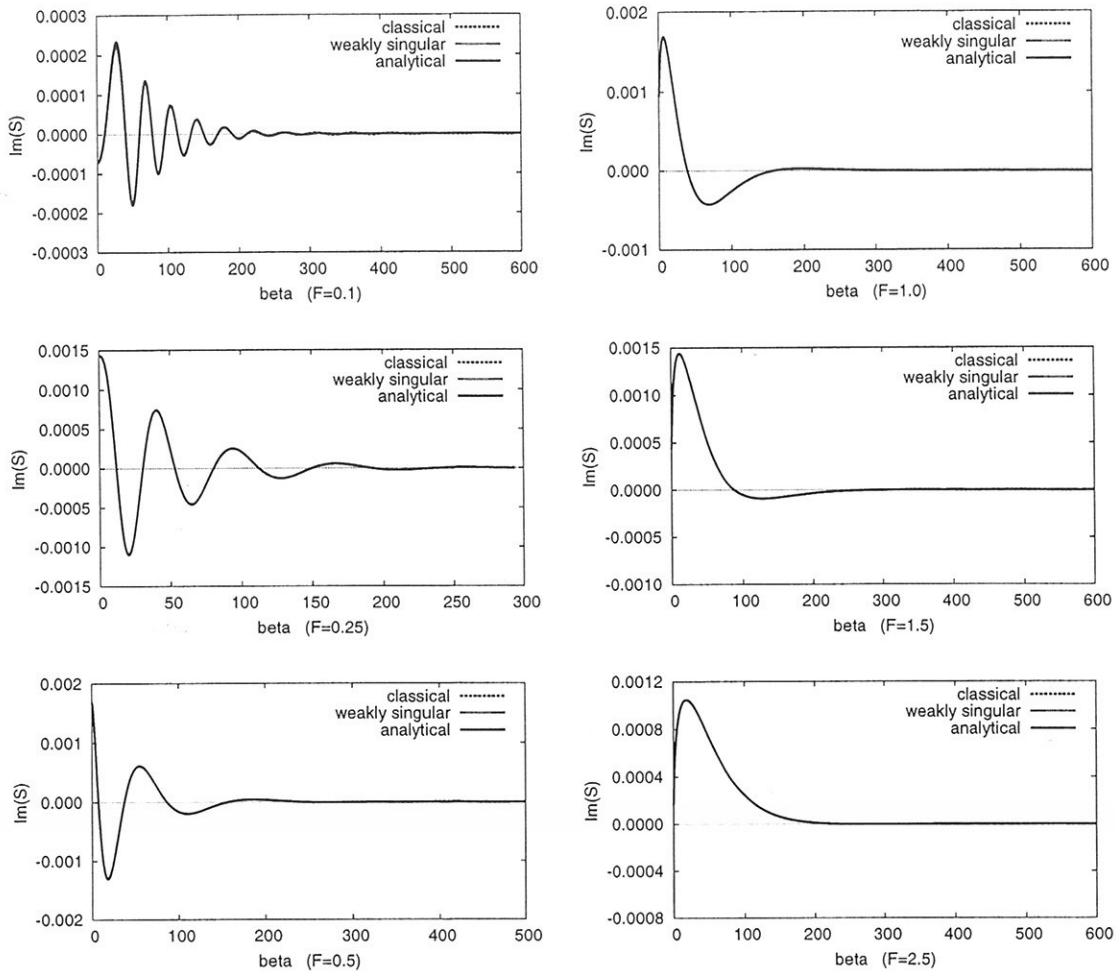

Fig. 1 Wave-spectrum functions of the steady free-surface flow generated by a source-sink pair at an ellipsoidal boundary surface for $F = 0.1\,, 0.25\,, 0.5$ and $F = 1.0\,, 1.5\,, 2.5$ (left and right columns)

Comparison of wave-spectrum functions

The surface and curve wave-spectrum components S^B and S^Γ in (1) that correspond to the classical and weakly-singular potential representations are compared in [1] for the flow generated by a source-sink pair (located at $x = \pm 1/2\,, y = 0\,, z = -\delta$ with $\delta = 0.02$) at a boundary surface Σ_B taken as a half ellipsoid (Thus, the intersection curve Γ of the boundary surface Σ_B with the free surface is an ellipse). Three Froude numbers are considered in [1]: $F = 0.25\,, 0.316$ and 0.408. Although these three Froude numbers cover the range of most practical applications, it is useful to compare the surface and curve components S^B and S^Γ related to the classical and weakly-singular potential representations for a broader range of Froude numbers. The comparison reported in [1] is then reconsidered here for six Froude numbers : $F = 0.1\,, 0.25\,, 0.5\,, 1.0\,, 1.5$ and 2.5. Furthermore, numerical results are presented here in a clearer way (Fig.4 in [1] contains 3 curves, which makes it hard to clearly ascertain differences between the classical and weakly-singular potential representations).

For the flow generated by a source-sink pair considered here, [1] shows that the real part of the wave-spectrum function S is null, and the imaginary part of S is given by the simple analytical expression

$$S(\beta) = 2\,q\; e^{-\delta\, k}\; \sin(\alpha/2) \tag{3}$$

where k and α are given by (2), $q = 0.001$ stands for the strength of the source and sink, and $\delta = 0.02$

is the submergence-depth of the source and sink. Fig. 1 depicts the imaginary parts of the wave-spectrum functions $S(\beta)$ given by the classical and weakly-singular potential representations. The analytical result (3) is also depicted in Fig. 1. The fact that the three curves depicted in Fig. 1 cannot be distinguished provides a verification of the mathematical expressions given in [1] for the classical and weakly-singular representations of the wave-spectrum function, and of the accuracy of the numerical calculations reported here (the boundary surface Σ_B is approximated by 45,402 flat triangular panels).

Figs 2a-f depict the real parts (top row) and imaginary parts (bottom row) of the surface and curve components $S^B(\beta)$ and $S^\Gamma(\beta)$ of the wave-spectrum function $S = S^B + S^\Gamma$ associated with the classical potential representation (left column) and the weakly-singular representation (right column). Figs 2a,b,c,d,e,f depict the surface and curve components S^B and S^Γ for $F = 0.1\,, 0.25\,, 0.5\,, 1.0\,, 1.5\,, 2.5\,,$ respectively. The left columns of Figs 2a-f show that the surface and curve components S^B and S^Γ associated with the classical potential representation do not decay as $\beta \rightarrow \infty$, and that the components S^B and S^Γ largely cancel out (the real parts of these components cancel out exactly). The right columns of Figs 2a-f show that the surface and curve components S^B and S^Γ related to the weakly-singular potential representation decay as $\beta \rightarrow \infty$, and that numerical cancellations between the components S^B and S^Γ are greatly reduced (in comparison to the left columns). The foregoing numerical results confirm the asymptotic analysis given in [1].

Conclusion

The numerical results depicted in Figs 2a-f establish that — for steady free-surface flow — the wave-spectrum function related to the weakly-singular potential representation given in [1] is much better suited for numerical evaluation than the classical wave-spectrum function. This conclusion is shown here to hold for a broad range of Froude numbers, including small and large Froude numbers not previously considered in [1].

For wave diffraction-radiation without forward speed (e.g. by an offshore structure), the classical wave-spectrum function only involves the surface component S^B (the curve component S^Γ is null if $F = 0$). Thus, no numerical cancellations can occur in this case, and the classical wave-spectrum function is preferable to the wave-spectrum function related to the weakly-singular potential representation (for which S^Γ is not null).

For the general case of wave diffraction-radiation with forward speed, the wave potential $\widetilde{\phi}$ at a flow-field point $\widetilde{\mathbf{x}}$ is given by $\widetilde{\phi} = \widetilde{\phi}^i + \widetilde{\phi}^- - \widetilde{\phi}^+$ where $\widetilde{\phi}^i$ and $\widetilde{\phi}^\pm$ are associated with the inner and outer dispersion curves I and $O^\pm$, respectively, defined in [2]. The wavenumber k and the related Fourier variables α and β are bounded for the inner dispersion curve I but are unbounded for the outer dispersion curves $O^\pm$. Thus, the classical representation and the weakly-singular representation can be expected to be preferable for the wave potentials $\widetilde{\phi}^i$ and $\widetilde{\phi}^\pm$, respectively; see [3].

References

[1] Noblesse F., Yang C. (2004) *Weakly-singular boundary-integral representations of free-surface flows about ships or offshore structures*, Jl of Ship Research, 48:31-44

[2] Noblesse F., Yang C. (2004) *A simple Green function for diffraction-radiation of time-harmonic waves with forward speed*, Ship Technology Research, 51:35-52

[3] Noblesse F. (2005) *Generalized boundary-integral representation of 3D flow about a ship advancing in regular waves*, submitted for presentation at 10^e Journées de l'Hydrodynamique

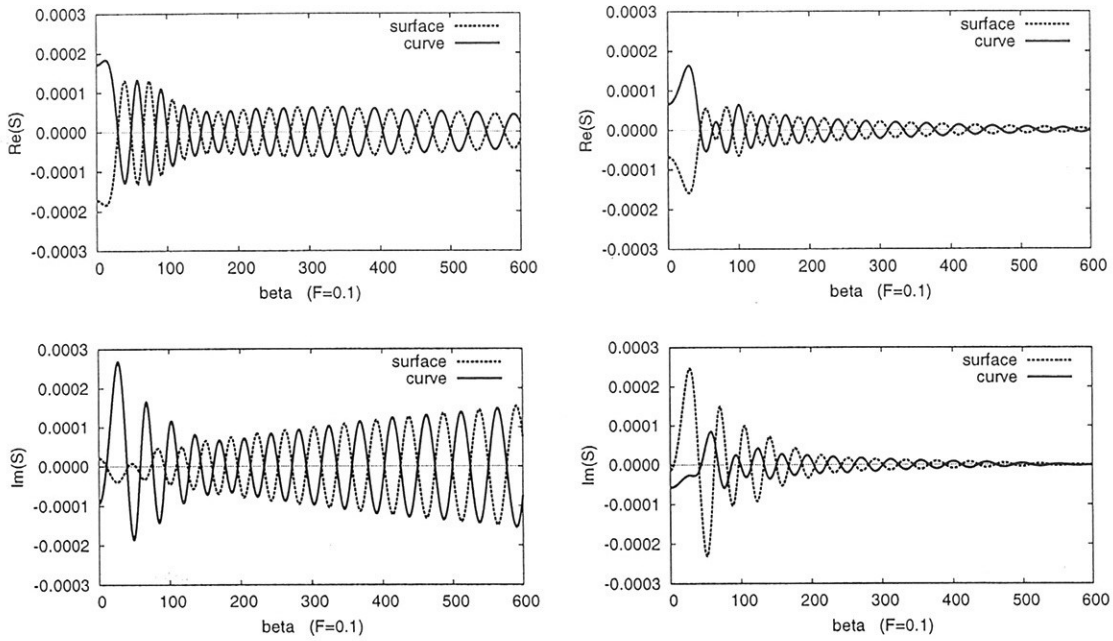

Fig. 2a Real and imaginary parts (top and bottom rows) of the surface and curve components S^B and S^Γ of the wave-spectrum function $S = S^B + S^\Gamma$ associated with the classical and weakly-singular potential representations (left and right columns), Froude number = 0.1

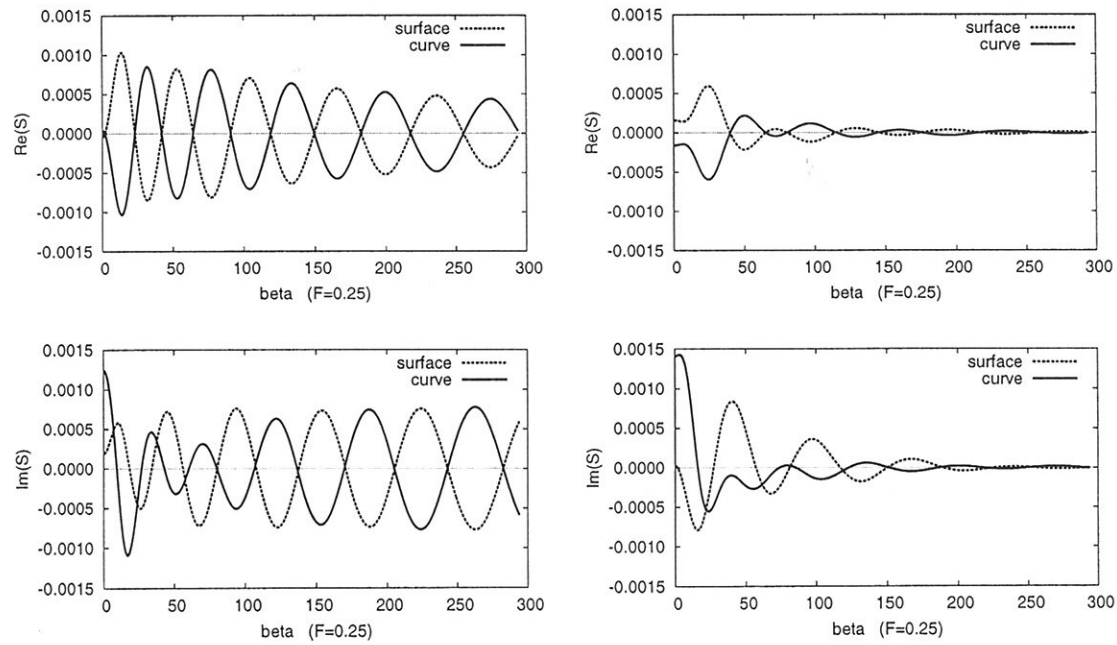

Fig. 2b Real and imaginary parts (top and bottom rows) of the surface and curve components S^B and S^Γ of the wave-spectrum function $S = S^B + S^\Gamma$ associated with the classical and weakly-singular potential representations (left and right columns), Froude number = 0.25

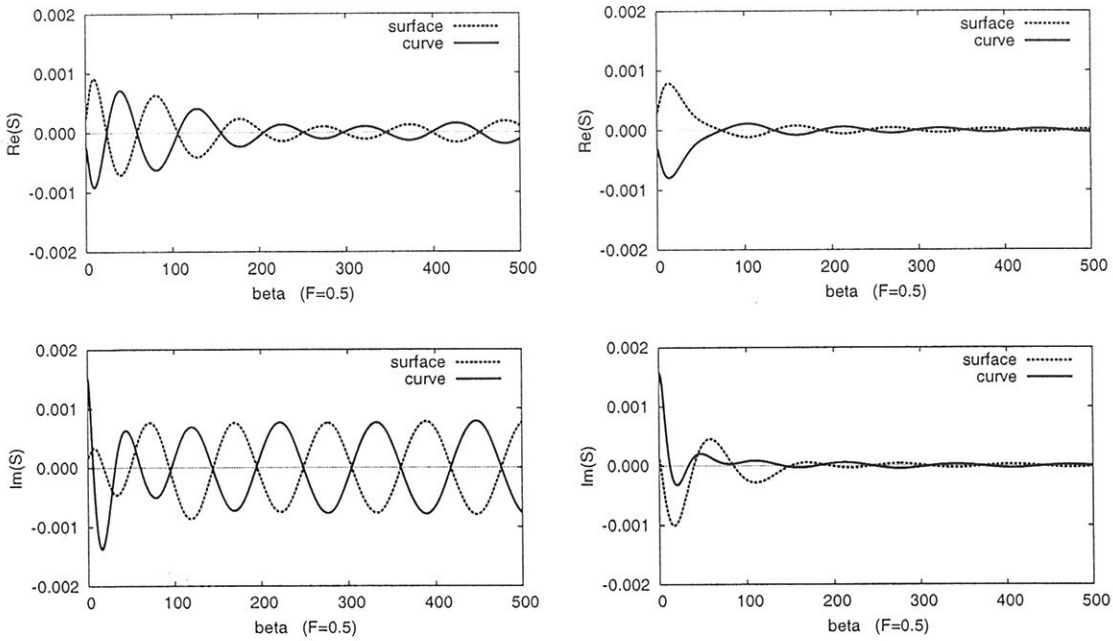

Fig. 2c Real and imaginary parts (top and bottom rows) of the surface and curve components S^B and S^Γ of the wave-spectrum function $S = S^B + S^\Gamma$ associated with the classical and weakly-singular potential representations (left and right columns), Froude number = 0.5

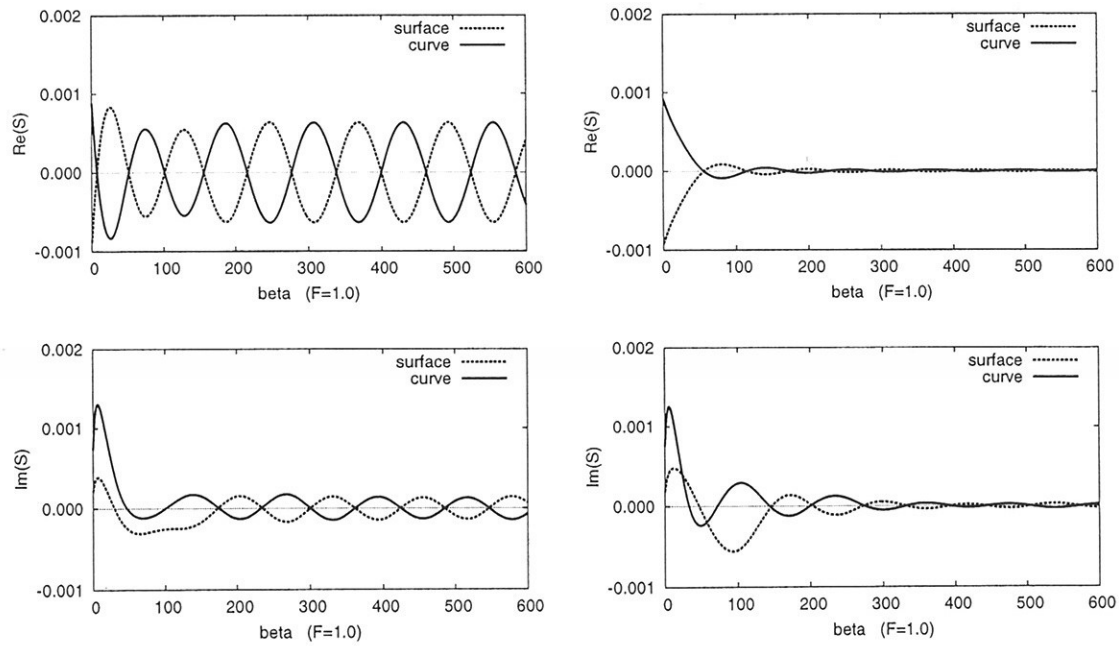

Fig. 2d Real and imaginary parts (top and bottom rows) of the surface and curve components S^B and S^Γ of the wave-spectrum function $S = S^B + S^\Gamma$ associated with the classical and weakly-singular potential representations (left and right columns), Froude number = 1.0

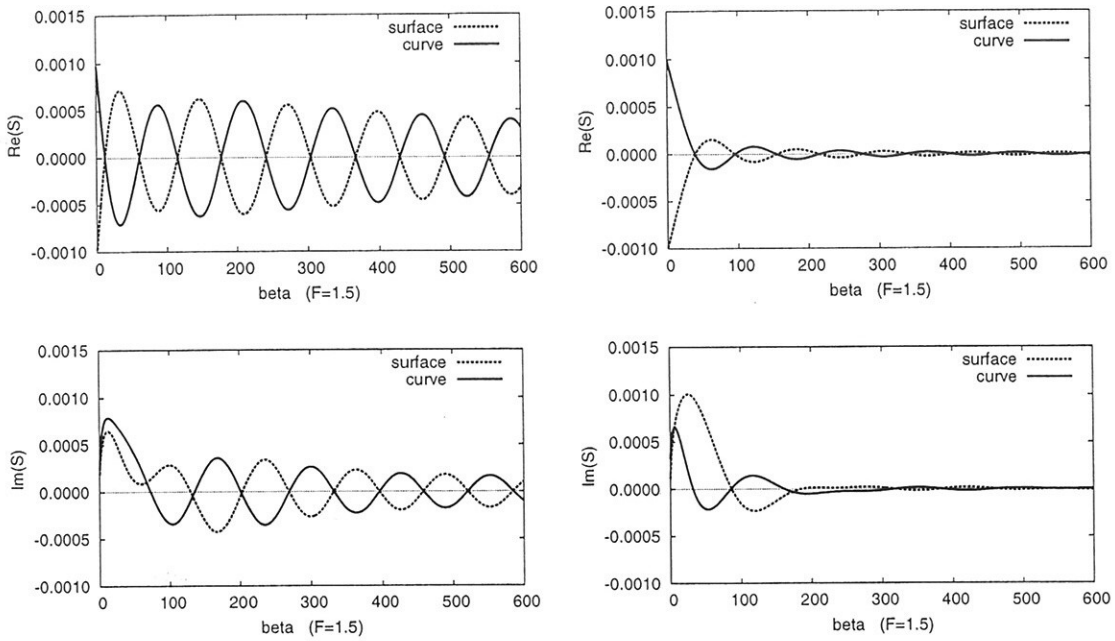

Fig. 2e Real and imaginary parts (top and bottom rows) of the surface and curve components S^B and S^Γ of the wave-spectrum function $S = S^B + S^\Gamma$ associated with the classical and weakly-singular potential representations (left and right columns), Froude number = 1.5

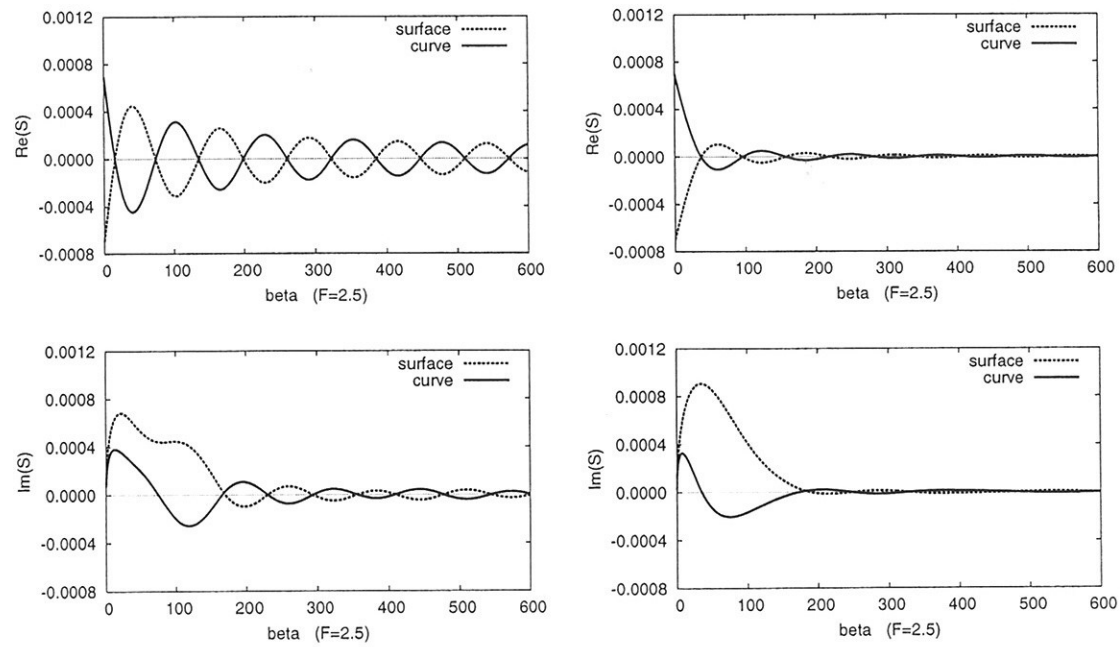

Fig. 2f Real and imaginary parts (top and bottom rows) of the surface and curve components S^B and S^Γ of the wave-spectrum function $S = S^B + S^\Gamma$ associated with the classical and weakly-singular potential representations (left and right columns), Froude number = 2.5

Fifth Framework
Programme of the
European Community

8th Numerical Towing Tank Symposium (NuTTS'05)

Varna, Bulgaria
2-4 October 2005

Bulgarian
Ship Hydrodynamics
Centre

Sponsored by the European Commission under the project HyTech

Topics:

- Nonlinear flows around marine structures (LES, RANSE, Euler with or w/o free surface)
- Free-surface flows around marine structures (3-d seakeeping, free-surface viscous flows)
- Related topics (validation experiments, numerical techniques, grid generation, etc)

Deadlines:	Early feedback:	30 April 2005
	Extended Abstracts received:	**31 July 2005**
	Last possible update (for a fee):	4 September 2005

You are invited to participate in the above event. The objective of the event is to provide a forum for informal discussions among experts in the field and to disseminate latest results. The event will be held in a conference hotel at the seaside near Varna with all participants staying in the venue. All participants stay and have meals together to maximize interaction and discussion. The extended abstracts of the proposed talk will be directly reproduced in the proceedings. There will be no full paper as such. Proceedings will be in black and white. Work in progress, encountered problems, etc. should be discussed in an open, informal atmosphere (no ties!) among colleagues.

Extended abstracts are limited to 6 pages A4 format with 2.5 cm margin everywhere. The first page of the extended abstract should be headed with the title and authors' full names and email addresses in a compact form to economize on space. Font size shall not be less than 10pt times new roman. Academic titles and page numbers shall be omitted. The extended abstract shall neither contain an abstract of the abstract, nor keywords, nor further headers.

An early reply will help us in organizing the event better. For the early feedback, a tentative title or topic will suffice. The initial abstract shall be already sufficient to evaluate the work, i.e. give theory and figures of preliminary results.

Following the tradition of previous NuTTS events, the fees will be kept low to allow a maximum number of scientists to attend. The **fees including accommodation** (3 nights in a four-star hotel starting from Sunday night) **and meals** during the symposium will be:

200 Euro	PhD candidates and students (expected to share double)
300 Euro	authors (in single room)
400 Euro	others (in single room)

Reduced fees possible if hotel not supplied.

The fees are due cash on arrival.